Instrument Systematics Calibration and Performance Validation for High Precision Photometry Missions

by

Akshata Krishnamurthy

Submitted to the Department of Aeronautics and Astronautics
in partial fulfillment of the requirements for the degree of

Doctor of Philosophy

at the

MASSACHUSETTS INSTITUTE OF TECHNOLOGY

February 2020

Author ... Signature redacted .....
Department of Aeronautics and Astronautics
January 6th, 2020

Certified by ... Signature redacted .....
Sara Seager
Professor of Planetary Science, Physics, and Aeronautics and Astronautics
Thesis Supervisor

Certified by ..... Signature redacted .....
Jeffrey Hoffman
Professor of Aeronautics and Astronautics

Certified by .... Signature redacted .....
George Ricker
Senior Research Scientist, Kavli Institute for Astrophysics and Research

Certified by ..... Signature redacted .....
Rebecca Masterson
Principal Scientist, Aeronautics and Astronautics

Accepted by ..... Signature redacted .....
Sertac Karaman
Associate Professor of Aeronautics and Astronautics
Chair, Graduate Program Committee

Instrument Systematics Calibration and Performance Validation for High Precision Photometry Missions

by

Akshata Krishnamurthy

Submitted to the Department of Aeronautics and Astronautics
on January 6th, 2020, in partial fulfillment of the
requirements for the degree of
Doctor of Philosophy

Abstract

Exoplanet detection using planetary transits requires very high precision photometry. The systematic noise requirement on photometry missions is limited to tens of parts per million over few hour timescales. The present work focuses on developing a generalized framework to improve bright star photometry for both large space-based telescopes and small satellite missions. The framework uses active integration with inherent feedback mechanisms in order to maximize the utility of results from three functional areas: simulation and modeling, laboratory characterization, and flight data analysis techniques. We systematically assess the performance of the system by identifying, characterizing, calibrating, and removing the major systematic noise sources from the flight data with the goal to establish a noise floor for the mission. We present two applications namely the Transiting Exoplanet Survey Satellite (TESS) and Arcsecond Space Telescope Enabling Research in Astrophysics (ASTERIA).

TESS is a NASA Astrophysics Explorer mission that was successfully launched in April 2018. The present work establishes a noise floor of 16 ppm at 4 hours for TESS by evaluating hundreds of non-variable bright stars over multiple sectors of observation. We also develop methods to improve the photometric performance for outliers that do not conform to the noise floor. In addition, we develop laboratory techniques to very precisely characterize key detector properties such as absolute quantum efficiency and charge blooming.

ASTERIA is a 6U CubeSat that was deployed into a low-earth orbit in November 2017. The present work provides a framework to assess the photometric performance of ASTERIA by developing one of the first data analysis pipelines for CMOS science. We demonstrate photometric precision of 65 ppm at 2 hours for HD219134, and 15 ppm at 2 hours for Alpha Centauri. We also present in-flight calibration and ground characterization tests of the camera assembly to characterize and remove significant noise sources such as fixed pattern noise and temperature variations.

Using the results from this research, we develop a pipeline-driven approach for calibration test development for SPARCS, an upcoming JPL CubeSat mission to

demonstrate UV photometry, and provide guidelines for early design phase noise budgeting and detector selection for the ASTERIA constellation concept.

Thesis Supervisor: Sara Seager
Title: Professor of Planetary Science, Physics, and Aeronautics and Astronautics

Thesis Committee Chair: Jeffrey Hoffman
Title: Professor of Aeronautics and Astronautics

Thesis Committee Member: George Ricker
Title: Senior Research Scientist, Kavli Institute for Astrophysics and Research

Thesis Committee Member: Rebecca Masterson
Title: Principal Scientist, Aeronautics and Astronautics

Acknowledgments

I am sincerely thankful to all the people who have supported me in this incredible journey at MIT. I would like to express my deepest gratitude to my advisor Sara Seager for the opportunity to work with her over the past six and half years; five and half as a graduate student and for inspiring me in countless ways during my time here. I owe a debt of gratitude to my committee chair and academic advisor, Jeff Hoffman for his support and guidance throughout, and for this wonderful opportunity to pursue my PhD in Aero-Astro. I would like to thank my thesis committee members: George Ricker, for the incredible opportunity to work on TESS and Becky Masterson, for her invaluable feedback and discussions on calibration testing. I would like to thank my readers: Roland Vanderspek, without whose guidance and direction a huge portion of my thesis wouldn't have been possible, and Deb Woods, for taking time out from her busy schedule to read my thesis and provide feedback.

It has been a special privilege to work with many people in the ASTERIA team. I am forever indebted to Mary Knapp and Matt Smith for the many opportunities they have presented to me and for their invaluable insights during our frequent telecons. I would also like to thank Sarah Hornbeck, Brice, Vanessa, Kyle, Lorraine and Chris Pong for their help and support.

I would like to thank the TESS team members for being a great team to work with and for their camaraderie. I owe special thanks to Michael Fausnaugh for all his help, insights and discussions on noise, whitening, and error bars. Thanks to Carolyn, Joel, Sormeh, Steve, Robb, Tom, Ron, Bev, Natalia, Chelsea for their help and support.

I would like thank David Ardila for the opportunity to work on SPARCS and for his invaluable insights.

Thanks also to all the past and present members of the Seager group including Tajana, Ana, Zahra, Julien.

I am grateful to the MIT Kavli Institute for providing me a home department; special thanks to Debbie, Teresa and Jean for their incredible kindness, and for keeping my spirits high every time I ran into them in the hallways of 37. I would like to

thank Beth and Jennie in Aero Astro, and Karen Willis at EAPS for their support. Special thanks to Oli de Weck for his mentorship.

I would like to express my deepest gratitude to my mother Sumana, father Krishnamurthy, and sister Anusha for always being supportive of everything I ever wanted to do, and for making my life better in a million ways. I am thankful to my new family members, Anjana, Shankar and Ajay for their love and encouragement. I am forever indebted to my husband, Alok for his support, compassion and selfless commitment over the last five years. He's always believed in me, encouraged me to aim higher, and continues to inspire me in a countless ways.

I am sincerely grateful to the Schlumberger Foundation for supporting me with the Faculty for the Future fellowship for five years. I have also received support through the Zonta Amelia Earhart Fellowship, the SPIE Optics Education Scholarship, the MKI travel grant, MIT GSC travel grant and I am grateful for their support.

This work was funded by the NASA JPL SURP Grant, and the NASA grant (NNG14FC03C).

Contents

List of Figures

List of Tables

Chapter 1

Introduction

Planets orbiting other stars are called exoplanets. A little over two decades ago, 51 Peg, the first planet to orbit a Sun-like star was discovered [1]. Since then, exoplanet discovery has emerged as an exciting and vibrant field of science. Over 4099 planets have been discovered using five different techniques: radial velocity, transits and occultations, microlensing, direct imaging, and astrometry. While radial velocity and transit detection techniques are sensitive to planets that orbit closer to the host star, microlensing, direct imaging, and astrometry are preferential towards planets in wider orbits, making the techniques complementary [2]. With technological advancement, we are now closer than ever to answer key questions such as: Are there other Earth-like planets? Can they support life? With missions such as PLAnetary Transits and Oscillations of stars (PLATO) [3], James Webb Space Telescope (JWST) [4] and the ongoing development of Coronograph [5] and Starshade technology [6], the field of exoplanets is rapidly moving towards the discovery and atmospheric characterization of smaller planets, with the hope that one day we can directly image and characterize an Earth analog [7].

The present work focuses on developing techniques to improve bright star photometry using both large space-based telescopes and small satellite missions. Bright stars are especially interesting because they facilitate easier followup measurements of planet masses and characterization of atmospheres by other ground-based and space-based observatories. The objective of the thesis is to advance our understanding of

systematic noise sources using novel modeling and laboratory techniques, and developing flight data analysis techniques for systematic noise calibration and removal, thus improving photometric performance.

1.1 Overview

The study of exoplanets is one of the most exciting and rapidly evolving fields of science. Especially interesting are those systems where the planet's orbit carries it directly across the face of its host star. If a planet passes directly between a star and the observer's line of sight, it blocks out a tiny portion of the star's light, thus reducing the star's apparent brightness as shown in Figure 1-1. The main advantage of the transit method is that the planet radius can be determined from the magnitude of the drop in the star's brightness seen in the light curves. When combined with the radial velocity data, which provides the planet's mass, the planet's density can be estimated. In addition, by monitoring the depth of the transits at different wavelengths, the absorption spectrum, and hence the atmospheric composition can be deduced. By observing both the primary and secondary transits, the planet's actual spectrum and temperature can be inferred.

The transit method is currently the most effective and sensitive method that has revolutionized the field enabling the detection of thousands of planets. The field of exoplanets, planets orbiting stars other than the Sun, has grown rapidly since the first exoplanet around a main-sequence star was discovered in 1995. As of November 2019, the transit method has discovered 3157 planets out of a total of 4099 confirmed planets. Figure 1-2 shows the number of exoplanets detected by different detection techniques and the corresponding discovery year. Several ground-based observatories such as the MEarth Project [9], SuperWASP [10], KELT [11], and TRAPPIST [12] have been carrying out large-scale search surveys together with the space-based observatories.

In this thesis, we develop a comprehensive framework for assessing, validating and improving performance for high precision transit photometry missions using high-

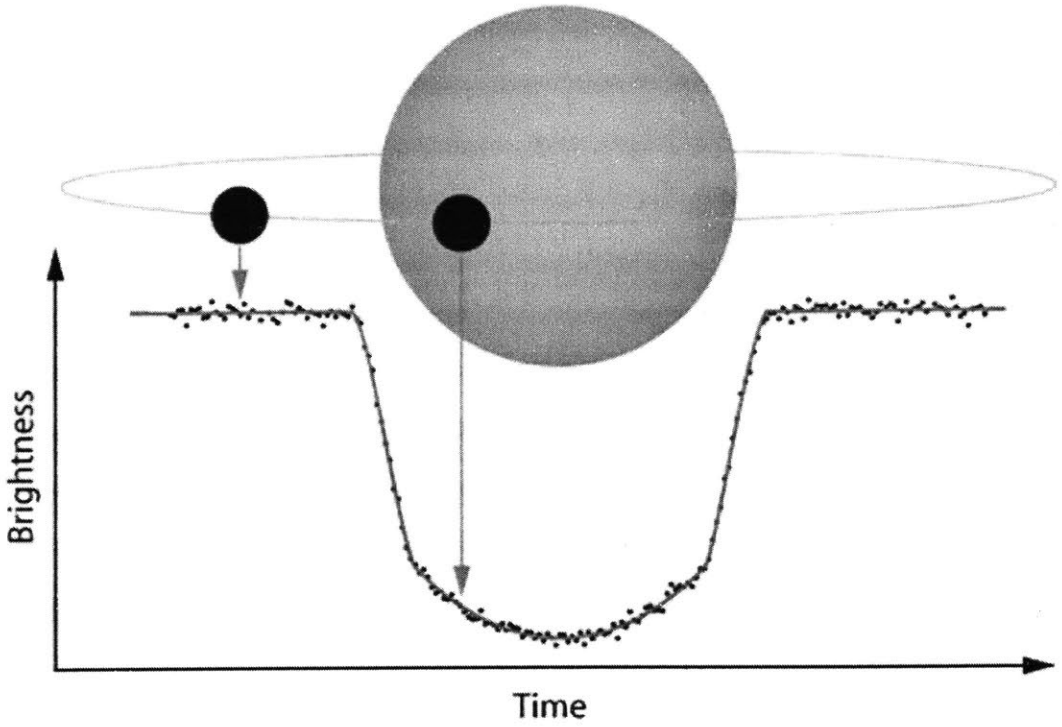

Figure 1-1: Illustration of a transiting planet and the host star showing the reduction in the apparent brightness caused when the planet passes directly between the star and the observer's line of sight.[8]

fidelity simulation and modeling, novel laboratory techniques, and science and telemetry data analysis for systematics calibration. Results from pre-launch simulation and laboratory testing, along with post-launch telemetry data enhances our understanding of the instrument noise sources and effect on instrument performance. We demonstrate the methodology using two case studies; Transiting Exoplanet Survey Satellite (TESS) [14] and Arcsecond Space Telescope Enabling Research in Astrophysics (ASTERIA) [15].

TESS is a NASA Explorer mission with a primary goal to survey over 200,000 main sequence stars over a period of two years, and discover thousands of planets smaller in size than Neptune. TESS employs four state-of-the-art cameras; each camera with four Charge Coupled Device (CCD) detectors optimized to observe bright dwarf stars. With TESS, we focus primarily on establishing the noise floor for bright star photometry, and evaluating the impact of factors such as jitter, aperture size, time bin size and temperature variations on photometric performance.

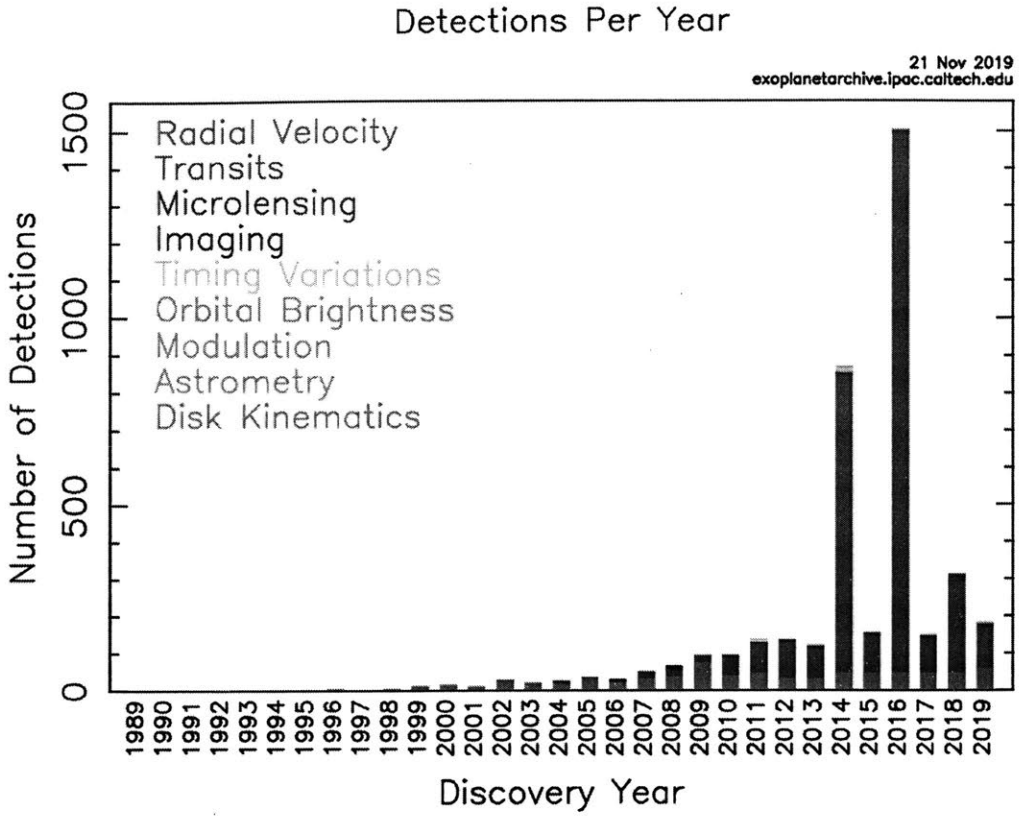

Figure 1-2: Number of confirmed exoplanet detections by different techniques and the corresponding detection year. The x-axis shows the discovery year and the y-axis shows the number of detections. The transit method is currently the most sensitive method and has enabled the discovery of thousands of planets.[13]

ASTERIA is the first CubeSat mission to detect the transit of a known exoplanet. ASTERIA employs a newer generation of scientific-grade Complementary Metal Oxide Semiconductor (CMOS) detectors and is aimed towards advancing both CubeSats and CMOS detector technologies for precision photometry applications. With ASTERIA, we present a comprehensive evaluation of key technologies such as the piezo-stage fine pointing system that demonstrates arcsecond-level pointing control, and CMOS detector technology that provides a low-mass camera package for CubeSat-platforms with the ability to stare at very bright stars such as Alpha Centauri [16] without saturating. We study instrument properties that significantly contribute to systematic noise and develop an optimal calibration framework to remove correlated noise from the data and improve photometric precision.

Finally, we present an application of key takeaways to two future missions. First, we perform early phase error budgeting and detector selection for the ASTERIA Constellation, a fleet of CubeSats dedicated to detecting an Earth Analog. Second, we develop and implement a model-based framework to inform instrument calibration testing for future smallsat science missions. The goal is to reduce in-flight calibration time thus saving a significant amount of science operations time and operations cost. We present an application to Star-Planet Activity Research CubeSat (SPARCS) [17], a UV photometry mission to study the effect of stellar variability on exoplanet atmospheres of low-mass M stars.

1.2 Motivation

The following section presents the motivation for the thesis. We discuss the need for an integrated approach to systematics calibration and photometric performance validation. We present the motivation to improve photometric performance for bright stars using ground and in-flight calibration techniques. Next, we discuss a brief background on science output from CubeSat-based missions. We also illustrate the need for alternative detector technology development for transit photometry. Lastly, we discuss the need for introducing more rigor into integration and test plans using model-based methodology.

1.2.1 Need for Integrated Approach to Systematics Calibration

Traditionally, instrumentalists design, build, test and qualify a space telescope over a period of a decade or more, and scientists around the world analyze the vast amount of science data downlinked after launch. With recent missions, efforts have been made to transfer the knowledge acquired during calibration and testing to the data analysis pipeline development teams, and results have been published in the instrument and data processing handbooks that document key characteristics of the instrument,

especially in the case of large missions like Kepler [18] and TESS. The knowledge transfer is more linear between the instrumentalists and scientists. When it comes to understanding instrument behavior and impact of systematic noise sources on photometric performance, there has not been a systematic framework to link results from various phases of the missions: such as simulations from early design phase, laboratory characterization and in-flight calibration. For smaller missions like ASTERIA, often times, the data analysis pipelines are developed after testing of the instrument has been completed, sometimes even after launch, leaving little opportunity for interaction and collaboration between data analysts and instrumentalists. In this thesis, we develop a framework that relies on instrument physics to characterize sources of systematic noise in the data, and incorporates results from simulations, ground and in-flight instrument characterization and calibration into the science data analysis pipeline to achieve improvement in photometric precision.

Tremendous progress has been made in advancing precision ground testing and instrument characterization techniques. Extensive testing of the cameras at various integration levels (detector, detector array, camera, and telescope) is performed for large telescopes prior to launch using testbeds with high photometric stability and flight-like operating conditions [19] [20]. Independently, instrument-agnostic data analysis techniques such as pixel-level decorrelation [21] [22] have been developed to correct for systematic noise and improve detection of small planets around bright stars. With the advancement in machine learning for big data applications, present-day research is moving towards developing planet-finding algorithms that heavily rely on learning patterns in the data, and identifying exoplanets based on supervised learning techniques such as convolutional neural networks [23] [24]. While these techniques are helpful when we have large amounts of data to classify, and human vetting becomes monotonous and very time consuming, recent work by Dittman et al. [25] has demonstrated that infusing domain knowledge to identify correlation with sources of systematic noise make the planet-finding algorithms more efficient. Hence, there is a need to integrate the knowledge acquired from simulation and ground testing with flight data analysis techniques to improve reliability and efficiency of

these techniques.

1.2.2 Performance Improvement for Bright Star Photometry

Ground-based radial velocity (RV) and transit searches are capable of discovering and following up exoplanets around bright stars. While RV surveys continue to discover exoplanets below Neptune to Earth masses, ground transit surveys now have milli-mag photometric precision and can discover Neptune-size planets. We can obtain an estimation of the planet radius from transit measurements, and mean planetary density when combined with mass determination from radial velocity measurements. With this knowledge, we can further constrain and test planet structure, formation and evolution theories. Upcoming space-based telescope missions like CHEOPS (CHaracterizing ExoPlanet Satellite) [26] offer the capability to perform very high signal-to-noise occultation photometry of bright targets thus enabling spectro-photometric observations and atmospheric characterization.

Photometric precision requirement for space-based telescopes like CHEOPS is very stringent [27]. For the detection of an Earth-size planet transiting a 9th magnitude G5 dwarf star in the V band with a transit depth of 100 ppm, photometric precision of 10 ppm in 6 hours of integration time is required. This corresponds to a signal-to-noise ratio of 10. For a brighter star of 7th magnitude for example, the same photometric precision yields a higher signal-to-noise ratio. Conversely, to detect an Earth-size planet around a 7th magnitude star, a photometric precision of 35 ppm in 6 hours of integration time is required for a similar signal-to-noise ratio of 10. Given the photometric capabilities of present-day ground and space-based telescopes, the ease of detecting and following up small planets around bright stars is higher than around faint stars. Hence, in this thesis, we focus on improving our understanding of noise sources in bright star photometry and developing techniques to correct them.

1.2.3 Achieving Science Output Using CubeSat Missions

In 2016, the National Aeronautics and Space Administration (NASA) and the National Science Foundation (NSF) tasked the National Academies of Sciences, Engineering and Medicine (NASEM) with establishing a Committee on 'Achieving Science Goals with CubeSats' to evaluate the current state of CubeSats and potential of CubeSats to achieve science output, recommend areas of investments, and identify sample priority science goals. The committee published a report [28] that detailed statistics of number of science-based CubeSat missions over the last decade and half, success rates, and potential areas of improvement.

CubeSats are miniature satellites that are built to standard dimensions of 10 x 10 x 10 cm^3 units or 'U', shown in Figure 1-3. Each U typically weighs 1.33 kg or lesser. They are launched as auxiliary payloads along with bigger, planned satellite launches. The low cost and risk associated with CubeSats make them attractive as technology development and demonstration platforms and more recently, for science missions.

The report stated that CubeSats excelled at focused, short-duration missions that perform targeted science that require multipoint measurements or swarms of spacecraft collecting a distributed array of measurements. CubeSat success and reliability has improved considerably from 2000 to 2015. 67 percent of all science-based CubeSats launched through 2015 achieved either partial success (34 percent) or full success (33 percent), as shown in Figure 1-4.

The committee report also noted that more than 80% of all CubeSat-based science missions were launched between 2012 and 2016. Figure 1-4 shows full and partial success rate by year for all deployed science CubeSats. A mission is defined as full-success when the CubeSat has achieved primary mission objectives during nominal mission, and partial-success when the CubeSat has completed commissioning and is in nominal operations working towards achieving primary mission objectives.

Figure 1-5 shows the number of CubeSats launched between 2000 to 2015 by application type. From 2003 to 2006, Cubesats were used primarily as education

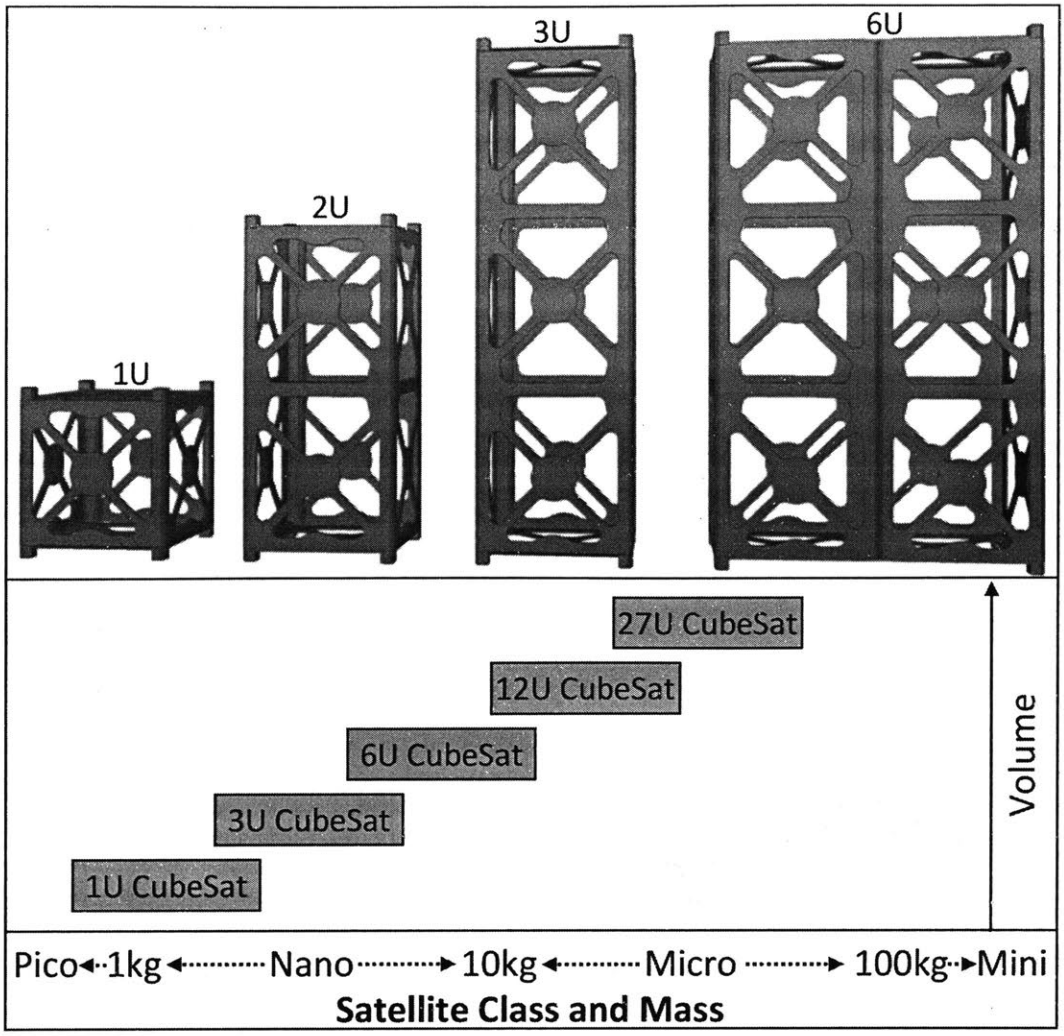

Figure 1-3: Small satellite classification showing 1U, 2U, 3U and 6U sizes along with satellite mass and volume. The volume of 1U unit equals to 10x10x10 cm^3.[29]

platforms for students and early career professionals. The number of CubeSats used for technology demonstration, science and imaging applications has skyrocketed since then. The rises in 2014 and 2015 are primarily due the imaging CubeSat constellation by Planet Labs.

Figure 1-6 shows the number of CubeSats funded by NASA and NSF that were launched between 2000 to 2015, organized by Science category. Majority were technology development to begin with. Lately, CubeSats with focused objectives in solar and space physics, and Earth science are gaining momentum. There were no astrophysics missions until 2016. Figure 1-7 lists all science-based CubeSat missions

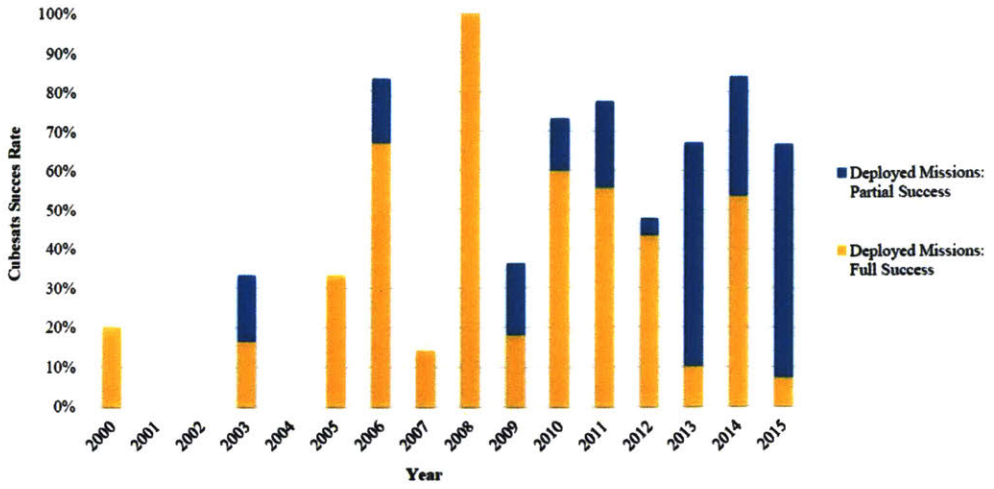

Figure 1-4: Success rate for deployed science CubeSats by year from 2000 through 2015. A mission is defined as full-success when the CubeSat has achieved mission objectives during nominal mission, and partial-success when the CubeSat has completed commissioning and is in nominal operations working towards achieving mission objectives [28].

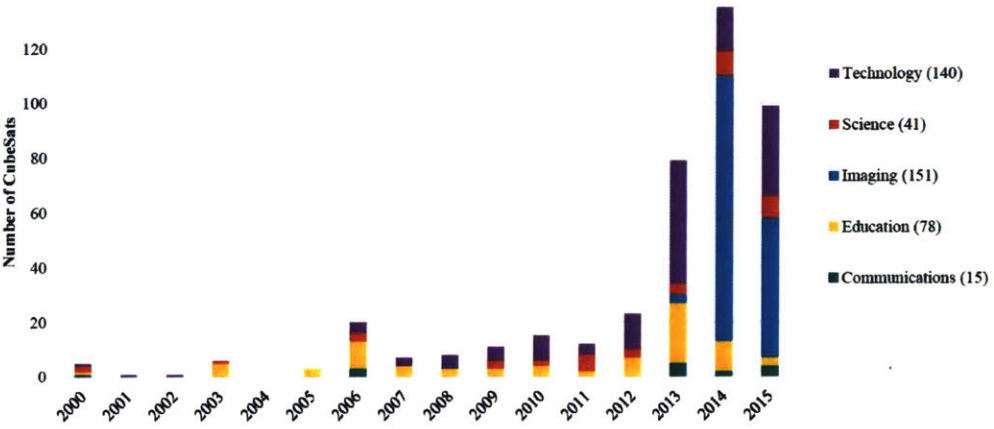

Figure 1-5: Total number of CubeSats launched per year catogorized by mission type. The rises in 2014 and 2015 are primarily for the imaging CubeSat constellation by Planet Labs [28].

launched before 2016 and planned missions until 2018. Small aperture sizes and low pointing accuracy have severely limited the use of CubeSats for astronomy and astrophysics applications. In order to achieve science objectives such as exoplanet

CubeSats (number of missions) by Science Category

Launch Dates	Technology	Astronomy and Astrophysics	Biological and Physical Science	Earth Science	Solar and Space Physics	Planetary Science	Total
2006-2015	28 (12)	0 (0)	4 (4)	1 (1)	14 (9)	0 (0)	47 (26)
Planned 2016-2018+	32 (26)	1 (1)	4 (3)	7 (3)	10 (10)	3 (3)	57 (46)
Total	60 (38)	1 (1)	8 (7)	8 (4)	24 (19)	3 (3)	104 (72)

NOTE: Some missions consist of more than one CubeSat, or the original single CubeSat was reflown. These CubeSat statistics include all launched missions, including those that were lost due to launch failures. Launch dates from 2016-2018 are presented as a forecast of future activities.

Figure 1-6: CubeSats launched between 2006 and 2015 or in-development for launch between 2006 and 2018 classified by application type. The CubeSats were funded by NASA or NSF [28].

detection, arcsecond-level pointing capability is needed. The ASTERIA mission is focused on achieving just that.

The committee recommended focusing on high-priority science and using science-based CubeSats to develop principal investigator leadership, scientific, engineering and project management skills among students and early career professionals. The committee also recommended implementing large scale constellations of 10 to 100 science spacecraft that enable critical measurements in space science, astrophysics and planetary science topics.

1.2.4 Need for Advancing Alternative Detector Technology

For several decades, Charge Coupled Device (CCD) detectors have dominated space-based imaging and spectroscopy due to their single-photon sensitivity and moderate frame rates. More recently, scientific Complementary Metal Oxide Semiconductor (sCMOS) detectors that provide lower readout noise at higher frame rates have been developed, thus providing distinct advantages over CCD detectors for ultra-low-light applications. sCMOS detectors can be operated at room temperature as they generate ultra-low-dark current (20 e-/pixel/s) compared to 250-500 e-/pixel/s generated by CCDs at the same temperature. Hence, sCMOS detectors do not require passive cooling systems that would otherwise add significantly to the mass and size of the spacecraft. sCMOS detectors with increased sensitivity (>95% at 560 nm at all incident angles) and dynamic range have now been created using back-illuminated

Funding Program	CubeSat Missions Launched	CubeSat Missions Planned	Launch Years
NASA			
Heliophysics	MinXSS	CeREs, CuSP, ELFIN,[a] HeDI, SORTIE, TBEx	2015-2018
Earth Science	GRIFEX, IPEX, MCubed/COVE (2)	CIRAS, CIRiS, CubeRRT, HARP, IceCube, LMPC, MiRaTA, RainCube, RAVAN, TEMPEST-D	2011-2018
Planetary Science	O/OREOS	INSPIRE (2), LunaH-Map, MarCO (2), Q-PACE Technology Development Only: DAVID, HALO, MMO	2010-2018
Astrophysics		HaloSat	2018
Advanced Exploration Systems and Human Exploration and Operations	GeneSat, PharmaSat, SporeSat (2)	BioSentinel, EcAMSat, Lunar Flashlight, Lunar IceCube, NEA Scout, Skyfire	2006-2018
Space Technology	EDSN (8),[b] NODeS (2), OCSD-1, PhoneSat (5)	CPOD (2), CSUNSat-1, ISARA, iSAT, OCSD (2)	2013-2017
Centers (Internal)			2008-2018
Ames Research Center	PreSat,[c] TechEdSat (3)	KickSat, TechEdSat-5	
Ames Research Center and Marshall Space Flight Center	NanoSail-D (2)		
Goddard Space Flight Center		CANYVAL-X, Dellingr, ESCAPE, RBLE	
Jet Propulsion Laboratory	LMRST, RACE[d]	ASTERIA, MITEE	
Kennedy Space Center		Cryocube, StangSat	
NASA IV&V Facility		STF-1	
National Science Foundation			
	CADRE, CSSWE, CINEMA-1, DICE (2), ExoCube, FIREBIRD (4), Firefly, RAX (2)	ELFIN,[a] ISX, IT-SPINS, LAICE, OPAL, QBUS/QB50 (4), TRYAD (2)	2010-2018

NOTE: NASA has sponsored 57 missions (80 CubeSats total) and NSF has sponsored 15 missions (24 CubeSats total) for a total of 72 missions with 104 CubeSats across NASA and NSF.

CubeSats are counted by individual spacecraft, but missions are counted once even if they involve a reflight or multiple spacecraft. Numbers in parentheses after a mission name indicate the total number of CubeSat spacecraft counted in the mission. Acronyms are defined in Appendix E.

[a] The ELFIN (Electron Losses and Fields Investigation) mission, originally a part of the University Nanosatellite Program, is now funded jointly by NASA and NSF.

[b] Super Strypi launch failure.

[c] Falcon-1 launch failure.

[d] Antares launch failure.

Figure 1-7: Names of known Science CubeSat launches between 2006 and 2016 and planned launches between 2016 and 2018 classified by application and funding from NASA centers. ASTERIA is one of the four CubeSats funded by the Jet Propulsion Laboratory. [28].

sensor technology. In addition to CCD-like quantum efficiency (QE) in the visible wavelengths, a significant improvement in QE in the UV (>80% at 250 nm) and in the near Infrared (>25% at 950 nm) wavelengths has also been achieved providing a broader spectral range of 200-1100 nm. In addition, sCMOS detectors have smaller and compact electronics packages that appeal to the space and mass constraints of a small satellite or CubeSat mission. Hence, it is important to demonstrate and validate

this alternative detector technology for precision applications. ASTERIA is the first CubeSat to demonstrate CMOS detectors for high precision transit photometry.

1.2.5 Need for Model-based Methodology for I&T

Almost all large space telescopes have encountered cost overruns, schedule delays and utilized some operations time for in-flight systematics calibration. CubeSats have very little time and budget to perform ground testing and calibration, and for most missions, they are launched without a thorough characterization of systematic noise sources. In many cases, these problems have been traced to deficiencies in the error budgeting and ground calibration test plan prioritization. The methodology described in the last section of this thesis improves early phase error budgeting and calibration test plan generation through the use of modeling in order to calibrate major noise sources on ground, and save valuable science operations time and cost. Adding systems engineering rigor to the calibration test plan generation process and using a model-based approach to generate an incompressible test list will simplify commissioning and in-flight calibration required.

1.3 Thesis Objectives

The use of an integrated approach to systematic calibration and performance improvement for space-based photometry has clear advantages. In order to advance the state of the art, we create a high fidelity simulation model of the instrument pipeline for photometric performance assessment and systematic noise analysis. With this methodology, major noise sources to which the photometric performance is sensitive are identified and studied in the laboratory. Techniques to analyze telemetry and science data are developed, and a variety of sources of systematic noise are probed. Uncertainty analysis is performed, where uncertainty in the systematic noise estimation can be propagated through a model to estimate the uncertainty in the system performance and the noise floor for the mission. Furthermore, lessons learned can be incorporated into instrument design and calibration for future missions.

Using the integrated approach to systematic noise calibration and correction, we aim to achieve the following thesis objectives:

1. Develop a high fidelity simulation of the camera to assess the expected photometric precision of the mission.

2. Develop a systematic framework to establish the actual noise floor and evaluate the impact on science capability of the mission.

3. Systematically assess various sources of systematic noise using novel laboratory characterization and flight data analysis techniques, and identify the major sources affecting photometric precision.

4. Develop techniques to correct for systematic effects and improve photometric performance for bright stars.

5. Develop an optimal systematics correction framework for CMOS detectors to achieve sub-millimag precision for photometry applications.

6. Develop recommendations for future science CubeSat missions, especially for early design phase error budgeting and I&T test plan development.

1.4 Scope

The scope of the thesis is limited to analyzing major instrument systematic noise sources and improving photometric performance by calibrating these effects for two missions: TESS and ASTERIA. First, only issues pertaining to the two missions will be considered. Second, we focus on developing flight data analysis techniques to calibrate and correct for specific systematic effects. Therefore, instrument-agnostic techniques such as principal component analysis (PCA) and other machine learning algorithms that model trends in the data and remove them are outside of the scope of this work. In considering the various objectives, the focus is on augmenting existing modeling, data reduction, and numerical conditioning techniques, with novel laboratory techniques as necessary.

We limit the scope of the present work to analyzing the effect of instrument-related systematics. Hence, analyzing stars with high intrinsic variability and incorporating

algorithms to correct for astrophysical effects is outside of the scope of the present work. By limiting the number of systematic effects considered, and using existing modeling and optimization techniques, the scope of the photometric performance evaluation problem is limited to a reasonable size, while still providing invaluable information on tackling major systematic noise sources and analyzing data from two missions that use different types of detectors.

Lastly, the model-based calibration test plan development is focused on systematic noise sources that affect photometric performance and does not address other important and valuable tests that are required prior to launch. The incompressible test list is a direct contribution to an upcoming mission, SPARCS but also to other science CubeSat missions as they are all very constrained in testing time and budget, and are often faced with trading off calibration tests with schedule.

1.5 Thesis Contributions

The primary contributions of this thesis are summarized below, and will be discussed in detail in Chapter 7.

1. Characterized QE and its variation with temperature with 2% accuracy in the laboratory that led to photon noise limit estimation, and setting of operating temperature of the TESS detectors

2. Quantified the effect of temperature variation in TESS flight data on photometric precision: 30 ppm at 1-hour

3. Established the noise floor for TESS: 16 ppm at 4-hours that will drive future transit photometry mission limits

4. Established one of the first data analysis pipelines for CMOS science

- Demonstrated photometric precision for HD219134 to within 2 times photon noise.

- Established a residual systematic noise floor of 15 ppm at 2-hours for the brightest of stars like Alpha Cen.

5. Demonstrated improvement of 15% in photometric precision for ASTERIA

flight-like detectors through incorporation of laboratory calibration

6. Developed noise budget and detector trade study for ASTERIA constellation concept

7. Developed data analysis pipeline-driven incompressible test list for systematics calibration for SPARCS

1.6 Thesis Outline

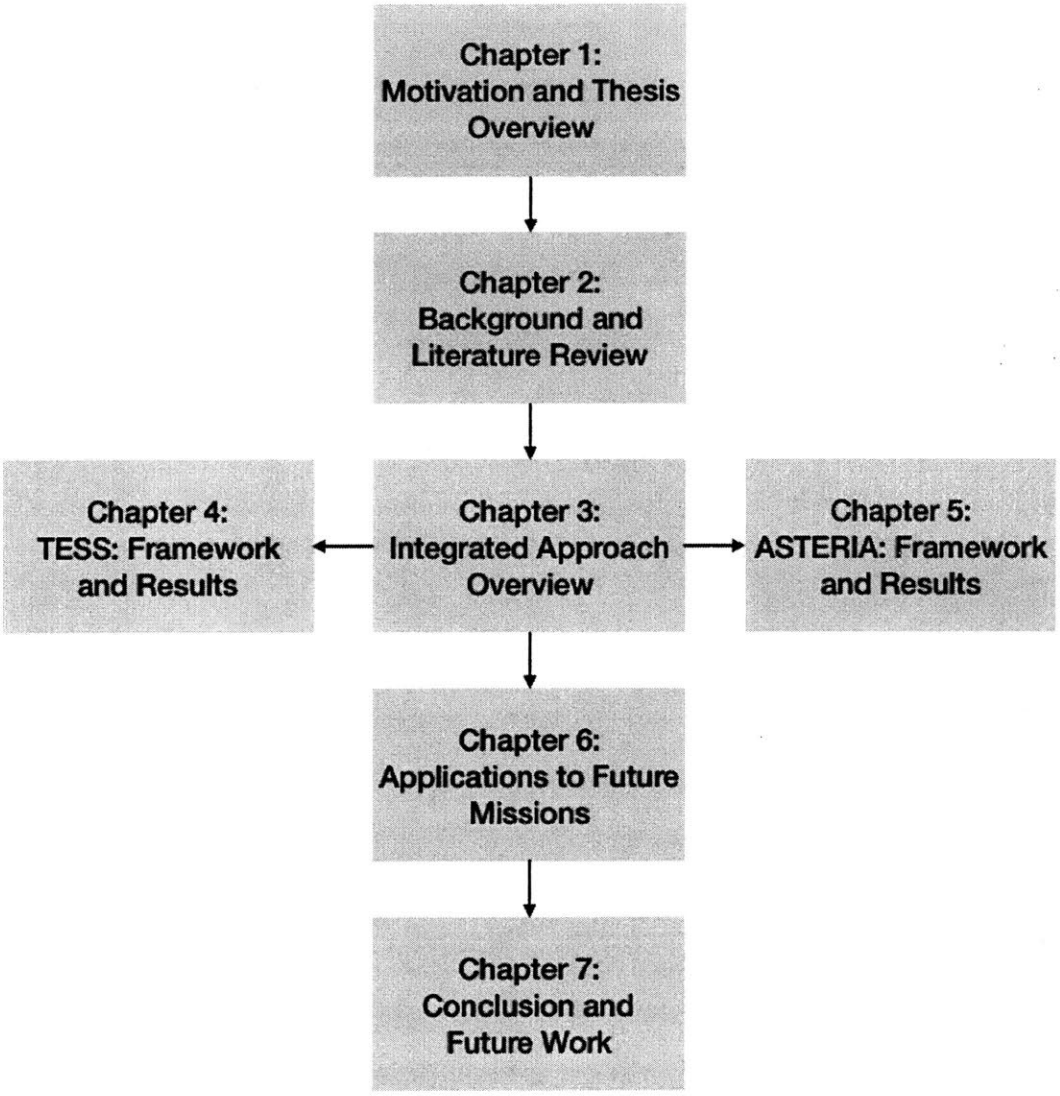

Figure 1-8: Thesis outline showing a roadmap of different chapters.

Figure 1-8 shows an outline of the thesis. Chapter 1 provides an overview of the

thesis, in addition to background and motivation. We discuss the four-fold thesis objectives of improving bright star photometry, advancing CubeSats to perform exoplanet detection, developing systematics calibration framework for sCMOS detectors for precision applications and lastly, developing a model-based approach to calibration and performance testing of instrument systems.

Chapter 2 presents a thorough review of the literature covering various topics such as space-based telescopes for transit photometry, CubeSat-based Astrophysics missions, instrument systematics calibration using laboratory, data processing and in-flight techniques, and lastly detectors used for precision photometry.

Chapter 3 presents a comprehensive framework for systematics calibration that consists of generating a high fidelity simulation model of the detector and producing realistic science data, performance validation of the flight data, development of systematics calibration techniques using laboratory and flight data analysis techniques, that finally demonstrate photometric performance improvement.

Chapter 4 presents the first case study on the Transiting Exoplanet Survey Satellite (TESS). We present an overview of the mission and instrument, followed by the approach. Next, we present results from the high fidelity simulation of the Charge Coupled Device (CCD) detector along with photometric performance assessment for realistic jitter profiles. Following that, we present a comprehensive systematics evaluation framework for bright stars by studying various factors such as aperture size, stack depth, jitter, temperature and detector location. We develop a systematics correction framework, demonstrate improvement in photometric performance and establish a noise floor for the mission.

Chapter 5 presents the second case study on the Arcsecond Space Telescope Enabling Research In Astrophysics (ASTERIA). We present an overview of the mission and instrument, followed by the approach. Next, we present results from the high fidelity simulation of the scientific-Complementary Metal Oxide Semiconductor (sCMOS) detector along with photometric performance assessment for realistic jitter profiles. Following that, we present a comprehensive systematics evaluation framework for science target stars by studying various factors such as aperture size, stack

depth, jitter, temperature and detector location. We develop a systematics correction framework, demonstrate improvement in photometric performance and establish a noise floor for the mission. We conclude the chapter by summarizing the learnings from ASTERIA.

Chapter 6 presents application to future missions namely the ASTERIA constellation mission and the Star-Planet Activity Research CubeSat (SPARCS) mission. We discuss the photometric precision requirement for the ASTERIA constellation, noise budget allocation, and tradespace exploration for detector selection. For SPARCS, we provide a mission overview, and discuss relevant requirements. We develop a data analysis model to inform error budgeting. The error budget then feeds into an Incompressible Test Plan (ITL) for instrument calibration. Applying a model-based approach adds rigor to calibration and performance testing, with the clear advantage of trace-ability and a systematic path to revisit decisions efficiently.

Chapter 7 summarizes the thesis and discusses research contributions. In addition, we present avenues for future work in areas of systematic calibration and CubeSat-based science missions.

Chapter 2

Background and Literature Review

In this chapter, we present an overview of the various methods used for exoplanet discovery. We discuss past, present and upcoming space-based telescope missions for high precision photometry. We then present a discussion of the current state-of-the-art techniques for instrument systematics evaluation and data analysis for space telescopes. Lastly, we present advances in model-based systems engineering applications, in the context of instrument calibration.

2.1 Methods for Exoplanet Discovery

Exoplanets are planets around stars outside of our solar system. Until 1992, we did not know if there are planets around any other stars besides the sun. As of November 2019, we have discovered close to 4,099 extrasolar planets [13]. Several methods have been used to discover these exoplanets: radial velocity, planetary transits, microlensing, direct imaging and astrometry. The precision of each of these techniques has been advanced through innovations in the past two decades. In this section, we provide a brief description of the various methods used for exoplanet discovery [7].

2.1.1 Radial Velocity

More than 250 planet discoveries including the first and many milestone exoplanet detections were made using the radial velocity technique [2]. The radial velocity technique relies on the Doppler effect that measures the reflex velocity that an orbiting planet induces on the host star. An emitted photon of wavelength, λ in the rest frame of the source is detected at a different wavelength, λ_o by an observer moving with respect to the emitter.

$$\lambda = \lambda_o(1 + (1/c)\mathbf{k}.\mathbf{v_o}) \tag{2.1}$$

In Equation 2.1, $\mathbf{k}$ is the unit vector in the rest frame of the observer pointing from the observer to the source, $\mathbf{v_o}$ is the velocity of the source detected by the observer and c is the speed of light in vaccum. After adding the barycentric correction to shift the frame of reference from the Earth to the solar system barycenter known as the International Celestial Reference System (ICRS), we obtain Equation 2.2, where Φ_o is the gravitational potential at the observer.

$$\lambda = \lambda_o \frac{1 + \frac{1}{c}\mathbf{k}.\mathbf{v_o}}{1 - \frac{\Phi_o}{c^2} - \frac{v_o^2}{2c^2}} \tag{2.2}$$

Obtaining absolute stellar radial velocity using Doppler shift is a very difficult task due to systematic effects such as blueshifts of stellar lines, line asymmetries, gravitational redshift, instrument and wavelength calibration systematics, etc. In 1995, Mayor and Queloz [1] modeled the Doppler signal for 51 Pegasi, with a velocity precision of about 13 ms^{-1} that enabled the detection of a Jupiter-mass planet in a 4.23-day orbit. Over the years, the Doppler technique has showed remarkable improvement to almost 3 ms^{-1} in 1998 and about 1 ms^{-1} in 2005 [7]. A Doppler shift of 1 ms^{-1} corresponds to a shift of stellar lines across a thousandth of a pixel in a CCD detector.

2.1.2 Transits

The first transiting extrasolar planet HD 209458b was discovered in 2000 [30] [31] and the number of transiting exoplanets discovered each year has exponentially grown since then due to a number of ground-based observatories such as SuperWASP [32], HATNet [33], KELT [11], TRAPPIST [12], and space-based observatories such as Kepler [18], CoRoT [34], Spitzer [35] and HST [36] (see Section 2.2.1 for more on space-based telescopes). In this thesis, we focus on developing frameworks, tools and techniques to improve the sensitivity of exoplanet detections for space-based observatories.

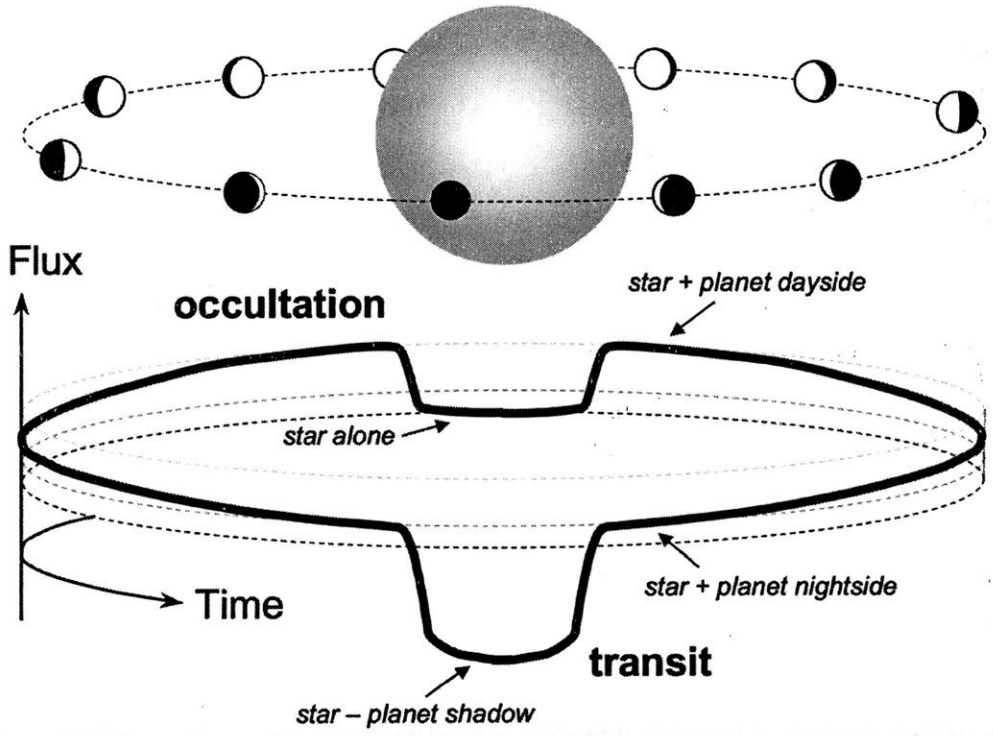

Figure 2-1: Illustration of planetary transit or eclipse and secondary transit or occultation around a host star. Image Credit: NASA/TESS

The passage of a smaller body in front of a larger body is an eclipse or transit, and the passage of the smaller body behind the larger body is an occultation or secondary eclipse, as seen in Figure 2-1. We can learn about the planet's orbit, radius, mass, temperature, and atmospheric composition using eclipse and occultation observations.

Transiting exoplanets are detected by high precision stellar photometry, where light from the target star is monitored continuously for several hours or days such that any periodic dip in brightness that occurs when a planet passes between the host star and line of sight of the observer can be detected. The drop in brightness is given by the transit depth and is proportional to the ratio of the planet radius to that of the host star. The radius of the planet can be determined from the magnitude of drop in the stellar brightness using Equation 2.3.

$$\frac{R_p}{R_*} = \sqrt{\delta} \tag{2.3}$$

In this equation, R_p is the radius of the planet, R_* is the radius of the host star and δ is the transit depth, normalized to the total flux of the star. Along with the radial velocity measurement of the planetary mass, the transit method provides the bulk density of the planet that is virtually free of astrophysical assumptions. By studying the combined light from the star and the planet in a transiting system, characterization of atmospheres has been performed successfully by several works; a partial list includes Charbonneau et al. [37] [38] [39] [40], Deming et al. [41] [42] [43], Grillmair et al. [44] [45], Harrington et al. [46] [47], Knutson et al. [48] [49] [50], and Swain et al. [51] [52].

2.1.3 Microlensing

Gravitational microlensing events occur when two stars are within 1 mas of each other on the plane of the sky. The foreground star acts as a lens and bends light rays from a background star producing two unresolved images. If the two stars are perfectly aligned, the background star is lensed into a ring called the Einstien ring. If a planet is present around the foreground star, the planet also acts as a lens and causes a short-lived perturbation of the image resulting in a characteristic signature of the planet in the microlensing light curve of the host star [53]. The first microlensing planet was a 2.6 M_{Jup} planet discovered in 2003 [54], and several planets have been discovered since then. Although the analysis of microlensing datasets is complicated

and time consuming, the method is of interest because microlensing is sensitive to low-mass planets beyond the point in the protoplanetary disk where ice exists, that is impossible to probe using other methods. The true potential of microlensing can only be realized through a space-based survey, which has clear advantages of fewer systematic errors, the absence of weather, better resolution and improved photometric precision.

2.1.4 Direct Imaging

The direct imaging of a spatially resolved planet is a powerful technique and is primarily suitable for planets with wide orbits a $>$ 5 AU. This technique also allows photometric characterization. So far, there have been successful discoveries of massive young self-luminous planets. In 2008, near-infrared composite images of three exoplanets HR 8799 b, c, d that are at angular separations of 1.7, 1.0, and 0.6 arcsec from the star were published [55]. The biggest technical challenge is being able to separate the light of the planet from that of the host star. With the development of Coronograph [5] and Starshade [6], imaging of a planetary system may be well within reach in the next decade.

2.1.5 Astrometry

Astrometry measures the barycentric motion of a star caused by a companion by observing the star's position relative to the background sky. Astrometry is more sensitive to wider orbits where orbital periods are typically several years. Astrometry can determine the planet mass m_2, if the host star mass m_1 is known, by measuring the value of $m_2^3/(m_1 + m_2)^2$, without the ambiguity of radial velocity measurements. For ground-based observations, Earth's atmospheric turbulence is the most dominant source of systematic error. Using repeated imaging of the target's motion relative is background stars has been used to achieve astrometric precision better than 0.1 mas [56] [57]. However, to detect an Earth-like planet around the closest stars the precision required is 1 micro-arcsecond. The Gaia mission has achieved astrometric

accuracies of 10 micro-arcsecond for stellar magnitudes V = 7 to 12 [58].

2.2 Transit Photometry: Metric for Performance Evaluation

The metric used to evaluate the performance of a high precision transit photometry mission is photometric precision. Photometric precision is measured as the root mean square of the detrended light curve and has contributions from shot noise or photon noise, stellar variability, and instrument systematic noise, as shown in Equation 2.4. Photometric precision is normalized to the total flux from the star and expressed in percent or parts per million (ppm). In this equation, $\sigma_{photometric}$ is the photometric precision, σ_{photon} is the photon noise, $\sigma_{variability}$ is the noise from stellar variability, and $\sigma_{instrument}$ is the noise from instrument systematics.

$$\sigma_{photometric} = (\sigma^2_{photon} + \sigma^2_{stellar\ variability} + \sigma^2_{instrument\ systematics})^{1/2} \tag{2.4}$$

The arrival of photons from the target star is assumed to be a Poisson distribution. Hence, photon noise is calculated as the square root of the number of incoming photons normalized to the total flux from the star. Stellar variability refers to the intrinsic variability of the star either due to flares or sun spots. Instrument noise refers to the various sources of systematic noise from the instrument and spacecraft. The goal is to get as close to the photon noise limit as possible by calibrating and removing sources of systematic noise. The prominent sources of systematic noise are fixed pattern noise, gain variations, thermal variations, jitter noise due to spacecraft jitter, inter-pixel and intra-pixel sensitivity variations. In this thesis, we focus on characterizing and evaluating the systematic noise sources and minimizing them to get close to the photon noise limit.

The photometric precision requirement for typical space-based transit photometry missions like Kepler, TESS, CHEOPS, PLATO, etc. is of the order of few tens of parts per million over transit timescales. The photometric precision requirements for past,

Missions	Launch Date	Photometric Precision Requirement
CoRoT	2006	700 ppm for a V=15.5 star
Kepler	2009	20 ppm over 6.5 hrs for V=12 star
ASTERIA	August 2017	Best possible
TESS	April 2018	60 ppm over 1 hr for I=8 star
CHEOPS	2020	20 ppm over 6 hours for V=9 star
PLATO	2024	34 ppm over 1 hr for V=11 star

Table 2.1: Photometric precision requirements for past, present and future exoplanet discovery missions. Due to its status as a technology demonstration, ASTERIA does not have a photometric performance requirement.

present and future exoplanet discovery missions is shown in Table 2.1. In order to achieve this stringent requirement, we need very sensitive instruments, and thorough characterization of the instrument systematics. While ASTERIA does not have a photometric precision requirement due to its status as a technology demonstration, the goal is to achieve the best possible result.

2.2.1 Space-based Telescopes

Spitzer Space Telescope

The Spitzer Space Telescope is the fourth mission in the NASA's Great Observatories Program that included the Hubble Space Telescope (HST), Compton Gamma-Ray Observatory (CGRO), and the Chandra X-Ray Observatory. It was launched in 2003 into an Earth-trailing solar orbit with a planned mission length was 2.5 years. The Cryogenic Telescope Assembly contains the 85-cm telescope and three scientific instruments. The entire assembly was cooled to -273 degree Celsius using a tank of liquid helium [35]. As of May 2009, the coolant was depleted and Spitzer's warm mission began.

The telescope is a Ritchey-Chretien lightweight reflector design that weighs less than 50 kg. The Infrared Array Camera (IRAC) is the four-channel imaging camera that is designed to detect light at near- and mid-infrared wavelengths ranging from 3.6 to 8 microns. IRAC has four detector arrays each measuring light at a particular wavelength including 3.6, 4.5, 5.8 and 8.0 micros with the ability to take images

simultaneously and providing a field-of-view of 5.2 arcmin x 5.2 arcmin. Each detector array consists of 256 x 256 pixels with a pixel size of 1.2 arcsec x 1.2 arcsec. The two short wavelengths use InSb detector arrays while the two longer wavelengths use Si:As detectors. The attitude control system consists of reaction wheels, gyroscope and star trackers with a noise equivalent angle of approximately 0.11 arcseconds using an average of 35 guide stars. Spitzer achieved a 1σ pointing stability of 0.03" over 10 minutes. Peak-to-peak flux fluctuations due to spacecraft pointing wobble and intra-pixel variations without correction was calculated to be 5% [59]. On-orbit subpixel sensitivity characterization was performed on a single pixel, the results of which are discussed in Section 2.3.2.

CoRoT

The Convection, Rotation and planetary Transits (CoRoT) was the first high precision photometric space mission dedicated to the detection of transiting exoplanets. It was led by the French Space Agency (CNES) in conjunction with the European Space Agency (ESA), and other international partners, and successfully operated between 2006 and 2013. The objective of the mission was to simultaneously observe up to 12,000 stars in a field of view of 4 square degrees during a 150-day period [60]. At least five such different fields of view and 60,000 stars were observed. The focal plane was composed of four CCD cameras by E2V Technologies. The detectors were thinned, back-illuminated, frame-transfer CCDs with 2048 x 2048 pixels in the imaging area. The pixel size was 13.5 μ m with a corresponding angular size of 2.32 arcsec. The photometric precision requirement for the mission was 7 x 10^{-4} for a V=15.5 magnitude star for one-hour integration time [61].

Kepler Space Telescope

Kepler is a NASA Discovery-class mission launched in March 2009 into a 372.5-day Earth-trailing, heliocentric orbit with the primary mission goal of detecting Earth-size planets in the habitable zone of F through M dwarf stars. Kepler observed up to 170,000 target stars at its long-cadence sampling interval of 29.4 min and up to 512

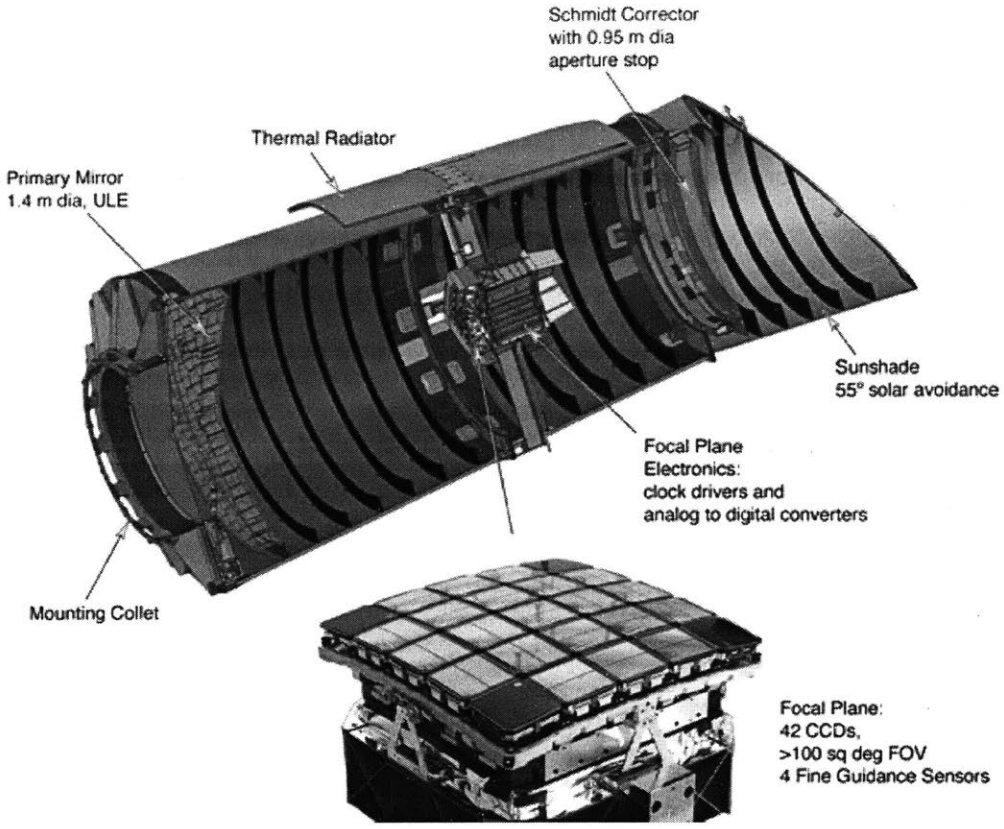

Figure 2-2: An image of the Kepler space telescope and the focal plane assembly. The focal plane array has a total of 42 science CCDs and 4 fine guidance CCDs. The science CCDs are thinned, back-illuminated and anti-reflection coated devices from e2v Technologies. [18]

target stars at its short-cadence sample interval of 58.8 sec [18]. Every 3 days, one or more reaction wheels were desaturated as they approached maximum operating angular velocity, by firing hydrazine thrusters. This caused significant degradation of the photometric precision for at least one long-cadence interval and several short-cadence intervals.

The primary instrument is a 0.95-m aperture Schmidt telescope with a field-of-view of 115 deg^2. The photometer consists of a 95-megapixel focal plane with 21 CCD modules, each with two 2200x1024 pixel CCDs. It has a total of 42 science CCDs and 4 fine guidance CCDs. The science CCDs are thinned, back-illuminated and anti-reflection coated devices from e2v Technologies. The pixel size is 27 μm^2 and the plate scale is 3.98 arcsec/pixel. The photometer utilizes a broad bandpass

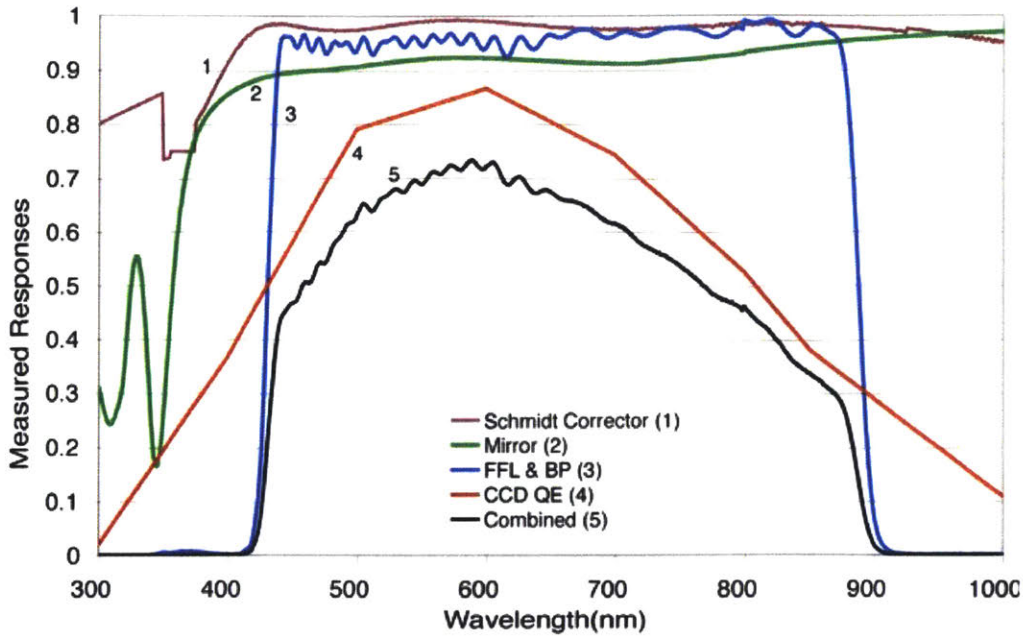

Figure 2-3: Transmission curves for all the optical elements and CCD quantum efficiency curve for the Kepler detectors. The combined photometer response is also indicated. [62]

ranging from 420 nm to 900 nm. The transmission curves of all the optical elements including the Schmidt corrector, primary mirror assembly, field flattener lenses and the quantum efficiency of the detectors, and the combined spectral response of the photometer is shown in Figure 2-3. The Kepler telescope was defocused by 40 μm during commissioning to reduce the photometer's sensitivity to image motion. The pointing jitter was determined to be 0.003 arcsec in 15 minutes per axis [63].

One of the key requirements for the mission was to be able to detect three transits of a planet in the habitable zone of a sun-like star, which required a mission length of at least three years [64]. An Earth-Sun analog transit produces a signal of the ratio of their areas (84 ppm) with a transit duration of 13 hours. The noise threshold to be able to detect the transit of 84 ppm in half the transit duration, 6.5 hours, was determined using a combination of three sources: 1) shot noise (photon noise) 2) stellar variability 3) measurement or instrument noise. The instrument noise includes the detector and electronic noise, pointing jitter, image drift, thermal, optical and

Source	Expected Noise [ppm]	Reality [ppm]
Photon Noise	15.3	16.1
Instrument Noise	6.9	14.1
Stellar Variability	10	19.5
RSS Total	19.5	28.9

Table 2.2: Expected and observed noise sources for the Kepler mission. The stellar variability and instrument noise components were found to be twice the individual expected noise components and the total observed noise was 10 ppm more than the total expected noise. [68]

integration-time stability, stray light, video and optical ghosting and sky noise [65]. The combined differential photometric precision (CDPP) was defined as the root sum square total of the shot noise or poisson noise, σ_{shot}, stellar variability noise, $\sigma_{stellarvariability}$, and instrument noise, $\sigma_{instrument}$, and is given by Equation 2.5:

$$CDPP = (\sigma^2_{shot} + \sigma^2_{stellar\ variability} + \sigma^2_{instrument\ noise})^{1/2} \tag{2.5}$$

For a 4σ detection, the CDPP required is 20 ppm for V=12 stars over a 6.5-hour integration time. The allocation of expected noise for each of the sources is shown in Table 2.2. In the first year of operation, it was found that the median value of observed total noise was 29 ppm for V=12 sun-like stars as shown in Table 2.3. The instrument noise and stellar variability were twice the expected numbers. Initially, the increase in noise was attributed to the variability of Sun-like stars being greater than the Sun. A few years later, studies with a larger dataset concluded that it could not be confirmed that Sun-like stars are more variable than the Sun [66] [67].

In order to overcome the effect of the increased noise, an extended mission was proposed. With extended mission that was twice the nominal duration, the estimated number of reliable detections of Earth-size planets within the habitable zone would be more than thrice that can be discovered during the nominal mission length, thus meeting the mission goal. The proposed cost requested by the Kepler team to accomplish the extended mission goals is shown in Table 2.4. NASA allocated 20 Million US$ per year for the extended mission.

The first massive transiting exoplanet survey was performed by NASA's Kepler

Mission Length	3.5 yr (baseline)	5.5 years	7.5 years
$1R_{\oplus}$	8	16	27
$1.3R_{\oplus}$	40	74	109

Table 2.3: Estimated number of reliable detections with mission duration for the baseline mission of 3.5 years and the extended mission duration of 7.5 years. [68]

	2012 (M$)	2013 (M$)	2014 (M$)	2015 (M$)	2016 (M$)
In-guide	19.6	13.6	0.2	0	0
Augmentation	0	4.9	16.7	16.4	16.5
Total	19.6	18.5	17.0	16.4	16.5

Table 2.4: Proposed cost requested by the Kepler team for the extended mission. [68]

Mission. Since its launch, the Kepler space telescope has contributed to the discovery of a few thousand planets. Figure 2-4 shows Kepler planet candidates, most of which are confirmed exoplanets, that have been detected by Kepler in the first 3 years, categorized into planetary systems. As of mid-November 2019, Kepler has discovered 2,347 confirmed exoplanets and revealed the existence of an additional 2,420 planet candidates that are yet to be confirmed. K2 has discovered 392 planets and an additional 892 planet candidates, thus revolutionizing the field of exoplanet discovery. The total number of confirmed planets discovered by all observatories is 4099.

The Kepler data processing pipeline [69] developed by the Science Operations Center takes into account pixel-level calibrations as shown in Figure 2-6 and Table 2.5. Laboratory measurements of sub-pixel response variations were not performed as they were considered to be more difficult than doing the pixel level non-uniformity measurements. Because of experimental difficulties, simulations were performed based

Source	Description
Read Noise	read noise per channel
2D Black	2D map of black/bias
Gain	ADU-to-photoelectrons conversion factor
Linearity	corrects nonlinearity in the gain transfer function
Undershoot	corrects artifacts induced by the detector electronics
Flat Field	corrects for pixel-to-pixel sensitivity

Table 2.5: List of pixel-level noise sources used for the pixel-level calibrations in the Kepler data processing pipeline. [69]

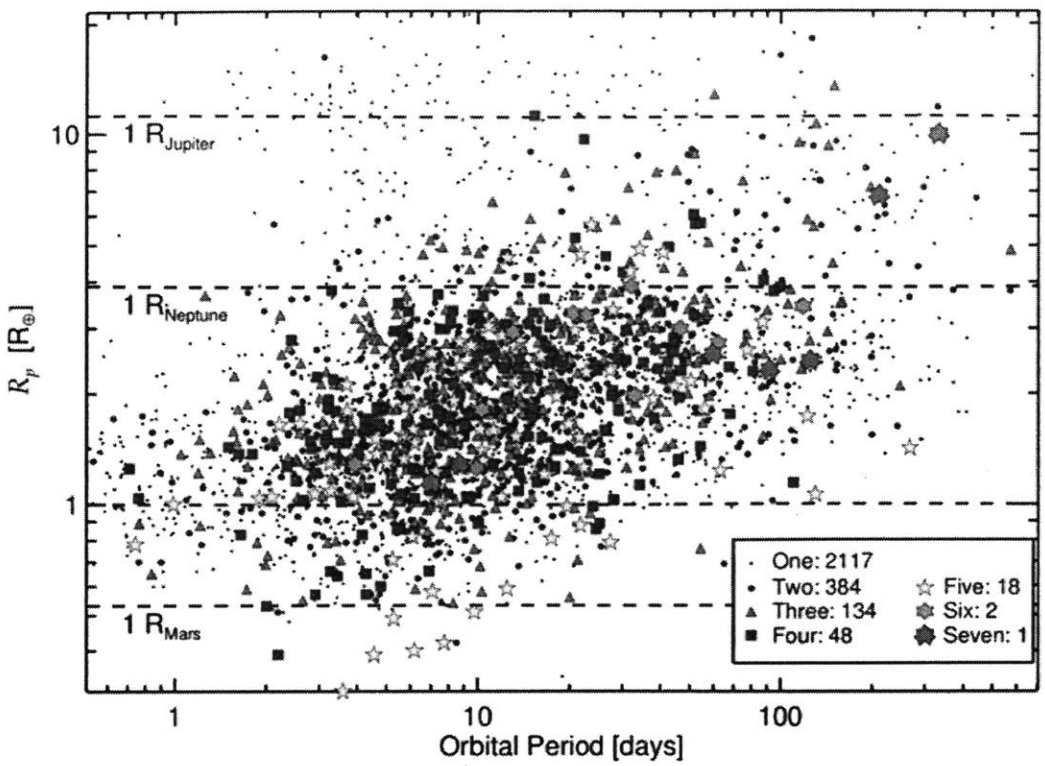

Figure 2-4: Detections by Kepler space telescope in the first three years of the mission along with the number of single and multiple planet systems. The x-axis shows orbital period in days and the y-axis shows radius of the planet in Earth radii. The Kepler mission was not able to meet the primary mission goal as the mission only lasted for 4 years, which ended due to failure of two of the reaction wheels. [13]

on the Tektronix 1024 studies by Jorden et al., 2014 [70]. The results from the Tektronix 1024 experiments are discussed in Section 2.3.1.

The photometric precision of K2 is observed to be consistently less precise than Kepler due to decreased fine pointing control [71]. The spacecraft counteracts Solar radiation pressure by pointing along the spacecraft's orbital plane and using thrusters to mitigate the residual spacecraft drift. During the K2 mission, spacecraft pointing jitter has been found to be the dominant source of systematics. When coupled with inter- and intra-pixel sensitivity variations of the detector, pointing jitter produces intensity fluctuations that must be removed from the photometry in order to measure the subtle eclipses caused by exoplanets. Hence, calibration of systematic noise specifically spacecraft jitter is important to improve the photometric precision. [72].

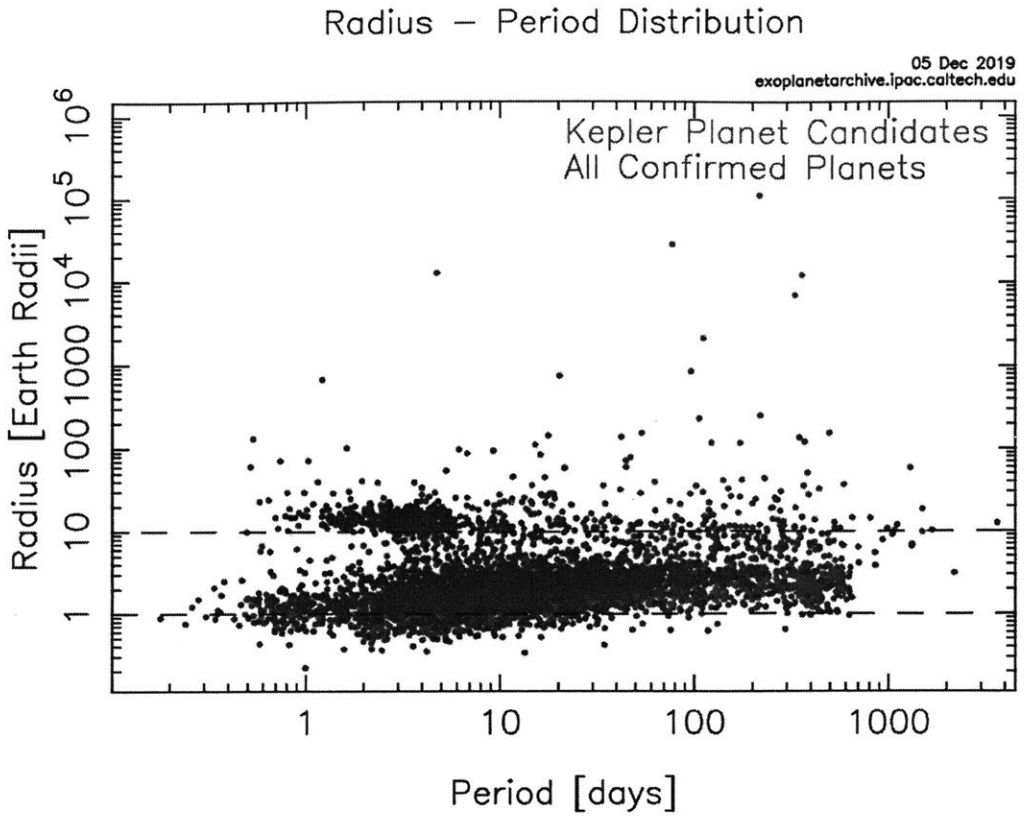

Figure 2-5: The figure shows all Kepler planet candidates and confirmed planets with orbit period and planet radius including Earth-size planets. The number of Earth-size planets discovered around Sun-like stars did not meet the mission goals as Kepler only had a 4-year mission, which ended due to failure of the reaction wheels. The K2 mission utilized the Kepler spacecraft to observe target stars in the ecliptic plane. [13]

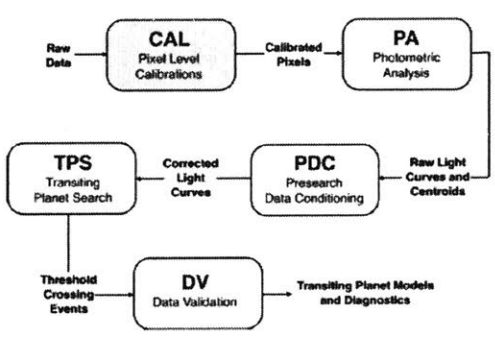

CAL	Calibrate pixels (collateral, background and target) for long cadence, short cadence, and full frame images
PA	Extract raw flux and compute photocenter (centroid) for each target and cadence from associated target pixels
PDC	Correct systematic and other errors in raw light curves, remove excess flux due to aperture crowding, and condition light curves for the transiting planet search
TPS	Perform transiting planet search and return Threshold Crossing Events (TCEs) for detections
DV	Fit transiting planet model to light curves with TCEs, search for additional transiting planets, and perform statistical tests to validate candidate planets

Figure 2-6: Kepler data processing pipeline uses pixel-level calibrations including read noise, 2D black, gain, linearity, undershoot and flat field maps, followed by pre-search data conditioning (PDC) to correct for systematics and other errors. [69]

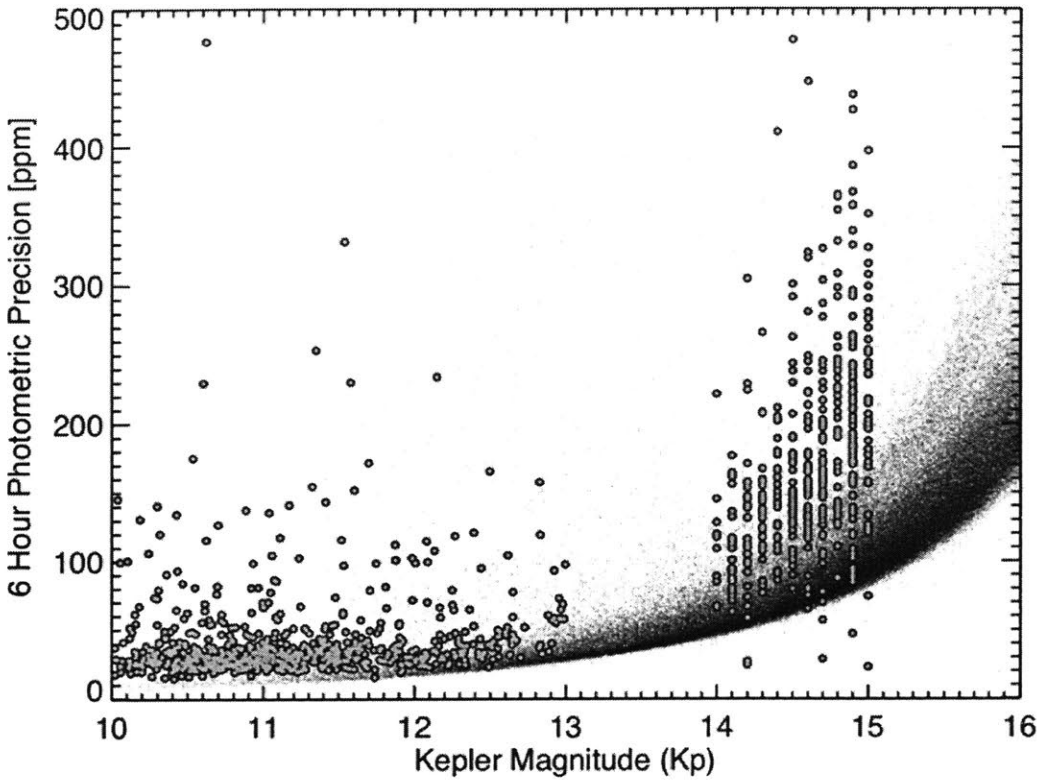

Figure 2-7: Photometric precision of K2 versus that of Kepler. The x-axis shows Kepler magnitude and y-axis shows 6-hour photometric precision in ppm. The orange points in the plot are stars observed by K2 during the Two-Wheel Concept Engineering Test, and the blue distribution indicates the density of stars observed during KeplerâĂŹs Quarter 10 operations. K2 photometry is consistently less precise than KeplerâĂŹs. The gap between magnitudes 13 and 14 is due to the selection of dwarf stars targeted for the test. [71]

CHEOPS

The CHaracterising ExOPlanet Satellite (CHEOPS) is a high precision photometry mission being developed by ESA and is scheduled for launch in 2020 [27]. The photometric precision requirement for CHEOPS is 20 ppm in a 6-hour integration period for the detection of Earth and super-Earth planets orbiting G5 dwarf stars with a V-magnitude range of $6 < V < 9$. For Neptune-size planets orbiting K-type dwarf stars with V-band magnitudes as faint as V=12, the photometric precision requirement is 85 ppm over 3-hour integration time. The primary science goal of the CHEOPS mission is to study the structure of exoplanets smaller than Saturn orbiting bright

stars. The pointing stability of the instrument is estimated to be 8" over 10-hour observing periods. The optical configuration consists of a Ritchey-Chretien telescope that includes a primary mirror of diameter 32 cm and a secondary mirror of diameter 68 mm. The focal plane diameter is 11.23 mm with a field-of-view of 0.4°. The focal plane assembly consists of a single e2V CCD detector with 1k x 1k pixels and a pixel size of 13 μm.

2.3 Traditional Treatment of Instrument Systematics

For large space-based telescope missions, the science team develops mission objectives and requirements, the instrument team develops the instrument design, and the instrument and engineering teams perform Integration and Testing, and Verification and Validation of the instrument. The end users of the data are scientists, typically located all around the world. The wealth of knowledge acquired about system behavior from calibration and performance testing during Integration and Testing are summarized in the instrument and data processing handbooks, and passed on to the data analysis pipeline team that is typically different from the integrating and test team.

Recent data analysis frameworks have focused on developing techniques to self-calibrate instrument systematics, specifically effects of spacecraft jitter in the data and have achieved some success [71] [21]. One example is the TERRA framework [73] that uses Principal Component Analysis (PCA) to find common trends in a large ensemble of stars and cotrends them. This method is an extension of differential photometry. The framework also runs the data through a high pass filter to remove thermal settling events before computing principal components. Potential drawbacks include discarding of photometry that contains a transit, suppression of transit signals, and reduction in signal-to-noise ratio.

The effect of spacecraft jitter on photometric precision can be reduced by correct-

ing for either the motion of the spacecraft, and hence the stellar centroid movement, or by calibrating the inter- and intra-pixel sensitivity variations of the detector, and hence the intensity fluctuations in the photometry. The former topic is addressed in detail in Chapter 4, and the latter is discussed in the upcoming subsections. Inter- and intra-pixel sensitivity of the detector can be calibrated in the laboratory to some extent using techniques presented in Section 2.3.1 or by developing self-calibration techniques using flight data as discussed in Section 2.3.2.

2.3.1 State-of-the-Art Laboratory Techniques

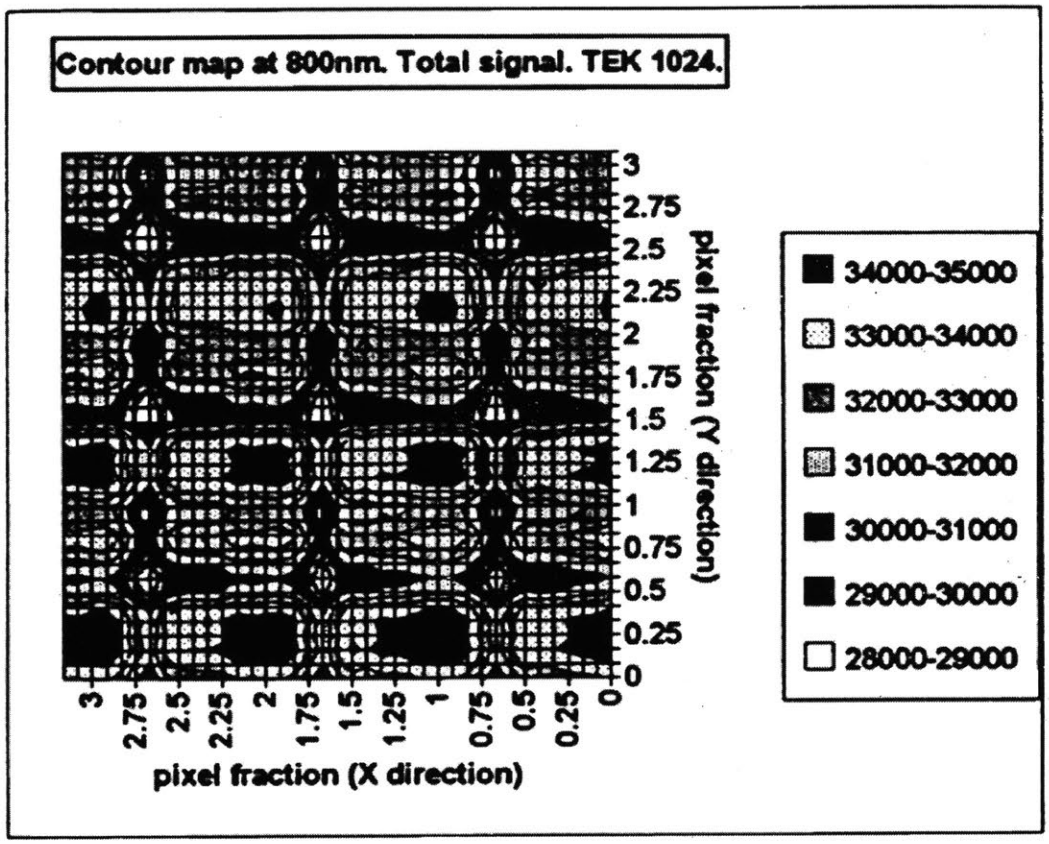

Figure 2-8: Two-dimensional contour map of the Tektronix 1024 intra-pixel response at 800 nm. The x and y-axes display the pixel fraction. The measurements were made at 800 nm on a back-illuminated CCD detector using a halogen bulb as a light source to create a 2.5 micron nominal projected spot with a demagnifying ratio of 10:1. Up to 20% variation relative to the peak pixel value was observed in the intrapixel quantum efficiency response [70]

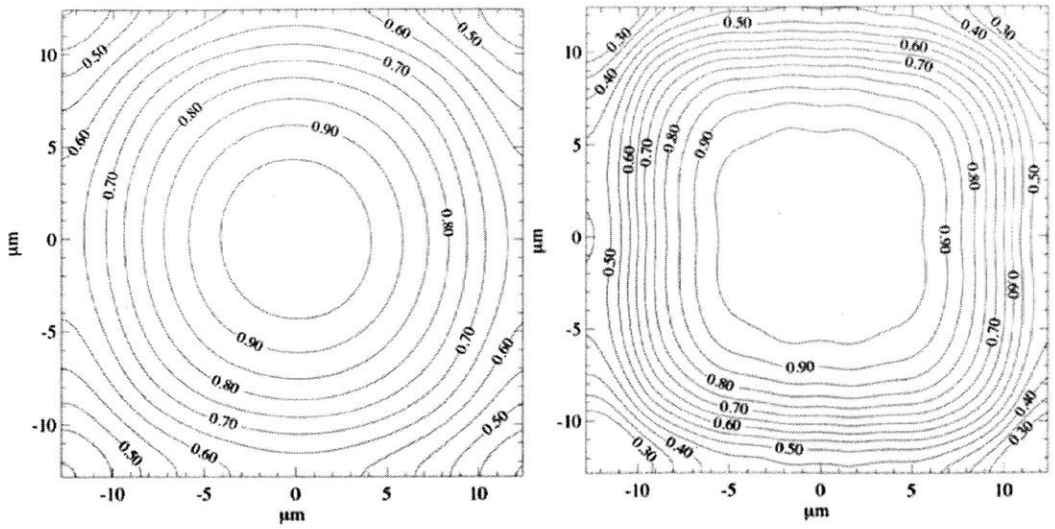

Figure 2-9: Pixel response function measured for a back-illuminated CCD for one pixel with (left) Bessel V filter and (right) Bessel I filter. The x- and y-axes display the distance from the center of a representative pixel in microns. The subpixel sensitivity maps using the filters exhibit strong symmetry. The maximum sensitivity is at the center of the pixel and the minimum sensitivity is at the four corners. The sensitivity map is slightly elongated along the row direction for the Bessel I filter. [74]

Jorden et al. performed intrapixel characterization of front-illuminated and back-illuminated CCD detectors [70]. The Kepler simulations used the results from the Tektronix 1024 back-illuminated CCD detectors performed at 800 and 900 nm. The measurements were made using a halogen bulb as a light source to create a 2.5 micron nominal projected spot with a demagnifying ratio of 10:1. Intrapixel sensitivity variations of up to 20% were observed as shown in Figure 2-8. The temporal variation of light intensity modulates the signal making it difficult to isolate from true spatial position modulation. The X and Y micrometers allowed movements of the spot in steps of 1 micron on the surface of the CCD. Without an automated positioner, it was difficult to get precise alignment of the CCD and the source which in turn affected the scanning precision, due to both optical aberrations and misalignment of the lens. In addition, studies were conducted at selected wavelengths only. As the response modulation varies strongly with wavelength, mainly due to interference effects, calibrating at several wavelengths would be necessary.

A. Piterman et al. [74] studied the non-uniform pixel response in a back-illuminated

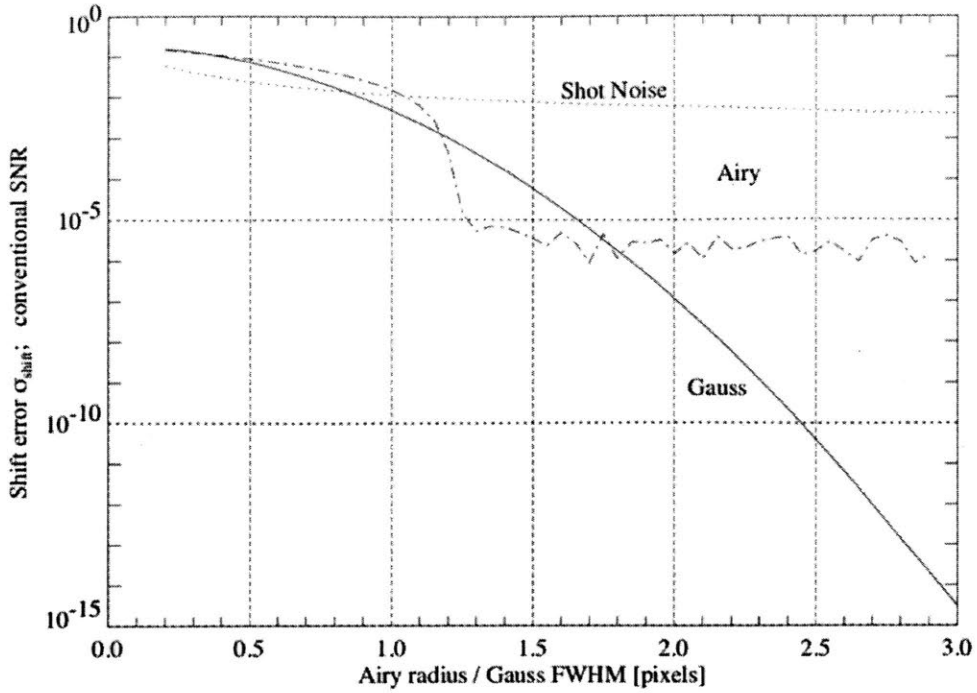

Figure 2-10: Shift error for Airy (dashed line) and Gaussian (solid line) input PSFs as a function of image size using a Bessel V filter. The x-axis displays the image size in number of pixels and y axis displays shift error. The shift error is defined as the standard deviation of the signal, normalized by the average signal. It can be seen that for an image size less than 1.1 pixels, non-uniform PRF is the limiting factor for photometric precision.

CCD as seen in Figure 2-9. The light source used is an Oriel lamp with an optical feedback loop and contributes to an uncertainty in measurement of at least 0.05%. The scans were performed in a 3x3 pixel area with 26x26 scan points. The subpixel sensitivity maps were produced using a Bessel V filter and Bessel I filter, and were found to exhibit strong symmetry. It was found that shot noise is never the dominant noise in the undersampled images regardless of the form of the PSF, as seen in Figure 2-10 [75]. For the width of the image less than 1.1 pixels, the errors introduced by the non-uniform PRF is always the limiting factor for photometric precision.

Intrapixel response measurement of JWST infrared detector arrays was performed in 2008 using a simple experimental setup with a pinhole illuminated by a non-stabilized LED source and a plano-convex glass lens ([76]). A hybridized HAWAII-

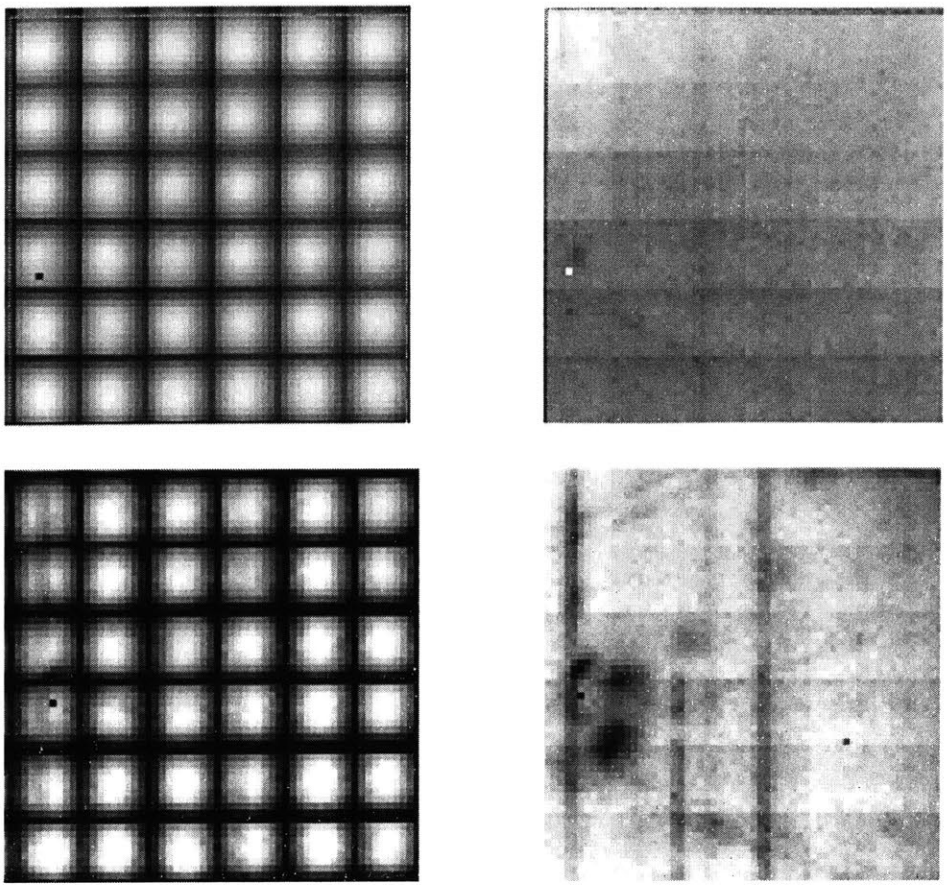

Figure 2-11: Scans of 6x6 pixel area of the HAWAII-2RG detector array at 650 nm and a temperature of 80K (above) and 40k (below). The left hand panels display isolated pixel scans while the right hand panels display total charge scans. The scans show intrapixel response variations and defects at the subpixel resolution [76]. Intensity of the light measured, either relative or absolute, were not indicated on the images.

2RG device with a 5 micron cutoff substrate-removed HgCdTe detector layer was used. A subpixel resolution of 5 micron was used and a series of small images were taken while stepping the pinhole image in steps of 0.1 pixel across the array. The images were then combined into a pixel response map as shown in Figure 2-11. One pixel in each image is chosen and the value of the pixel is plotted in each image as a function of the position of the source for the image.

S. B. Mahato et al. measured the intra-pixel sensitivity variations of a CMOS front-illuminated Image Sensor [77]. The experimental setup consisted of an 250W incandescent lamp mounted on a housing with a lens at the exit port. The pixel size

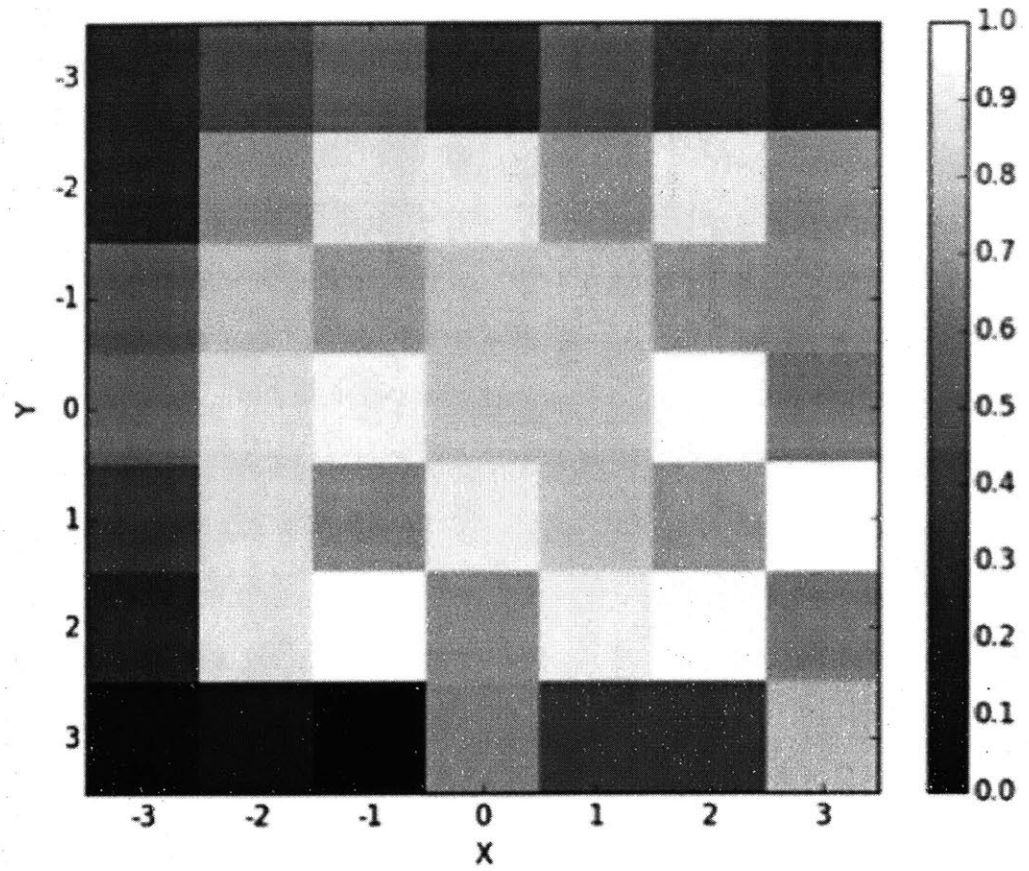

Figure 2-12: Intrapixel sensitivity map for a single pixel in a front-illuminated CMOS image sensor. The map is divided into 7x7 subpixels and the x- and y-axes show the subpixel numbers. The intensity varies between 0 and 100% with higher sensitivity towards the center and lower sensitivity towards the edge of the pixel. [77]

of the detector was 6 μm x 6 μm, and the step size selected was 0.6 μm. The spot was scanned over a 5x5 pixel area starting from the center of a pixel. The response map of a single pixel with 7x7 sub-pixels aggregated into a single 2D raster is shown in Figure 2-12. The intrapixel response varies between 0 and 100% with lower sensitivity towards the edge of the pixel.

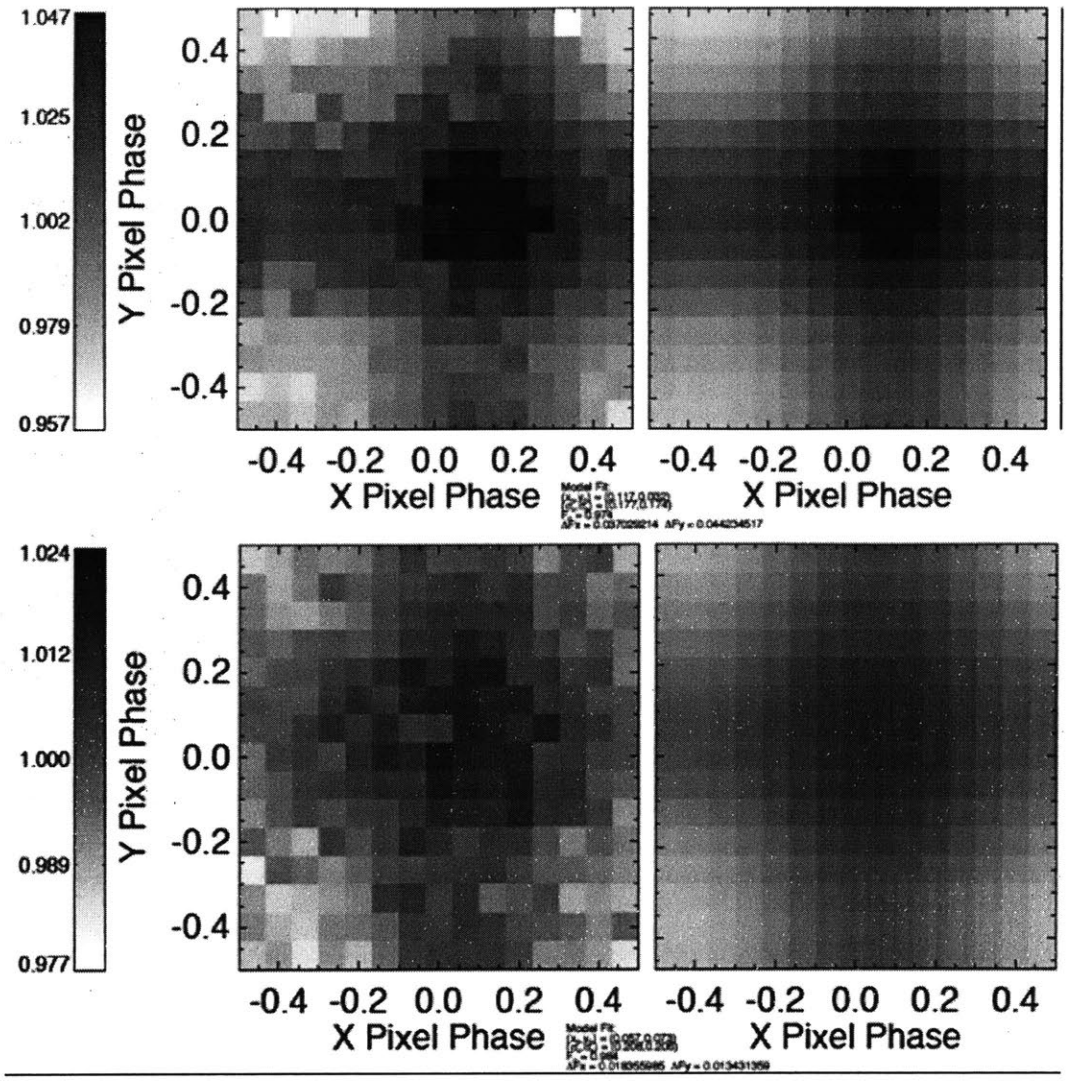

Figure 2-13: Intrapixel map generated by performing on-orbit observations for channels 1 and 2 of Spitzer's IRAC Camera. The top panels show the pixel-phase maps for 3.6 μm and bottom panels for 4.5 μm. The panels to the left display binned relative photometry while the panels to the right display residuals from fitting the model to the binned data. [78]

2.3.2 State-of-the-Art Data Processing Techniques

Spitzer Space Telescope Data Processing

Due to the undersampled nature of the PSF, the IRAC arrays show a variation in photometry of as high as 8% as the center of the source moves across a pixel due to spacecraft wobble and drift. This effect is called the pixel phase effect and is

caused primarily due to the intrapixel quantum efficiency variations [79]. In order to map out a single pixel, the star $NPM1p67.0536$ was observed using 0.4 second integrations at the 3.6 and 4.5 μm channels, mapping each pixel in 0.1 arcsecond steps. Each map was repeated 10 times for the full array observations. A signal-to-noise ratio of better than 0.1% was obtained per 0.1 pixel step. In channel 1, the response varied by 7.4% and for channel 2, the response varied by 3.4%. The center pixel of each field of view was mapped and then an average map was produced. To generate the pixel-phase correction, the star was centroided, the flux was calculated using aperture photometry and the correction was calculated as a weak function of aperture size. The model developed to fit the binned data was a double Gaussian fit, the sum of Gaussians in the x and y plane. An intra-pixel gain map was produced for a sub-region called the "sweet spot" of the center pixel as shown in Figure 2-13. The high precision map only works if the Spitzer Pointing Calibration Reference Sensor (PCRS) is used to ensure that a target arrives on the sweet spot. In order to extend this mapping to cover even a few pixels at the desired resolutions, 1-3 months of observation time would be required.

Efforts led by S. Ballard et al. [80], show that using a polynomial intrapixel sensitivity function would achieve a precision of 230 ppm per 20-minute bin size, while a novel self-calibration technique that utilizes flight data outside of a transit to develop a point-by-point weighted intrapixel sensitivity function, could improve the precision up to 71 ppm per 20-minute bin. The caveat was that flat fielding the data or creating an interpixel sensitivity map had the effect of suppressing the depths of transits and introduced additional correlated noise outside of the transits.

Hubble Space Telescope Data Processing

Tests of the photometric precision have been performed on the Wide Field Planetary Camera 2 (WFPC 2) of the Hubble Space Telescope by measuring stellar magnitudes for a set of dithered images in ω Cen. A set of 20 exposures were taken with dithering of 0.2 pixels between exposures, and dithers were made along rows and columns. At each pointing, several dozen stars were measured. A mean brightness was found for

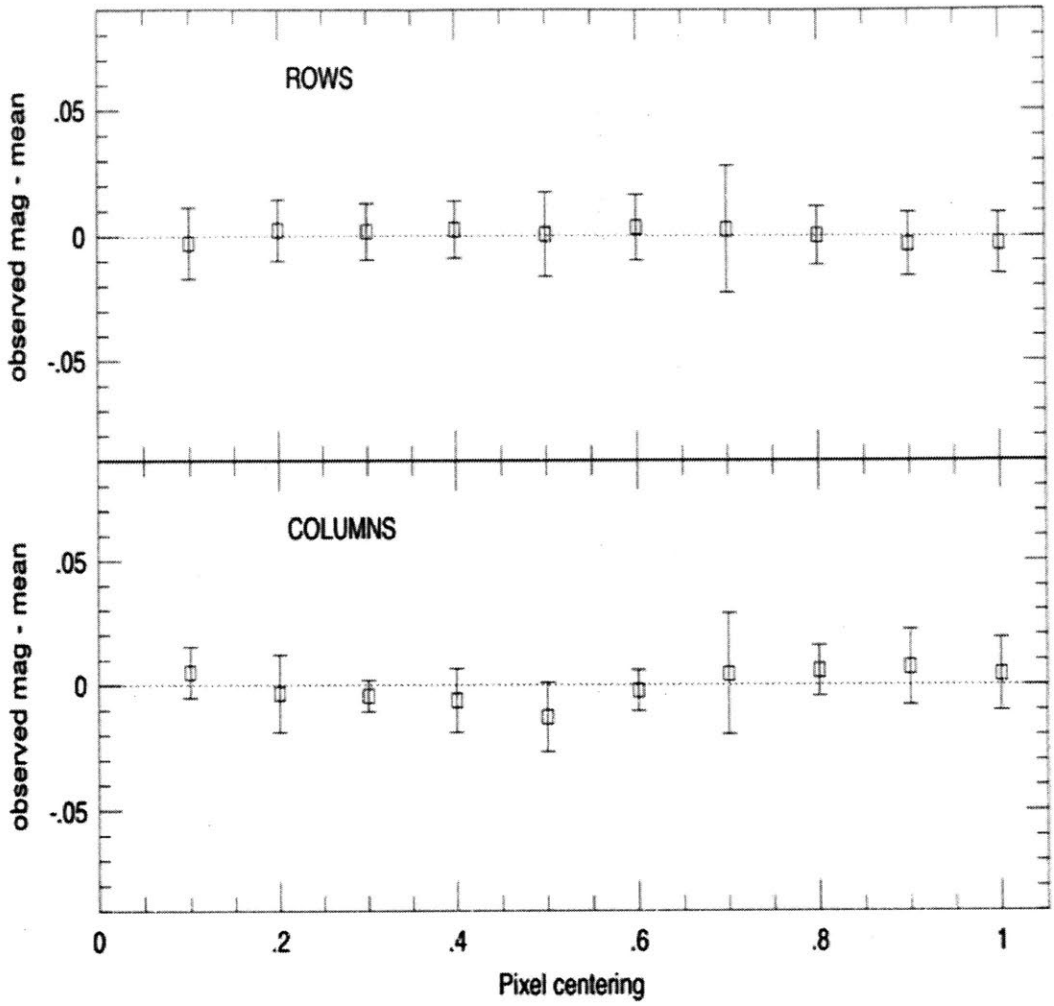

Figure 2-14: Deviation of stellar magnitudes from the mean magnitudes for a set of dithered images as a function of pixel centering in ω Cen taken by the WFPC2 of the Hubble Space Telescope. The x-axis shows pixel centering in steps of 0.2 pixels and y-axis shows the observed magnitude deviation from the mean. The systematic error in photometry due to subpixel variations was estimated to be at 2% level along the columns and lesser than that along the rows. [81]

each star based on the 20 observations. The deviations from the means is shown in Figure 2-14, as a function of pixel centering along rows (top panel) and columns (bottom panel) for stars with at least 1000 DN. The data are binned into 0.1 pixel intervals. The results show a systematic error in photometry as a function of centering along columns at 2% level.

Dithering requires noticeable amount of spacecraft overhead in terms of obser-

vation time. Processing dithered data is also substantially more demanding than processing undithered data. In addition, if the primary goal is to measure time-series photometry, dithering would increase the noise level. The potential drawbacks of dithering are substantial including addition load on the full system, lowered overall efficiency of observations, and difficulty to perform parallel science observations [81]. Hence, it is not used extensively for in-flight calibration of space telescopes.

2.4 Research Gap

There currently does not exist an integrated approach or framework that systematically brings together the knowledge acquired from design phase modeling and simulation, laboratory testing of the camera during I&T, and in-flight data processing techniques to identify major sources of instrument systematic noise, and calibrate and correct for them in the science data processing pipeline with an objective to establish a noise floor for the mission. In this chapter, we reviewed the key photometry missions, their photometric precision requirement, and limitations in achieving the requirement. We identified state-of-the-art laboratory techniques developed independently by the detector community to study intra-pixel sensitivity variations in the detector. Subsequently, we also reviewed the state-of-the-art data processing and in-flight calibration techniques used by scientists to calibrate and remove systematics from the data for key missions such as Spitzer, Hubble and Kepler. The dominant sources of systematic noise addressed in this chapter are spacecraft jitter, intra-pixel sensitivity variations, and thermal events.

In the rest of this thesis, we focus on developing a generalized framework that integrates knowledge from simulation and modeling, laboratory characterization of the telescope, and in-flight data analysis techniques to characterize and calibrate the sources of systematic noise that are limiting factors in achieving higher photometric precision.

Chapter 3

Integrated Approach to Systematics Calibration

In this chapter, we describe a generalized systematic noise calibration and performance improvement framework for space telescopes. The framework uses active integration with inherent feedback mechanisms in order to maximize the utility of results from three functional areas: simulation and modeling, laboratory characterization, and flight data analysis techniques. The goal is to systematically assess the performance of the system by identifying the major systematic noise sources, characterizing, calibrating, and removing them from the flight data. More specifically, we develop techniques to improve bright star photometry and establish a noise floor for the mission. In addition, we also develop a pipeline-driven approach to noise budgeting and calibration test plan development for missions in the early design phase in order to address the gaps in ground characterization and calibration of the instrument. Figure 3-1 describes an overview of the framework.

We apply the framework to two high precision photometry missions; TESS and ASTERIA. TESS is a NASA Explorer mission with the objective to survey several hundred thousand main-sequence nearby bright dwarf stars and discover thousands of planets smaller in size than Neptune. ASTERIA is a CubeSat-based astrophysics mission, and the first mission to demonstrate high precision photometry in space using CMOS detectors. Finally, we develop a model-based calibration test plan for

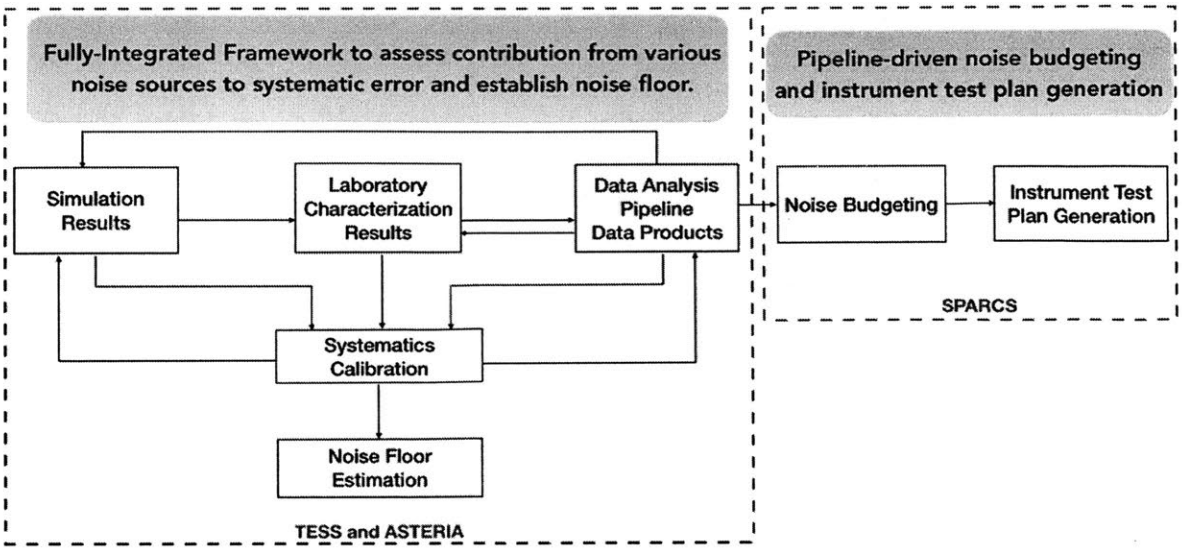

Figure 3-1: High-level description of the fully-integrated framework to systematics calibration and performance improvement. The framework aims to maximize the utility of results from three key functional areas: modeling and simulation, laboratory characterization, and flight data analysis pipeline development. The ultimate goal to achieve optimal systematics calibraton and perform noise floor estimation. In addition, we develop a bottom-up approach to noise budgeting and calibration test plan generation using the data analysis pipeline as the first step in the process.

SPARCS, a CubeSat-based UV photometry mission.

The rest of this chapter is a detailed description of the methodology. We begin by describing the high-fidelity simulation of the instrument system to assess the performance of the mission. Next, we develop precision noise characterization techniques in the laboratory, followed by in-flight calibration and data analysis techniques to identify major noise sources. Then, we improve performance by integrating an optimal systematic noise calibration software with the flight data processing pipeline. The last step is to summarize the results and inform error budgeting I&T plans for future missions, ASTERIA constellation and SPARCS.

3.1 Photometric Precision Assessment

The photometric precision assessment step provides an estimate of the photometric precision and expected noise floor for the mission. The first block in Figure 3-2 shows

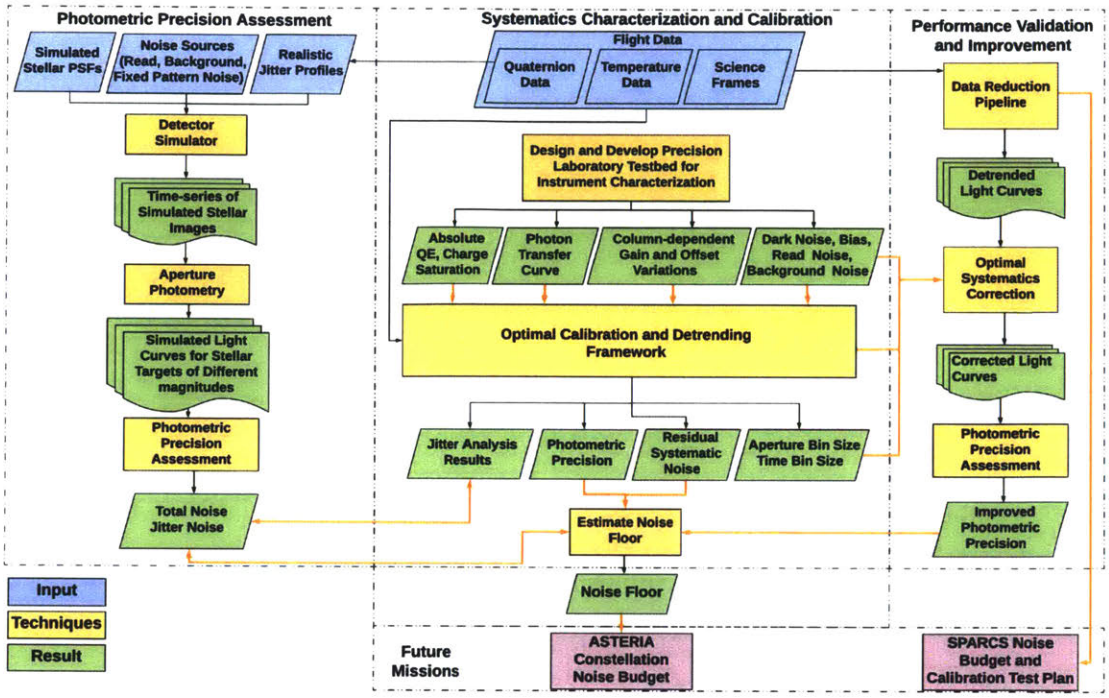

Figure 3-2: Detailed description of the various steps in the integrated approach to systematics calibration and performance improvement. We describe the framework in three key steps: photometric precision assessment, systematics characterization and calibration, and performance validation and improvement.

the software architecture for this step. It consists of a high-fidelity simulation of the camera detector. The simulator takes stellar images as input and provides total noise and jitter noise as a function of stellar magnitude as output. The total noise represents the photometric precision, a key metric to measure performance of the system.

The heart of the simulation step is the detector simulator. We set up the simulator by defining the size of the imaging array and pixels. We add major noise sources to the detector simulator such as inter-pixel and intra-pixel sensitivity variations depending on the type of detector. The type of detector (CCD, CMOS, or hybrid), is mission-dependent and the choice is driven by the functional, performance and operational requirements of the space telescope. CMOS detectors exhibit higher pixel response non-uniformity and intrapixel response variations compared to CCD

detectors. We draw estimates from laboratory measurements for inter-pixel variations and from the literature for intrapixel variations. We simulate the detector array using relevant specifications from the sensor datasheet such as effective imaging area, pixel size, and quantum efficiency. Depending on the type of detector, we simulate a range of sub-pixel response variations to evaluate the effect on photometric precision, especially in the presence of spacecraft jitter. Subpixel response variations are due to variation in detector response as we go from the center of the pixel to the edges of the pixel. The varying quantum efficiency causes fluctuations in the light intensity when there is movement of the stellar image on the detector even by a fraction of a pixel, caused typically due to spacecraft jitter or temperature variations, thus affecting the photometric performance.

There are three inputs to the simulation: simulated stellar point spread functions (PSFs), noise sources such as photon noise, read noise, background noise and fixed pattern noise, and realistic jitter profiles. Photon noise is directly proportional to the square root of the number of photons arriving at the detector for a Poisson distribution. We generate the simulated stellar point spread functions (PSFs) for target stars of varying stellar magnitudes by calculating the total light intensity from the targets. We derive read noise from laboratory measurements and background noise from models. We add realistic jitter profiles to simulate the effect of spacecraft jitter. Spacecraft jitter causes the target star to move on the detector in steps of fractions of a pixel. Using the jitter profile, we produce a time-series of simulated stellar images. We then develop an aperture photometry pipeline that places an aperture mask on the stellar image and adds the charge within the mask to produce simulated light curves. We then bin the light curve to the required time bin size. In the last step, we calculate the photometric precision of the light curve. The two main outputs from the simulation are total noise that indicates the photometric precision, and jitter noise that quantifies the effect of jitter on photometric precision.

Deals with Photons	Deals with Electrons
Pixel response function	Gain
Flat field	Shot noise
Effective area	Pixel response non-uniformity
Focus changes	Linearity
Optical aberrations	Read noise
Thermal variations	Intra-pixel response variations
Jitter	Digitization
Drift/spacecraft flexure	Clocking smear
	Fixed pattern noise
	Saturation
	Blooming
	Undershoot
	Charge transfer inefficiency
	Cross talk
	Start of line ringing
	Straps
	Fringing

Table 3.1: List of instrument properties and noise sources affecting photometric performance and system throughput.

3.2 Systematics Characterization and Calibration

Systematics Characterization and Calibration is the second step in the framework, as shown in Figure 3-2. In this step, we develop an optimal systematics correction framework that enables us to remove instrument noise sources effectively from the flight data using a combination of ground characterization and in-flight calibration techniques.

Before diving into the details of the systematics characterization and calibration framework, we provide a brief introduction to the different types of noise sources. We categorize noise sources as spacecraft and instrument noise sources depending on the source of the losses. Spacecraft noise sources include jitter, differential velocity aberrations, drift, thermal variations, and spacecraft flexure. Instrument noise sources include absolute quantum efficiency (QE), intrapixel sensitivity, focus changes, undershoot, saturation, blooming, clocking smear, and many more. These noise sources affect the overall system throughput and the systematic error expected in the data.

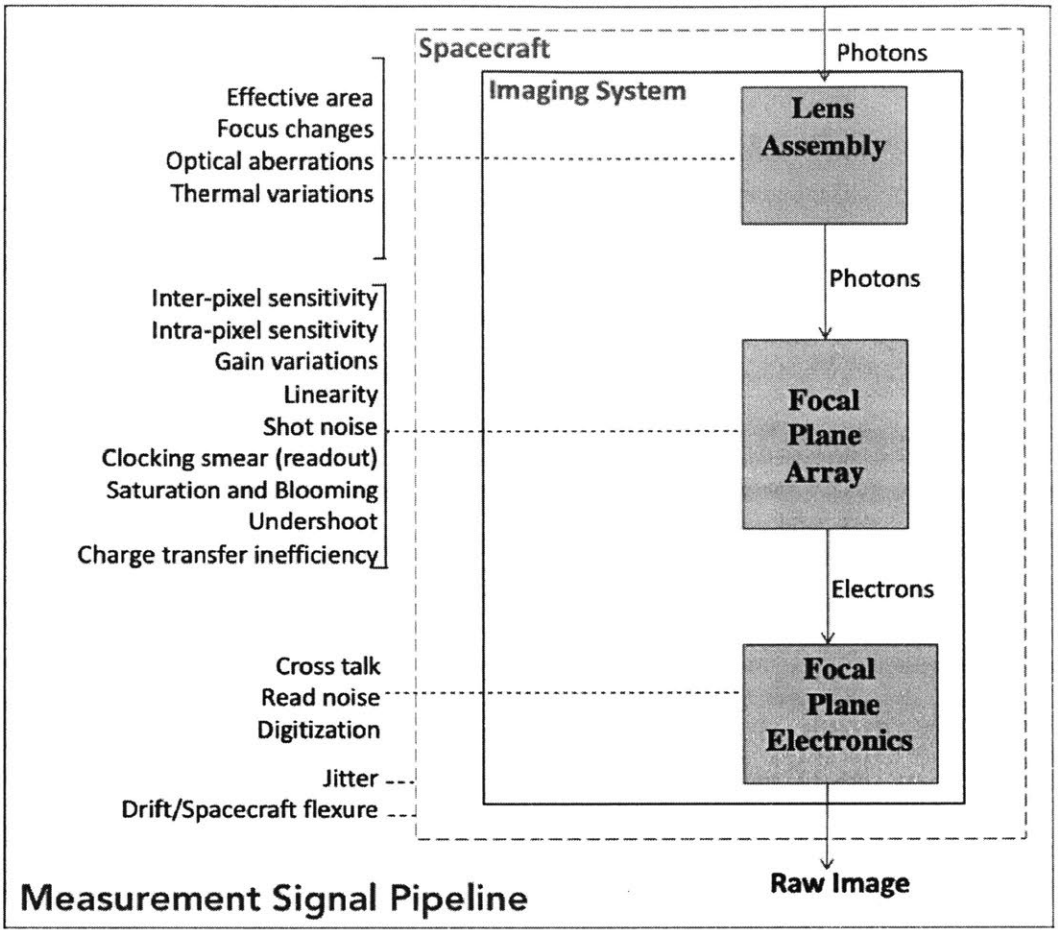

Figure 3-3: Measurement signal pipeline showing the components of the imaging system and the various instrument properties and noise sources affecting the overall performance of the system.

In addition to the instrument and spacecraft-related noise sources, there are several noise sources like the cosmic rays, stellar variations, zodiacal noise, etc. that are further categorized as astrophysical noise sources.

The noise sources can be grouped into two modules; one that deals with electrons and the other that deals with photons. A comprehensive list of the noise sources is shown in Table 3.1. We present noise sources in the form of a measurement signal pipeline as shown in Figure 3-3. This method of decomposition of noise sources into different levels gives a better understanding of how the measured signal traces through the system, and how various physical phenomena affect the measured signal.

We decompose the measurement signal pipeline into four components: lens assem-

bly, detector focal plane array, focal plane electronics, and the spacecraft, and show the noise sources associated with each component. The focal plane array converts the photons into electrons, and the analog-to-digital converter in the focal plane electronics amplifies and converts the electrons into digital numbers. There are several noise sources that contribute to losses at every step in the measurement pipeline. Using the laboratory and flight data analysis techniques, we characterize and calibrate noise sources that affect the overall system throughput and total systematic error.

3.2.1 Laboratory Testing and Characterization

We present novel laboratory techniques developed to characterize TESS CCD detectors and ASTERIA CMOS detectors. Specifically, for TESS, we develop techniques to characterize the absolute quantum efficiency, charge saturation and blooming. For ASTERIA, we develop techniques to characterize and correct for the fixed pattern noise. Typically, for larger space-based telescope missions, there is an opportunity to perform a more involved test campaign and take ground data required for flight data calibration before launch whereas for smallsat missions, the testing time is often short and the missions are both time and cost constrained. In the case of TESS, we performed the characterization tests prior to launch. Whereas, due to schedule constraints and ASTERIA's status as a technology demonstration mission, we could not perform detector characterization before launch. Hence, we performed the tests on the ASTERIA testbed with a flight-like detector along with flight-like electronics, after launch in order to get a better understanding of systematics in the flight data.

Integration Level

We perform laboratory characterization at various levels of integration. Typically, we test the detector along with associated electronics, and characterize the various detector properties such as absolute quantum efficiency, charge saturation and blooming, dark noise, read noise, bias, fixed pattern noise, etc. Following this, we test the camera which consists of the detector assembly and the lens assembly along with

associated electronics. Lastly, we characterize the entire telescope during verification and validation. For TESS, we present results from various tests at the detector level, whereas for ASTERIA we performed the tests using the entire camera assembly.

Environment

Laboratory characterization of certain instrument properties requires simulating on-orbit conditions such as very high photometric stability of the light source and temperature stability to obtain precise measurements of the throughput. One example is the measurement of absolute quantum efficiency. A variation in temperature or the intensity of light source can induce significant variations in quantum efficiency.

3.2.2 Optimal Calibration and Detrending Framework

We take in-flight calibration data to compare with the ground calibration data and to validate the performance of the telescope. In the case of CubeSats, we typically need more in-flight calibration data to fill gaps in the ground test campaign due to schedule and cost constraints.

We develop an optimal systematic noise correction framework using results from the first step (photometric precision assessment) and the laboratory characterization results. The main results from this step are photometric precision, residual systematic error, jitter noise, temperature noise, and effects of aperture bin size and time bin size.

3.3 Performance Validation and Improvement

The last step in the framework is performance validation and improvement, as shown in Figure 3-2. We develop a data analysis pipeline to validate the science performance of the mission. The flight data analysis pipeline takes the raw images as input and performs aperture photometry to produce a time-series of stellar flux. We further process the data by developing detrending algorithms to improve the photometric

performance. We calculate the photometric precision by taking the root mean square (RMS) of the light curve.

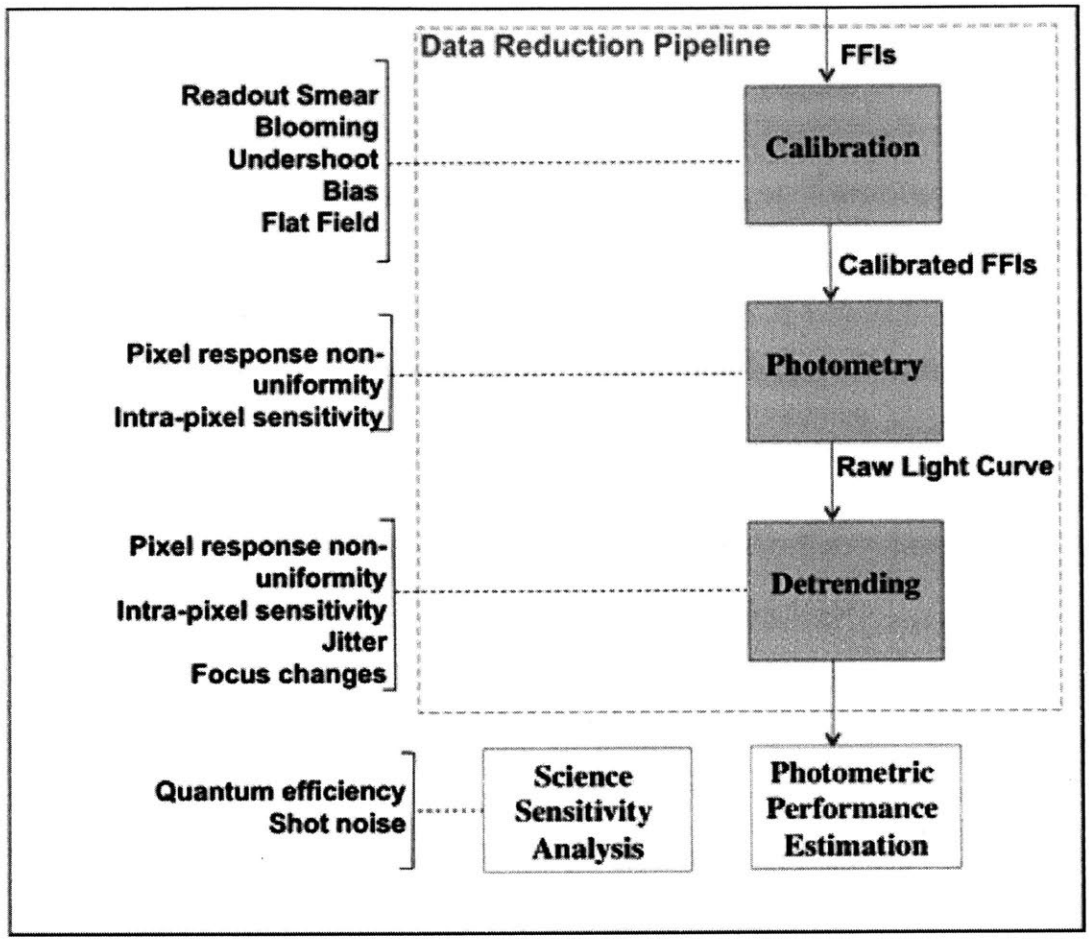

Figure 3-4: Data analysis pipeline showing the various steps in data reduction and noise sources that are detrended at these steps.

We model the noise effects that were characterized in the previous sections and integrate them with the data reduction pipeline at different stages of data processing. The Figure 3-4 shows the methodology to evaluate the effect of noise on the photometric performance and the science yield of the mission.

In the first step, we remove the effects of charge saturation, blooming, undershoot, straps, flat fielding, clockout smear (also called readout smear) and sector-specific voltage bias from the Full Frame Images (FFIs). We then remove variations in inter-pixel and intra-pixel sensitivity during the photometry and detrending steps. Then, we feed raw light curves from the photometry stage into the detrending algorithm

to remove jitter, and focus change effects due to temperature variations. Next, we use the clean light curves obtained from this process to calculate the overall signal-to-noise ratio, and to estimate the photometric performance of the system. We use QE and shot noise to calculate the signal throughput for the system, and to perform a rough-order of magnitude science yield estimation. The process described here is a generalized approach to data reduction. In the following sections, we describe the pipelines developed specifically for TESS and ASTERIA and discuss the processing done prior to applying these pipelines by the TESS and ASTERIA data processing pipelines.

In addition, we demonstrate an improvement in photometric precision for bright stellar targets by incorporating the optimal systematics correction from the previous step into the flight data analysis pipeline. Using results from the previous step and this step, we establish a noise floor for the mission.

3.4 Applications to Future Missions

We develop a framework to perform early design phase error budgeting for future missions including the ASTERIA constellation, and develop an incompressible calibration test plan for CubeSat-based science missions including SPARCS using the results from the previous stwps. We begin by calculating the photometric precision requirement for the mission. We then calculate the contributions of various noise sources based on instrument design, detector selection, and Level 3 and Level 4 requirements. With CubeSat missions, often, calibration requirements are either missing or vaguely defined. We create a data analysis pipeline-driven model that indicates all the noise properties that need calibration. We then generate an incompressible calibration test list which consists of all the tests that have to be absolutely performed on the ground in order to analyze the data using the data reduction pipeline. Tests that can be performed on-orbit are indicated as optional for ground testing.

3.5 Summary

In this chapter, we described the fully-integrated framework demonstrating feedback mechanisms from the threee key functional areas: simulation and modeling, laboratory characterization and fight data analysis. We described the framework in three steps: photometric precision assessment, systematics characterization and calibration, and performance validation and improvement. The key results from the first step, photometric precision assessment, were total noise that represents the photometric precision, and jitter noise that quantifies the effect of spacecraft jitter on photometric performance. These results are used in the second step, specifically, in developing the optimal systematics calibration framework. The inputs to this framework come from the flight data analysis pipeline that provides the data products, and the laboratory characterization techniques that provide an insight into the instrument behavior. The laboratory techniques characterize detector effects such as absolute quantum efficiency, charge saturation and blooming, inter-pixel variations, fixed pattern noise, dark noise, bias, etc. The results from the optimal systematics calibration framework include photometric precision, jitter noise, temperature noise, and effects of time bin size and aperture bin size on photometric performance. The results from this step feed into the last and final step: performance validation and improvement, where we develop techniques to remove the systematics and calculate the improved photometric precision. The results from the second and final steps feed into the noise floor estimation.

Further, we use the noise floor to inform noise budgeting for the ASTERIA constellation concept. We use the data analysis pipelines to inform the calibration test plan development for SPARCS. These two examples demonstrate the utility of the results from the framework for future missions.

Chapter 4

TESS: Framework and Results

In this chapter, we present the integrated systematics framework for TESS, and results including photometric precision assessment, optimal systematics calibration and correction framework, residual systematic error and noise floor for the mission. We begin by providing a brief overview of the misson followed by instrument overview, and TESS data products. Next, we explain the integrated systematics calibration framework for TESS, and present the results in three steps: photometric precision assessment, systematics characterization and calibration, and performance validation and improvement. We establish feedback mechanisms to utilize results from each step at various other steps in the framework. We will present these relationships and explain the significance of the framework as we progress through the chapter.

4.1 Mission Overview

The Transiting Exoplanet Survey Satellite (TESS) is a NASA Explorer-class mission with the primary objective of searching for planets transiting FGKM bright dwarf stars [14]. TESS will detect planets by performing differential time-series photometry and facilitate follow-up measurements of planet masses and atmospheres by other ground-based and space-based observatories. It is expected to discover a thousand or more planets that are smaller in size than Neptune, including dozens of Earth-sized planets during a two-year near all-sky survey. TESS will observe from an elliptical

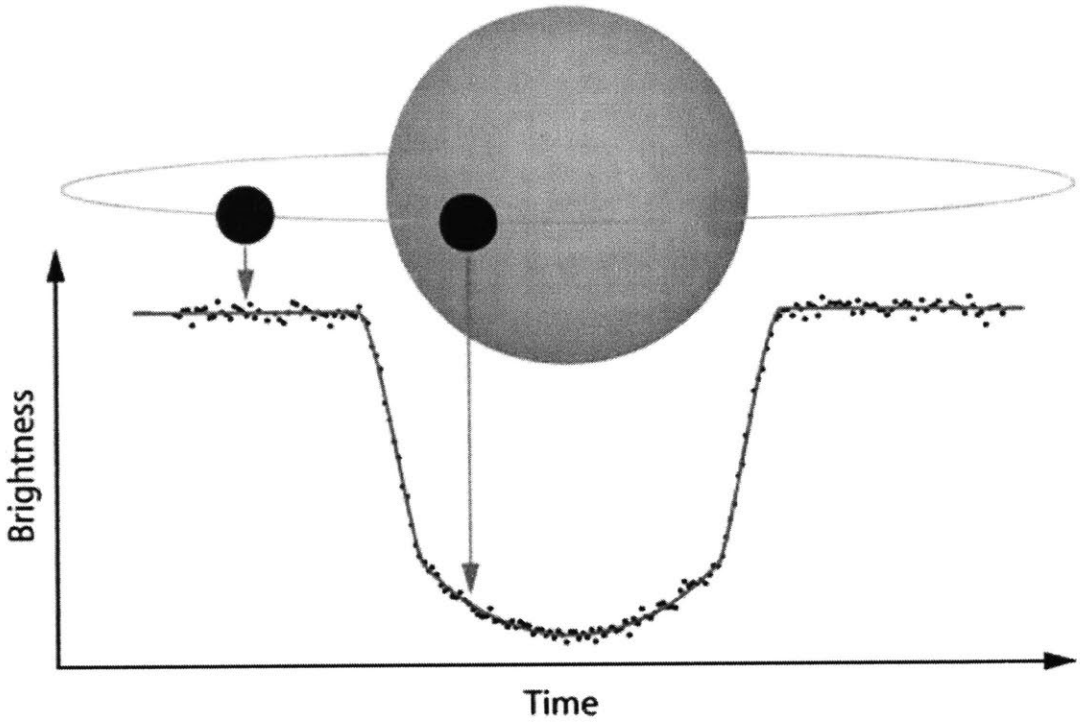

Figure 4-1: Illustration of a planetary transit and the corresponding temporary drop in brightness of the host star. TESS employs four wide-field optical charge coupled device (CCD) cameras to monitor more than 200,000 main sequence dwarf stars. TESS has discovered 37 confirmed planets and 1417 planet candidates using the transit method [8].

orbit in 2:1 resonance with the Moon's orbit, and with a 13.7-day period that has the nominal perigee and apogee at 17 $R_{\oplus}$ and 59 $R_{\oplus}$ respectively achieved through a series of apogee-raising burns and a lunar gravity assist [82]. The orbit remains above the Earth's radiation belts and in a relatively low radiation environment. TESS was successfully launched from Cape Canaveral by the SpaceX Falcon 9 rocket on April 18, 2018.

TESS employs four wide-field optical charge-coupled device (CCD) cameras with a band-pass of 600 nm to 1050 nm to detect temporary drops in brightness of stars due to planetary transits. All four cameras are mounted onto a single plate. TESS has two operational modes namely the Low Altitude Housekeeping Operations (LAHO) near perigee and the High Altitude Science Operations (HASO) near apogee. Ka-band science data downlink and S-band uplink and downlink for commands and teleme-

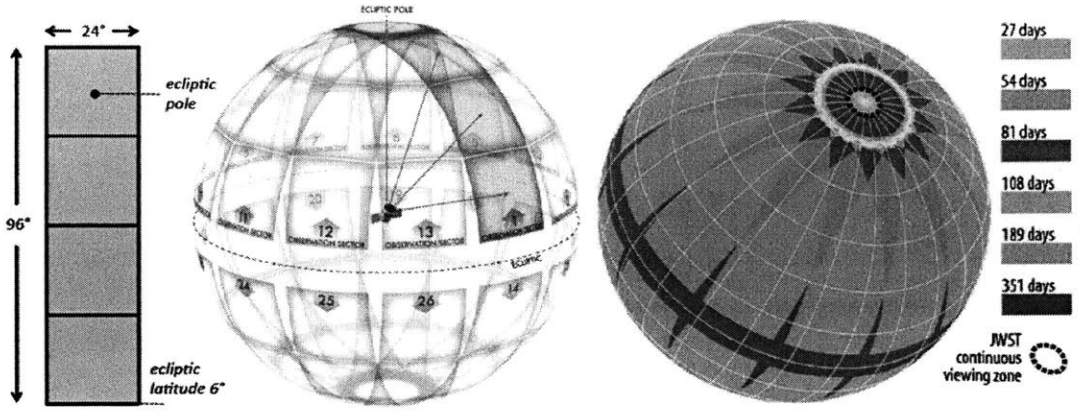

Figure 4-2: TESS field of view and observational sectors including regions of overlap. Left: The instantaneous combined field of view of the four TESS cameras is 24° x 96°. Middle: TESS has 26 observational sectors, with 13 per hemisphere. Right: shows the overlap between sectors and duration of observations including the region which JWST will be continuously viewing at all times [14].

try respectively, are performed during the 16-hour LAHO mode while the science operations are carried out during the HASO. The four cameras provide a combined field-of-view of 24° x 96°, extending from an ecliptic latitude of 6 to the ecliptic pole. The north and south ecliptic hemispheres are divided into a total of 26 partially overlapping observational sectors as shown in Figure 4-2 and each sector is observed continuously for two spacecraft orbits, 27.4 days.

4.1.1 Instrument Overview

Each camera with an effective aperture size of 10 cm, consists of an f/1.4 custom lens assembly, and a CCD detector assembly, which consists of four deep depletion back-illuminated MIT Lincoln Lab CCID-80 devices with associated electronics [83]. The electronics consist of three compact double-sided printed circuit boards, each 12 cm in diameter. The detectors are designed for enhanced sensitivity to the redder wavelengths because it is easier to detect small planets around small red stars. The surface of one of the lens elements has a long-pass filter coating to enforce the band-pass cutoff at 600 nm. The upper limit of the band-pass cutoff at 1050 nm is driven by the quantum-efficiency curve of the detectors. A higher QE over the red wavelengths

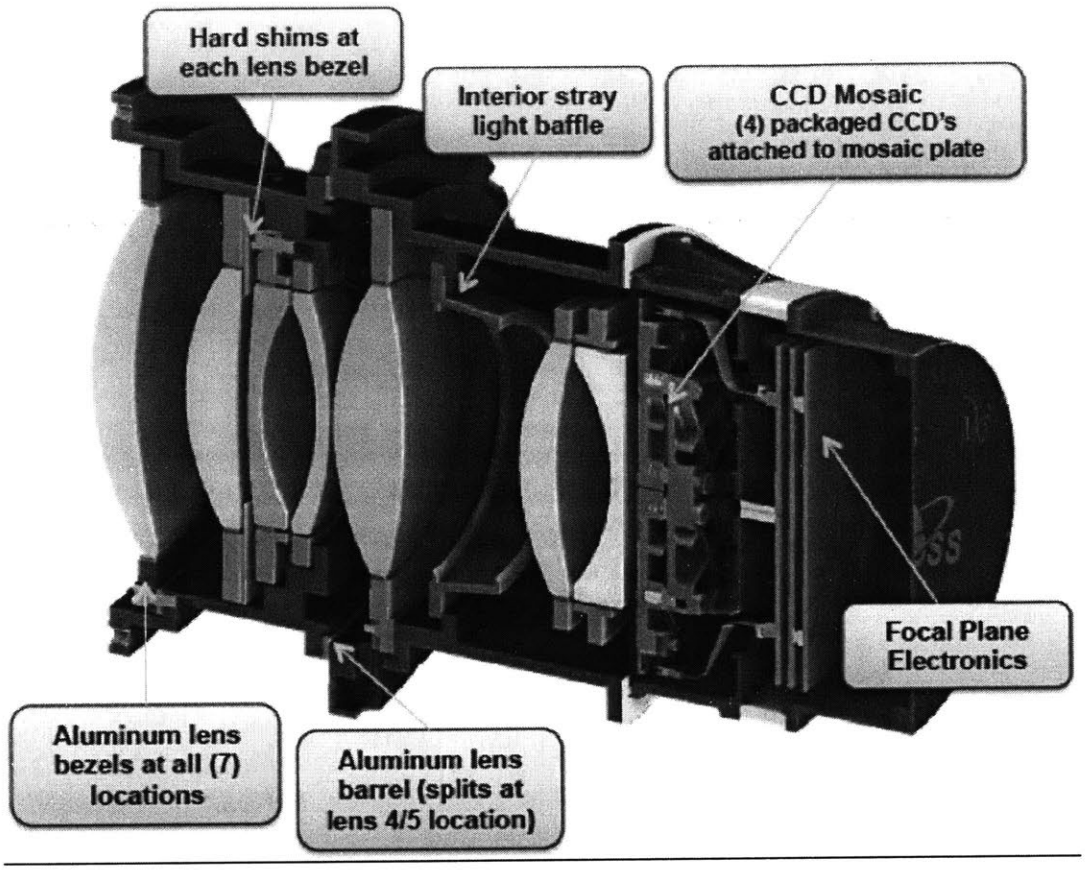

Figure 4-3: TESS camera assembly consisting of the lens assembly, CCD focal plane array, and detector electronics. The CCD detector assembly consists of four deep depletion back-illuminated MIT Lincoln Lab CCID-80 devices. The detector electronics consist of three compact double-sided printed circuit boards, each 12 cm in diameter [14].

will yield a higher photon count, and thus higher planetary detections. The detectors are maintained in a nearly constant thermal environment at $-80°$ C, with temeprature variations of <0.01 ° C/hr for 90% of the orbit. The general instrument characteristics are listed in Table 4.1

Each CCD is read out through four output nodes at a rate of 625 pixels/s. The CCDs produce a continuous stream of images with an exposure time of 2 s. These images are summed into consecutive groups of 60 such that the effective exposure time is 2 min. The full frame images (FFIs) are stacked every 30 min and stored in the solid-state buffer (SSB) cards in the TESS Data Handling Unit (DHU), which are then downlinked every 13.7 days at perigee.

Characteristic	Value
Field of View	24° x 96°
Number of Cameras	4
Number of CCD Detectors	4 per camera
CCD Imaging area	2048x2048 pixels
Pixel size	15 μm^2
Pixel Depth	100 μm
Lens	Custom 146 mm, f/1.4
Bandpass	600-1050 nm
CCD Operating Temperature	−85° C

Table 4.1: Instrument Characteristics. [8]

CCD Detector

In a CCD detector, each pixel has p-doped metal-oxide semiconductor capacitors that allow conversion of incoming photons into electrons due to photoelectric effect. The electric charge accumulates in a potential well and is proportional to the incoming light intensity at that pixel. The stored charges flow from one capacitor to another during readout by applying a voltage to electrodes called gates at each pixel. A change in voltage potential allows the charge to be shifted along the columns from one pixel to the other. The last capacitor transfers the charge into a charge amplifier that converts the charge into voltage which is then digitized and stored in memory.

Each CCID-80 device consists of imaging array and frame store regions. The imaging array as seen in Figure 4-4, consists of 2048 rows by 2048 columns plus one set of buffer rows each at the top. The buffer rows do not count the signal consistently, and hence not used in our output signal calculations. The image array and the buffer rows are transferred to the frame store. The frame store region also measures 2048 x 2048, and has two sets of buffer rows, one at the top and one at the bottom, adding up to 2068 rows by 2048 columns. There are also 10 buffer columns on either side of the imaging array and frame-store regions that are not clocked into the serial register.

There are 10 smear rows that are created during parallel clocking, and are transferred from the image array to the frame store, and 10 virtual rows, as shown in Figure 4-4, that are clocked during the frame-store readout that are not exposed to any illumination, and hence can be used as a measure of the dark current. The

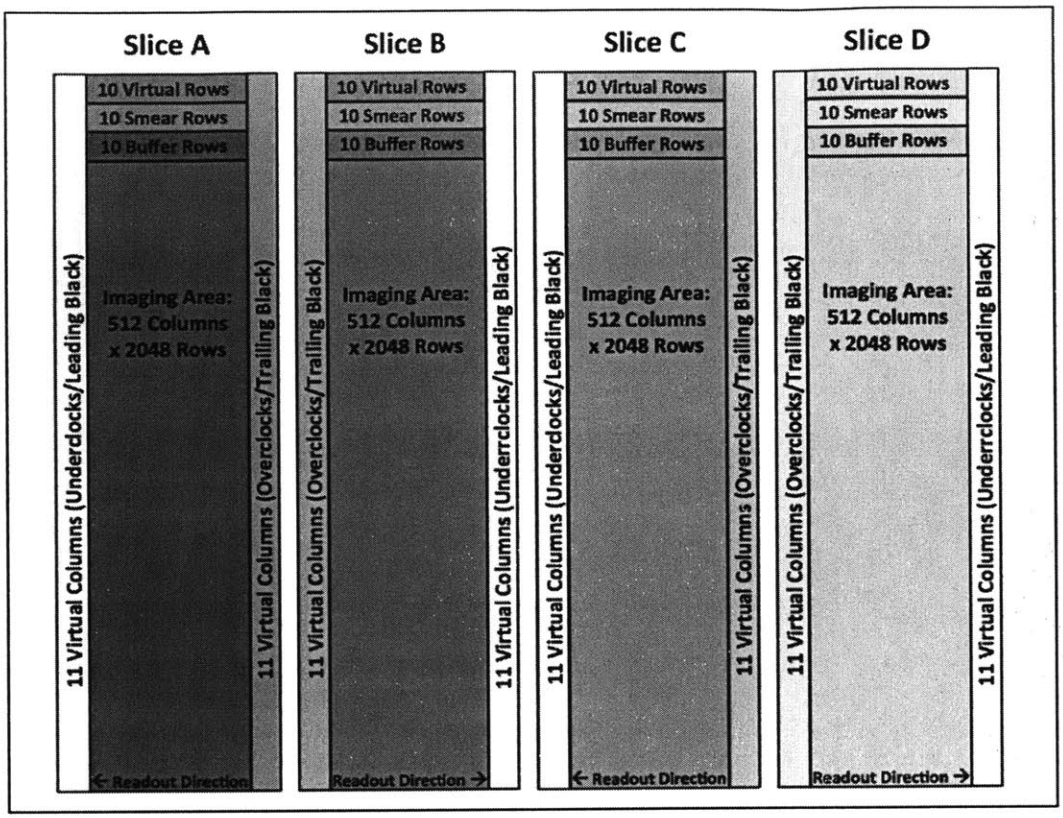

Figure 4-4: Schematic of the CCID-80 device showing the imaging array and frame-store regions. The imaging array has 2048 x 2048 pixels with 512 columns. In addition, there are 10 virtual rows, 10 smear rows and 10 buffer rows, and 11 virtual underclock and 11 virtual overclock columns. [8]

transfer of rows into the frame-store region is performed at a total read out time of 19.95 ms. The pixel outputs are then transferred to the serial register, and read out individually [84].

The CCD readout has four output registers as shown in Figure 4-5: A, B, C, and D. The readout of the pixels from sectors B and D occur in the opposite direction from those through outputs A and C. This is accounted for in the generation of the FITS images. For detector characterization experiments, we use a single flight-grade engineering CCD with pre-flight electronics, and the output from the CCD is obtained in a FITS-format file with the pixels reconstructed such that the four outputs are placed adjacent to each other.

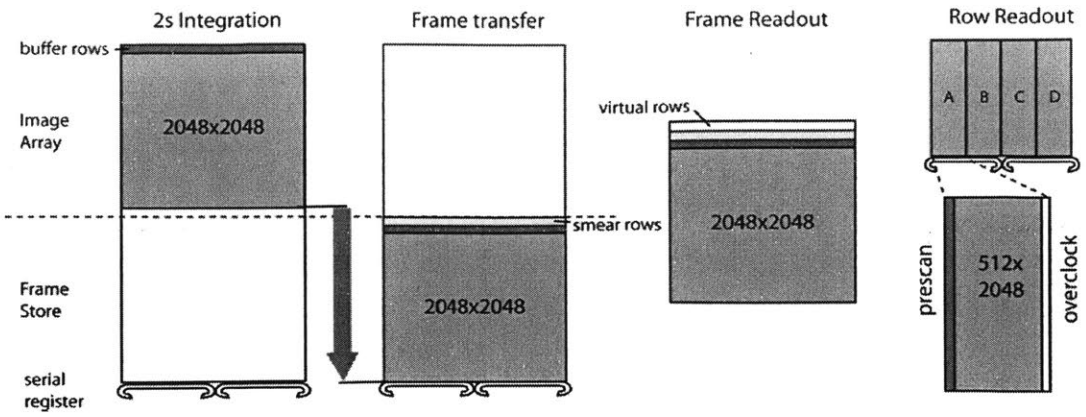

Figure 4-5: Schematic of the CCID-80 device showing the readout directions for the four sectors A, B, C, and D. The imaging array has 2048 x 2048 pixels with 512 columns allocated to each of the four sectors A, B, C, and D. [84]

4.1.2 Data Products from TESS

During nominal operations, the four cameras continuously clock frames with an integration time of two-seconds. Two basic data products are created by the Data Handling Unit (DHU): two-minute "postage stamp" or stacked subarrays and 30-minute Full Frame Images (FFIs). The 30-minute FFIs offer wide variety of target stars that can be targets for exoplanet discovery, asteroseismology or other astrophysical phenomena, whereas the two-minute frames are centered on potential targets of interest for exoplanet discovery, asteroseismology and calibration.

Full Frame Images

The FFI contains all pixels within a single CCD. A set of 1200 30-min full frame images with an effective exposure time of 1440 seconds are produced for every sector's observation. The reduced exposure time is due to the cosmic-ray mitigation applied to the FFIs. Each FFI uses data from 900 consecutive two-second images. Three types of FFIs (calibrated, uncalibrated and uncertainty) are delivered.

Two-minute Postage Stamps

For most stars, 11x11 pixel postage stamps are produced, which sufficiently encloses the optimum aperture around the target star along with the background pixels. Each two-minute frame uses data from 60 consecutive two-second images. The postage stamps are calibrated and formatted into Target Pixel Files in the FITS (Flexible Image Transport System) format.

Target Pixel Files

Target Pixel Files (TPF) contain all the pixels for a given target star over one entire sector. The TPF files are delivered in Flexible Image Transport System (FITS) format with four Header Data Units (HDUs). The HDUs contain basic information about the target star such as TIC (TESS Input Catalog) ID, brightness of the star, image data, quality of the data, aperture that was used for photometry, and cosmic ray corrections that were applied to the calibrated image. The image data contains flux, background flux, time stamp, and uncertainty.

Light Curve Files

Light curve files contain all the outputs from the photometric analysis that is applied to the target pixel files. The photometric analysis also includes cotrending using the Pre-search Data Conditioning (PDC) algorithm. The file contains Simple Aperture Photometry (SAP) flux, PDCSAP flux, time stamps, uncertainties, Cumulative Differential Photometric Precision (CDPP), number of pixels in the aperture, background flux, centroid calculations, correction for differential velocity aberration (DVA).

Auxiliary Data Products

All Threshold Crossing Events (TCEs) have Data Validation (DV) time series with phase-folded light curves, in both whitened and unwhitened domains. The light curves have harmonics removed, level adjusted, egdes detrended, normalized, gap filled and

if the target appears in multiple sectors, the data is stitched. In addition, engineering files are available with laboratory and in-flight calibration data.

4.2 Integrated Systematics Calibration Framework

Figure 4-6 presents the integrated framework for TESS. We develop a variety of techniques to characterize and calibrate TESS instrument systematic noise sources. In the first step of photometric precision assessment, we simulate the noise sources, and the effect of jitter noise and sub-pixel variations on photometric performance using a high-fidelity model of the CCD detector. In the second step of systematics characterization and calibration, we develop precision laboratory techniques to characterize the absolute quantum efficiency, quantum efficiency changes with temperature variations, charge saturation, blooming, and undershoot effects. Next, we perform flight data analysis to analyze systematics in the TESS data such as effect of aperture size, time bin size, jitter and temperature variations. We present an optimal systematic calibration framework to address each of these issues. In the last step of photometric performance validation and improvement, we perform corrections for aperture size, and present improvement in precision for various time bin sizes. Lastly, we calculate the residual systematic noise and establish the noise floor for the mission.

4.3 Photometric Performance Assessment

In this section, we explain the first block in Figure 4-6 titled photometric precision assessment. First, we develop a framework to evaluate the photometric precision using Python by simulating a high-fidelity CCD detector with dominant noise sources such as inter-pixel and intrapixel sensitivity variations. Next, we add realistic jitter profiles to simulate flight-like systematic noise due to spacecraft jitter. We simulate a time-series of stellar images for varying levels of jitter using simulated stellar point spreaf functions (PSFs). Then, we perform aperture photometry to generate light curves that are used to assess photometric precision. We obtain the photometric precision

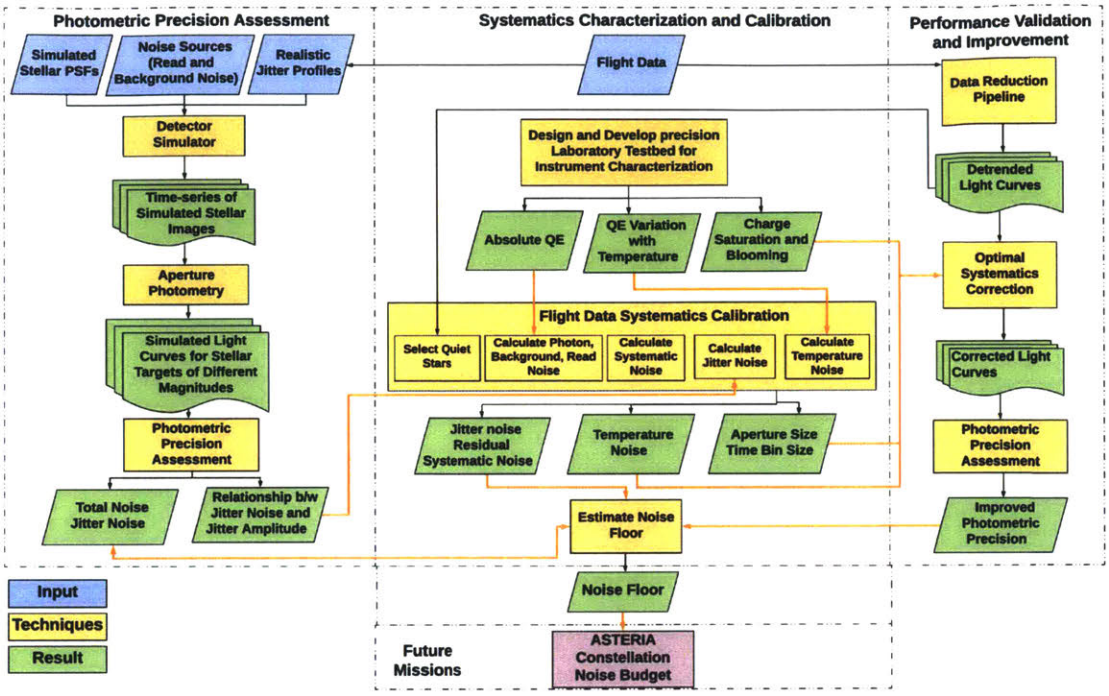

Figure 4-6: Integrated systematics calibration framework for TESS showing the three key steps: photometric precision assessment using simulation and modeling, systematics characterization and calibration using laboratory techniques and flight data calibration, and performance validation and improvement using optimal systematics correction.

by calculating the standard deviation of the light curves. This step provides two main results: first, total noise and jitter noise that indicate the photometric precision and effect of jitter on photometric precision respectively, and second, we establish a relationship between jitter noise and jitter amplitude. This result is crucial in developing the flight data calibration framework in step 2 of the framework.

4.3.1 Detector Simulator

We first develop a detector simulator showing a region of interest with 8 x 8 pixels. Pixel response non-uniformity is found to be 0.6% based on laboratory characterization of the detectors [84]. We generate the quantum efficiency of each pixel as a normal random variable in every iteration. Then, we model intrapixel variations with

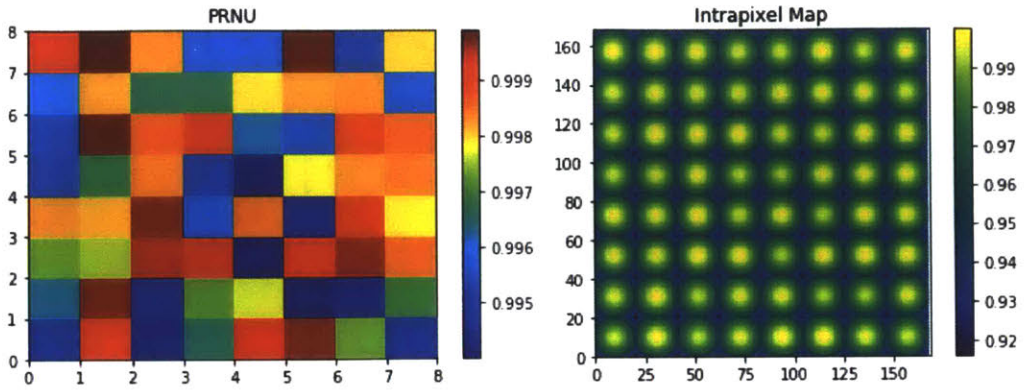

Figure 4-7: (Left) Simulation of the detector showing an 8x8 pixel area with pixel-to-pixel QE variation of 0.6%. (Right) Intrapixel response simulation with 20 subpixels per pixel, and 100% light intensity at the center and 90% at the corner of each pixel.

a resolution of 20 x 20 subpixels per pixel using Gaussian distribution. Figure 5-12 shows an 8 x 8 pixel map with 100% charge intensity at the center and 90% at the edges. The Gaussian distribution is given by Equation 4.1. We then add the noise sources such as zodiacal noise or sky noise, and read noise based on previously established models for both [82].

$$s(x, y) = exp(-\frac{(x - x_0)^2 + (y - y_0)^2}{2\sigma^2}) \tag{4.1}$$

4.3.2 Simulated PSFs

We simulate stellar PSFs by calculating the input charge intensity from Equation 4.2, that is calculated from the system throughput using QE, lens transmission efficiency and effective area. In this equation, Tmag denotes TESS magnitude. The multiplication factor of 2 accounts for the integration time of 2s. We set the input charge as a Poisson variable to account for the star noise or photon noise.

$$Total\ charge = 15400 * 10^{(-0.4*(Tmag-10))} * 2 \tag{4.2}$$

We compute the simulated images at each time step by taking the dot product of the stellar image and the detector map with interpixel and intrapixel variations. The

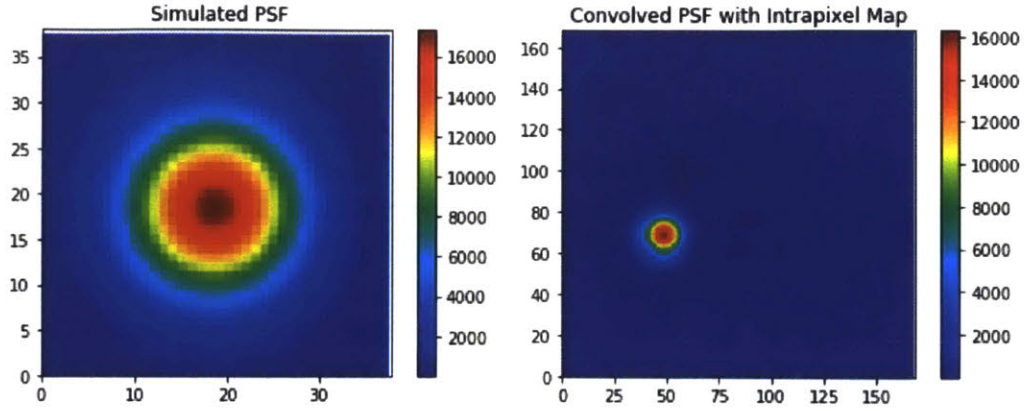

Figure 4-8: (Left) Simulated stellar PSF in a 2x2 pixel area with subpixel resolution. (Right) Resulting image of 8x8 pixel area after taking the dot product of the simulated stellar image with the intrapixel map at subpixel resolution. The light intensity varies from 0 to 16,000 ADU.

resulting image is at the higher resolution of 160 x 160 pixels which we then bin to obtain the original resolution of 8 x 8 pixels as shown in Figure 5-13.

4.3.3 Realistic Jitter Profiles

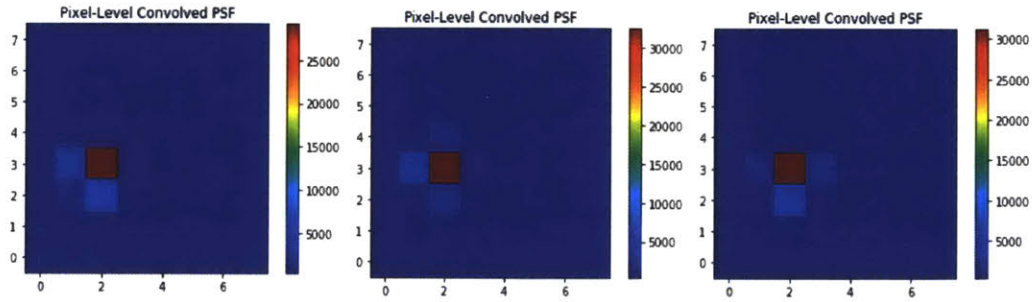

Figure 4-9: Binned PSF at various offset positions. (Left) offset of (0,0) pixels. (Middle) offset of (0.2, 0) pixels. (Right) offset of (0, 0.2) pixels.

We bin the convolved PSFs to discrete 8x8 pixels as shown in Figure 4-9. Next, we apply various offset positions of (0, 0), (0, 0.2) and (0.2, 0) pixels to simulate spacecraft jitter to test the effect on the image PSF. We see in the figure that the pixel response changes significantly with the centroid movement of a fraction of a pixel.

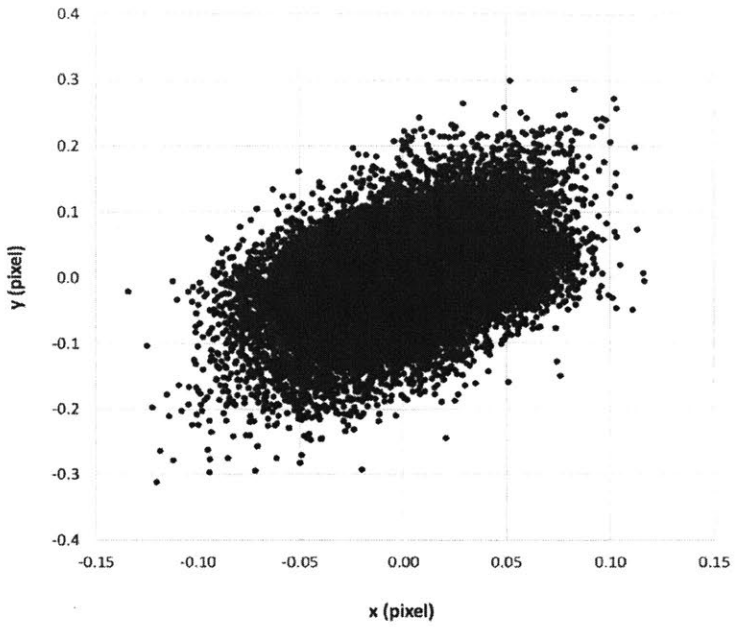

Figure 4-10: Jitter profile showing 1s ACS data from Sector 6, camera 4 of TESS flight data, showing one of the quaternions (q1). The x-axis and y-axis show pixel offset relative to the center of the pixel. The jitter offsets the centroid of the stellar image. Aperture photometry is performed on the images to then evaluate photometric precision.

Following this, we add flight jitter profiles from sector 6 shown in Figure 5-15, with a sampling frequency of 0.5 Hz. We choose sector 6 because it is one of the best sectors in terms of spacecraft pointing performance. Jitter offsets the centroid of the PSF in the x-y direction in subpixel steps. We can then use the series of stellar images to generate a light curve using simple aperture photometry.

4.3.4 Light Curve Generation

We perform aperture photometry by fitting a circular aperture mask on the target star and summing the charge within the mask. We optimize the aperture size by iterating over the size of the aperture mask until we have maximized the signal-to-noise ratio. Figure 4-11 shows an example light curve from the simulation. The root mean square of the light curve gives the photometric precision.

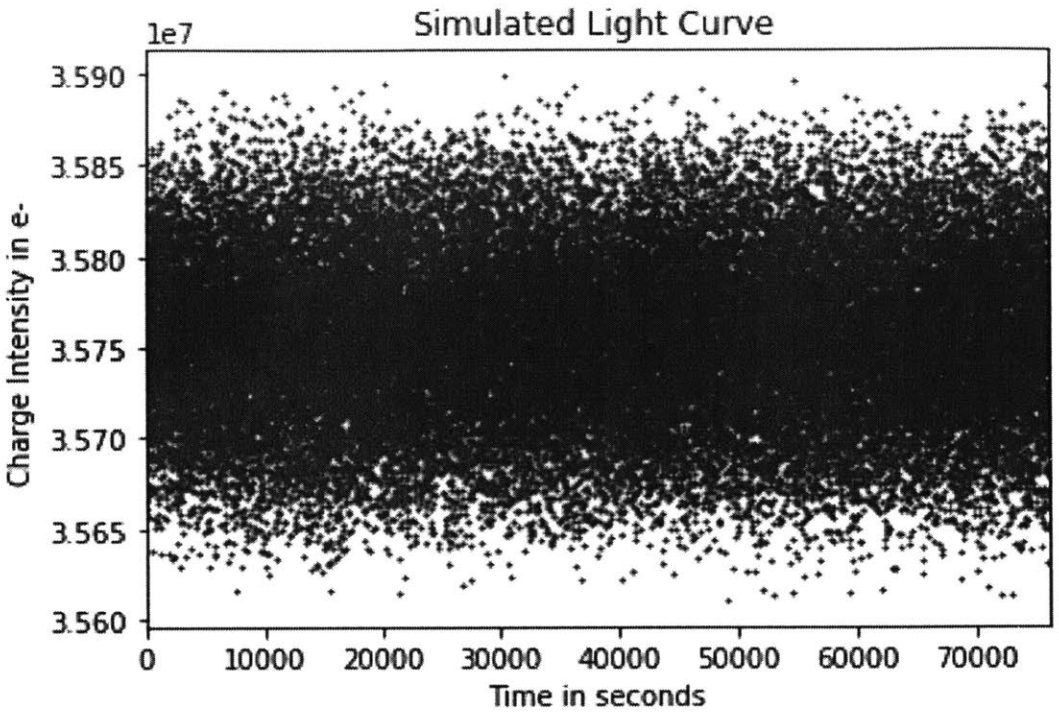

Figure 4-11: Time-series produced by the detector simulation using flight jitter profiles from sector 6.

4.3.5 Total Noise and Jitter Noise

We calculate the photometric precision as a function of stellar magnitude by varying stellar brightness and iterating through the simulation. We calculate the zodiacal noise, read noise, and star noise components for each stellar magnitude and remove these contributions to derive the jitter noise component as a function of stellar brightness as shown in Figure 4-12. The jitter noise indicates the effect of spacecraft jitter on photometric precision. Jitter noise is a dominant source of systematic noise for stars brighter than TESS magnitude 6.0 and for stellar brightness between Tmag 11.0 and 15.0, as shown in Figure 4-12. While total noise, shown with a dotted black line in the figure, denotes the overall photometric precision.

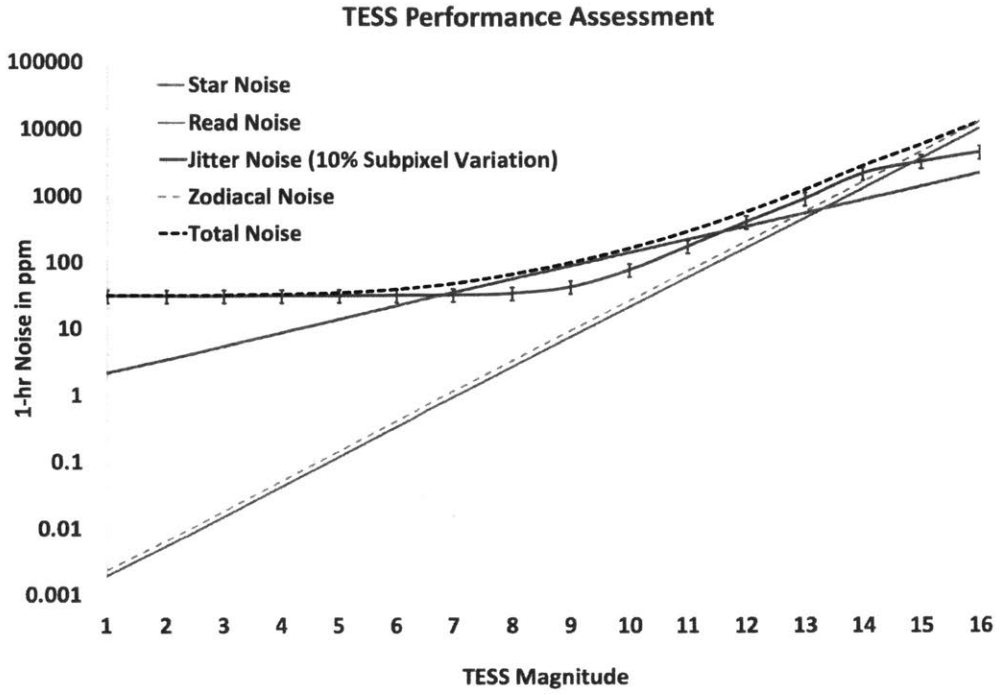

Figure 4-12: Photometric precision as a function of stellar brightness. We plot the sources of noise such as read noise, sky noise, star noise, and jitter noise as a function of stellar magnitude.

Jitter Noise and Jitter Amplitude

We assess the relationship between jitter noise and jitter amplitude by inducing jitter of varying amplitudes. In order to do this, we use different time intervals within the sector 6 ACS data and run the simulation for those jitter amplitudes. Figure 4-13 shows the distinct noisy and quiet intervals in the sector 6 ACS data that were used for the simulation. Figure 4-14 shows that the jitter noise increases linearly with increase in jitter amplitude. Using these two results, we build a flight data systematics analysis model for stars brighter than 6.0 in Section 4.5.

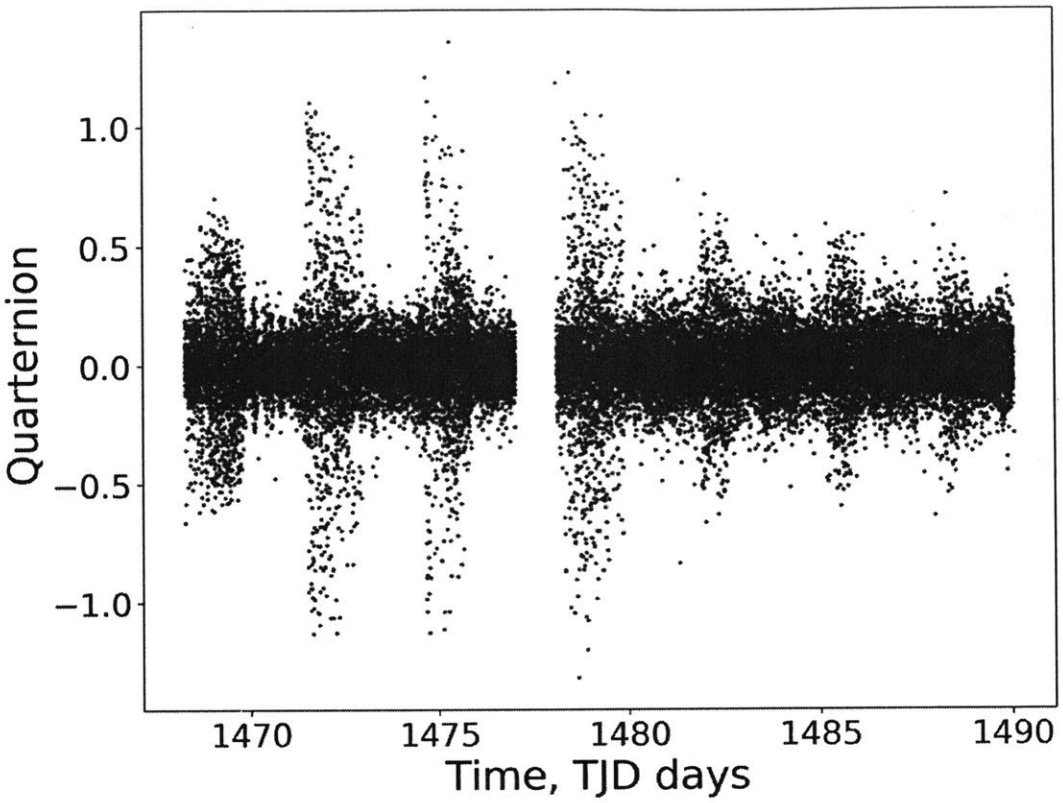

Figure 4-13: Quaternion, Q2 as a function of time. The figure shows distinct noisy and quiet intervals, which are used for the jitter simulation.

4.4 Systematics Characterization and Calibration

In this section, we present the second block from Figure 4-6 where we explain the framework for systematics characterization and calibration. We begin by presenting the precision laboratory techniques that we developed in order to study the key detector properties such as absolute QE, QE variations with temperature, charge saturation and blooming, undershoot, and effect of straps. We then present the flight data systematics calibration framework that uses results from both step 1 (photometric precision assessment) and the laboratory results. Using this framework, we calculate the jitter noise, residual systematic error, photometric precision, and temperature noise. From these results, we also calculate the noise floor for the mission.

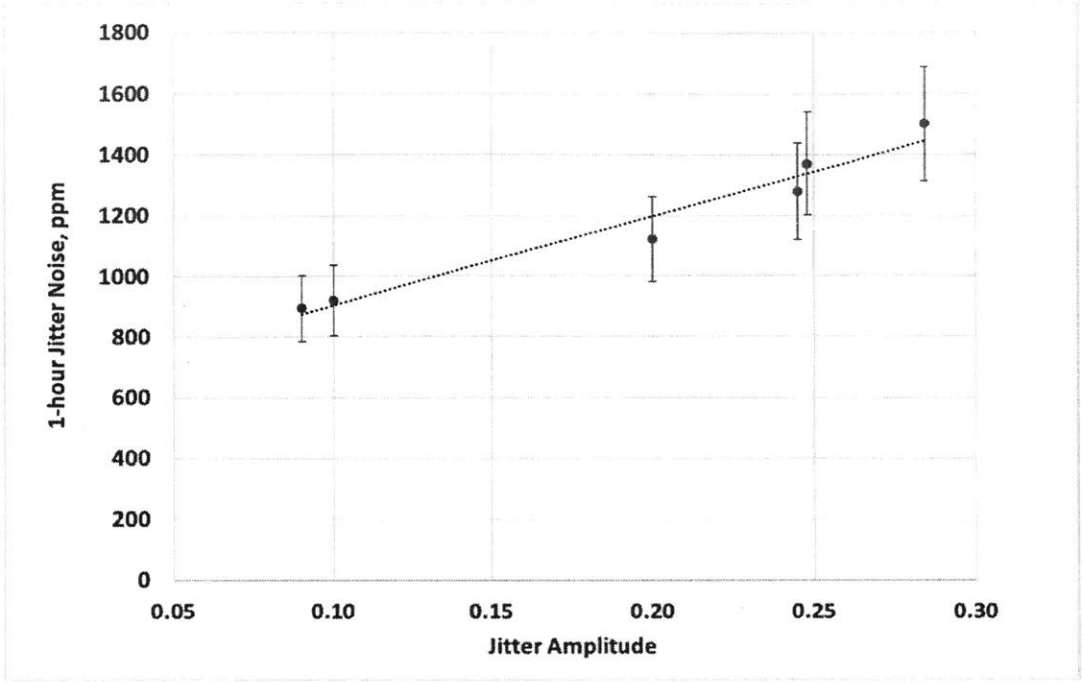

Figure 4-14: Jitter error as a function of jitter amplitude. We establish that jitter error is linearly proportional to jitter amplitude.

4.4.1 Precision Laboratory Techniques

In this section, we develop novel laboratory techniques for the precise characterization of instrument systematics. We specifically focus on detector properties and noise sources that directly impact throughput and science capability of the mission. We measure absolute quantum efficiency (QE), and effect of temperature on QE, in addition to modeling charge saturation and blooming, and undershoot effects. This section identifies and characterizes major noise sources that can not be characterized on-orbit, and informs the flight data calibration process in Section 4.5. The outline for this section is shown in Figure ??.

We develop a precision optical test bench [85] capable of automated absolute quantum efficiency measurements over the spectral range of 650-1050 nm with an absolute error of less than 2%. The QE measurements will help refine the prediction accuracy of the TESS science output models especially over redder wavelengths where QE of the CCD drops precipitously and transit detections are highly dependent on the

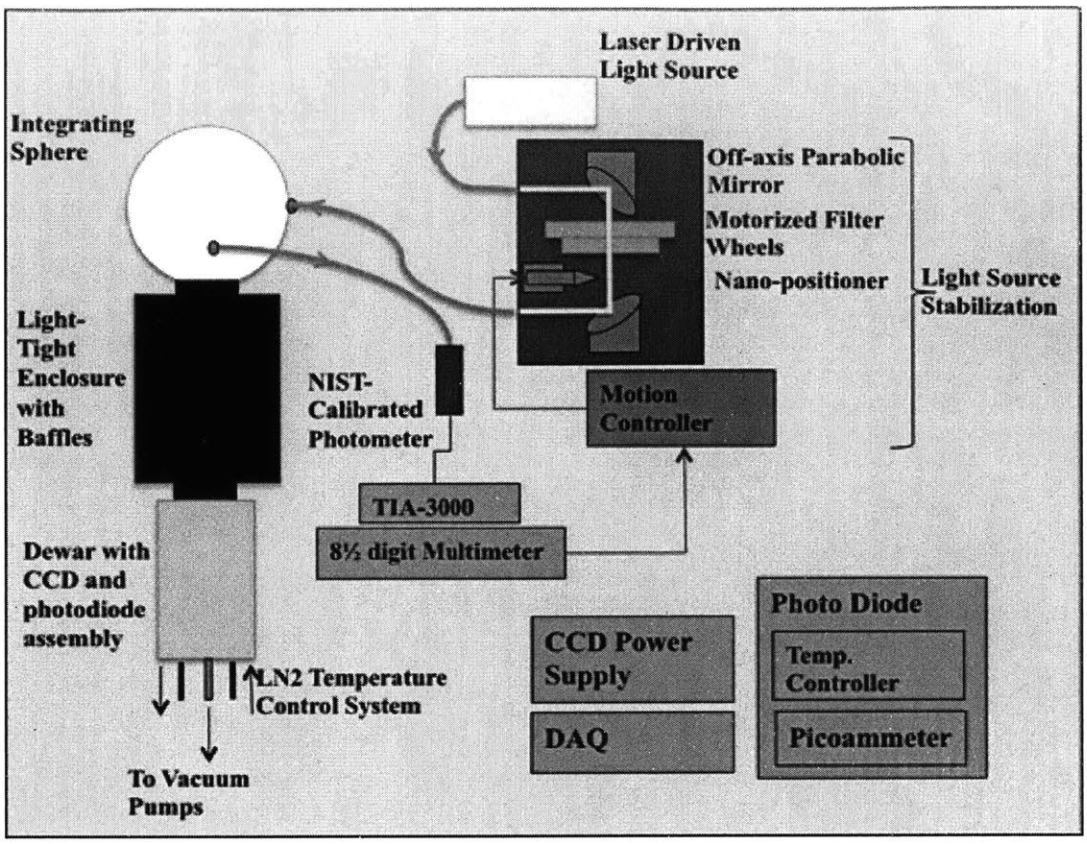

Figure 4-15: Precision optical test bench for the characterization of absolute quantum efficiency showing the various components such as the laser driven light source, the light source stabilization unit, associated electronics, integrating sphere for uniform illumination of the CCD and reference photodiode that are housed inside the dewar.

photon count rate. Light source selection and stabilization, filter selection, reference detector calibration and placement are some of the important factors that affect a very sensitive measurement like absolute QE. In order to accurately interpret the signals obtained from the CCD, we perform precision gain measurements. The quantum efficiency of the CCD is given by the ratio of the signal produced by the CCD to the incoming current measured by the calibrated photodiode [86]. Previous works have been able to measure absolute QE of a CCD detector with an absolute error of 3%-6% [87][88][89]. The present work builds on similar principles but with ultra-precise light stabilization, gain measurement, and reference photodiode calibration to achieve the design goal.

We designed and built the test setup [90], illustrated in Figure 4-15 and Figure 4-

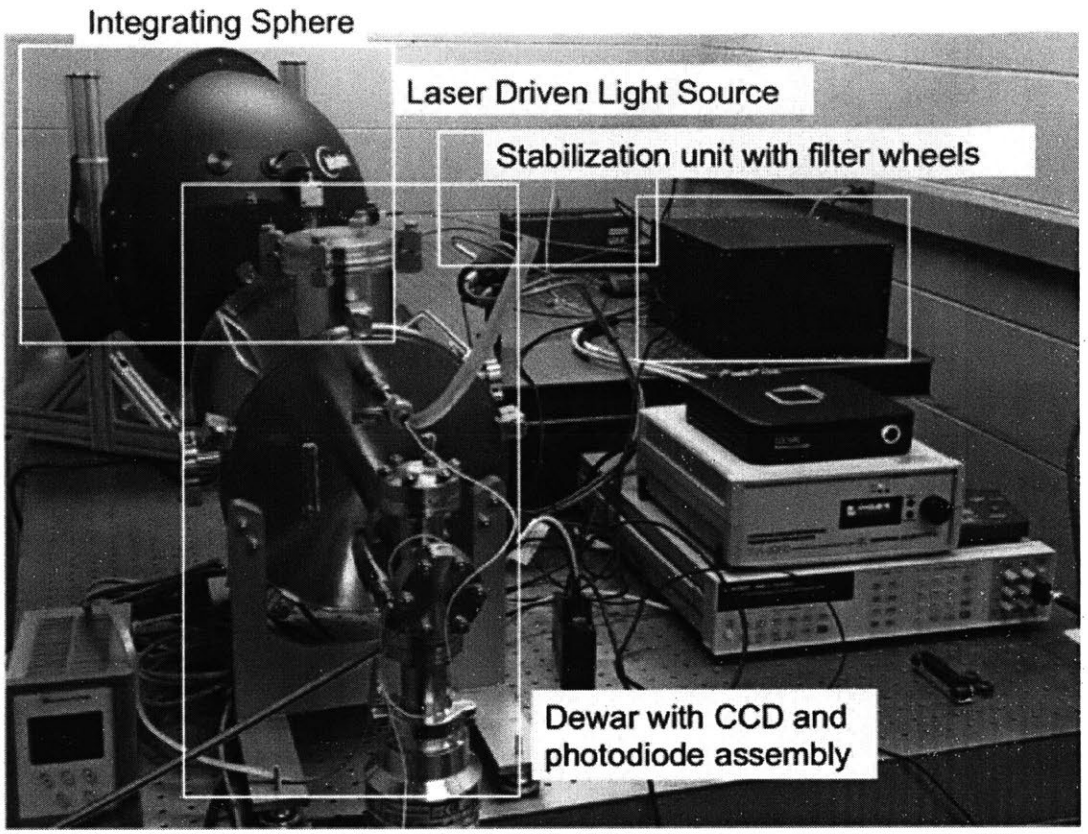

Figure 4-16: Precision optical test bench for the characterization of systematic error, consisting of the laser-driven light source, stabilization system, and dewar with a liquid nitrogen reservoir to cool the detectors to -75°C.

16 from scratch. It consists of a vacuum chamber with a single MIT Lincoln Lab CCID-80 device mounted on a cold plate that is maintained at the operating temperature of -70° C to reduce the dark current to a negligible level. It also consists of a calibrated reference photodiode that is mounted next to the CCD and maintained at the calibration temperature of 25°C. We use band-pass filters over the range of 600 nm - 1064 nm with 10-nm bandwidth for wavelength selection.

Next, we integrate a very stable laser-driven light source (LDLS) with the Super Stable Source (SSS) stabilization unit, a patented development by the Characterising ExOPlanetS (CHEOPS) Team at the University of Geneva [19], to control variations of the light source down to a few parts-per-million when averaged over 60 s. Light from the stabilization unit enters a 20-inch integrating sphere to produce near-

uniform diffuse illumination on the CCD and on the calibrated reference photodiode simultaneously. We install a light-tight enclosure between the integrating sphere exit port and the CCD to obtain near-uniform illumination of the CCD and to eliminate light leaks. We use a set of baffles inside the black interior to prevent stray light and secondary reflections from entering the vacuum chamber.

Uniform Optical Illumination

The Energetiq Laser-Driven Light Source (LDLS) technology consists of a continuous wave laser plasma discharge with plasma size of 100 μm and a broad spectral spectrum of 190 nm - 2400 nm. The CW laser directly heats Xenon plasma created in a fused silica bulb using a traditional arc light igniter, to a very high blackbody temperature of 10,000 K. The light source has excellent power stability with instantaneous variation of about 1-3%, as shown in Figure 4-17. The electrodeless operation contributes to the long lamp life of over 9000 hours.

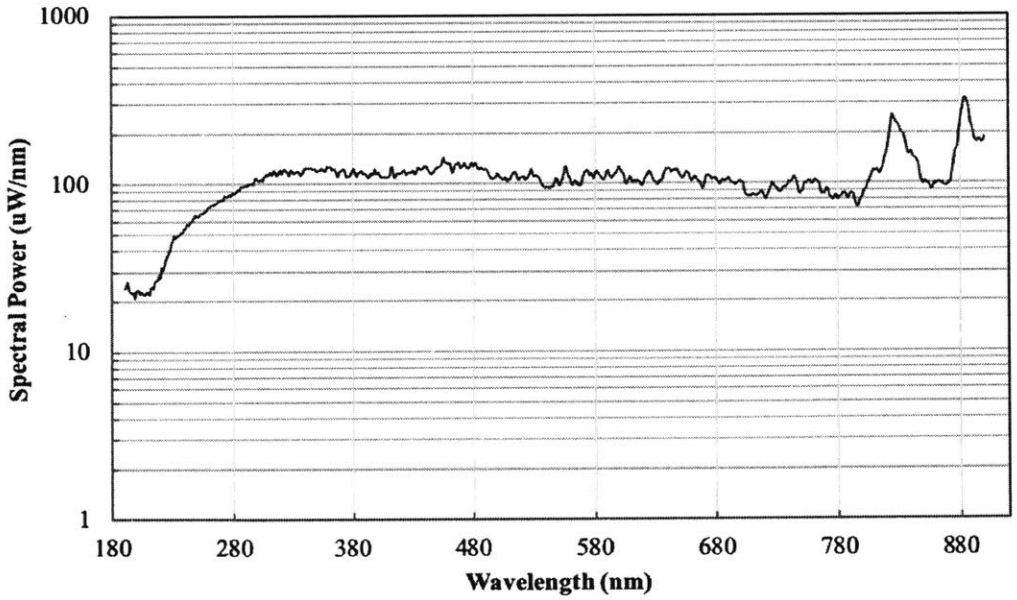

Figure 4-17: Typical performance of the Energetiq LDLS EQ-99XFC with the 450 μm diameter, 0.22 NA, 1 m long fiber (data provided by Energetiq).

Since we are focused on characterizing the absolute quantum efficiency of the CCID-80 device in the 650 nm - 1050 nm spectral range, we use a 12-position Thorlabs

motorized filter wheel to perform careful filter selection. It contains twelve hard coated band-pass filters from Edmund Optics that provide deeper blocking and higher transmission (>90%) compared to traditional coated filters. Eleven of them have a bandwidth of 10-nm and are over the range of 650 nm - 1064 nm while one filter at 1000 nm has a 25-nm bandwidth. In addition, we use a 6-position motorized filter wheel with 1-inch absorptive neutral density filters to control the intensity of the light entering the integrating sphere.

Integrating Sphere

We use a 20-inch custom-built integrating sphere from LabSphere to produce uniform diffuse illumination over the CCD and calibrate the photodiode assembly in the vacuum chamber. The integrating sphere consists of a hollow spherical cavity with a diffuse white reflective coating called Spectraflect with 98% reflectance over the 650 nm - 1050 nm spectral range. It has one 1-inch inlet port and one 4-inch outlet port placed at right angles to each other to make sure each ray of light is reflected at least once before exiting the output port. Light rays incident on any point on the inner surface are, by multiple scattering reflections, distributed equally to all other points thus preserving power and destroying spatial information producing diffuse light at the outlet. The port fraction i.e. the ratio of the area of the outlet to the inlet ports must be less than 0.05 for high uniformity (> 98%) of light exiting the integrating sphere. There is a 1-inch diagnostic port above the output port to make photometric measurements of the light inside the sphere that is used by the light stabilization unit to control the flux variations of the LDLS.

Light Stabilization

The light stabilization unit is a patented development by the Characterising ExOPlanetS (CHEOPS) Team at the University of Geneva [Wildi et al., 2015]. We integrate this unit with the test up in order to stabilize the Energetiq Laser-Driven Light Source. The stabilization unit consists of a fiber input and fiber output with a precision light control system implemented between the two. As shown in Figure 4-18,

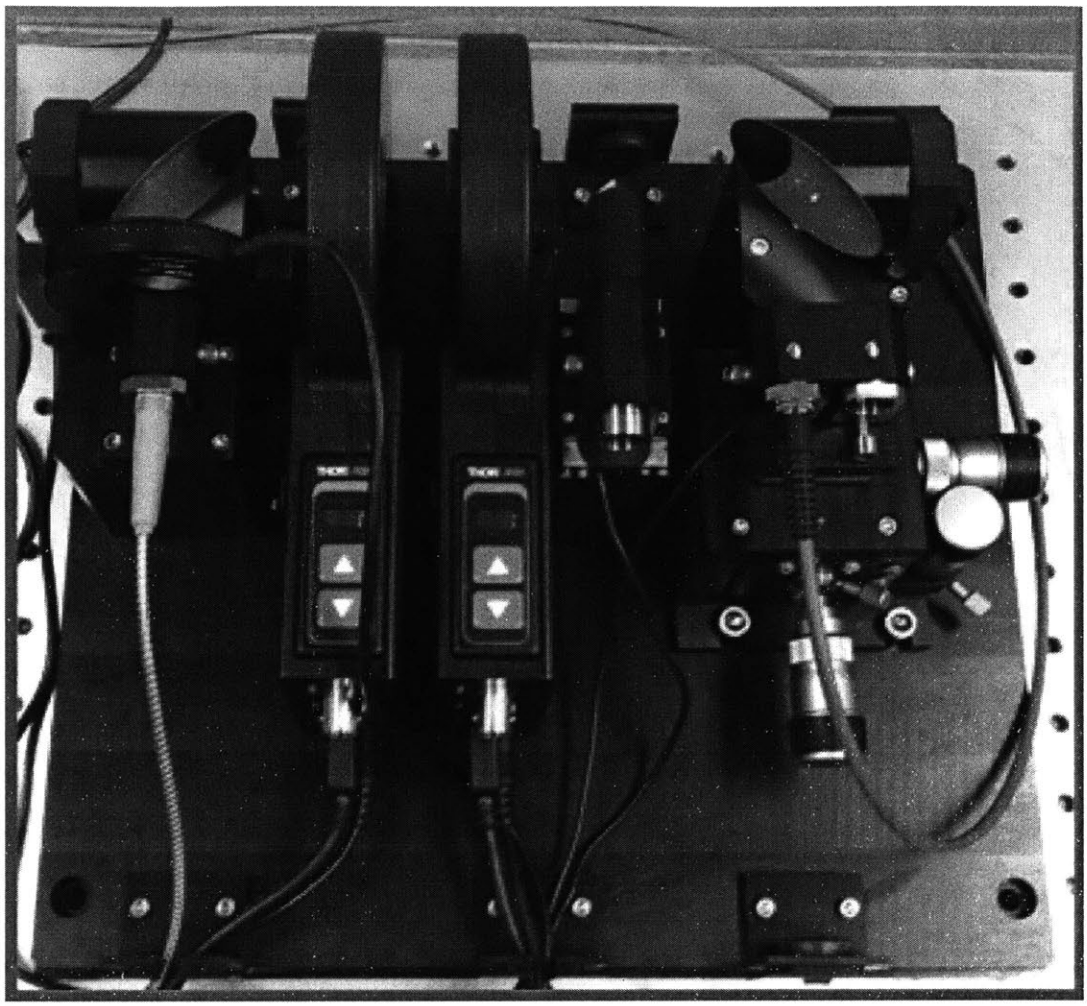

Figure 4-18: The figure shows the light stabilization unit, Super Stable Source (SSS) that consists of two off-axis parabolic mirrors, and a nanopositioner that control the movement of a knife-edge into and out of the light beam carefully controlling the flux intensity using a feedback control loop.

the unit has a collimator-decollimator assembly consisting of two off-axis parabolic mirrors, two motorized filter wheels for filter selection and intensity control, and a knife-edge attenuator. The knife-edge attenuator has a conical end towards the beam and is mounted on a precision positioner with a maximum reachable velocity of 4.5 mm/s to occult the beam and balance the flux variations of the LDLS. We mount a feedback loop with a NIST-calibrated precision photometer on one of the output ports of the integrating sphere to control the movement of the attenuator into the beam such that the variation of flux at the output fiber is minimum. The measurement

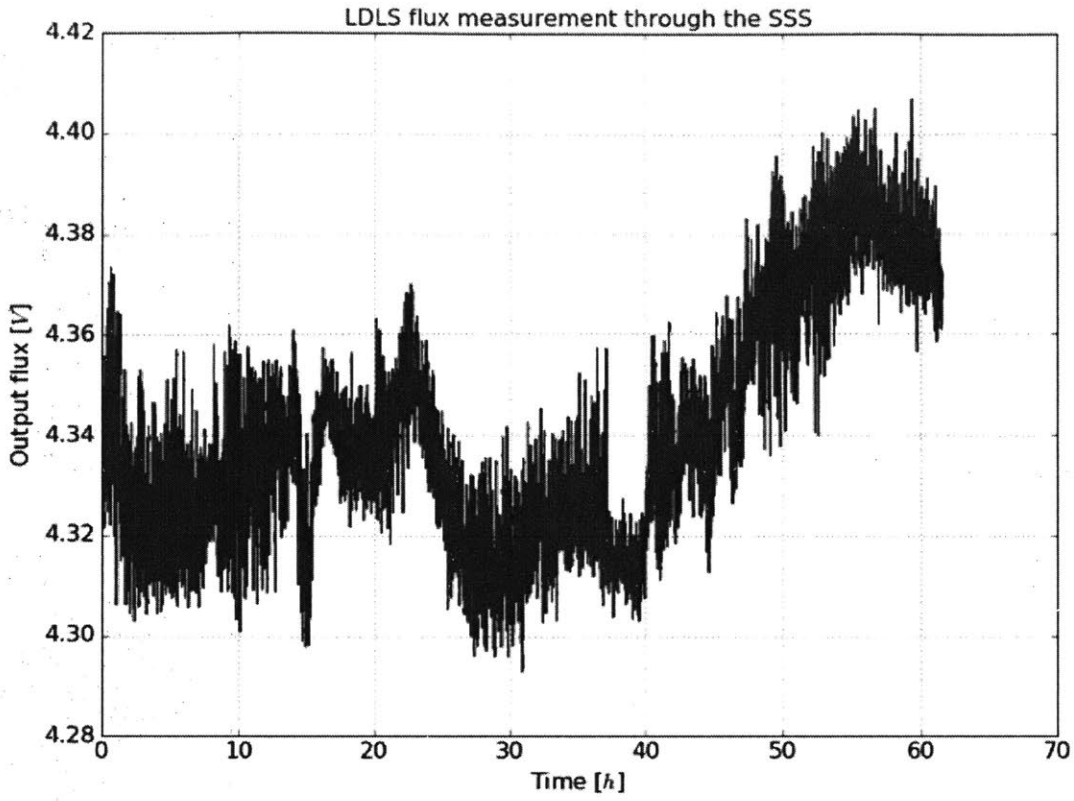

Figure 4-19: Instantaneous variation of output flux from the LDLS measured over time before stabilization. The x-axis shows time in minutes and y-axis shows output flux in voltage.

uncertainty of the photometer system is about 5 ppm at 15 Hz and 24-hour accuracy below 1 ppm.

We measure the variation of the flux from the LDLS using a photometer system consisting of a photodetector and multimeter. The instantaneous variation of the LDLS is only about 1-3%, which is further stabilized by the Super Stable Source (SSS) stabilization unit that controls the fluctuations down to a few parts per million. The photometer system has a temperature stability of 0.003 K over 24 hours with a measurement uncertainty of about 5 ppm at 15 Hz.

The closed loop stabilization stage operates in two modes; a slow mode that commands the attenuator and waits for it to reach the required position before measuring the next point, and a continuous mode where the photometer system measures the flux without waiting for the attenuator to reach the point previously commanded. The

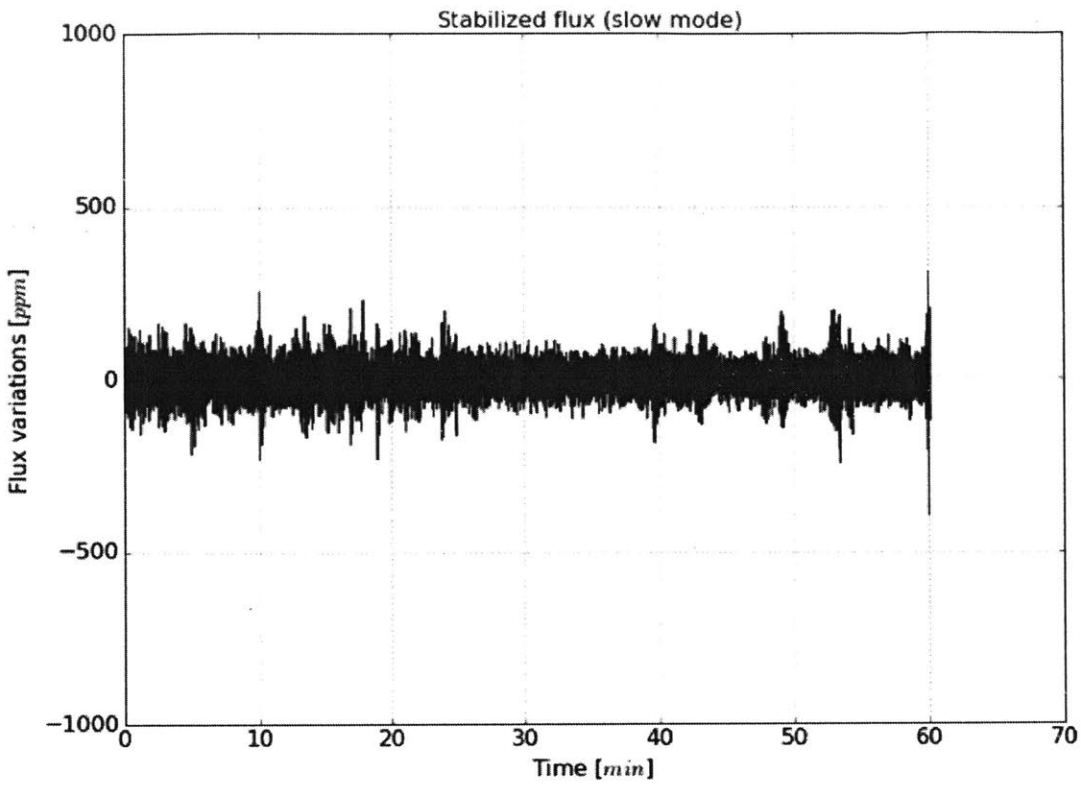

Figure 4-20: The stabilized LDLS flux measured by the photometer system in closed loop using the slow mode. The x-axis shows time in minutes and y-axis shows flux variation in parts per million. The slow mode yields a stability of 4.95 ppm when averaged over 60 s.

slow mode yields a stability of 4.95 ppm as shown in Figure 4-20 and the continuous mode yields a stability of 3.57 ppm when averaged over 60 s. We use the slow mode to stabilize the LDLS at each wavelength before recording the QE measurements.

Dewar Assembly

The dewar assembly consists of a custom-built stainless steel chamber that is 14 inch in length and 10 inch in diameter with a 7.37 inch optical quartz window. We mount the CCD and calibrated photodiode assembly on a 1/4" thick 6061 Aluminum cold plate attached to the front end of an annular liquid Nitrogen reservoir that maintains the CCD at the operating temperature of -70°C. We placed the CCD electronics behind the CCD and photodiode assembly. We use a black anodized plate as shown in Figure 4-21 mask the CCD and calibrated photodiode assembly with two apertures

to allow light passage over the CCD imaging array area and the photodiode.

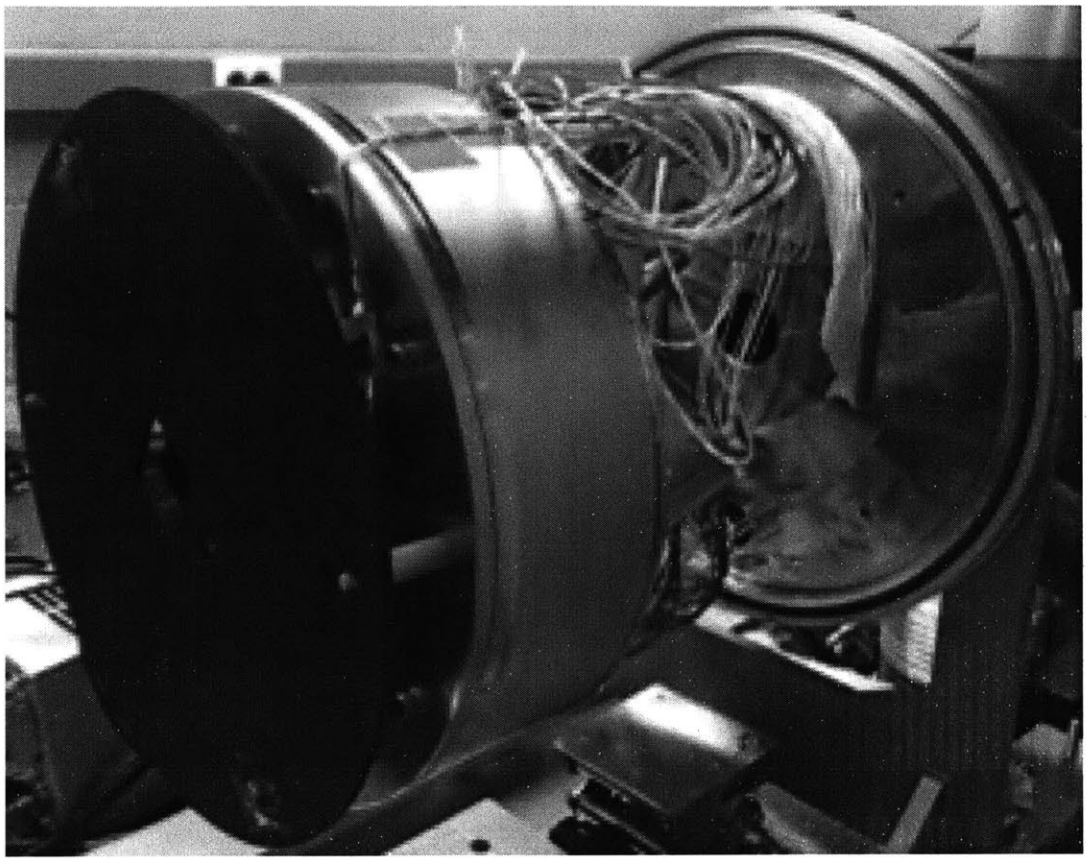

Figure 4-21: Open vacuum chamber showing the black anodized mask plate mounted on the cold plate using insulating standoffs, and the LN2 reservoir behind the cold plate that maintains it at the operating temperature of -70°C.

Calibrated Photodiode

We place the CCD and the calibrated reference photodiode next to each other on the cold plate, as shown in Figure 4-22, within a circular area of 4-inch diameter such that they are in the same focal plane and intercept the incoming light from the integrating sphere simultaneously. We use the the Hamamatsu S1337-1010BQ for the calibrated reference photodiode model to calculate the QE. The Hamamatsu S1337-1010BQ is a Silicon photodiode with a Quartz window, and a 10 mm x 10 mm photosensitive area. We cross-calibrate the reference photodiode using the precision photometer in the light stabilization setup to improve the accuracy of the measurements. We maintain

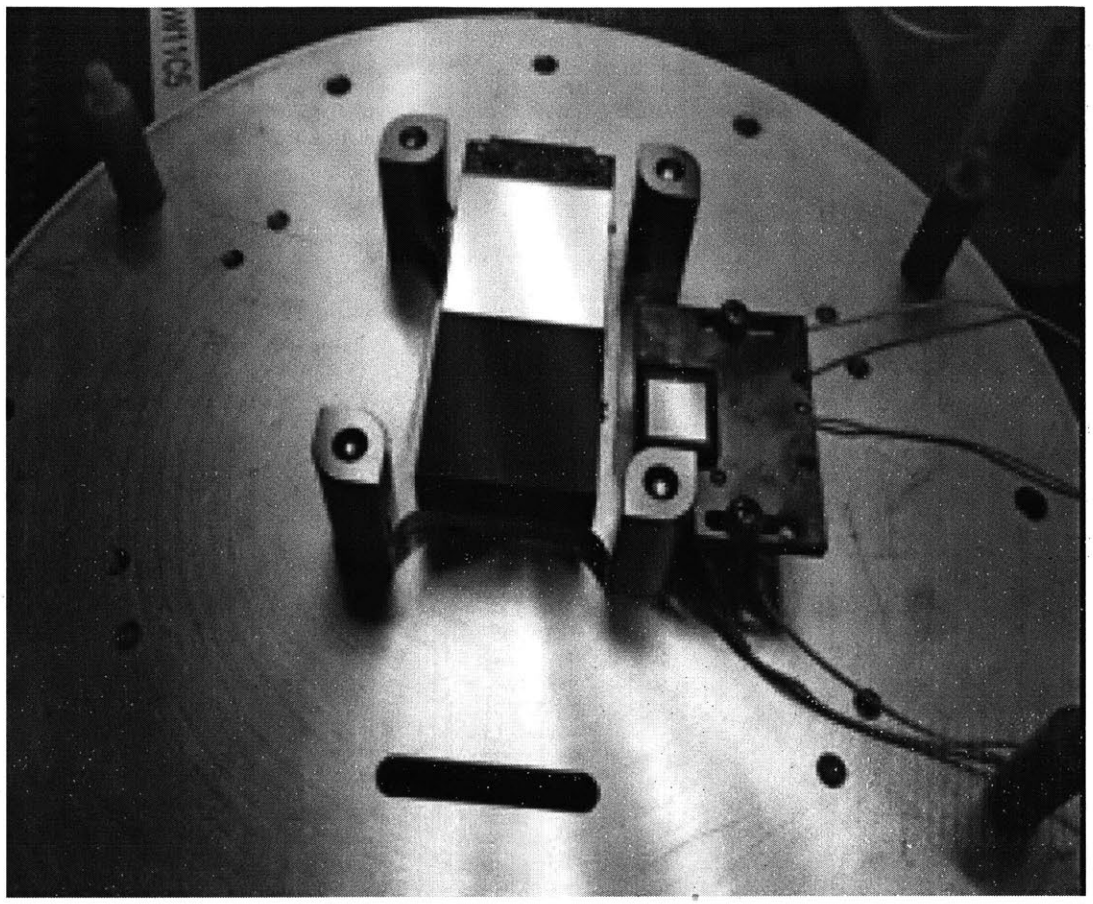

Figure 4-22: CCD and calibrated photodiode assembly mounted on the cold plate. The photodiode assembly is mounted using insulating standoffs, and has a heater to maintain the photodiode at an operating temperature of 25°C.

the CCD at an operating temperature of -70°C while the reference photodiode at the calibration temperature of 25°C using a 5W heater mounted on the bottom of the copper plate. Hamamatsu performed the sensitivity measurements of the photodiode and the calibration curve is shown in Figure 4-23.

4.4.2 Gain Measurements

The gain is the conversion factor between the electrons collected in the CCD and the Analog-to-Digital readout Units (ADU). Gain is dependent on the temperature of the CCD, and is measured using the Cd109 Kα and Kβ peaks. Using the known energies of the X-ray peaks (Kα = 22.1 keV, Kβ = 25.0 keV) [91], and the conversion of eV/e-

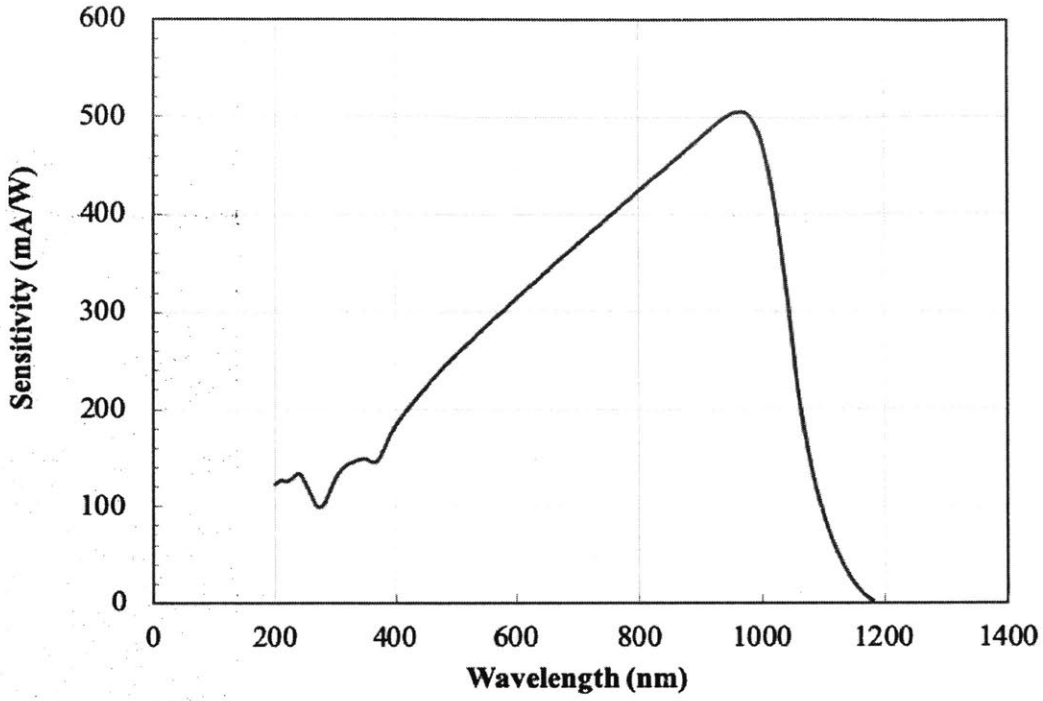

Figure 4-23: Reference calibrated photodiode sensitivity in mA/W plotted against wavelength.

for Silicon [88], we fit a line to the peaks whose slope gives the gain conversion factor as shown in Figure 4-24. The measured gain is 6.99 $\pm$ 0.01 e^-/ADU.

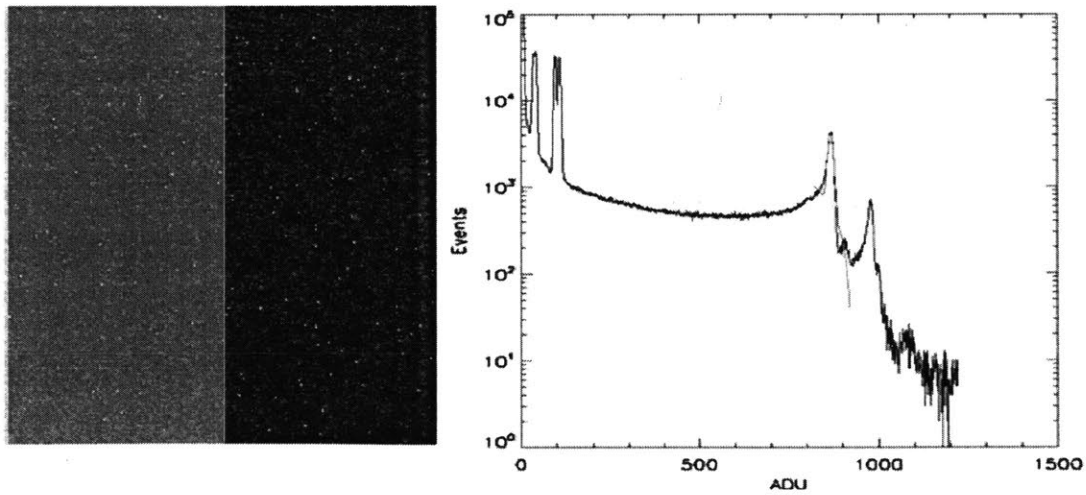

Figure 4-24: A Cd109 source is used to create X-ray events (left) and X-ray peaks for Cd109 (right).

4.4.3 Absolute Quantum Efficiency

The absolute quantum efficiency, QE is given by Equation 4.3. It is the ratio of the output signal to the incoming photon current. In this equation, S_o is the output signal per pixel is expressed in ADU, S_i is the incoming electrons per pixel measured using a photodiode and expressed in e^-. G is the gain conversion factor in e^-/ADU.

$$QE = \frac{S_o}{S_i} * G \tag{4.3}$$

In order to calculate the output signal, we take dark frames, and 20 2-second images with uniform illumination at each wavelength. We then subtract the median dark frame from the images and stack the 20 images together. We then calculate the median signal per pixel in ADU.

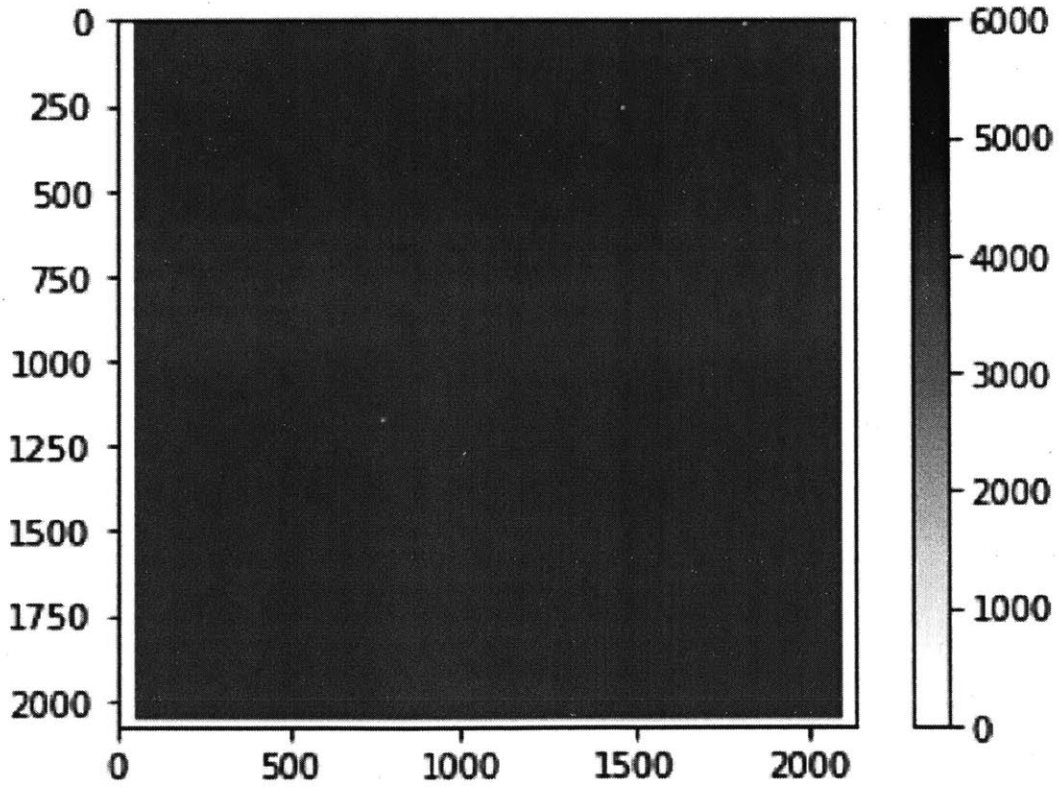

Figure 4-25: Laboratory image at 750 nm with uniform illumination. For wavelengths shorter than 800 nm, the CCD has a uniform spatial response, and the bright lines due to the straps and temperature sensors are not seen.

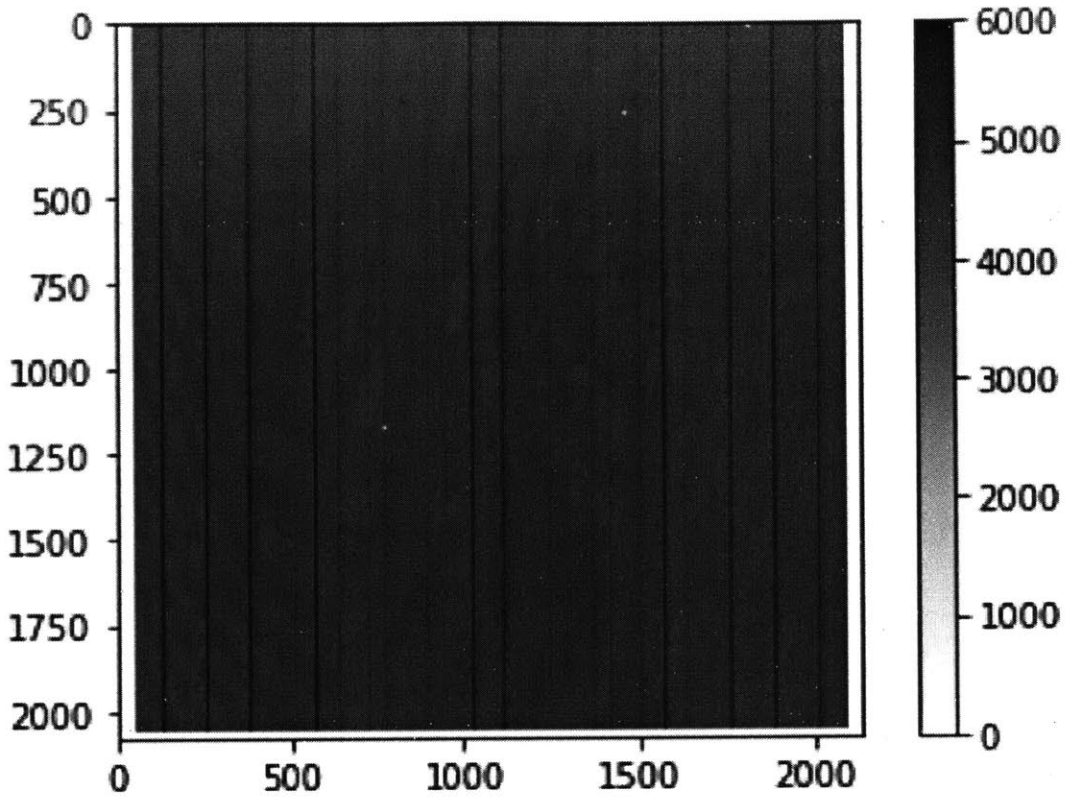

Figure 4-26: Laboratory image taken using uniform illumination showing bright lines and interference pattern at 905 nm. The bright lines are a result of reflection from the aluminum straps and temperature sensors underneath the surface, and the fringing is caused by the interference due to the variation in the thickness of the epoxy bonding of the silicon to the substrate. We sample in between the straps so that the calculation of absolute QE remains consistent across different wavelengths.

One important factor in determining what parts of the CCD to use in calculating the output signal is driven by the presence of aluminum straps and temperature sensors underneath the surface of the CCD that reflects light at certain wavelengths. For wavelengths shorter than 800 nm, the CCD has a uniform spatial response, as seen in Figure 4-25, but at longer wavelengths between 825 - 1050 nm, bright lines due to the straps and temperature sensors are observed, as seen in Figure 4-26. The increase in signal is between 0.5% - 14% as we sample across different wavelengths between 825 nm - 1050 nm. The absolute QE measured at the straps is up to 4% greater than the rest of the CCD. So, for the purpose of absolute QE measurements for the detector, we sample in between the straps so that the calculation of absolute

QE remains consistent across different wavelengths. In Figure 4-26, we also observe the phenomenon of fringing that is caused by interference of light at the boundaries of the epoxy layer. This feature is prominently observed between 905 nm - 1000 nm due to the longer wavelengths penetrating the features in the underlying structure.

We calculate incoming photons per pixel using Equation 4.4 by multiplying the photon current measured by the calibrated photodiode with the area of the pixel and the integration time.

$$S_i = \frac{I}{S} * \frac{1}{E_{photon}} * t \tag{4.4}$$

In this equation, I is the photocurrent [A] of the Hamamatsu photodiode, S is the sensitivity [A/W] of the photodiode at a given wavelength. Sensitivity of the photodiode is given by the calibration curve, as shown in Figure 4-23, obtained from the manufacturer of the photodiode. I/S gives the total incident power of the incoming photons in W, and E_{photon} is the energy per photon. t is the exposure time of 2 s.

Energy per photon, E_{photon} in J, is given by

$$E_{photon} = \frac{hc}{\lambda} \tag{4.5}$$

where h = 6.62607004 x 10^{-34} in m^2kg/s, c is the speed of light in m/s, and λ is the wavelength of light in nm.

The operating temperature of the CCD was -70 C and the exposure time was 2 s. Figure 4-27 shows the absolute QE measurements obtained from the precision optical test setup, plotted individually for the four output sectors A, B, C, and D. Sectors A and B have a slightly higher QE than sectors C and D at the shorter wavelengths, while the four sectors display identical quantum efficiency at the redder end of the spectrum. Sources of error like out-of-bandpass leakage from filters, light leaks, second-order reflections, and noise in the reference photodiode measurements were found to be negligible.

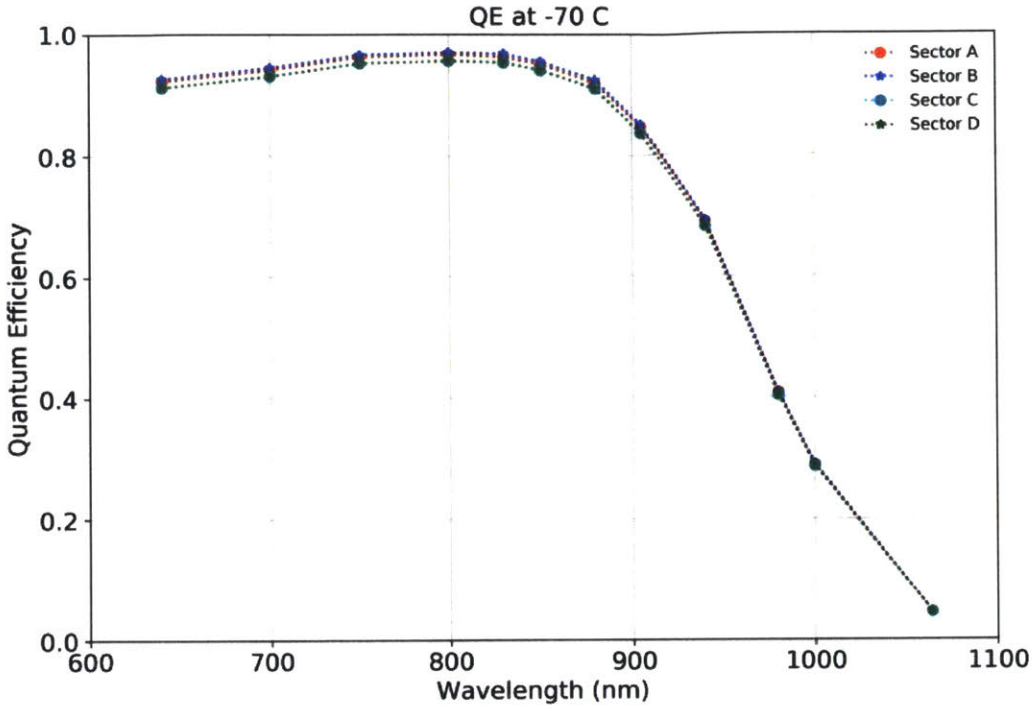

Figure 4-27: Quantum efficiency measurement for the TESS flight-grade 100-micron thick CCID-80 device with pre-flight electronics.

4.4.4 Temperature Variations

The QE measurement along with the lens throughput is used to calculate the spectral weightings, and thus the normalized photon counts for stellar spectra. Hence, it is important to characterize the performance of the detectors at different operating temperatures, in order to study the optimal operating temperature for specific stellar types. At -50°C, there is an increase in QE of about 4% at 1000 nm, and at -25°C, QE at 1000 nm is about 39%. However, dark current increases substantially at higher temperatures, negating the gain in QE. This result is used in our analysis of the effect of temperature variations on photometric precision in the flight data.

4.4.5 Charge Saturation and Blooming

In order to evaluate some of the detector characteristics such as charge saturation, blooming and undershoot, we require a point light source with increasing intensity.

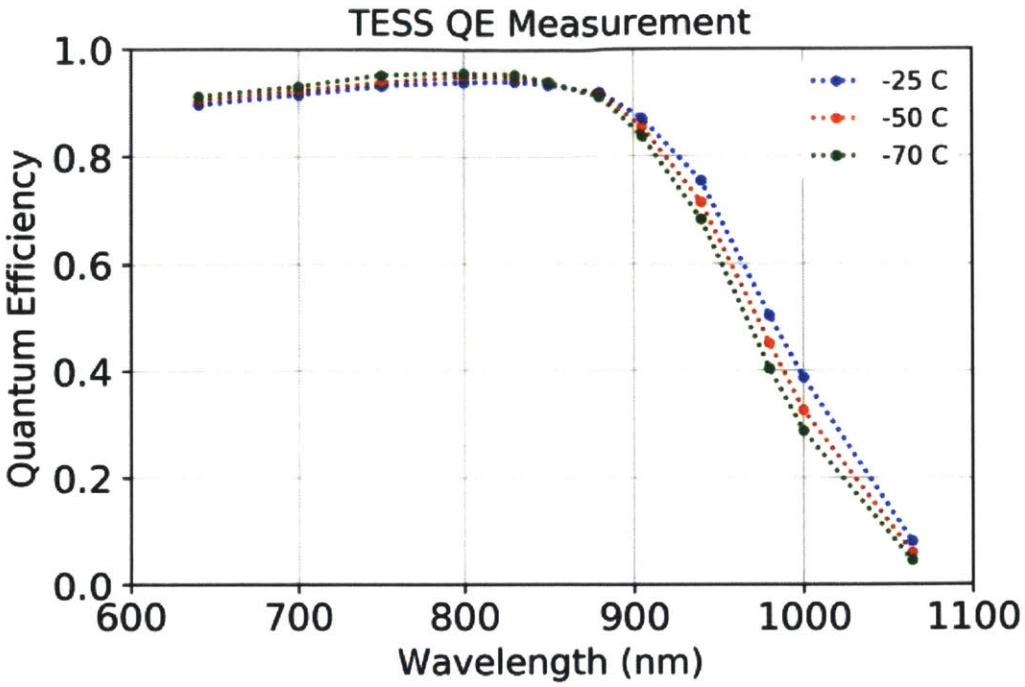

Figure 4-28: Temperature dependence of the absolute QE measurements are plotted individually for sectors A, B, C, and D of a 100-micron thick CCID-80 device. The operating temperature of the CCD was maintained at -25°C, -50°C and -70°C. The exposure time was 2 seconds.

We produce the point images using a pinhole system along with a pair of conjugate lenses as shown in Figure 4-29.

The objective of the charge blooming model developed in this section is to understand the process of pixel saturation, charge transfer and distribution into the neighboring pixels with increasing input light intensity, by analyzing the correlation between the input intensity and charge distribution.

In order to formulate the blooming model, we take a set of images with a flight-like TESS CCD detector using a number of LED pulses focused into a spot. The wavelength of the LED source chosen is 660 nm. The various images in Figure 4-30 show increase in input light due to increasing number of pulses such that the input charge varies from 0 to 20 full wells i.e. 0 to 695,000 ADU. ADU is the analog-to-digital unit that is a measure of the output voltage within each pixel.

Figure 4-31 shows an image taken at 20,000 pulses with an input intensity of 20

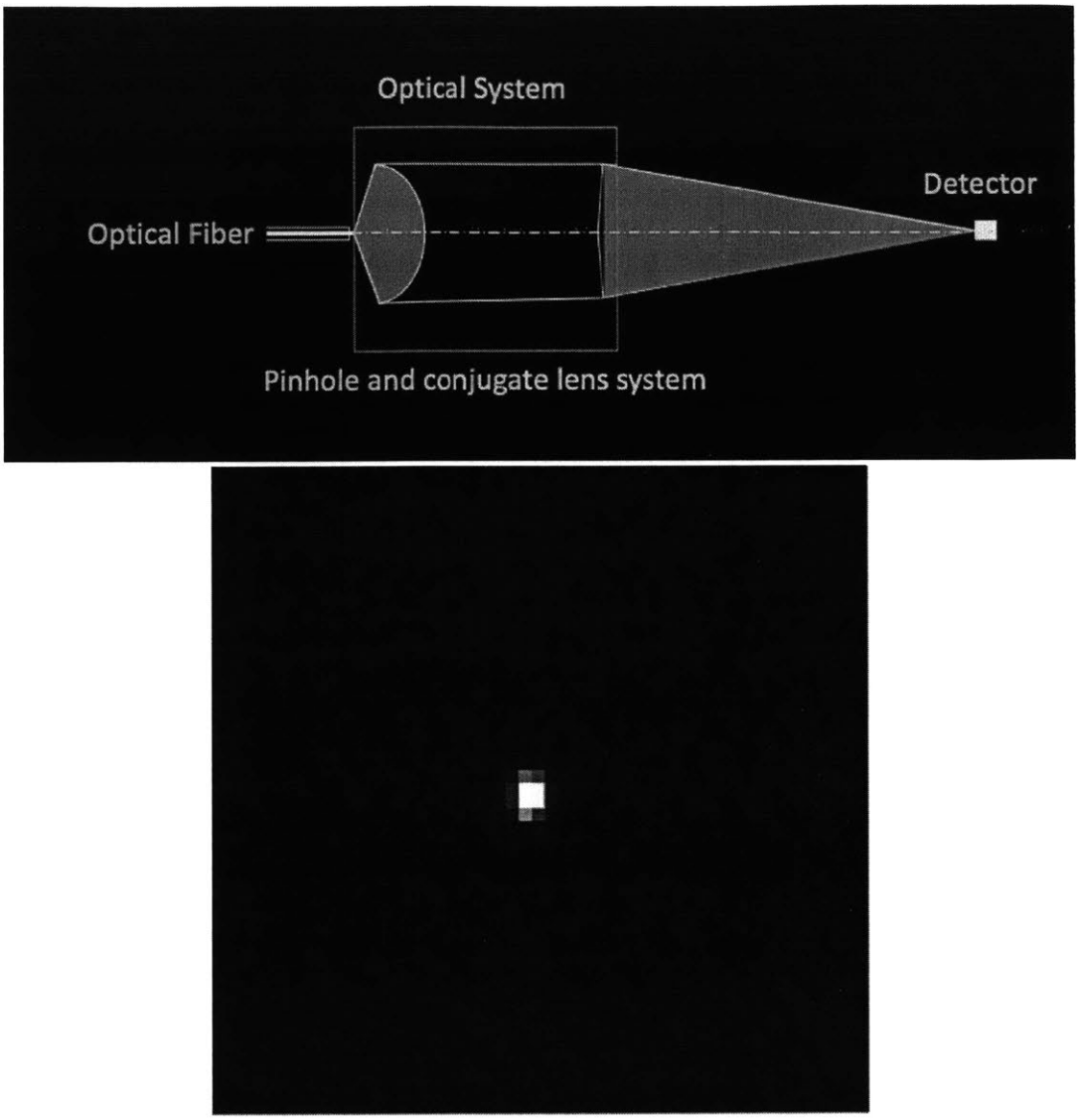

Figure 4-29: (Top) Optical setup that is part of the test setup and used to produce a stable spot size of a 10th of a pixel. (Bottom) An example image taken while fine-tuning and automating the system to focus the spot to the size of a pixel.

full wells. Charge blooming and distribution occurs along the vertical axis as seen in the image. The figure also shows intensity of bloomed charge along the vertical direction. The full width at half maximum of the curve increases as a function of peak pixel intensity.

Figure 4-32 shows a comparison of charge blooming for light of increasing intensities. It is interesting to note that charge blooming does not produce a smooth curve, but has features that can be attributed to amount of charge present in the neighbor-

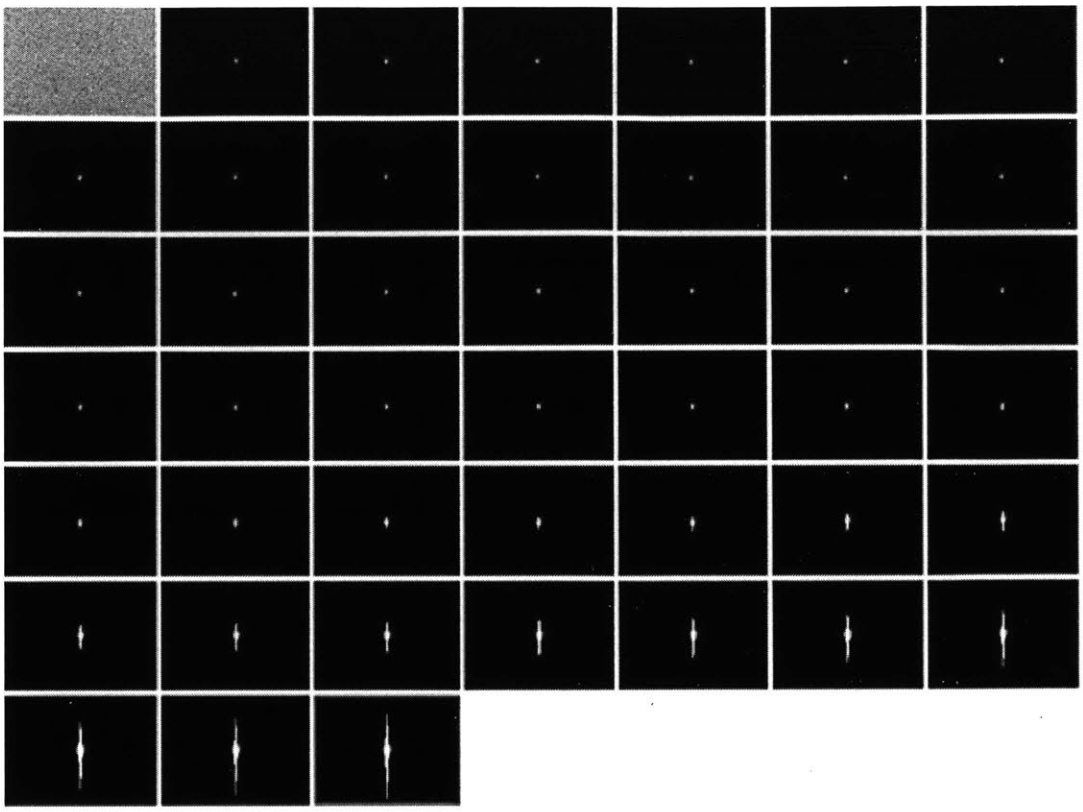

Figure 4-30: 200 x 200 pixel images generated using a flight-like TESS CCD detector with laser pulses of increasing intensities from 0 to 20 full wells.

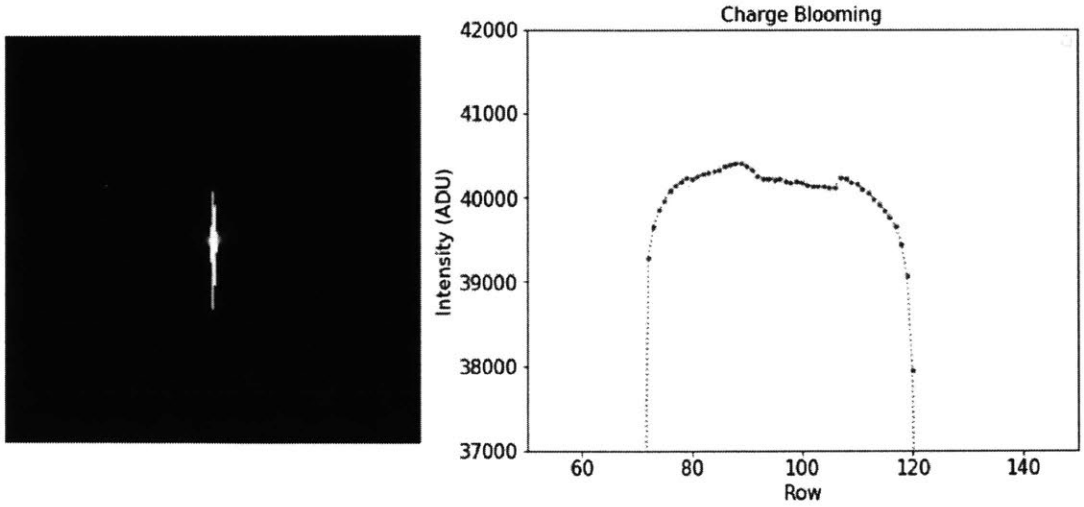

Figure 4-31: (Left) Image showing charge blooming effects on the TESS CCD detector. (Right) Plot of intensity of the bloomed charge along the vertical axis passing through the center of the spot. The intensity is in ADU (analog-to-digital units).

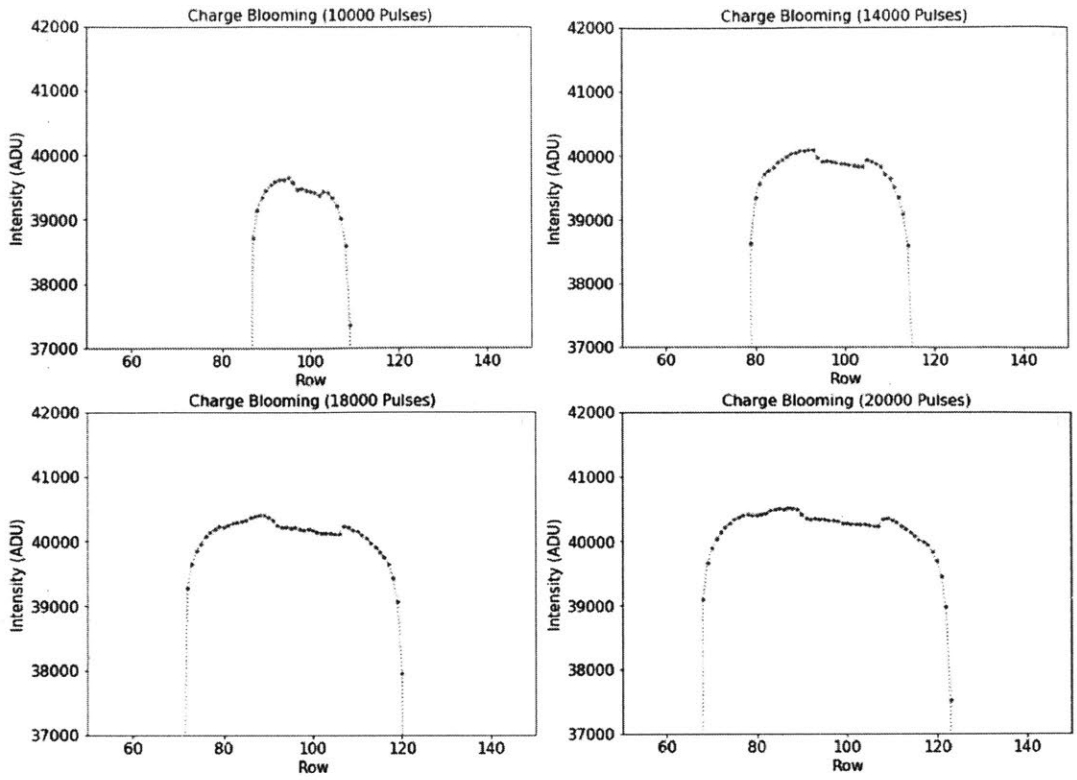

Figure 4-32: Charge blooming effects captured at 10000, 14000, 18000 and 20000 pulses of input light. The intensity is in ADU (analog-to-digital units).

ing pixel. The full well capacity in the central pixel is slightly lesser than the columns adjacent to it.

In order to compare the charge blooming pattern across various intensities, we make similar plots for all other intensities; a few examples are shown above. We observe that not only does the full width at half maximum increases with intensity, but the peak intensity on the plot also increases gradually as shown in Figure 4-33, indicating an increase in saturation limit as we increase intensity.

In order to establish the relationship between full width at half maximum and input light intensity, we use a polynomial curve fitting model as shown in Figure 4-34. The relationship between the full width at half maximum and input intensity is given by Equation 4.6. In this equation, fwhm is the full width at half maximum in pixels and I is the input intensity in ADU.

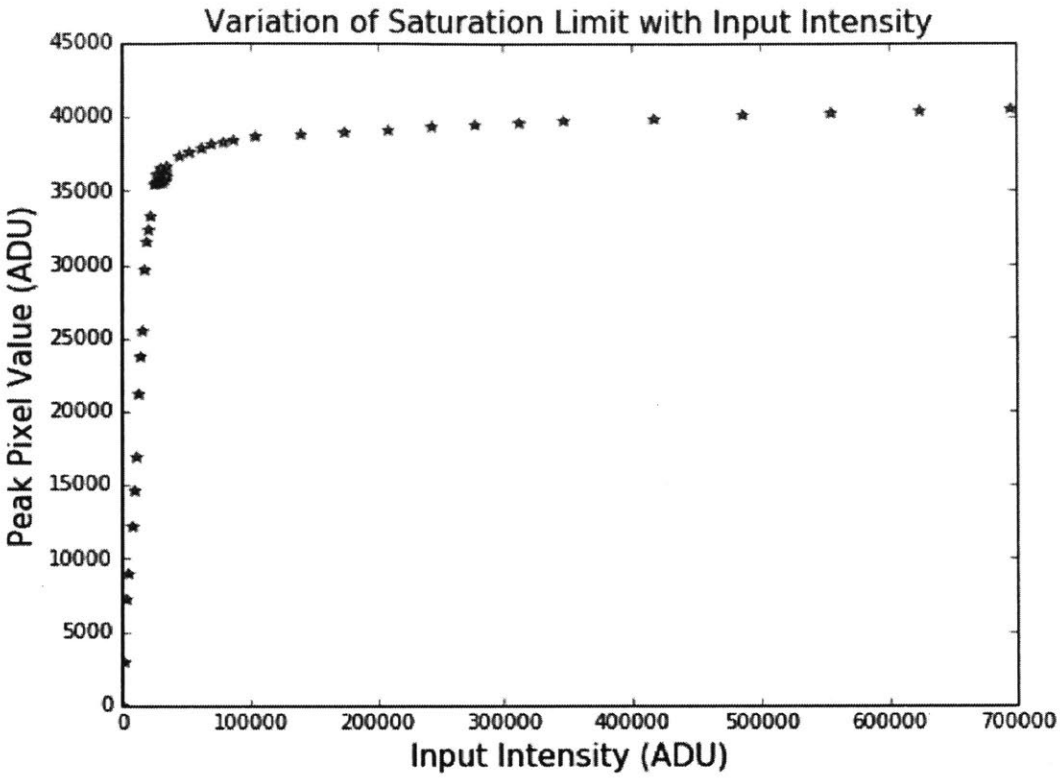

Figure 4-33: The plot shows the variation of peak pixel value with input signal intensity. The saturation limit continues to increase, although slightly, past the full well capacity at 36,000 ADU.

$$fwhm = 3.692e^{-11} * I^2 + 5.444e^{-05} * I + 1.561 \tag{4.6}$$

4.4.6 Undershoot

Undershoot is the distortion of signals with large pixel-to-pixel variation, in the direction of pixel readout. Low signal pixels immediately following very high signal pixels drop below zero relative to the local black level of the CCD. It is most noticeable in columns adjacent to charge blooming columns from saturating input light intensities as shown in Figure 4-35 and Figure 4-36.

In order to formulate the undershoot model, we use the same set of images with increasing intensity for the blooming model are analyzed in the histogram mode. The images show a set of black pixels in the center (indicating intensity values below

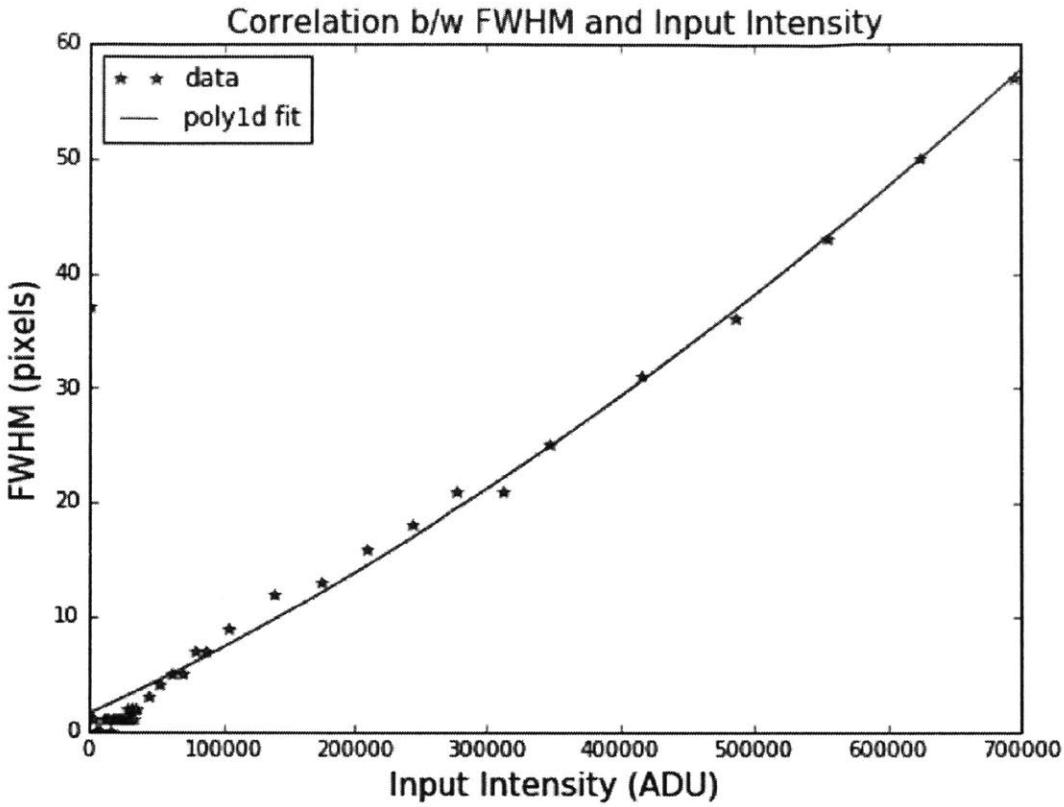

Figure 4-34: The plot shows the variation of full width at half maximum with input signal intensity. A polynomial fit is used to determine the relationship between them.

zero) that are attributed to undershoot effects in the CCD. The undershoot signal for TESS is found to be -0.14% of the flux level of the bright pixel adjacent to it, in the direction of readout.

4.4.7 Clocking / Readout Smear

When an exposure ends and CCD readout begins, a process called clocking is initiated where the voltages applied at each gate is cycled. The charge stored within each pixel during the integration is electronically shifted in a serial fashion along the columns from one pixel to another throughout the array. The CCID-80s have a frame store region that reduces smearing during readout, and allows for near continuous integration. The CCD is read out through four output nodes at a rate of 625 pixels/s. The dwell time for the 534 pixels (per detector) is about 0.85 millisec. For

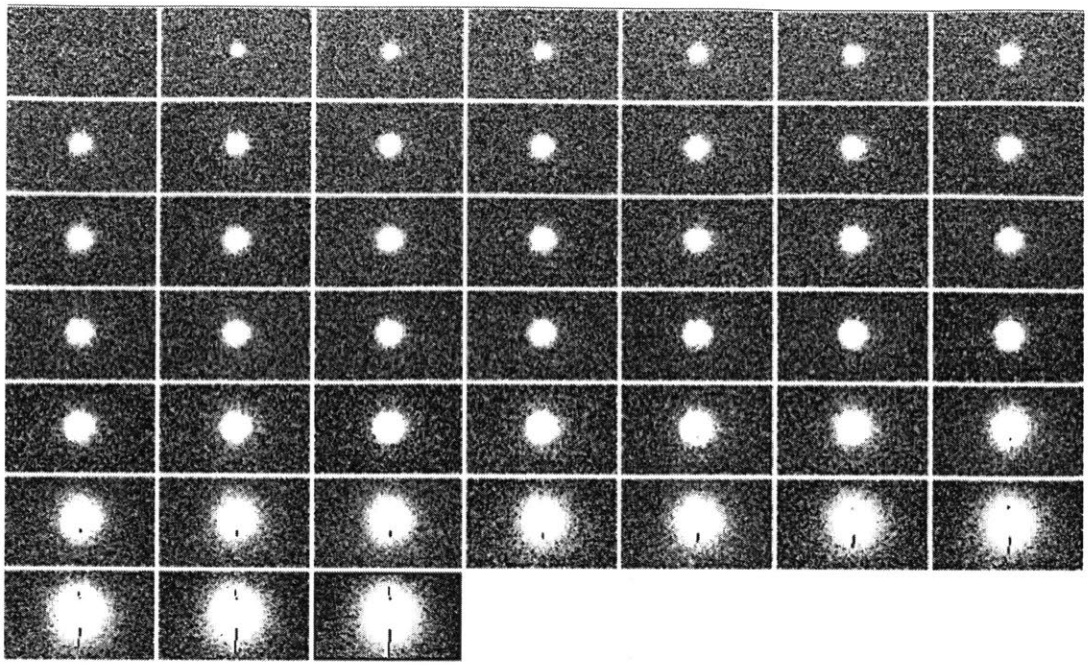

Figure 4-35: 200 x 200 pixel images were generated using flight-like TESS CCD detector with laser pulses of increasing intensities from 0 to 20 full wells, shown in the histogram scale. As the intensity increases, pixels with very low signal intensity (shown in black color), adjacent to the peak pixel column are produced. This is due to undershoot effects.

a 10th magnitude star, we calculate the residual charge that gets smeared to be 6.4 e^-/pixel. For brighter stars, as the charge collected increases, the residual charge also increases. The charge collected within each pixel is measured as a voltage. Each row of the CCD is shifted into the output register, until the entire array of pixels has been readout. The output voltage is converted to a digital number (DN), typically expressed as analog-to-digital units (ADU).

4.4.8 Straps and Fringing

One important factor in determining what parts of the CCD we should use in calculating the output signal for the QE measurement is driven by the presence of aluminum straps and temperature sensors underneath the surface of the CCD that reflects light at certain wavelengths. For wavelengths shorter than 800 nm, the CCD has a uniform spatial response, but at longer wavelengths between 825 - 1050 nm, bright lines due

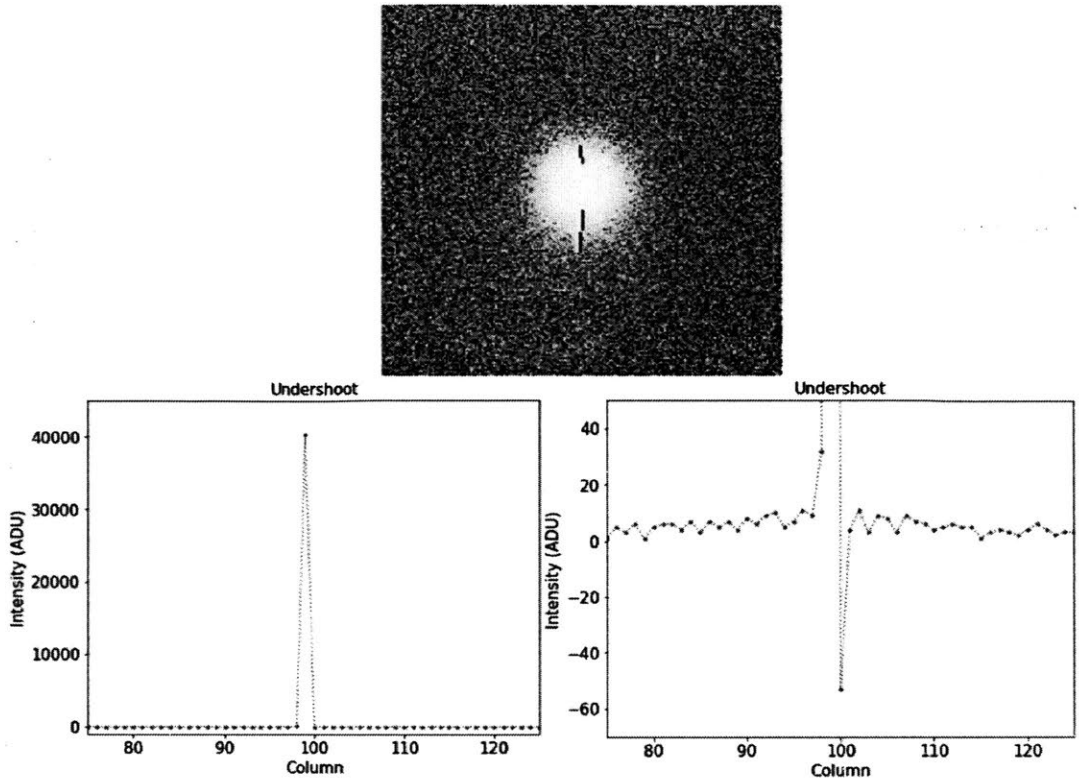

Figure 4-36: (Top) Undershoot signals are seen due to a drop below zero relative to the local black level of the CCD. This is observed adjacent to the charge blooming column. (Bottom left) A plot of intensity along the horizontal axis where the undershoot effects are seen. (Bottom right) A zoomed-in version of the image to the left that shows the undershoot signal of -57, which is about -0.14% of the bright pixel column to the left of the undershoot signal.

to the straps and temperature sensors are observed, as seen in Figure 4-37.

We observe the phenomenon of fringing that is caused by interference of light at the boundaries of the epoxy layer, between 905 nm - 1000 nm due to the longer wavelengths penetrating the features in the underlying structure. The interference patterns vary depending on the angle at which light falls on the CCD, as well as the distance of the light source, and hence are a source of aleatoric uncertainty. The straps, on the other hand, are a type of epistemic uncertainty.

The dark lines are a result of reflection from the aluminum straps and temperature sensors underneath the surface, and the fringing is caused by the interference due to the variation in the thickness of the epoxy bonding of the silicon to the substrate.

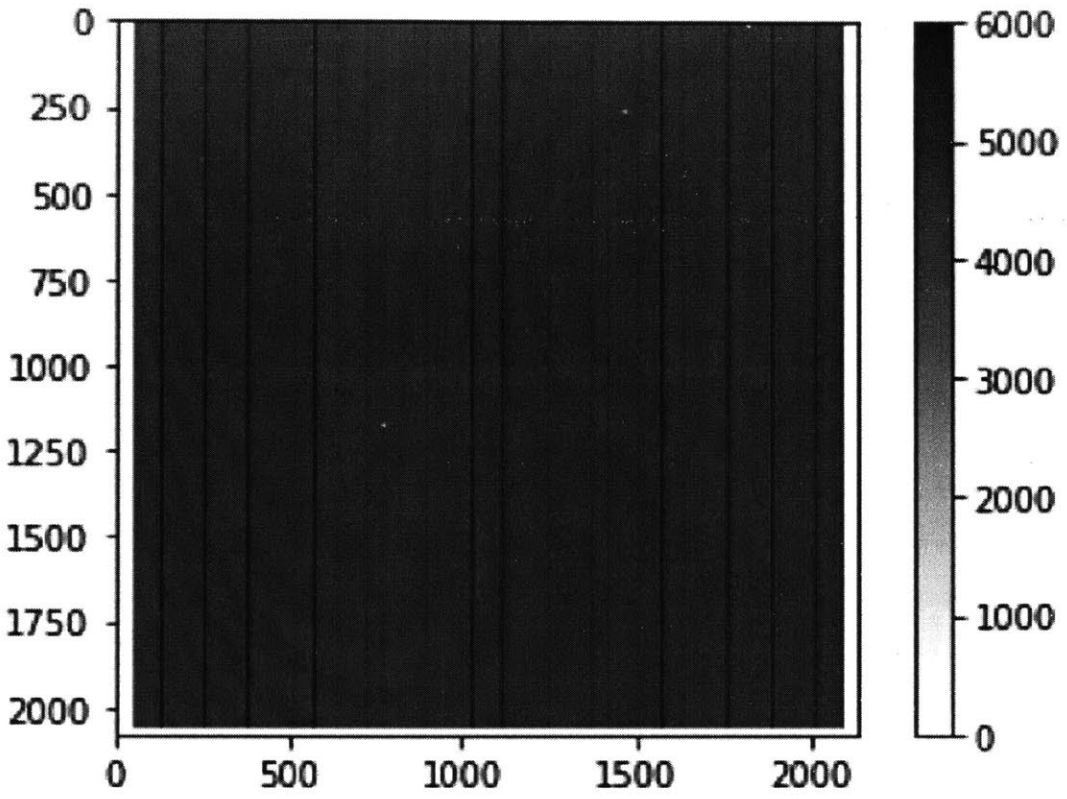

Figure 4-37: The image shows uniform illumination of the CCD at 980 nm. Post-processing of the data was performed using dark subtraction, and averaging 20 frames. The darker vertical lines represent reflection from aluminum straps and the lighter vertical lines represent temperature sensors embedded underneath the surface of the CCD. The fringes are caused by interference due to the variation in thickness of the epoxy layer that bonds the silicon surface to the substrate.

We plot the intensity of the signal along the horizontal axis to analyze the percentage of increase over the straps as shown in Figure 4-38. The increase in signal intensity ranges between 0.5% - 21% as we sample across different wavelengths between 825 nm - 1050 nm.

4.5 Systematics Evaluation and Calibration

Flight Data Calibration is a key step in understanding the performance of the TESS mission over various sectors of operation. We develop a data analysis pipeline to identify and analyze the contributions of major systematic error components in the

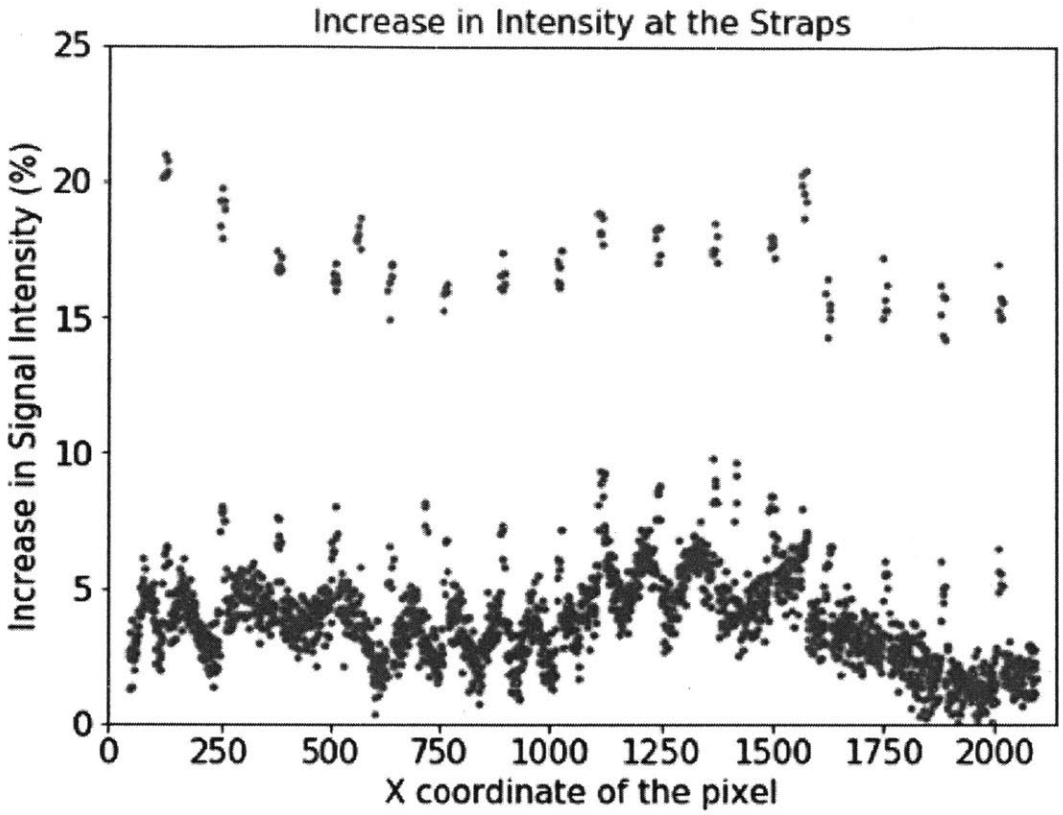

Figure 4-38: The plot shows the variation of signal intensity along the x coordinate for uniform illumination at 980 nm. Percentage increase in signal intensity is plotted against the x coordinate of the pixel. Maximum increase in intensity at the straps is observed to be 21%. The larger variations are a result of the aluminum straps, while the smaller variations are a result of the temperature sensors.

data. We validate photometric performance during the first year of operation and assess the impact of systematic noise sources. The overall framework is shown in Figure ?? in Section 4.4.1.

In order to evaluate the photometric performance, we first develop a data analysis pipeline that takes the TESS data products (SAP and PDCSAP flux from target pixel files and light curve files) as input and performs detrending to remove long timescale variations. We then assess the photometric performance metrics, which is the basis for target selection. We select a set of quiet stars for our analysis, and then proceed to fitting a model and estimating the noise floor for the mission. We also characterize the major noise sources and assess their contribution to systematic

error. We develop techniques to remove the noise from the data and improve the photometric performance. Lastly, we estimate the lowest detectable size of planets around M stars, given the noise floor.

4.5.1 Data Analysis Pipeline

We develop a data analysis pipeline, as shown in Figure 4-39, to process the Science Processing Operations Center (SPOC) data products that include the SAP flux and PDCSAP flux time-series. SAP flux is generated by SPOC by performing aperture photometry on the time-series. While PDCSAP flux is obtained by further processing the SAP flux and cotrending it to remove shared systematics with other stars.

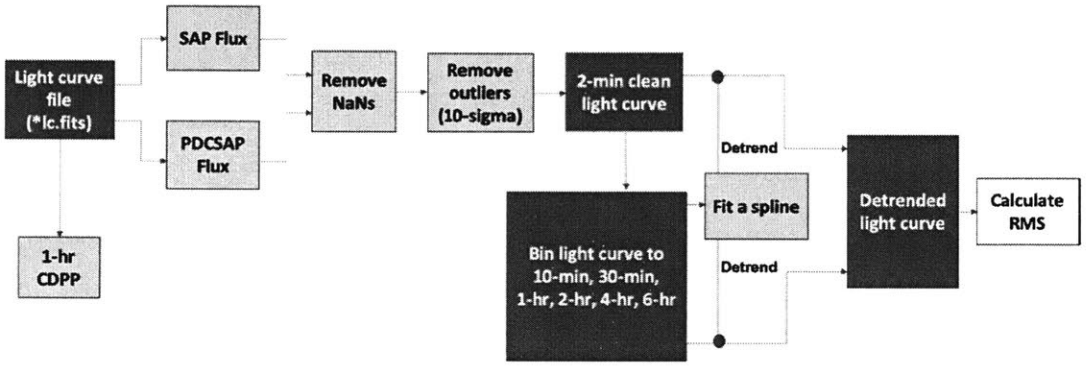

Figure 4-39: Schematic diagram showing the data analysis software architecture that takes *lc.fits files as input and produces 2-min and binned light curves, detrends them and calculates the RMS for both light curves.

The SPOC pipeline performs calibration of the 2-min images and 30-min FFIs by removing instrument and detector effects such as bias, dark and flat filed in addition to pixel-level calibration for cosmic rays, pixel sensitivity variation, and readout smear. Next, it identifies pixels of interest for each target star and extracts photometric measurements. The pipeline then fits and removes the background flux due to zodiacal light and diffuse stellar background. The calibrated pixel flux time series are available as SAP flux in the light curve FITS files.

In addition to pixel-level calibrations, the SPOC pipeline also performs a set of corrections to the light curves by removing instrumental signatures caused by changes

in focus or pointing, in addition to identifying and correcting outliers. This step is called Pre-search Data Conditioning (PDC) and the calibrated light curve is available as PDCSAP flux time series in the light curve FITS files.

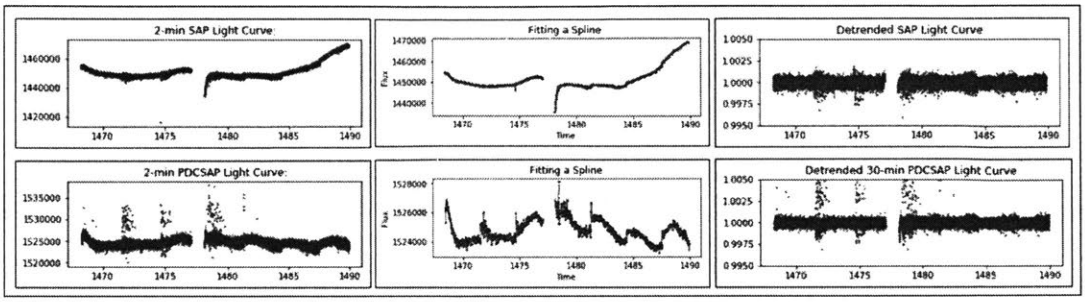

Figure 4-40: (Left) Example light curve showing 2-min SAP flux (top) and PDCSAP flux (bottom) vs. time obtained from *lc.fits file for TICID 30110465. (Middle) A spline is fit to the binned light curves which is used to detrend long timescale variations from the light curves. (Right) Detrended light curves after long timescale variations are removed.

We now present our data analysis pipeline and explain the steps we use to further process the data products from SPOC:

1. Obtain SPOC data products - We download the light curve files from MAST (Mikulski Archive for Space Telescopes). Each light curve file has three Header Data Units (HDUs) and the primary HDU has the basic information such as TIC ID, TESS magnitude, effective temperature, and so on. The second HDU has binary data tables with the SAP flux, PDCSAP flux, time, background flux, and CDPP at 0.5-hr, 1-hr and 2-hr. The third HDU has the aperture mask and number of pixels in the aperture.
2. Removing outliers and nulls from data - We use filters to remove null values and outliers greater than 10-sigma from the data.
3. Binning to various time bin sizes - We analyze the systematic noise at various timescales to understand the noise characteristics. For this, we bin the light curves from 2-min to 10-min, 30-min, 1-hr, 2-hr and 4-hr. We use 6-hr binned light curves as the reference for detrending.
4. Detrending - We fit a spline to the 6-hr binned light curves, and use that

to detrend the 2-min, 10-min, 30-min, 1-hr, 2-hr and 4-hr light curves. We present examples of detrended light curves along with SAP and PDCSAP light curves in Figure 4-40. We observe that the long timescale variations have been effectively removed and level adjusting has been performed. We also normalize the light curves at this step. Hence, the range of the y-scale is different from the original light curves.

5. Assessing photometric precision - We calculate the root mean square (RMS) of the light curve to assess photometric precision. For the rest of this chapter, photometric precision implies RMS of the detrended light curve.

The objective of the following sections is to quantify the effect of jitter on photometric performance. To begin with, we select the brightest and quietest stars for our analysis as we are interested in establishing the noise floor for bright stars. The same analysis can be further extended to study the photometric performance at different stellar magnitudes, if required.

We perform an outlier analysis to determine the reason for reduced photometric precision among the rejected star population. We then analyze the effect of time bin size where we evaluate the effect of binning to different timescales on photometric performance. Next, we analyze the effect of photon noise, background noise and read noise on total noise in the quiet stars, and calculate the residual systematic error. We develop a model to fit the residual systematic error as a function of jitter amplitude, and estimate the contribution of jitter noise to the residual systematic error. Then, we develop a model to analyze the impact of huge temperature variations. Lastly, we evaluate the effect of jitter noise and noise due to temperature variations on performance.

4.5.2 Target Selection

We begin by extracting SAP and PDCSAP flux for all bright stars (V<6) from sector 6. This sector corresponds to orbits 19 of TESS observations. We choose sector 6 because it has one of the best pointing performances in comparison to the earlier

sectors. We analyze more than 500 stars in sector 6 shown in Figure 4-41, and select 17 bright stars with magnitudes < 6.0 that have lower residual systematic error and appear to be quieter in comparison with the rest of the stars.

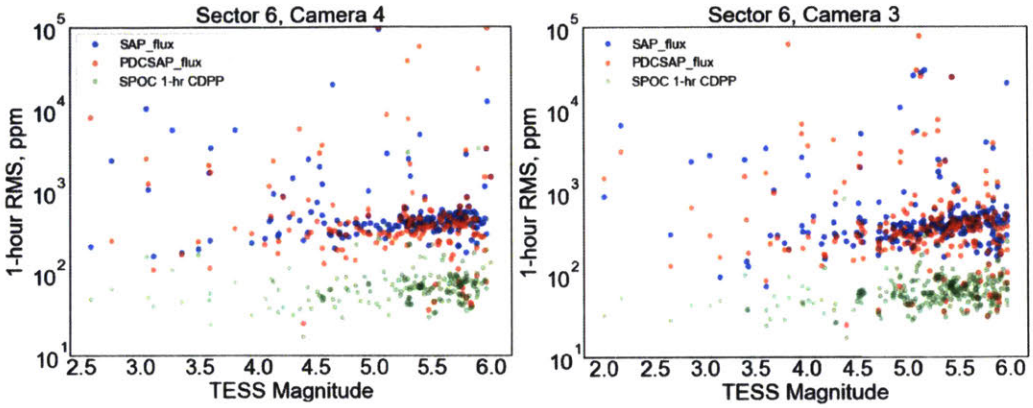

Figure 4-41: 1-hour photometric precision for detrended SAP and PDCSAP flux time series calculated for all stars in sector 6, cameras 3 and 4. We choose the quietest stars, i.e. the red points below 60 ppm. The green points show reference values for SPOC CDPP.

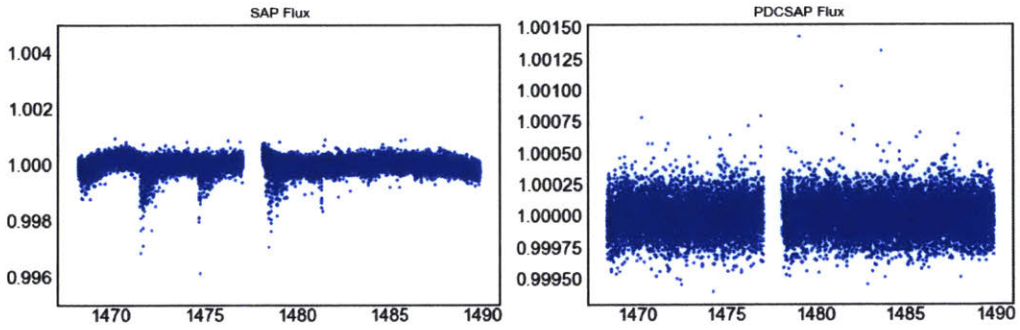

Figure 4-42: Example light curves showing 2-min detrended SAP flux time series (left) and 2-min detrended PDCSAP flux time series (right). The TICID of the target star in the figure is 156712422.0 and the TESS magnitude is 5.77.

Examples of detrended SAP and PDCSAP flux time series after running the SPOC products using our pipeline is shown in Figure 4-42. We note that the photometric precision calculated using the detrended PDCSAP flux time series after processing through the pipeline is way higher than the detrended SAP flux time series as shown

in Figure 4-43. The higher precision is due to the removal of systematic trends by PDC from the SAP flux, and the improvement in precision due to the detrending algorithm we applied to further process the PDCSAP flux. Hence, we use the detrended PDCSAP flux for the rest of our analysis in this chapter.

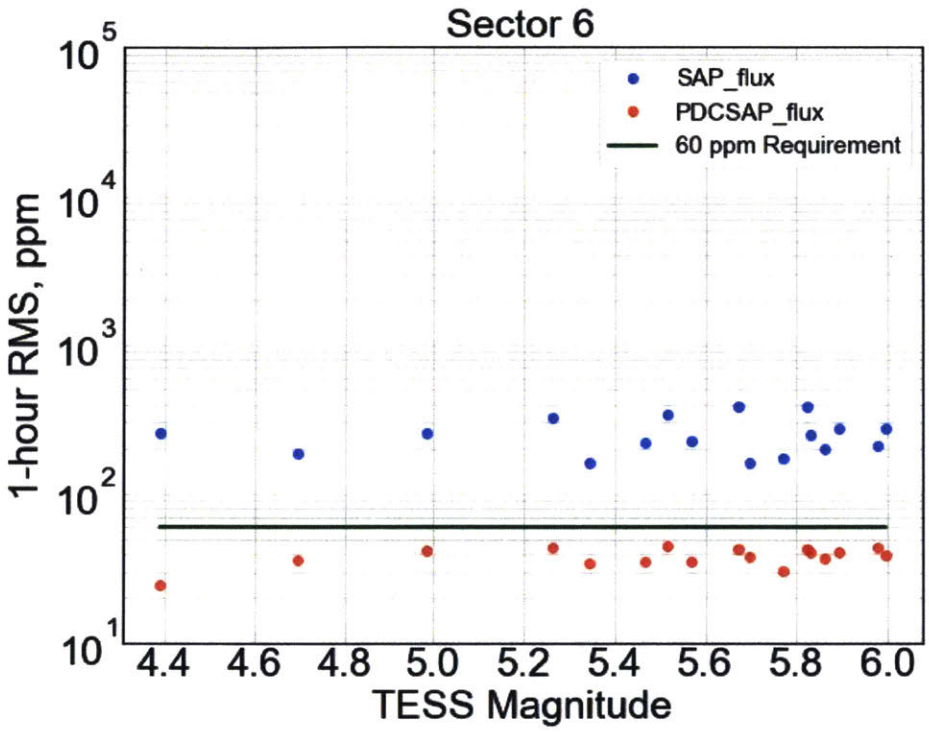

Figure 4-43: Photometric precision for 17 quiet stars in sector 6 calculated using detrended SAP and PDCSAP flux time series. The RMS values are well below the 60-ppm photometric performance requirement for TESS. The precision for PDCSAP flux is higher than SAP flux indicating that systematics have been removed to a large extent in the detrended PDCSAP flux.

4.5.3 Photon Noise, Background Noise and Read Noise

In this section, we calculate the four components that contribute to the total noise: photon noise, background noise, read noise and systematic noise. Total noise is given by the root mean square of the detrended PDCSAP light curve. The 1-hr noise contributions are shown in Figure 4-44. Equation 4.7 shows that total variance is the

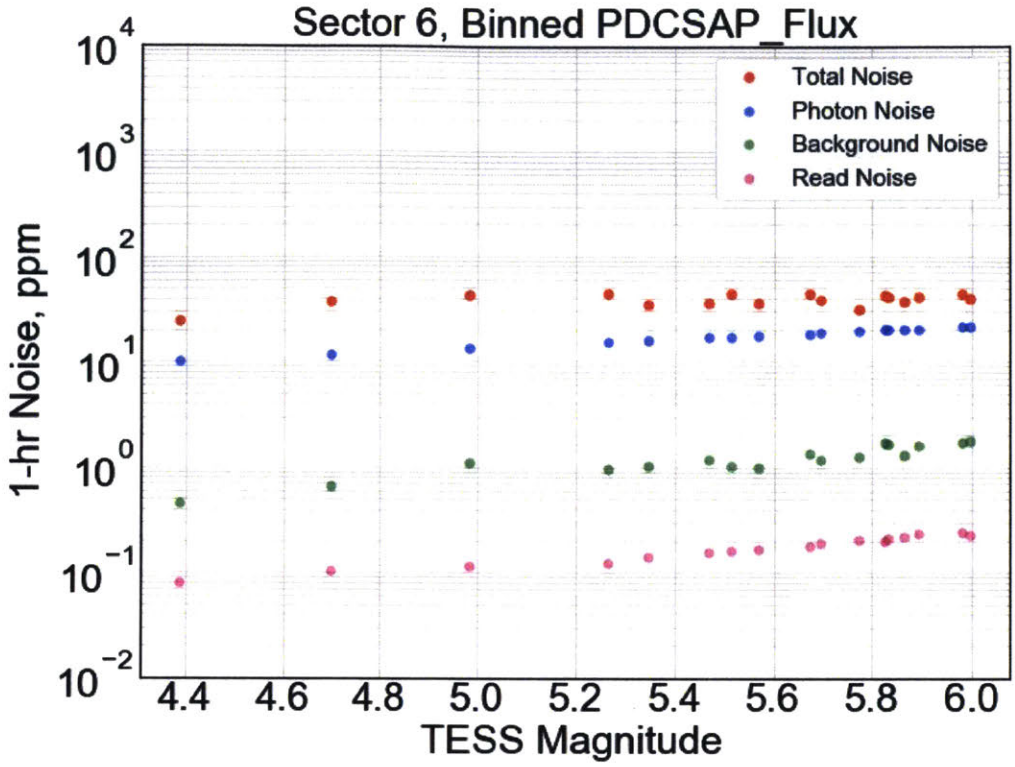

Figure 4-44: 1-hour total noise and contributors to total noise including photon noise, background noise, and read noise are shown. The dots represent the 17 individual quiet target stars from sector 6.

sum of the individual variances due to photon noise, background noise, read noise, and systematic noise. All the noise sources are normalized to the median detrended flux, and hence, dimensionless. In the rest of this thesis, we express noise in parts per million (ppm).

$$\sigma^2_{total} = \sigma^2_{photon} + \sigma^2_{background} + \sigma^2_{read} + \sigma^2_{systematic} \tag{4.7}$$

Photon Noise or shot noise is the time-dependent fluctuation in the light intensity, due to the discrete nature of the incoming flux. We model photon noise as a Poisson process. It varies as the square root of the incoming flux. We estimate the incoming flux using Equation 4.8, where counts is in e^-, t is the time bin size of the light curve and Tmag is TESS magnitude. We estimate the reference counts of 15400 counts/s

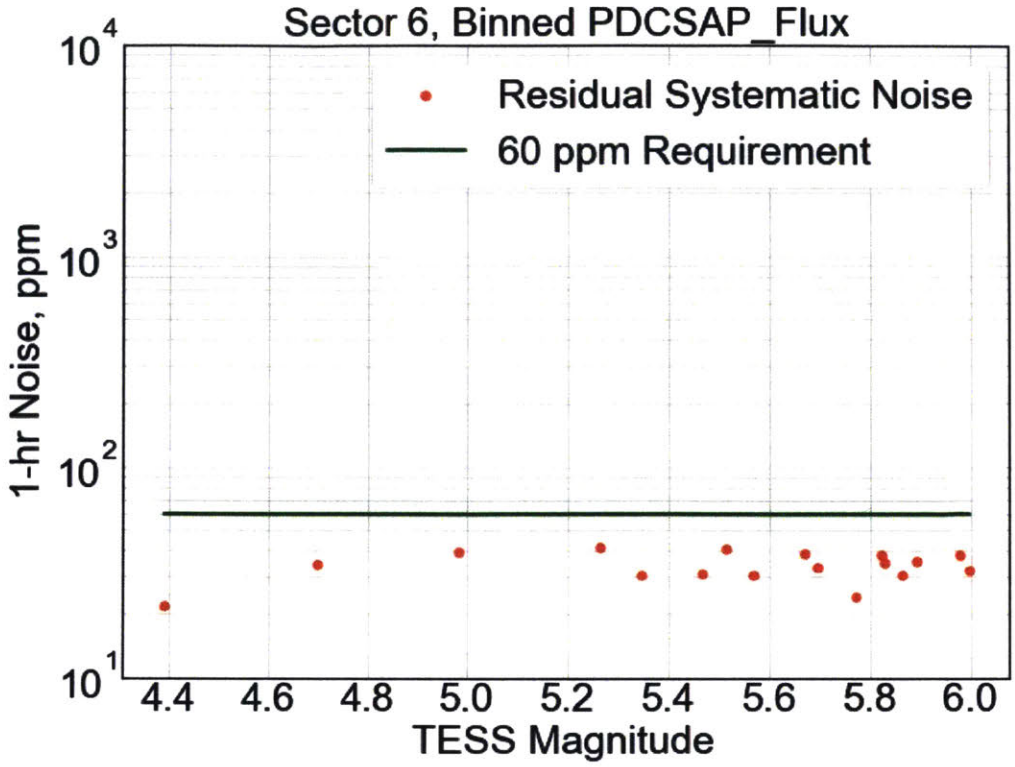

Figure 4-45: 1-hour residual systematic noise is shown for the 17 quiet stars in sector 6. The green line indicates the 60 ppm photometric precision requirement for TESS.

using the QE, lens transmission efficiency and the effective area. It is found that the observed counts is within 3% of the measured counts using laboratory techniques.

$$counts = 15400 * 60 * t * 10^{-0.4(Tmag-10)} \tag{4.8}$$

We calculate background noise by extracting the background flux information from the SPOC light curve files. Background flux is calculated by averaging the charge within an annulus outside of the target star, and multiplying by the number of pixels in the aperture. We calculate the background noise for the required timescale and normalize with the median detrended flux.

Read noise is the number of electrons per pixel introduced during the ADC conversion process because it is not perfectly repeatable. Read noise measured using laboratory experiments is 10 e^-/pixel/read. We multiply the read noise by the num-

ber of pixels in the aperture to derive the total read noise per read, where read time is 10 s to obtain the read noise in e^-. Again, read noise is normalized and expressed in ppm.

We calculate the residual systematic noise as shown in Figure 4-45 by subtracting the photon noise, background noise and read noise from the total noise. Residual systematic noise consists of instrument noise including effects from temperature changes and spacecraft jitter, and stellar variability. Hence, we pick quiet stars to limit the contribution from stellar variability. Now, the remaining noise is mostly comprised of instrument noise. In the next section, we focus on characterizing the residual instrument noise.

4.5.4 Jitter

Based on the jitter noise simulation in Section 4.3, we understand that jitter is linearly proportional to jitter amplitude, as given by Equation 4.9, where σ_jitter is the jitter noise, j is the jitter amplitude and A is the linear scaling factor.

$$\sigma_j = Aj \tag{4.9}$$

We begin by assuming contribution by any other sources of systematics to be "other noise". Then, the residual systematic noise can be defined using Equation 4.10, where σ_{other} is the other noise.

$$\sigma^2_{systematic} = \sigma^2_{jitter} + \sigma^2_{other} \tag{4.10}$$

$$Y = \alpha X + \beta \tag{4.11}$$

$$\sigma^2_{systematic} = A^2 j^2 + \sigma^2_{other} \tag{4.12}$$

We fit a linear regression model to obtain estimates for jitter noise and other noise using the Equation 4.11 where Y is $\sigma^2_{systematic}$, α is A^2, X is j^2 and β is σ^2_{other}. We

illustrate the same using Equation 4.12 where we solve for the slope A^2 and intercept σ^2_{other}.

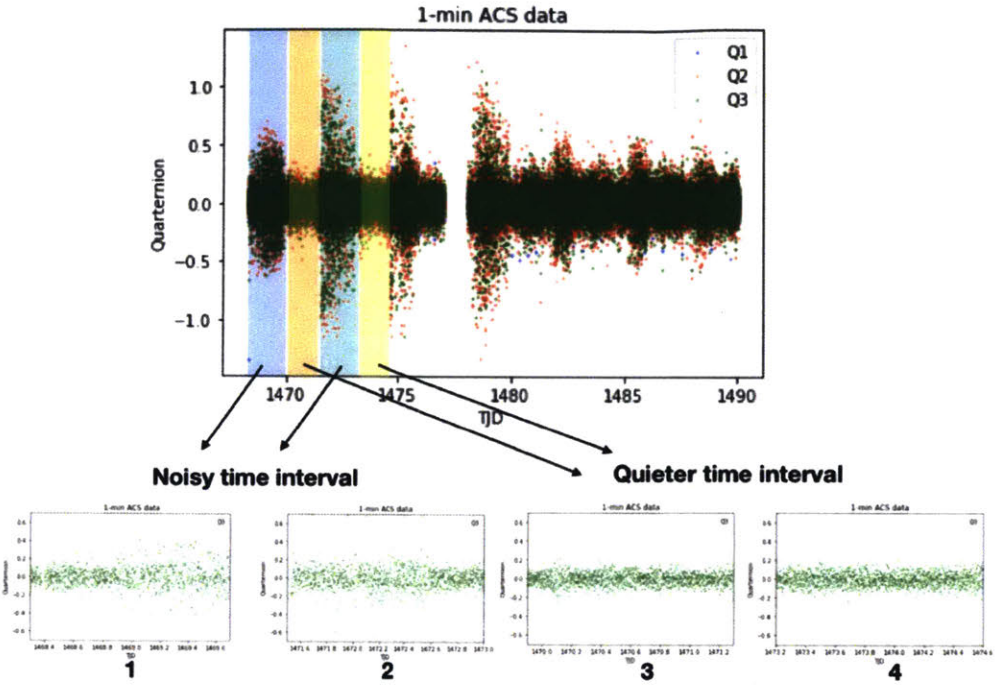

Figure 4-46: 1-min ACS data is shown as a function of time. The three quaternions Q1, Q2, and Q3 are shown. Q1 and Q2 correspond to motion along the x and y directions on the detector while Q3 corresponds to the roll axis.

We calculate the jitter amplitude as the standard deviation of Q2 across noisy and quiet time bins in the 1-min Attitude Control System (ACS) data as shown in Figure 4-46. We estimate the RMS within each of these time bins to calculate residual systematic error at a given jitter amplitude, which is then used to fit the model.

An example of the model fit for TIC ID 52687259.0 is shown in Figure 4-47. The x-axis is squared jitter amplitude and y-axis is squared residual systematic error, as given by the model. We note that the slope and intercept are both highest at 2-min, and decrease as we go down from 2-min to 4-hr binned data. Hence, we infer that the jitter noise and other noise are both time dependent.

We calculate and propagate errors from the model fit to the slope and intercept. The slope gives the squared scaling factor and the intercept gives the other variance.

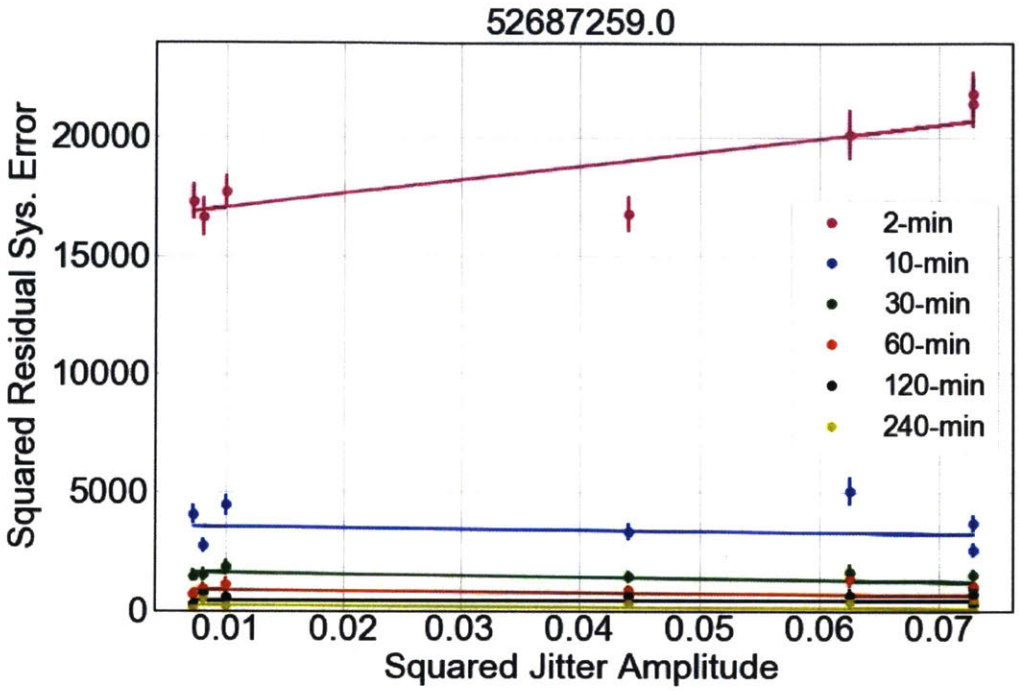

Figure 4-47: Linear regression model fit in the squared space with jitter amplitude and residual systematic error as the variables. The different colors represent the model fit for different timescales. The example corresponds to the target star with TICID 52687259.0.

We calculate the other error shown in Figure 4-54 and listed in Table 4.2. The other error is drops precipitously from 2-min to 10-min and continues to drop until 4-hr. We limit our model to 4-hr due to lower statistics within the jitter amplitude bins as we average further. The noise floor contribution of other error at 1-hour is 29.94 ppm.

We calculate jitter error as a function of jitter amplitude from the slope of the model fit as shown in Figure 4-49 and Table 5.1. We estimate the median jitter error by the square root of the slope from the model fit for all target stars and then taking the median of the individual slopes and multiplying by jitter amplitude. The noise floor contribution from jitter error at the lowest amplitude at 1-hour is 5.21 ppm.

We calculate residual systematic error as a function of jitter amplitude from the slope of the model fit as shown in Figure 4-50 and Table 4.4. We calculate median

Timescale	Median Other Error ppm
2-min	136.23±30
10-min	59.16±10
30-min	38.42±6
1-hr	29.94±5
2-hr	22.15±4
4-hr	15.51±4

Table 4.2: Median other error listed at different timescales. Median other error is calculated by taking the square root of the intercept from the model fit for all target stars and then taking the median of the individual other errors.

Timescale	Jitter Error at j_{min} ppm	Jitter Error at j_{max} ppm
2-min	23.63±8	75.08±25
10-min	12.00±3	38.13±9
30-min	6.18±3	19.65±9
1-hr	5.21±2	16.57±7
2-hr	3.25±2	10.35±7
4-hr	4.00±1	12.89±4

Table 4.3: Median jitter error listed at different timescales and for minimum and maximum jitter amplitudes.

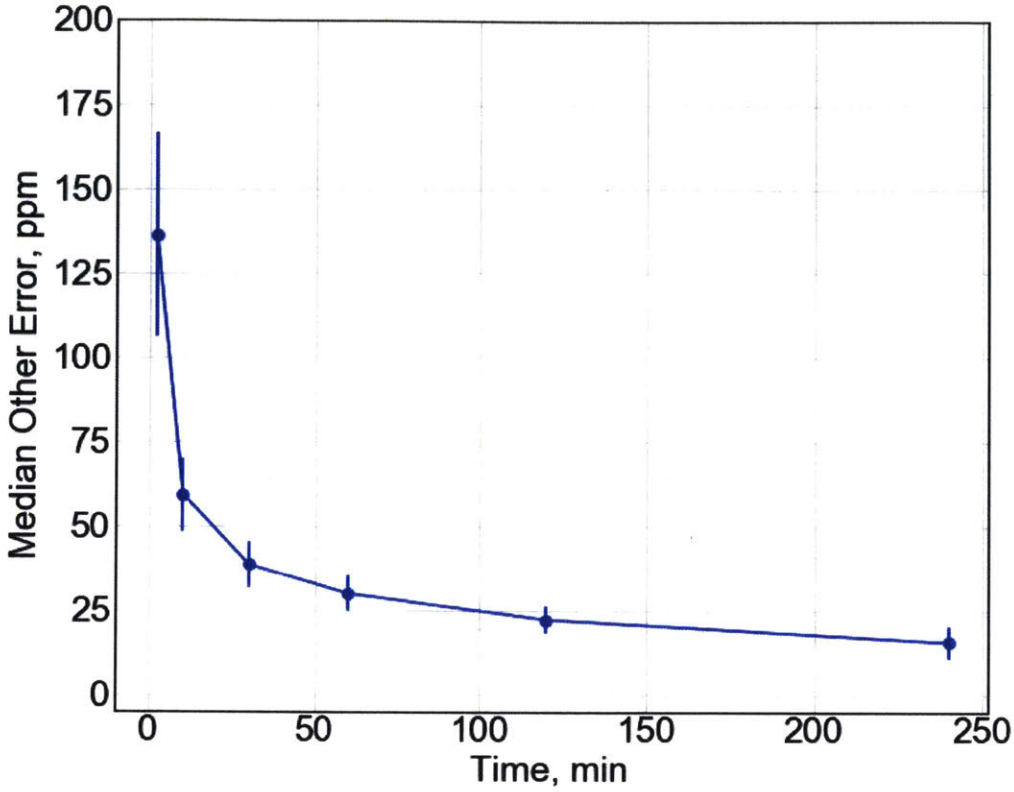

Figure 4-48

residual systematic error as the RSS total of the jitter error and other error for individual stars, and then taking the median. The 1-hour noise floor for quiet stars at the lowest jitter amplitude is 30.3 ppm, and at 4-hour is 16.0 ppm.

Plausible Source of Other Error

One plausible cause for other error is subpixel response variations in the detector. Due to the change in quantum efficiency within a pixel, depending on the phase of the target star and what fraction of the pixel it falls on, the detector response varies for one star to another. Moreover, the effect of subpixel variations is time dependent, and averages out rapidly just as the jitter amplitude averages out from 2-min to 4-hr.

The jitter noise calculation in the previous section does not capture the effect of subpixel variations. We model the effect of jitter as a function of jitter amplitude choosing noisy and quiet intervals. We then calculate the RMS of the light curve as

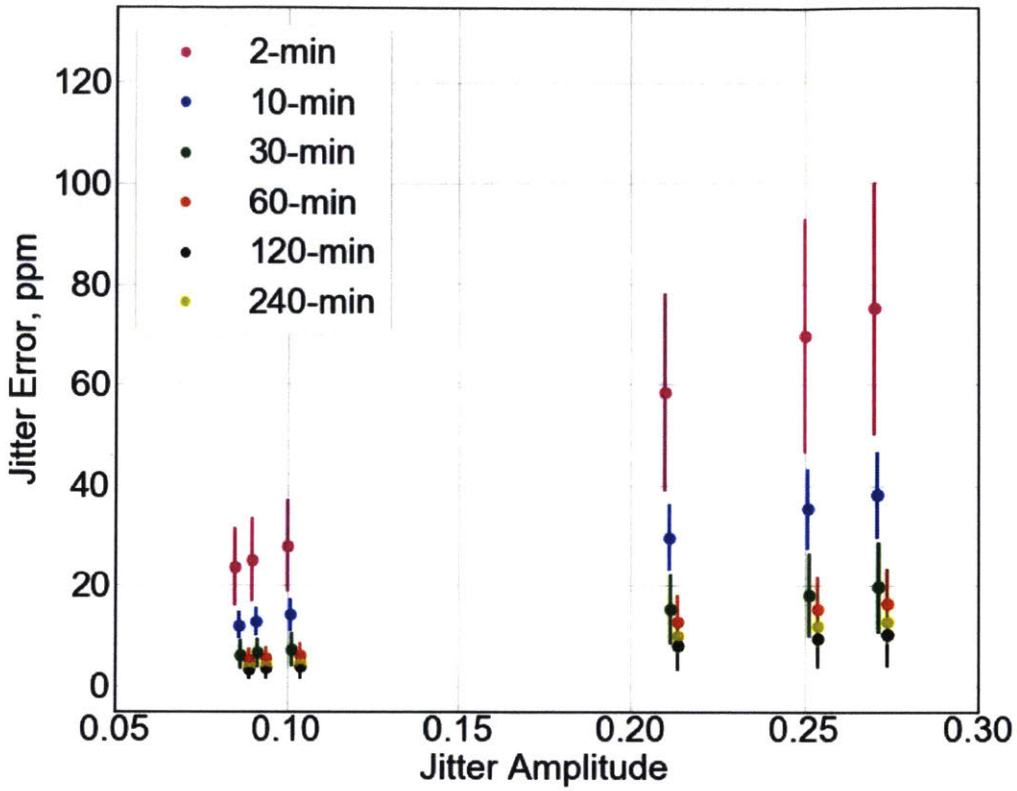

Figure 4-49: Median jitter error as a function of jitter amplitude at different timescales. Median jitter error is calculated by taking the square root of the slope from the model fit for all target stars and then taking the median of the individual slopes and multiplying by jitter amplitude.

a function of jitter amplitude. The other error is the term that is dependent on the difference in response due the position and phase of the star, but independent of the jitter amplitude.

The other plausible causes are heater effects and electronics. As the heater cycles, the associated noise varies with time. It is possible that this effect is higher at 2-min and averages out at 4-hr.

4.5.5 Temperature

In this section, we analyze the effect of huge temperature variations of 20 deg C or more on photometric precision. Figure 4-51 shows the focal plane temperature

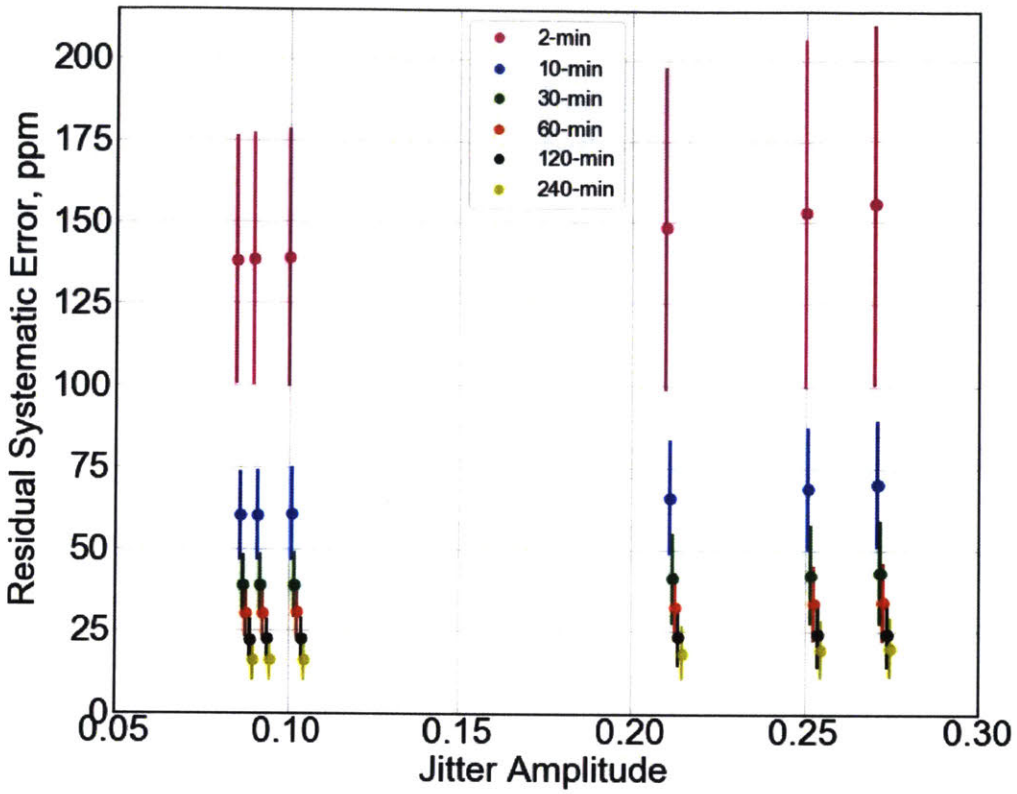

Figure 4-50: Median residual systematic error listed at different timescales as a function of jitter amplitude. Median residual systematic error is calculated as the RSS total of the jitter error and other error for individual stars, and then taking the median.

variation for camera 4 during Sector 4 observations. The change in temperature was of the order of 20° C.

In order to evaluate the effect of temperature variations on photometric precision, we select targets in sector 4 that are quieter compared to the rest of the stars, similar to sector 6. Figure 4-52 shows the photometric precision of quiet sector 4 targets as a function of stellar magnitude. It is evident that the quiet stars in Sector 4 are noisier than those in Sector 6, with very few stars having precision close to 60 ppm or less.

We select a total of 16 stars for the temperature analysis. The light curves in Figure 4-53 highlight the central section of the time series that has a huge drop in flux due to a temperature variation of over 20 deg C. In order to assess the effect of this temperature change, we remove the time series data during this temperature

Timescale	Residual Sys. Error at j_{min} ppm	Residual Sys. Error at j_{max} ppm
2-min	138.26±38	155.55±55
10-min	60.36±13	70.38±19
30-min	38.92±9	43.16±16
1-hr	30.29±7	34.22±12
2-hr	22.39±6	24.45±10
4-hr	16.03±6	20.17±9

Table 4.4: Median residual systematic error listed at different timescales at minimum and maximum jitter amplitudes.

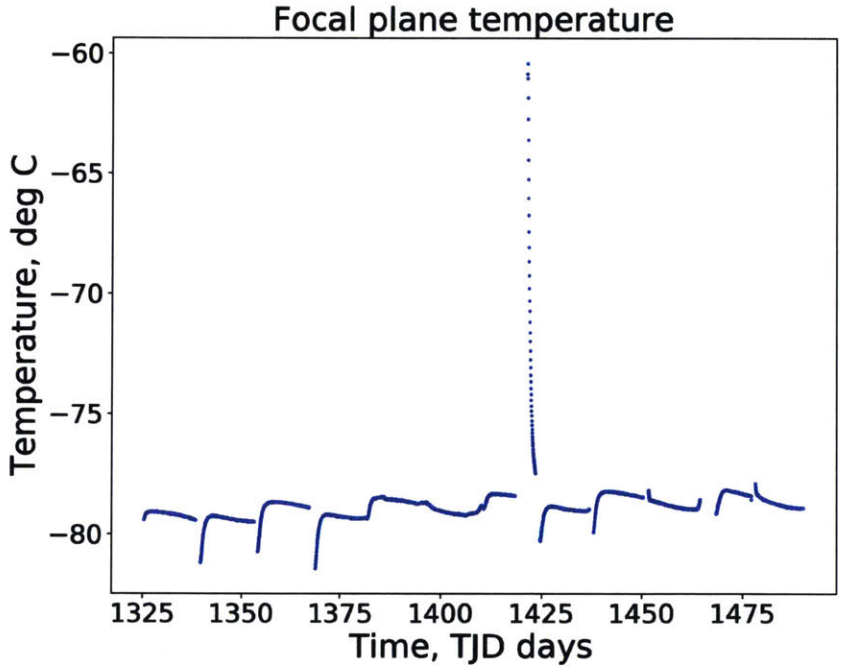

Figure 4-51: Temperature variation as a function of time for Sector 4, camera 4. The change in temperature was of the order of 20° C.

variation, and analyze the contributions of jitter error and other error in the rest of the time series.

We repeat the jitter analysis as shown in the previous section and determine jitter error and other error as shown in Figure 4-54. The contributions of jitter error and other error are slightly higher than sector 6 due to the stars in sector 4 being not as quiet as the ones in sector 6. We subtract the two error components from the systematic error to derive the temperature error specifically in the region where the

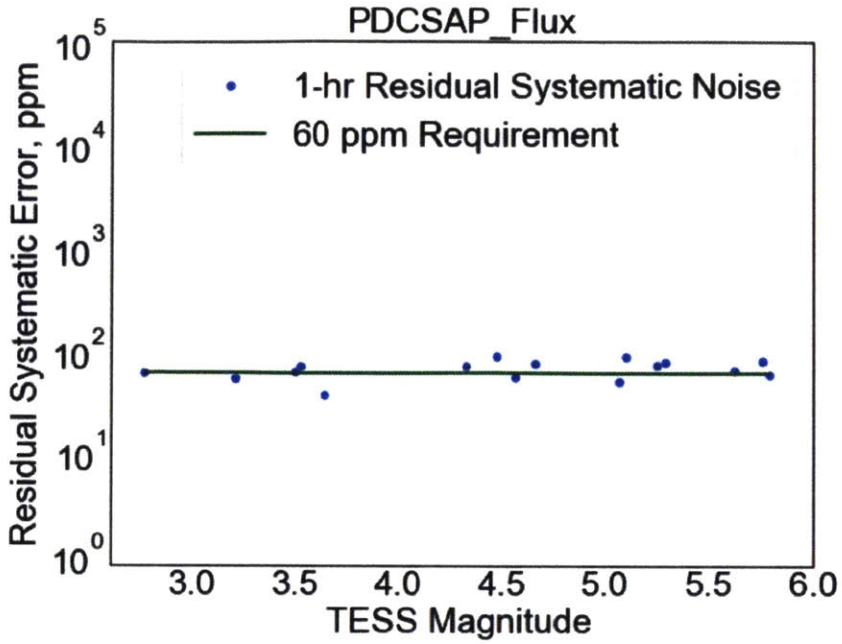

Figure 4-52: Photometric precision as a function of stellar magnitude for quieter Sector 4 targets.

temperature change occurred. We plot the temperature error for each target, as shown in Figure 4-55. The median 1-hour temperature error was found to be 33 ppm. This means that when there is a high temperature variation of 20° C, the error contribution due to this variation is 33 ppm.

4.6 Performance Validation and Improvement

In this step, we identify outliers from the larger dataset from sector 6, and analyze them to identify the causes for lower photometric precision. We also develop techniques to improve the precision. In addition, we present the variation of photometric performance with time bin size, and improvement in precision that can be obtained using ensemble averaging.

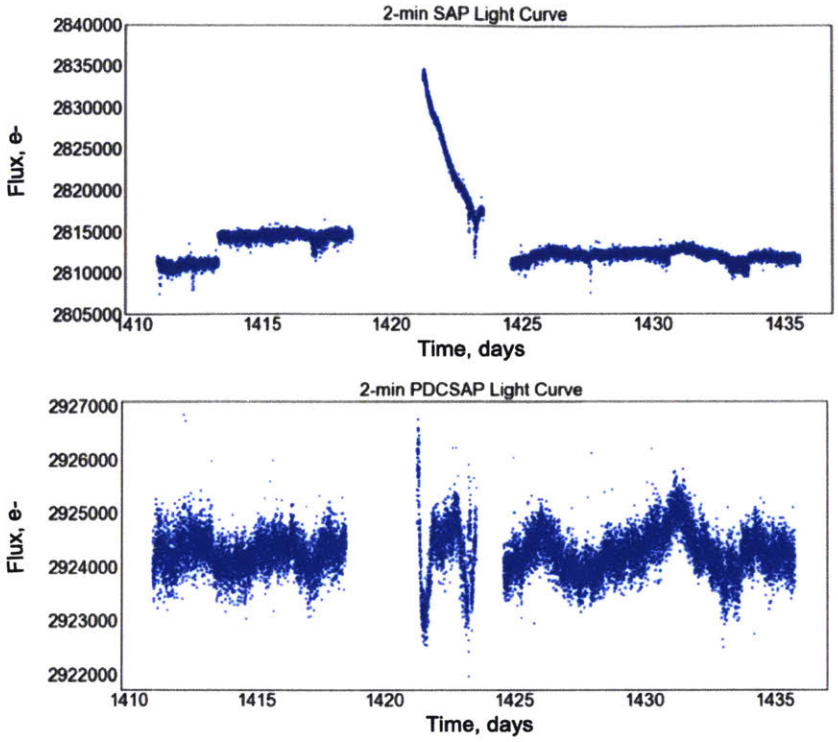

Figure 4-53: Light curves showing the huge change in flux towards the center of the light curve due to huge temperature changes of 20 deg C.

4.6.1 Outlier Analysis

We shift focus to evaluate plausible reasons for lower photometric precision in the outliers. We evaluate two factors that are dominant contributors to higher noise and decreased photometric performance in these stars: stellar variability and lack of optimal aperture size. We also evaluate the effect of charge blooming on photometric performance.

Stellar Variability

We analyze a few hundred outliers from sector 6 data that have 1-hour photometric error higher than 200 ppm. We conclude from the analysis that a majority of stars, up to 80% have intrinsic stellar variability which causes periodic trends at different timescales in different target stars making it difficult for the detrending algorithm designed for the ensemble study to optimize the correction for all the timescales.

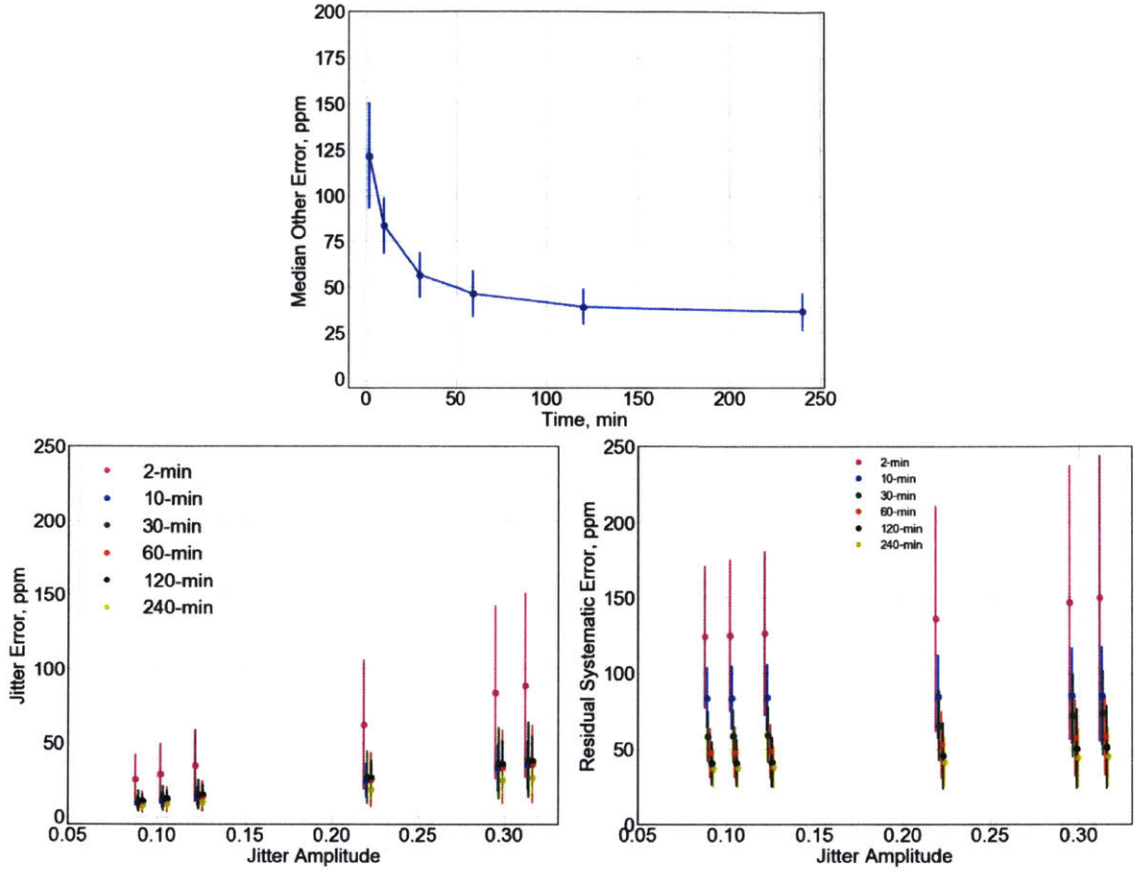

Figure 4-54: Other error, jitter error and residual systematic error error as a function of stellar magnitude.

Further, it has been demonstrated that stellar variability can be successfully removed to a large extent by using a median filter in the wavelet domain to correct for long timescale trends. The process of removing these systematic effects in the wavelet domain is adopted by SPOC for Threshold Crossing Events (TCEs), and the method is called whitening [92]. The whitened data products are not available in the target pixel files or the light curve files, but can be downloaded from the data validation (DV) time series available separately on MAST.

We limit the scope of the present work to analyzing the effect of instrument-related systematics. Hence, analyzing stars with high intrinsic variability and incorporating algorithms to correct for these astrophysical effects is outside of the scope of the present work.

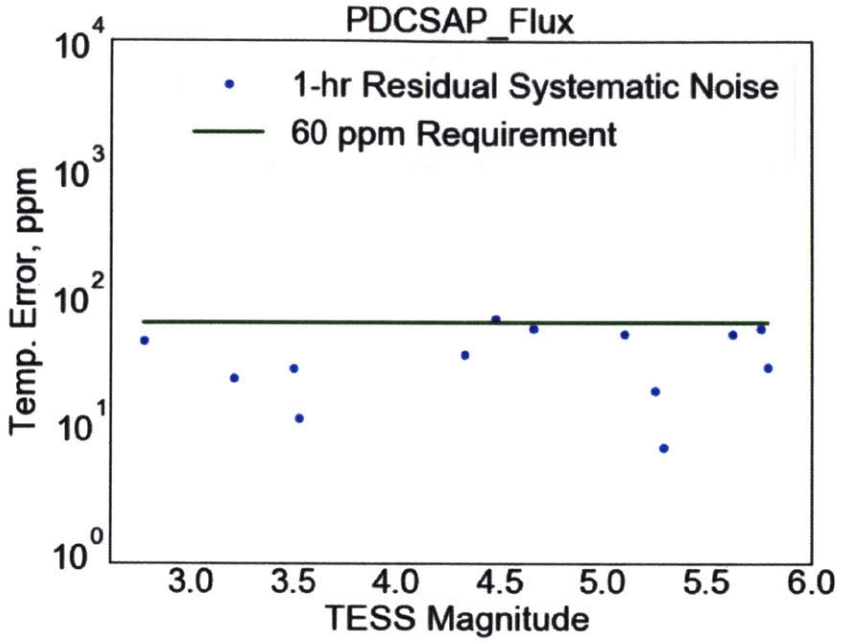

Figure 4-55: 1-hour Temperature error as a function of stellar magnitude.

Aperture Size and Charge Blooming

We analyze the importance of using an optimal aperture mask to perform simple aperture photometry in this subsection. We present examples in Figure 4-56 that show stars with highlighted aperture masks. The photometric measurements are missing the light intensity from parts of the stellar image that lie outside the mask. Moreover, in a lot of cases, if the aperture is not large enough, we risk losing a portion of the stellar flux when the centroid shifts even a fraction of a pixel due to spacecraft jitter or changes in PSF when there are huge temperature variations.

The second important aspect to consider in the context of aperture size is the pattern of bloomed charge, in the case of very bright, saturated stars. As we see in Figure 4-31, the charge does not bleed symmetrically in the x or y directions. Based on our laboratory experiments in Section 4.4.5, we understand that the number of bloomed pixels above and below the peak pixel are not equal. Similarly, the adjacent columns of bloomed pixels are also not aligned or symmetric. By defining large enough aperture masks and taking into account blooming patterns, we demonstrate

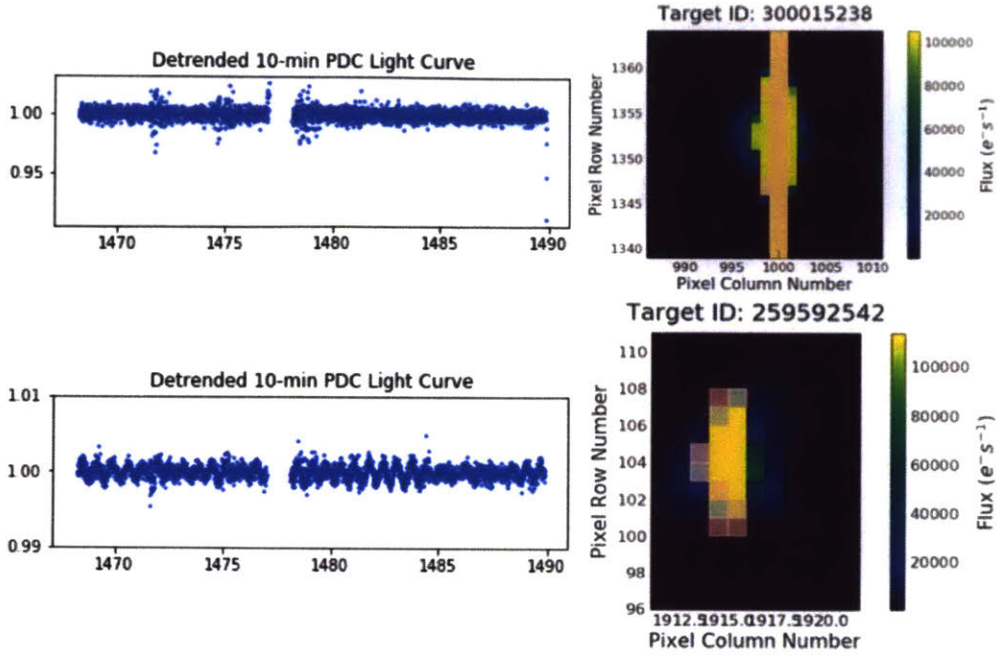

Figure 4-56: (Left) Example detrended light curves for outliers in sector 6 with rms > 200 ppm. We analyze the aperture size used to perform simple aperture photometry (right) using the lightkurve software.

improvement in photometric performance for saturated stars significantly as shown in Figure 4-57.

4.6.2 Time Bin Size

Data binning is a quantization technique used to reduce the effects of error in the data. For perfect Gaussian white noise, time binning provides an improvement in precision of the order of $\sqrt{N}$, where N is the ratio of the final cadence to the initial cadence. Figure 4-58 shows the RMS of the detrended light curves for various cadences. The 10-min, 30-min, 1-hr, 2-hr, and 4-hr data are produced by binning the 2-min data and detrending the data by fitting a spline to the 6-hr data.

The RMS ratios show the noise characteristics at different timescales. The gain in photometric precision is higher going from 2-min to 4-hr in comparison to 2-min to 10-min. On the other hand, the noise falls faster going from 2-min to 10-min, in

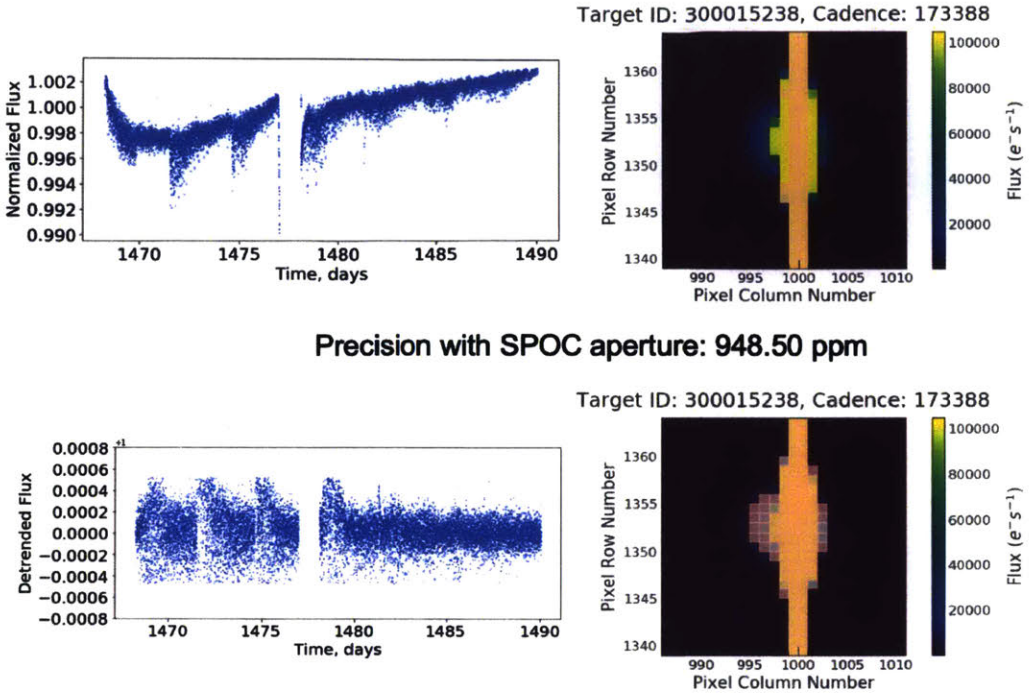

Figure 4-57: (Left) Example light curve before and after correction (before detrending). (Right) Aperture size before and after correction, plotted using lightkurve software.

comparison to 2-min to 4-hr. The intermediate ratios are also shown in Figure 4-59 and Table 4.5. We also present the ratio of ratios that indicates how close to the baseline the RMS ratio is. We observe the noise drops faster from 2-min to 10-min, followed by 30-min to 60-min, and 10-min to 30-min.

The the pointing error flattens out as we go to lower frequencies, as shown in Figure 4-60 that displays the power spectral density as function of frequency for sector 6 ACS data. In the next subsection we analyze the contributors to total error including pointing error from 60-min to 4-hour timescales.

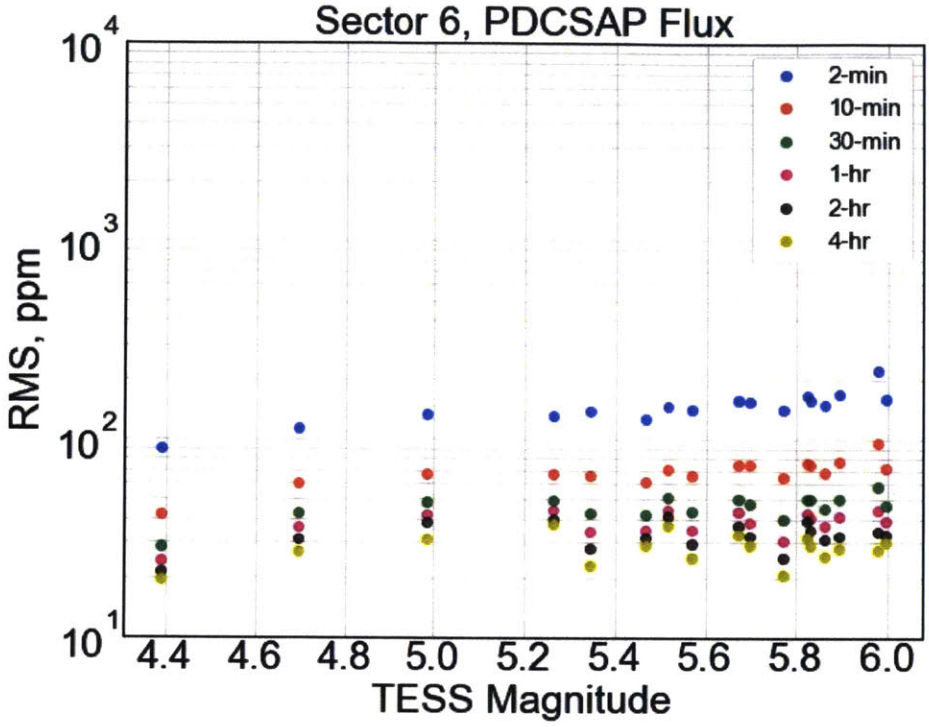

Figure 4-58: RMS calculated for detrended PDCSAP curves by binning 2-min to 10-min, 30-min, 1-hr, 2-hr and 4-hr light curves, and detrending by fitting a spline to the 6-hr light curve. The photometric precision improves with time binning, and appears to reduce after each time binning.

4.7 Results Summary

In this section, we presented the integrated systematics calibration framework for TESS. We first developed a high fidelity simulation of the TESS CCD detector and added all relevant noise sources. We then input flight jitter profiles to simulate jitter error. We estimated jitter error as a function of stellar brightness. We also established that jitter noise is linearly proportional to the jitter amplitude. We used this result to develop the flight data calibration framework.

We developed precision laboratory techniques to study detector properties such as absolute quantum efficiency, charge saturation and blooming that directly affect photometric precision. We characterized absolute quantum efficiency with an accu-

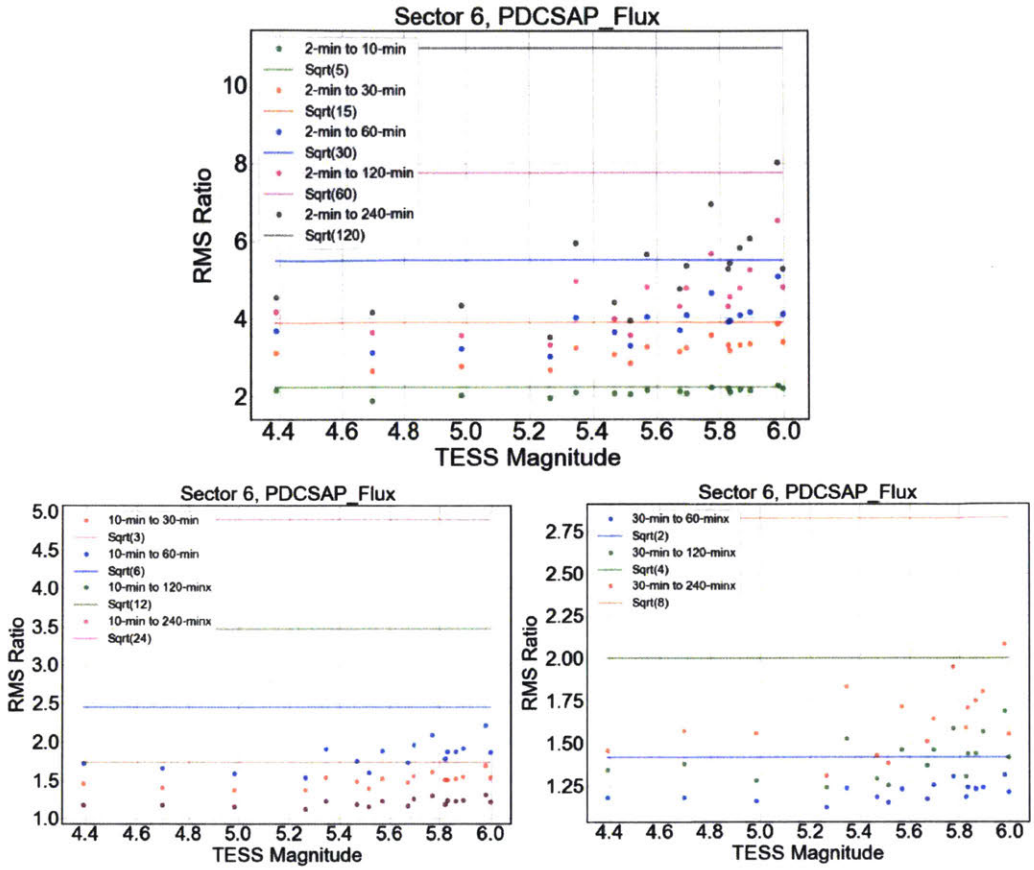

Figure 4-59: RMS ratios calculated for 2-min to 10-min, 2-min to 30-min, 2-min to 1-hr, 2-min to 2-hr, 2-min to 4-hr light curves. (Bottom Left) RMS ratios calculated for 10-min to 30-min, 10-min to 1-hr, 10-min to 2-hr, 10-min to 4-hr light curves. (Bottom right) RMS ratios calculated for 30-min to 1-hr, 30-min to 2-hr, 30-min to 4-hr light curves. The photometric precision improves slower than $\sqrt{N}$, as we see the points well below the $\sqrt{N}$ line for each set of ratios.

racy of less than 2%. Further, we concluded that huge changes in temperature of the order of what we see in Sector 4 can affect the detector response by over 5% at 1000 nm. We used results from this section to calculate photon noise in the flight data systematics calibration framework, and also used the results from QE variations with temperature to identify and analyze the effect of temperature change on photometric precision.

We developed a flight data analysis pipeline and performed an ensemble study to understand and characterize the systematics in TESS flight data. We developed a

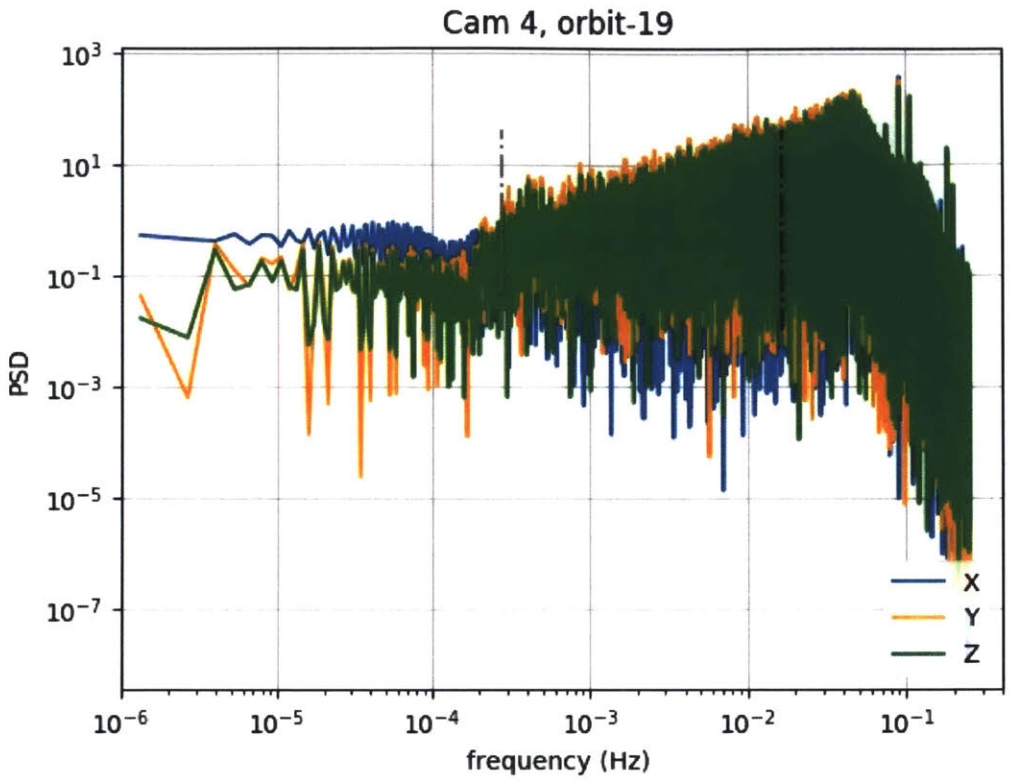

Figure 4-60: Power spectral density as a function of frequency shows pointing error flattens out at lower frequencies. [93]

model for jitter noise as a function of jitter amplitude. Then, we selected 17 of the quietest stars in sector 6, and estimated the contribution of jitter error. We discovered that there is a source of error in addition to jitter that we term "other error" that contributes significantly to the noise floor. Plausible sources for "other error" could be subpixel sensitivity variations, heater noise and electronics.

Next, we established the noise floor for TESS to be 30 ppm at 1-hour and 16 ppm at 4-hour timescales. We assessed the effect of huge temperature variations on photometric precision. We determined that a temperature change of 20 deg C would decrease the 1-hour photometric precision by 33 ppm.

Lastly, we assessed the outliers with RMS values over 200 ppm. We found two main causes for increased noise in these targets. First cause is stellar variability that can be removed using whitening techniques, demonstrated by SPOC [[92]]. The second

Timescale Ratio	RMS Ratio	Baseline $\sqrt{N}$	Ratio of RMS Ratio to Baseline
2-min to 10-min	2.11	2.23	0.94
2-min to 30-min	3.04	3.87	0.78
2-min to 60-min	3.75	5.47	0.68
2-min to 120-min	4.45	7.74	0.57
2-min to 240-min	5.01	10.95	0.45
10-min to 30-min	1.43	1.73	0.82
10-min to 60-min	1.77	2.44	0.72
10-min to 120-min	2.10	3.46	0.60
10-min to 240-min	2.36	4.89	0.48
30-min to 60-min	1.23	1.41	0.87
30-min to 120-min	1.46	2.0	0.73
30-min to 240-min	1.64	2.82	0.58

Table 4.5: RMS Ratios for various timescales derived by taking the ratio of mean RMS at the respective timescales. We also present the baseline $\sqrt{N}$ values that indicate the scenario where the noise is perfectly Gaussian. The third column shows the ratio of ratios and indicates how close to the baseline the RMS ratio is.

cause was insufficient pixels in the aperture for saturated stars. We demonstrated an improvement in precision of greater than 20% by using an aperture of optimal size.

As outlined in the framework, we used feedback mechanisms to maximize the utility of results from three key functional areas. We used the results from photometric precision assessment in developing models for systematics characterization and calibration, and assessing the noise floor. We used the results from both systematics calibration to inform flight data analysis steps, and the results from flight data analysis to assess the noise floor. We demonstrated improvement in bright star photometry using the framework. In Chapter 6, we demonstrate how the noise floor serves as a comparative metric for designing upcoming missions.

Chapter 5

ASTERIA: Framework and Results

In this chapter, we present the integrated systematics framework as applicable to ASTERIA, and evaluate the science capability of the mission. The author's work includes development of simulations for photometric precision assessment, generating an optimal systematics calibration and correction framework using both laboratory and flight data analysis techniques, and finally estimating the residual systematic error and noise floor for the ASTERIA science targets. We begin by providing a brief overview of the mission followed by instrument overview. Next, we explain the integrated systematics calibration framework for ASTERIA, and present the results in three steps: photometric precision assessment, systematics characterization and calibration, and performance validation and improvement. We establish feedback mechanisms to utilize results from each step at various other steps in the framework. Finally, we establish the noise floor for ASTERIA, and demonstrate how results from ASTERIA feed into future missions.

5.1 Mission Overview

The Arcsecond Space Telescope Enabling Research in Astrophysics (ASTERIA) is a 6U CubeSat that was launched in August 2017 and deployed from the International Space Station into a low-Earth orbit in November 2017 [15] [94]. The primary goal of ASTERIA was to demonstrate two key technologies: arcsecond-level pointing con-

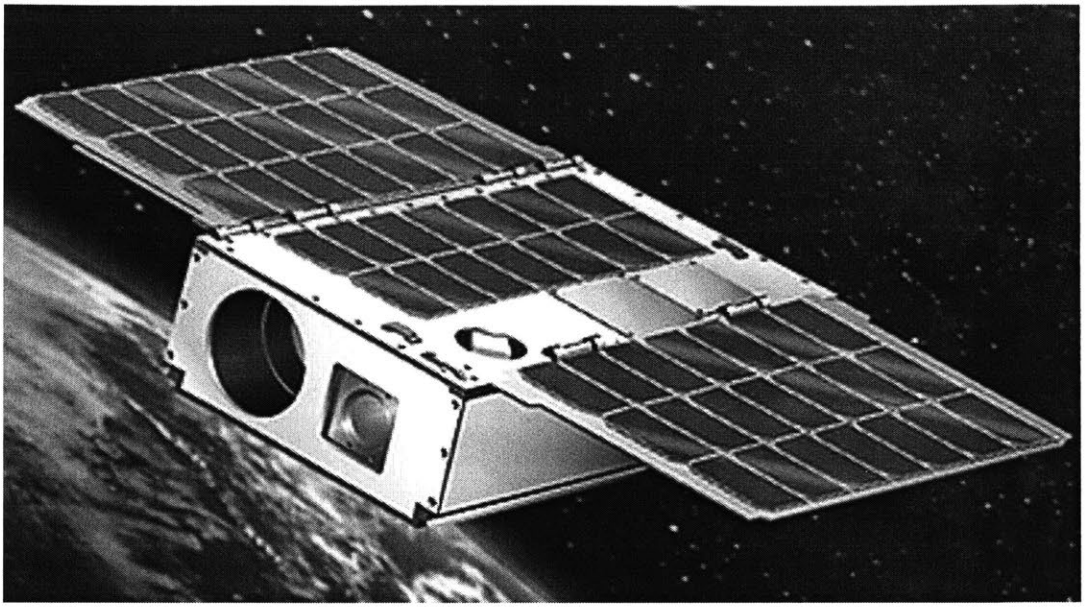

Figure 5-1: Artist rendering of the ASTERIA telescope. Image Credit: NASA/JPL

trol and highly stable temperature control, both of which are necessary to perform high precision photometric observations and detect transiting exoplanets. ASTERIA successfully demonstrated pointing stability of 0.5 arcsecond root mean square (RMS) and thermal stability of $\pm 0.01K$, both over 20-minutes [95] [96]. ASTERIA successfully detected the transit of known super-Earth 55 Cancri e [97].

ASTERIA operated successfully for two years before going silent in December 2019. During the extended mission, ASTERIA focused on high precision photometric observations for three science targets: 55 Cancri, HD219134 and Alpha Centauri. ASTERIA employs the scientific-grade complementary metal-oxide semiconductor (sCMOS) array detectors that are now becoming more widespread for science applications and are under active consideration for future JPL projects. However, due to ASTERIA's mission status as a technology demonstration, the team could not perform characterization of the detectors and validation of the photometric performance prior to launch. The present work outlines an optimal calibration framework for key science target observations and provides a framework to assess the photometric performance of ASTERIA. We also present in-flight calibration techniques and additional ground characterization tests of the camera assembly to characterize fixed

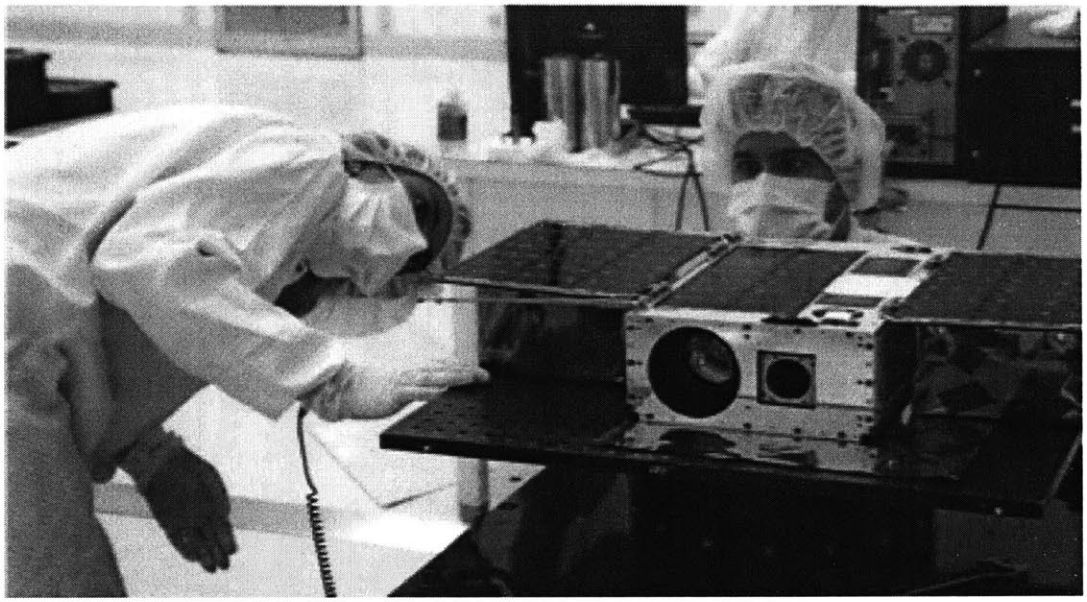

Figure 5-2: ASTERIA flight model with solar arrays in the deployed position. [98]

pattern noise and other systematic effects, such as jitter and thermal variations.

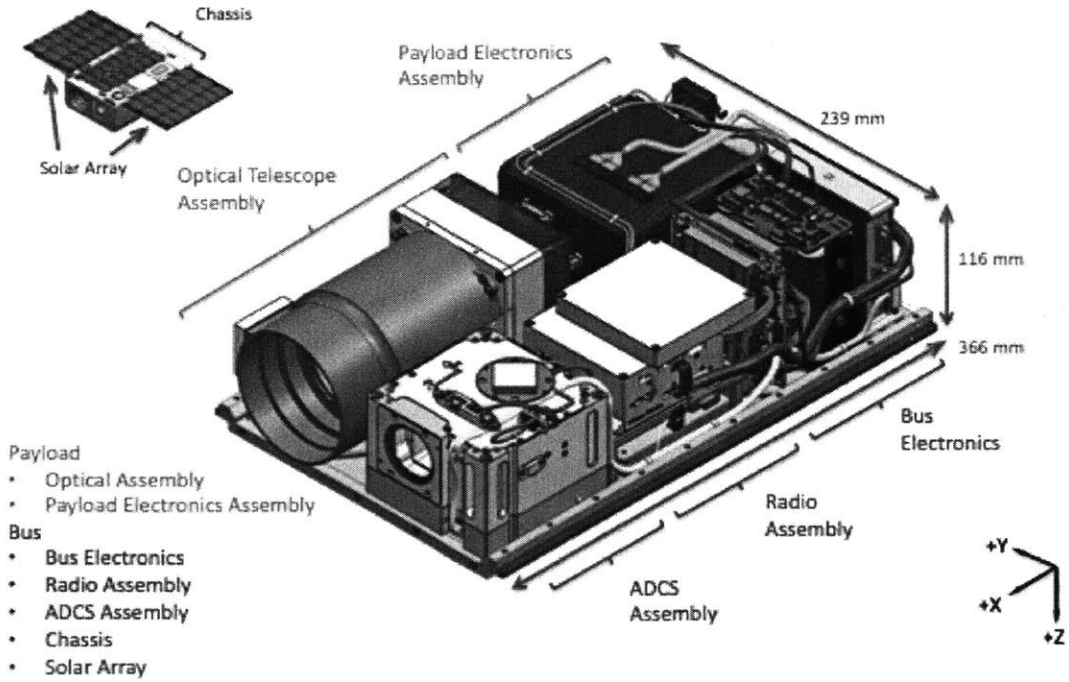

Figure 5-3: Internal view of the ASTERIA spacecraft. [96]

In addition, the results from the present work will inform error budgeting, and

verification and validation test campaigns for upcoming astrophysics missions such as SPARCS, a JPL CubeSat mission to demonstrate UV photometry, and provide guidelines for detector selection for future missions including the ASTERIA constellation, Large UV/Optical/Infrared Surveyor (LUVOIR), and Habitable Exoplanet Imager (HabEx).

Traditionally, CCD detectors have been used for high precision photometry applications. ASTERIA is the first space-based high precision transiting photometry mission to use scientific-grade CMOS detectors. In addition to providing proof of concept and performance validation for CMOS detectors in the context of precision astrophysics applications, the present work develops best practices for data reduction and calibration. Due to the lack of typical pre-launch ground calibration measurements, such as read noise (spurious electrons introduced during the analog-to-digital conversion (ADC) process), bias frames (that corrects for offsets and gain variations due to the ADC converters and amplifiers), dark frames (to remove the effect of thermal electrons generated at a given temperature in the absence of exposure to light) and flat frames (that calibrate pixel-to-pixel detector response variations using uniform illumination), we develop a combination of ground-based and in-flight calibration techniques to calibrate the noise sources.

The ability of a space-based telescope to detect a transiting exoplanet around a given science target is measured using photometric performance. Photometric performance is driven by various noise sources. For bright stars, one of the dominant sources is the instrument systematic noise which includes fixed pattern noise from the CMOS detector, and effects of temperature variations and spacecraft jitter. Fixed pattern noise is the noise due to the non-uniformity in response from one pixel to another. Spacecraft jitter primarily causes target centroid movement on the detector that leads to different measured intensity of the target due to the presence of inter-pixel and intra-pixel response variations of the detector. Temperature variations affect the flux throughput because quantum efficiency varies with temperature. In some cases, temperature variations can also lead to distortion of the PSF, causing centroid movement. In this chapter, we address these noise sources and their impact

on photometric precision.

In the following section, we present an overview of the instrument and detector, and describe the relevant systematic noise sources using the measurement signal pipeline. Then, we describe results from high-fidelity simulation, post-launch laboratory characterization and flight data analysis. We present in-flight calibration techniques to remove bias, dark noise and fixed pattern noise in the data in addition to obtaining flat frames to remedy the effects of pixel-to-pixel response variations. We present results from flight data reduction for HD219134 and Alpha Centauri, followed by jitter analysis to compare performance in different ACS modes. Lastly, we present an optimal systematics calibration framework for future high precision CMOS applications.

5.1.1 Instrument Overview

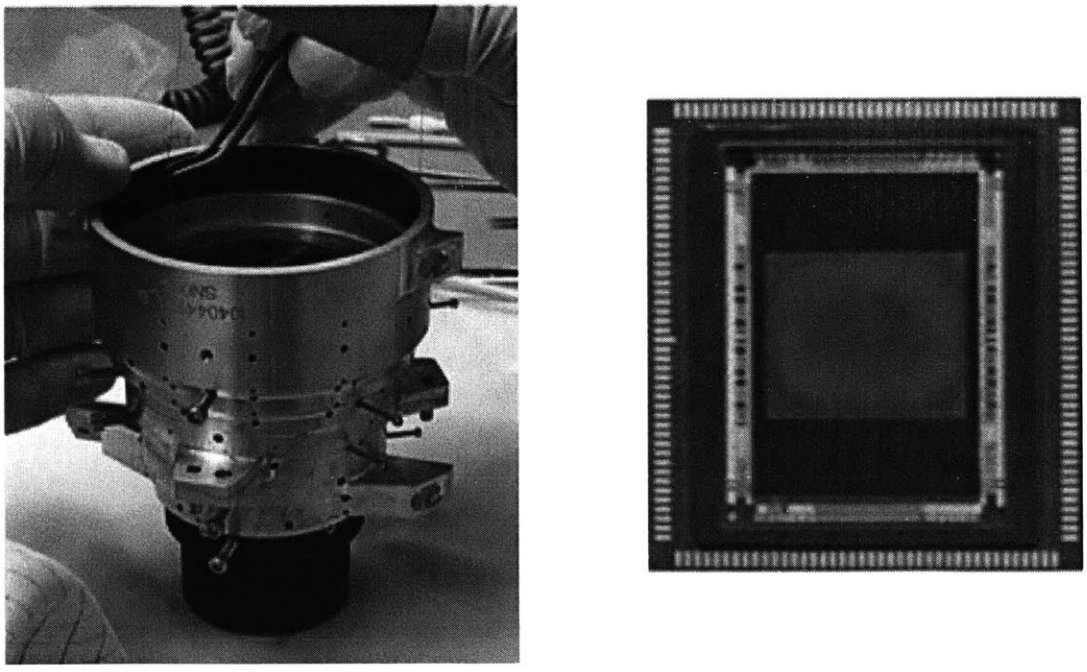

Figure 5-4: (Left) Image of the flight lens assembly. Image Credit: M. Smith (Right) Image of the Fairchild CIS2521F monochromatic CMOS sensor. [99]

The schematic of the ASTERIA optical telescope assembly along with the payload electronics, and spacecraft bus is shown in Figure 5-3 [96][95]. The payload consists

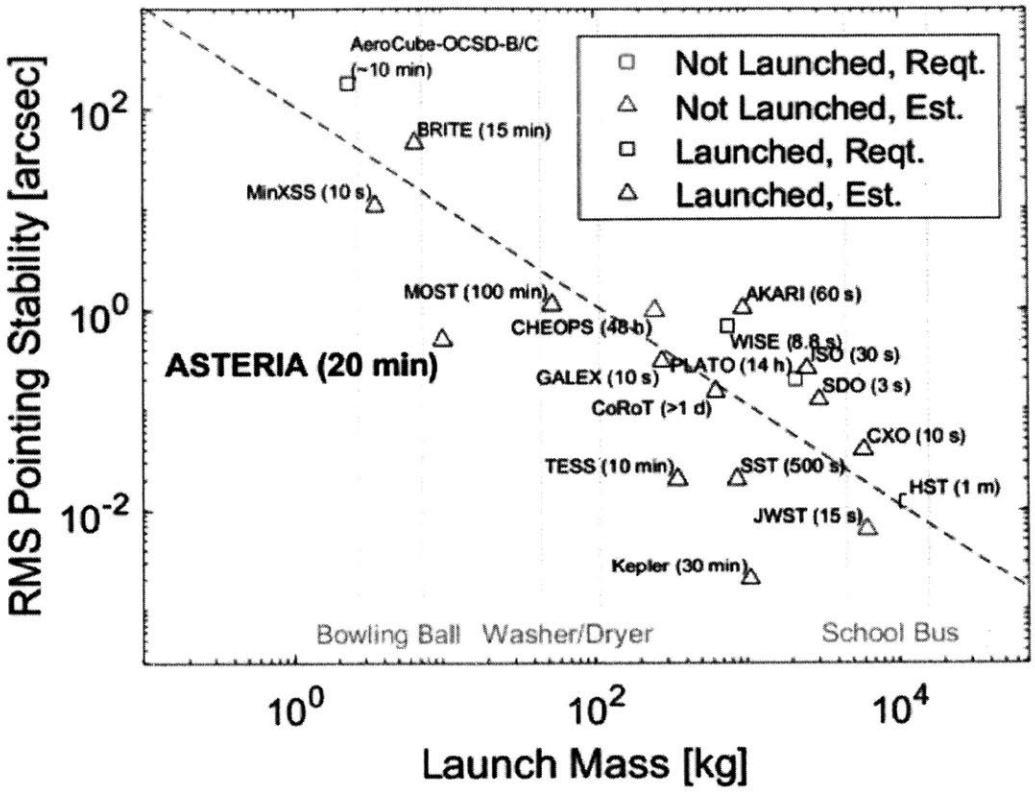

Figure 5-5: Pointing stability versus mass for various missions. [95]

of the optical telescope assembly and associated electronics. The optical telescope consists of a refractive optic (f/1.4), and a CMOS imager mounted to the piezoelectric stage. The piezo-stage is located in between the lens assembly and the focal plane. The attitude control system (ACS) is an integrated unit containing three reaction wheels, a star tracker, and torque coils that help desaturate the wheels.

The field of view is several degrees wide so that sufficient guide stars are available for fine pointing control. Fine pointing control is performed using a closed loop control system by measuring the centroids of guide stars on the detector and actuating the piezo-stage that translates the detector in the x-y direction. ASTERIA's 0.5 arcsecond RMS pointing stability is better than the pointing performance of any other spacecraft in the same mass and size category, as shown in Figure 5-5. The plate scale is 15"/pixel and 0.5" is approximately $1_{\overline{30}}^{th}$ of pixel width. The fine pointing feedback control

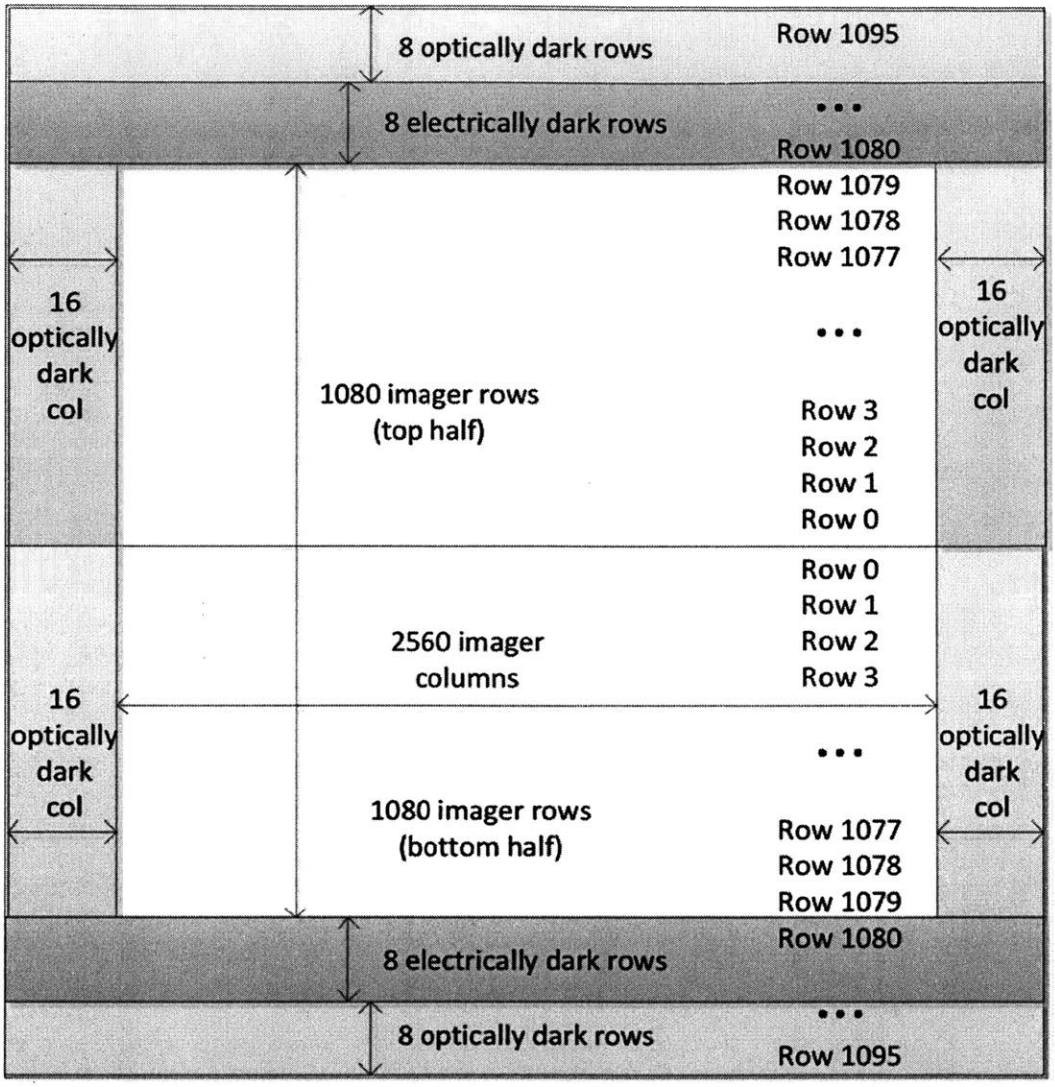

Figure 5-6: Detector layout showing the electrically and optically dark rows and columns. [99]

loop requires a high readout rate of 20 Hz which was the driving factor for choosing a CMOS rather than a CCD detector at the time.

The thermal control system uses a closed loop system that raises the temperature of the focal plane using resistive heaters and holds the set temperature to within 5 milliKelvin over a 20-minute period. The baffle, optics, focal plane, piezo-stage and readout electronics are all thermally isolated from the heaters.

The detector is a Fairchild 5.5 megapixel CIS2521F CMOS imager with 2560 x 2160 pixels and pixel size of 6.5 μm x 6.5 μm shown in Figure 5-4. The detector

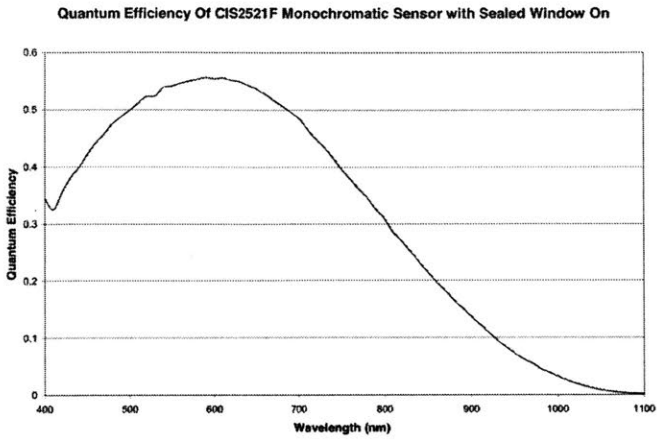

Figure 5-7: Monochromatic quantum efficiency measured at increments of 10 nm taken with the sealed window on the CMOS detector. [99]

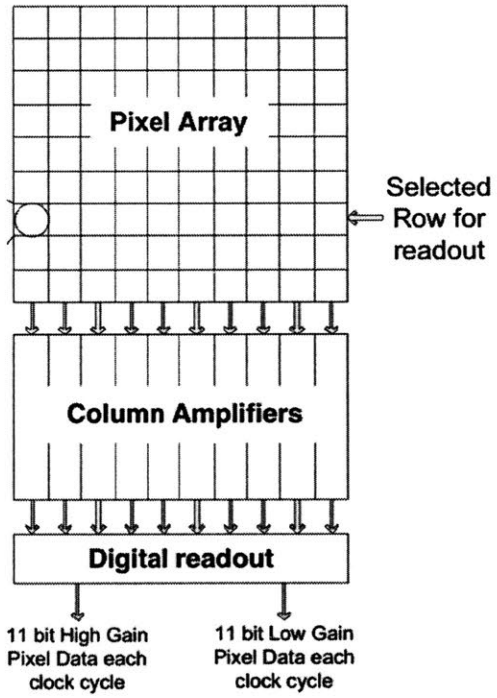

Figure 5-8: Column readout architecture for the CIS2521F CMOS detector. [99]

enables ultra-low-light imaging with $< 2.0\ e^-$ read noise and low dark current of < 36 e^-/pixel/second while operating at 20° Celsius which enables optimal science operation without deep cooling. It has high sensitivity through visible and near-infrared wavelengths. Figure 5-7 shows the monochromatic quantum efficiency measured at

increments of 10 nm taken with the sealed window on the detector [99].

The detector has two halves. There are eight electrically dark rows (bias rows) and eight optically dark rows on the top and bottom that correspond to the top and bottom halves of the detector. In addition, there are 16 optically dark columns on the left and right edges of the detector as shown in Figure 5-6. The optically dark rows are covered with metal so that light cannot enter, while electrically dark rows have their transistor gate tied to ground in addition to being covered with metal. The electrically dark rows are both optically and electrically dark, i.e. any dark current is also removed via a charge dump. We discuss calibration techniques using the bias and dark rows in Section 5.4.1.

Each half of the CIS2521F detector has pixels, column amplifiers and digital readouts. Using an amplifier and ADC (analog-to-digital converter) structure in each column minimizes the read noise and maximizes the dynamic range of the sensor. Each pixel has five transistors, and an anti-blooming protection gate. The fixed pattern noise seen as vertical stripes in Figure 5-9 are due to gain variations caused by each pixel amplifier and column amplifier, and offset from the ADC converter at every column.

The CMOS imager is customized to read out subarrays of the full frame shown in Figure 5-9 [97]. 24 images are collected per orbit and an average of 25-60 orbits comprise every science observation. In precision pointing control mode, eight 64x64 pixel windows are read out as shown in Figure 5-10. For example, if window 1 is a target star, window 8 will be the corresponding window containing bias and dark rows. We refer to this window as the calibration window or edge window. The rest of the windows such as 7, 4, 5 and 3 will be guide stars. Each image has 1200 frames that were taken at an integration time of 50 ms and coadded. This 1-minute coadded raw image is downlinked to the ground. The process of coadding increases the signal-to-noise ratio (SNR) without saturating the detector. Due to this reason, ASTERIA is one of the few space telescopes that can observe the very bright Alpha Centauri without saturating.

ASTERIA's orbit is nearly circular with an altitude of 400 km and at 51.6 degrees

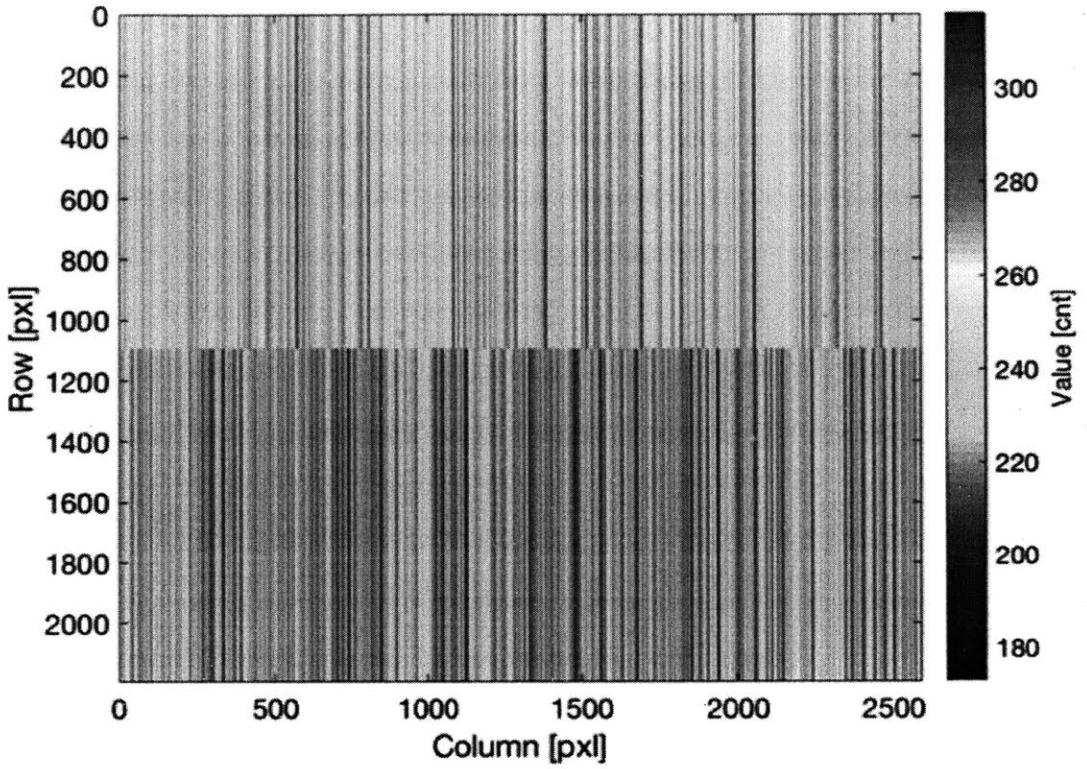

Figure 5-9: Example fullframe image taken using the CIS2521F CMOS sensor. [95]

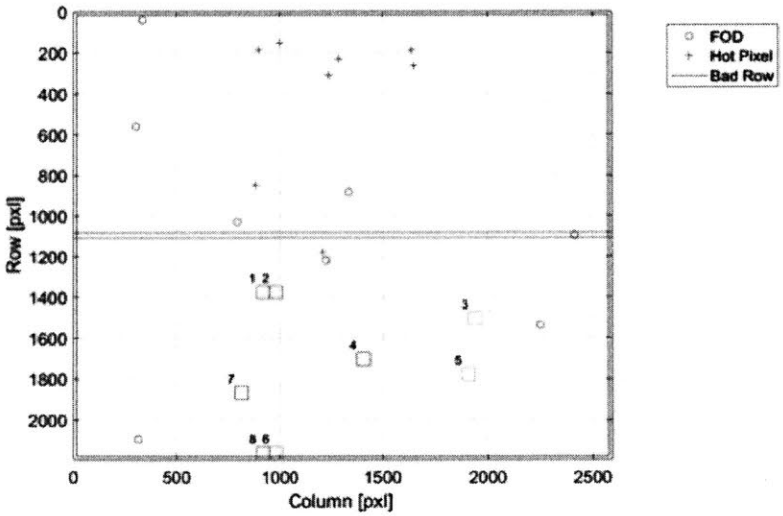

Figure 5-10: Image showing eight 64x64 pixel windows that are read out in precision pointing control mode. [97]

Parameter	Value
Aperture size	60.7 mm
Band-pass	0.4 μm (500-900 nm)
Field of view	11.2 x 9.6 deg Lens transmission efficiency
0.8	
Imaging array size	2592 x 2192
Pixel size	6.5 x 6.5 sq. μm
Plate scale	15.8 arcsec/pix
Mean quantum efficiency	0.42
Gain	6.4 e^-/ADU
PRNU	$<$ 3% RMS
Full well capacity	$>$30,000 e^-
Dark current	$<$35 e^-/pix/s
Read noise	$<$ 2 e^- 30 fps

Table 5.1: Instrument Characteristics.

to the Earth's equation. The duration of an Earth eclipse varies throughout the year, and is an average of 30 minutes out a 90-minute orbit. The camera is power-cycled and reinitiated at the beginning of each orbit, and at the end of the orbit, in to reduce the sync loss between the camera FPGA and flight computer. The limiting factor on the duration of observations is the size of image memory buffer that can hold up to 24-minutes of 1-min coadded images.

The attitude control system (ACS) on ASTERIA is the Blue Canyon Technologies' fleXible Attitude Control Technology (XACT). ASTERIA's ACS system 'XACT' is a fully integrated system with both hardware and software necessary to control ASTERIA's attitude. The system has four sensors including a star tracker, inertial measurement unit (IMU), sun sensor, and magnetometer, and actuators including three reaction wheels for attitude control and three torque rods for momentum dumping. The fine pointing system consists of a Physik Instrumente's two-axis high-precision piezoelectric nanopositioner, P-733K110. The piezoelectric stage is mounted behind the focal plane assembly to provide a tip/tilt correction. The target star is stabilized to within a fraction of a pixel by translating the camera assembly in directions orthogonal to the payload boresight.

5.2 Integrated Systematics Calibration Framework

Figure 5-11 presents the integrated framework as applied to ASTERIA. We use a variety of techniques to characterize and calibrate the ASTERIA instrument systematic noise sources. We establish feedback mechanisms to utilize results from each step at various other steps in the framework.

First, we simulate the noise sources, and the effect of jitter noise and sub-pixel variations to estimate the photometric performance using a high-fidelity model of the CMOS detector. Then, we present precision laboratory techniques developed to characterize various sources of noise including dark current noise, read noise, pixel response non-uniformity (PRNU), and fixed pattern noise. Next, we develop a data reduction framework using simulated stellar images in the laboratory. We then perform flight data analysis to analyze systematics in the ASTERIA data such as fixed pattern noise, spacecraft jitter and temperature variations. Lastly, we present an optimal systematic calibration framework to correct for each of these noise sources, improve photometric precision and establish a noise floor.

5.3 Photometric Performance Assessment

We develop a framework to evaluate the photometric precision using Python as shown in the leftmost block in the framework. First, we simulate a high-fidelity CMOS detector model with dominant noise sources such as pixel response nonuniformity (PRNU) and intrapixel sensitivity variations. The CMOS detector has an additional noise source called the fixed pattern noise due to column dependent gain and offset variations, that we add to the simulator. Next, we add realistic jitter profiles to simulate flight-like systematic noise. We perform aperture photometry to generate light curves which are used to assess the photometric precision. We simulate a time-series of stellar images for varying levels of jitter. Lastly, we use flight data from commissioning and nominal science operations to validate the estimates of photometric precision from this simulation.

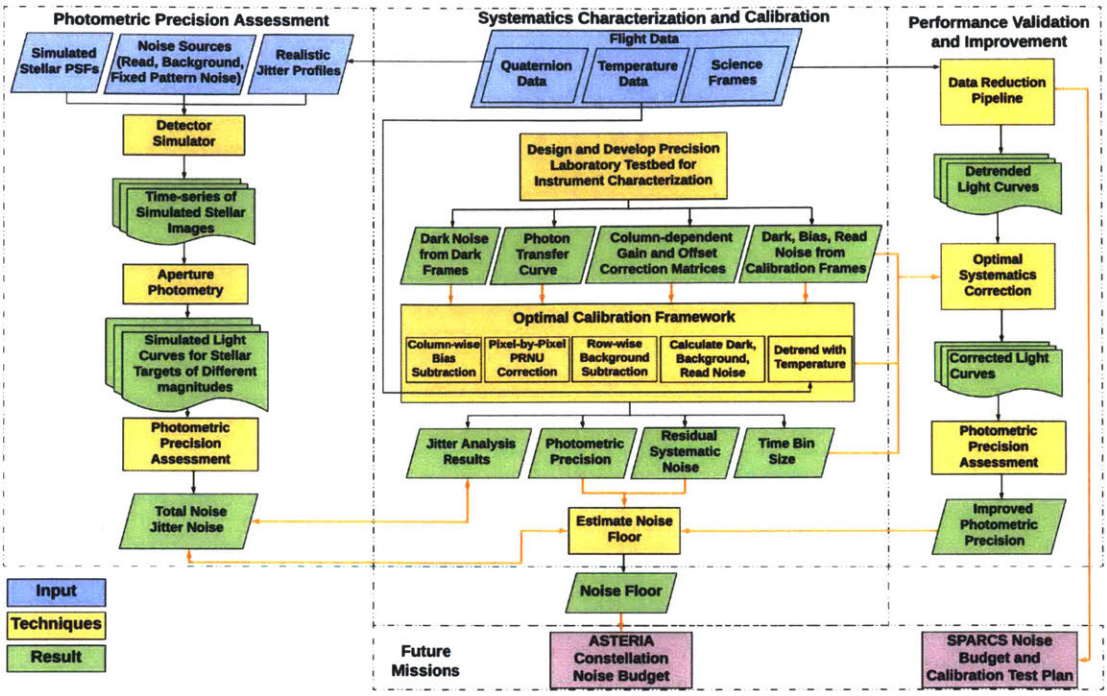

Figure 5-11: Noise characterization framework for ASTERIA showing the steps involved in evaluating the photometric performance of the ASTERIA mission. The four key steps are modeling and simulation, laboratory techniques, in-flight calibration, and optimal systematics correction for performance improvement.

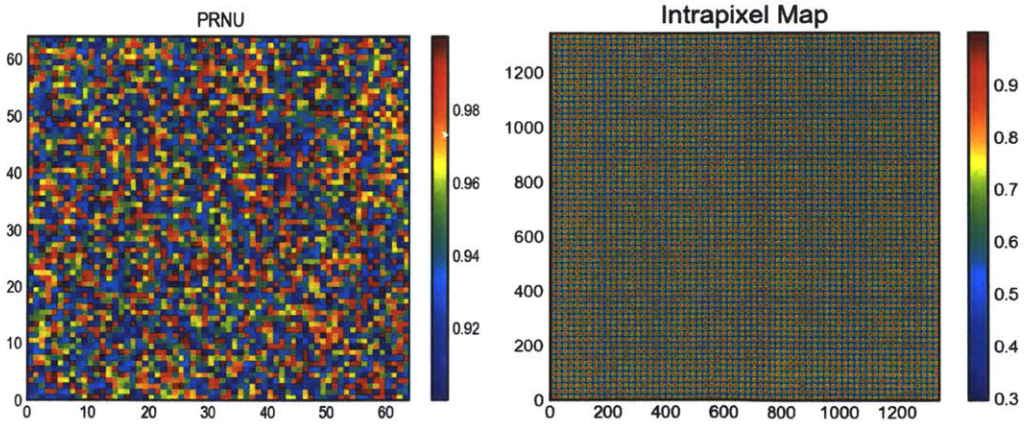

Figure 5-12: (Left) Simulation of the detector showing an 64x64 pixel area with pixel-to-pixel QE variation or PRNU of 1%. (Right) Intrapixel response simulation with 20 subpixels per pixel, and 100% light intensity at the center and 30% at the corner of each pixel.

We develop a detector simulator showing a region of interest with 64 x 64 pixels, which is the same size as the ASTERIA postage stamp images. We assume pixel response non-uniformity or pixel-to-pixel quantum efficiency variation to be 1% based on the Fairchild Imaging CIS2521F CMOS detector data sheet. In every iteration, we generate the quantum efficiency of each pixel as a normal random variable. Then, we simulate intrapixel variations with a resolution of 20 x 20 subpixels per pixel using a Gaussian model for simplicity. Figure 5-12 shows an 8 x 8 pixel map with 100% charge intensity at the center and 30% at the edges. The Gaussian distribution is given by the Equation 5.1. We then add dark current, sky noise and read noise contributions.

$$s(x,y) = exp(-\frac{(x-x_0)^2 + (y-y_0)^2}{2\sigma^2}) \tag{5.1}$$

5.3.1 Simulated PSFs

We compute the photometric error at each time step by taking the dot product of the stellar image and the non-uniform intrapixel sensitivity map. We bin the resulting image that is produced at the higher pixelated resolution to obtain the original resolution of 64 x 64 pixels as shown in Figure 5-13.

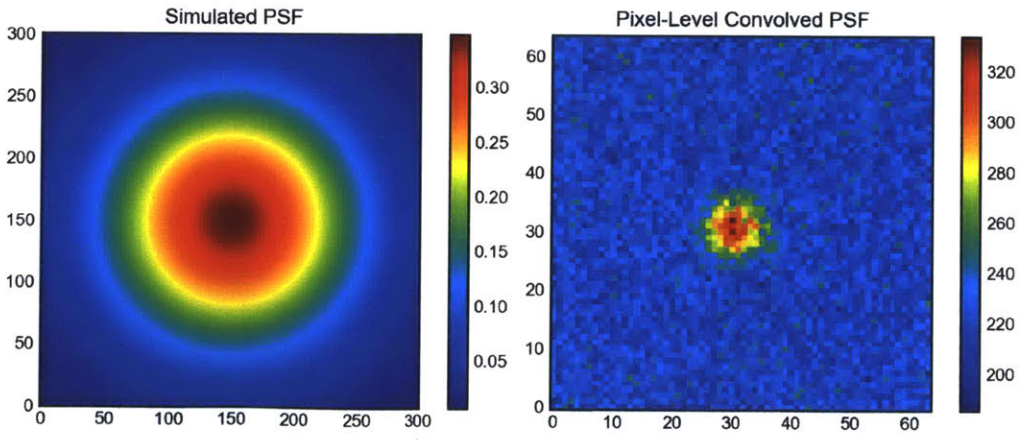

Figure 5-13: (Left) Simulated stellar PSF in a 15x15 pixel area with subpixel resolution. (Right) Resulting image after taking the dot product of the simulated stellar image with the detector simulator. The integtation time is 50 ms and the input light intensity is 11,408 e^- corresponding to the brightness of HD219134.

We add column dependent gain variations by calculating an offset that varies based on the input light intensity of the target star. The vertical striped pattern seen in Figure 5-14 is due to the column gain and offsets. These gain and offsets are due to the amplifiers and ADC converters at each column.

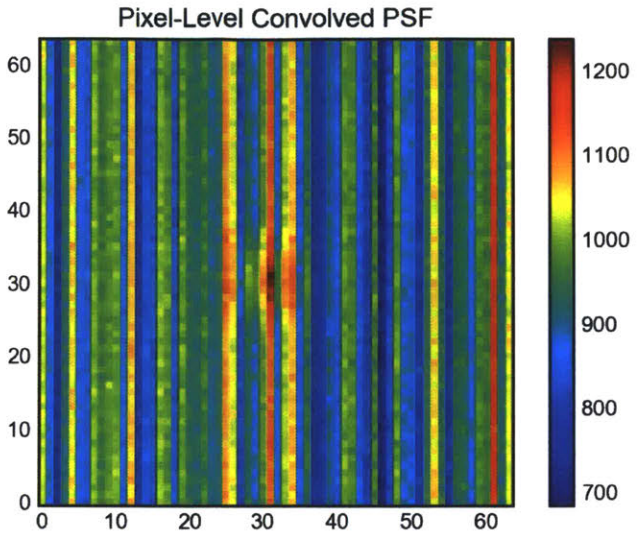

Figure 5-14: Simulated stellar image with column dependent gain variations.

We are now set up to add spacecraft jitter to the simulator and estimate the effect of jitter noise on photometric precision.

5.3.2 Realistic Jitter Profiles

We add flight-like jitter profiles shown in Figure 5-15 taken over several orbits with a sampling frequency of 100 Hz to offset the centroid of the PSF in subpixel steps. We generate a time-series of stellar images that we use to evaluate the jitter noise contribution and photometric precision.

5.3.3 Light Curve Generation

In order to generate a time series of corrected flux shown in Figure 5-16, we first take a series of images that are offset by the centroid displacement calculated from the

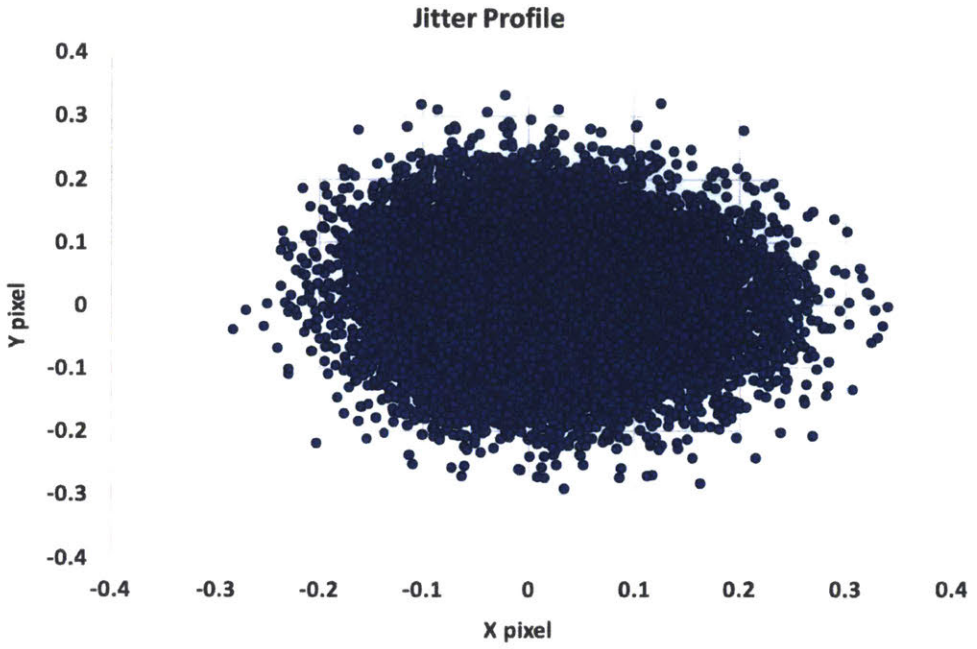

Figure 5-15: Jitter profile from ASTERIA flight data (so48 observations), showing one of the quaternions, over one-hour timescale at a sampling frequency of 100 Hz. The x-axis and y-axis show pixel offset relative to the center of the pixel. The jitter offsets the centroid of the stellar image. Aperture photometry is performed on the images to then evaluate photometric precision.

quaternion data. We then remove the contributions of the column dependent gain variations by calculating the median charge value for each column and subtracting that from the each pixel in that column. Next, we remove background noise by summing pixels in the neighborhood of the target star that are devoid of light from the star, and subtracting the average of this charge from each pixel. We place an aperture mask on the pixels occupied by the star, and plot the variation of the total charge in those pixels over time. We optimize the aperture size by iterating until we have maximized the signal-to-noise ratio.

5.3.4 Estimated Photometric Performance

We estimate the contributions of photon noise and jitter noise to the photometric performance of ASTERIA. Figure 5-17 shows the 1-min photometric precision as a

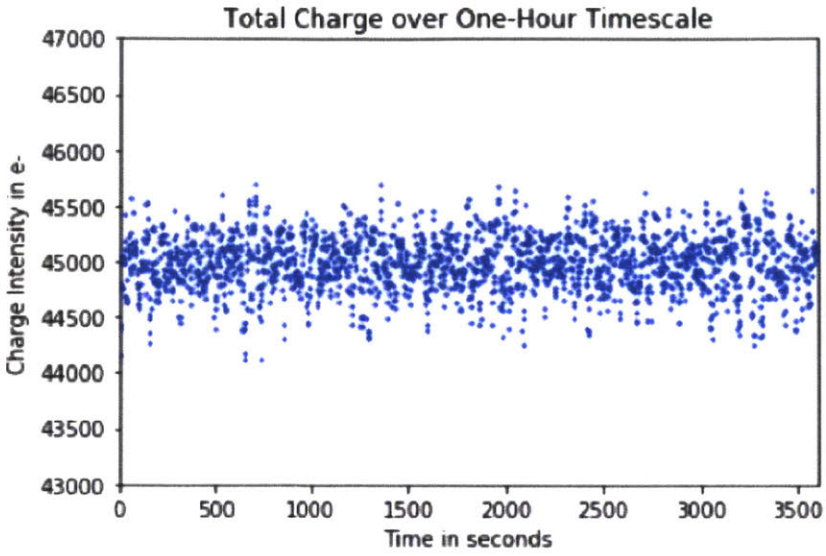

Figure 5-16: Example light curve generated by the simulation.

function of stellar magnitude.

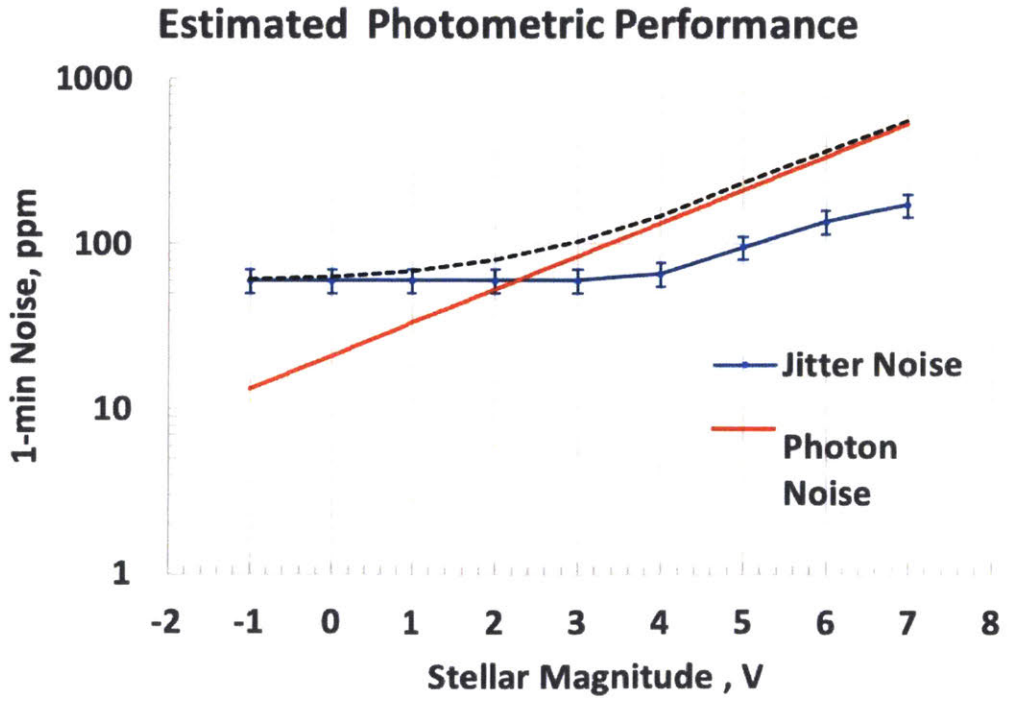

Figure 5-17: Predicted photometric performance for ASTERIA. The plot shows contributions of photon noise and jitter noise to total noise at 1-min.

5.4 Systematics Characterization and Calibration

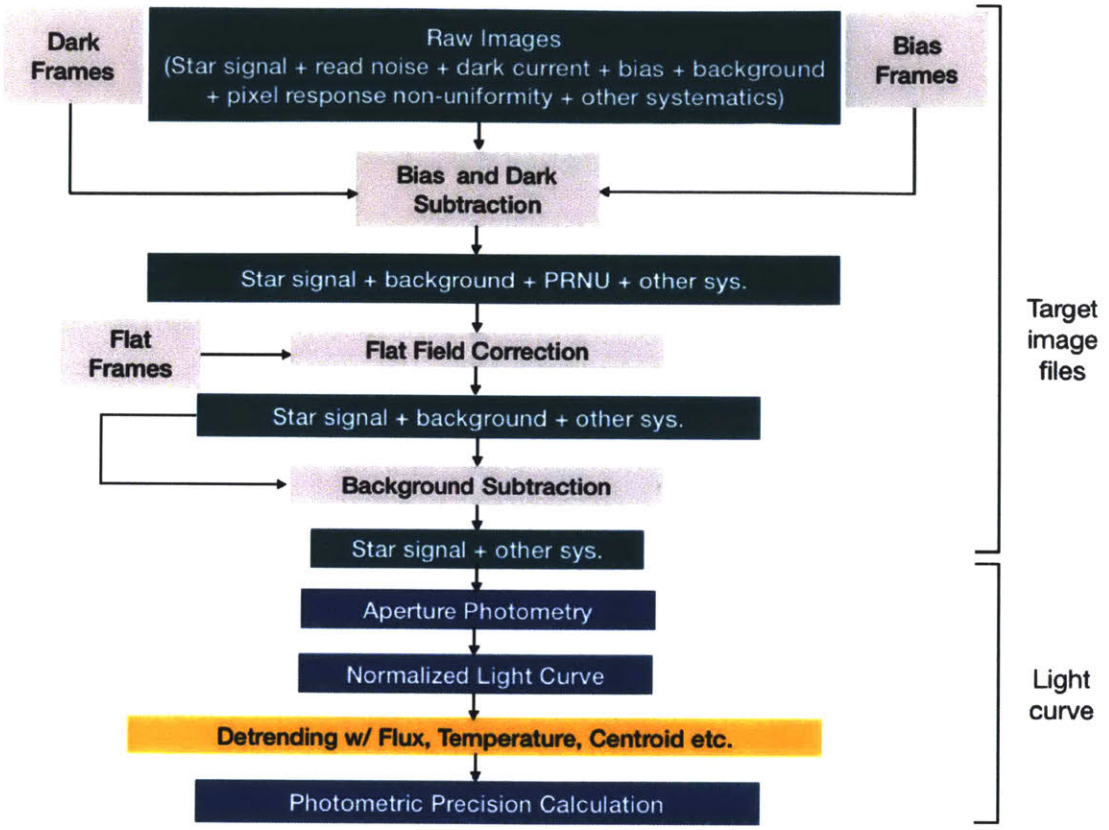

Figure 5-18: Data analysis pipeline for ASTERIA showing bias, dark and flat field corrections, and detrending steps to remove flux and temperature variations.

In this section, we develop laboratory techniques to characterize noise sources specific to the ASTERIA CMOS detector, and develop a flight data analysis and calibration framework. We use the results from this section to develop an optimal systematic correction algorithm with a goal to improve the photometric performance of ASTERIA.

We begin with a baseline data reduction pipeline based on prior knowledge of data analysis techniques used for CCDs, as shown in Figure 5-18. The raw image consists of the star signal along with noise sources such as read noise, dark current, bias, background or sky noise, and pixel response non-uniformity. In addition, there are systematic effects due to thermal variations, and spacecraft jitter.

The data analysis pipeline takes bias frames, dark frames and flat frames as inputs, and outputs bias-subtracted, dark-subtracted and flat-corrected frames which we obtain by subtracting a median bias and median dark frame, followed by dividing with a normalized median dark-subtracted flat frame. Further, we perform background subtraction by taking an annulus around the target star or by choosing a set of pixels away from the target star that are devoid of bright stars. After correcting the raw image, we perform simple aperture photometry by placing a circular aperture mask on the target star and integrating the charge inside the mask. We optimize the size of the mask by increasing the mask radius until the improvement in signal is overcome by the increase in background noise. The next step in the pipeline is to assess the effects of various parameters and detrend with respect to centroid locations and temperature variations in time. We implement temperature detrending by dividing the data set into separate orbits and running the detrending algorithm for each orbit rather than for the entire data set. The root mean square (rms) of the normalized ASTERIA light curve gives the 1-min photometric precision in ppm.

While this pipeline addresses noise sources common to both CCD and CMOS detectors, it does not address noise sources such as fixed pattern noise that are more dominant in CMOS detectors. In Section 5.4.1, we develop methods to characterize such noise sources and correct for them.

5.4.1 Laboratory Testing and Characterization

In order to study characterize noise sources from the ASTERIA CMOS detector, we perform ground characterization with a flight-like camera assembly and flight software. Typically, extensive instrument calibration tests are performed for larger space telescopes prior to launch. Due to ASTERIA's status as a technology demonstration mission, no detector calibration tests were performed prior to launch. Hence, we do not have bias, dark and flat frames that are required as inputs to the data analysis pipeline described above. Here, we present laboratory techniques to take the required calibration data using a flight-like detector and camera assembly in the laboratory. Using the laboratory data, we develop an optimal data calibration framework. Fur-

ther, using this framework, we propose in-flight calibration tests that are performed by the ASTERIA operations team. Then, we use data from in-flight calibration to perform flight data reduction.

Synthetic Stellar Images

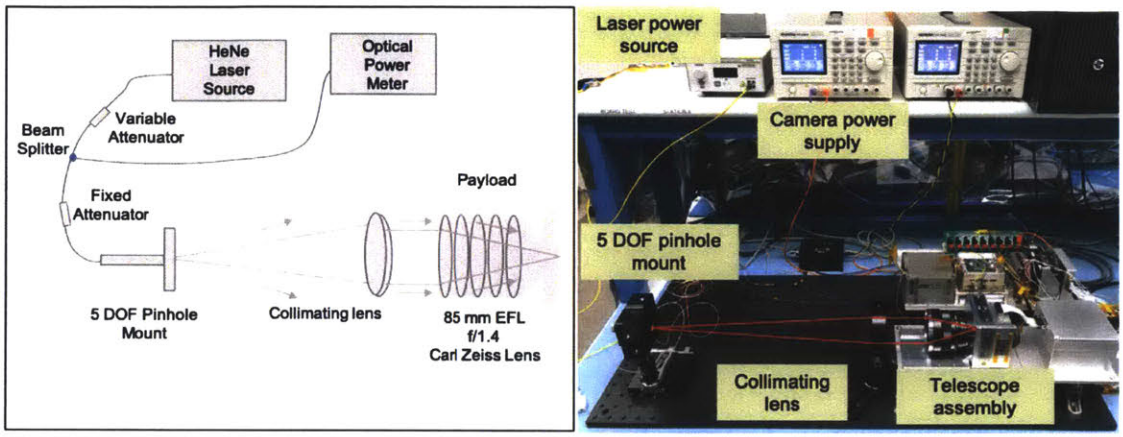

Figure 5-19: (Left) Schematic of the ground characterization testbed. (Right) Picture of the ground characterization testbed showing the laser power source, camera power supply, 5 degree-of-freedom (DOF) pinhole mount holding the fiber optic cable, the collimating lens and telescope assembly.

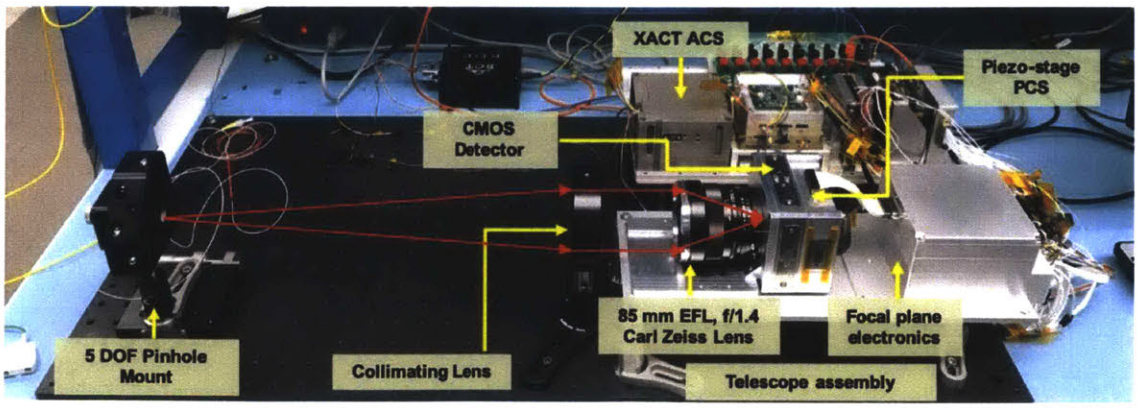

Figure 5-20: Ground characterization testbed showing the 5 degree-of-freedom (DOF) pinhole mount holding the fiber optic cable and connected to the laser source, the collimating lens, an 85 mm f/1.4 Carl Zeiss lens, focal palne detector and electronics, the piezo-stage pointing control system and the XACT attitude control system.

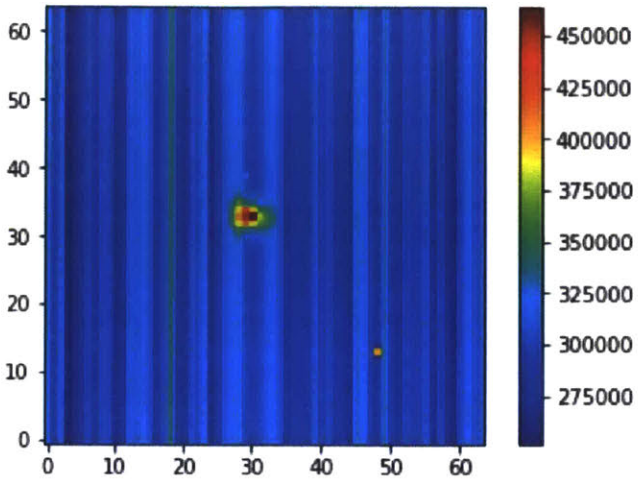

Figure 5-21: Example raw image of the simulated star (approximately V = 6.0) taken using the laboratory testbed consisting of the light source and flight-like telescope assembly.

First, we set up a synthetic star source using a Helium-Neon (HeNe) laser source at 660 nm. The output is connected to a fiber optic cable. Figure 5-19 shows the schematic of the laboratory setup and Figure 5-20 shows a picture of the setup. We use an optical power meter to measure the input power, and two attenuators to control the input light intensity. The first attenuator controls the light intensity before entering the optical power meter and the other controls the light intensity in between the laser source and the pinhole mount. Careful adjustment of the light source is necessary to maintain brightness approximately equivalent to the apparent brightness of a V=6.0 star that is close to HD219134, one of our science targets. The collimating lens assembly collimates the light on to the detector within the ASTERIA flight-like camera assembly. The setup with the collimating lens and camera assembly was previously setup by the ASTERIA team at JPL to perform software tests.

We start by taking full frame images of 50 ms integration time to calibrate the brightness of the synthetic star. We step through various levels of brightness using the two attenuators to arrive at the desired brightness. Then, we create a sequence similar to the sequence used during science operations, and take windowed images with 64 x 64 pixels that include both the target star and calibration frames. Each of

these frames has an integration time of 50 ms. 1200 frames are coadded to produce a single raw image. We repeat the same experiment for multiple simulated orbits, with each orbit generating 24 images, and at two different locations on the detector. We collected the synthetic stellar windowed images using a sequence that ran overnight for about 20 hours at each detector location. Figure 5-21 shows an example of a 1-minute coadded raw image.

Dark Frames

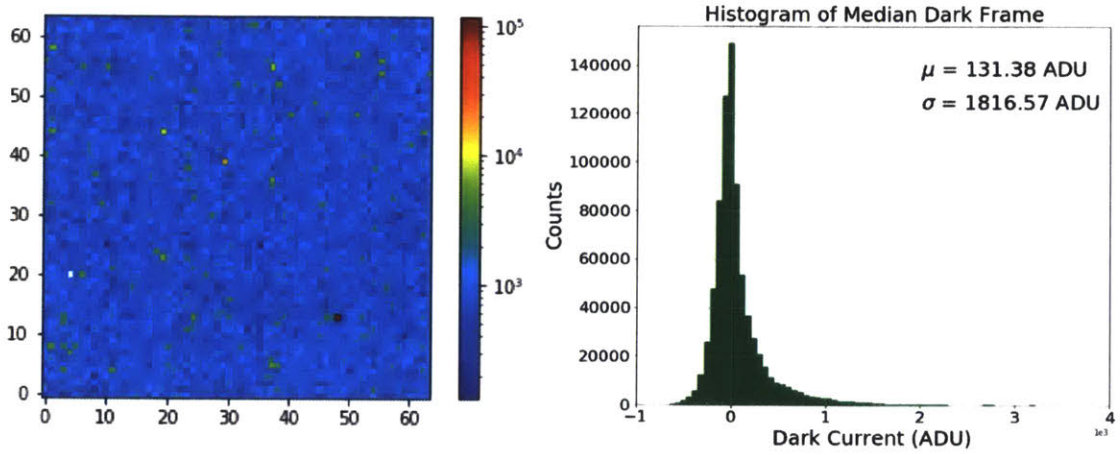

Figure 5-22: (Left) Example dark frame taken by place a shutter in front of the lens to block off light exposure. (Right) Histogram of median dark frame showing mean dark current and dark current non-uniformity in ADU/pix/min.

We take 200 windowed dark frames by placing a shutter on the Carl Zeiss Lens to block off any light exposure to the detector. Each frame has an integration time of 50 ms, and 1200 such frames are coadded by the flight software to generate a 1-minute raw image, as shown in Figure 5-22. The histogram shows the distribution of photons in the median dark frame. The mean flux gives the mean dark current in ADU/pix/min which can be converted to e^-/pix/s using the gain conversion factor of 6.4 e^-/ADU. The standard deviation gives dark current non-uniformity. The mean dark current and dark current non-uniformity are both within the maximum limit listed in the datasheet.

Noise Source	Measured Value ADU/pix/min	Measured Value e^-/pix/s
Dark current (from dark frame)	131.38	14.01
Dark current (from edge window)	177.53	18.94
Bias (from edge window)	6.03	0.32
Read (from edge window)	10.05	1.07

Table 5.2: The table shows measured values for dark current using the dark frame and calibration frames, and bias and read noise values from calibration frames.

Calibration Windows

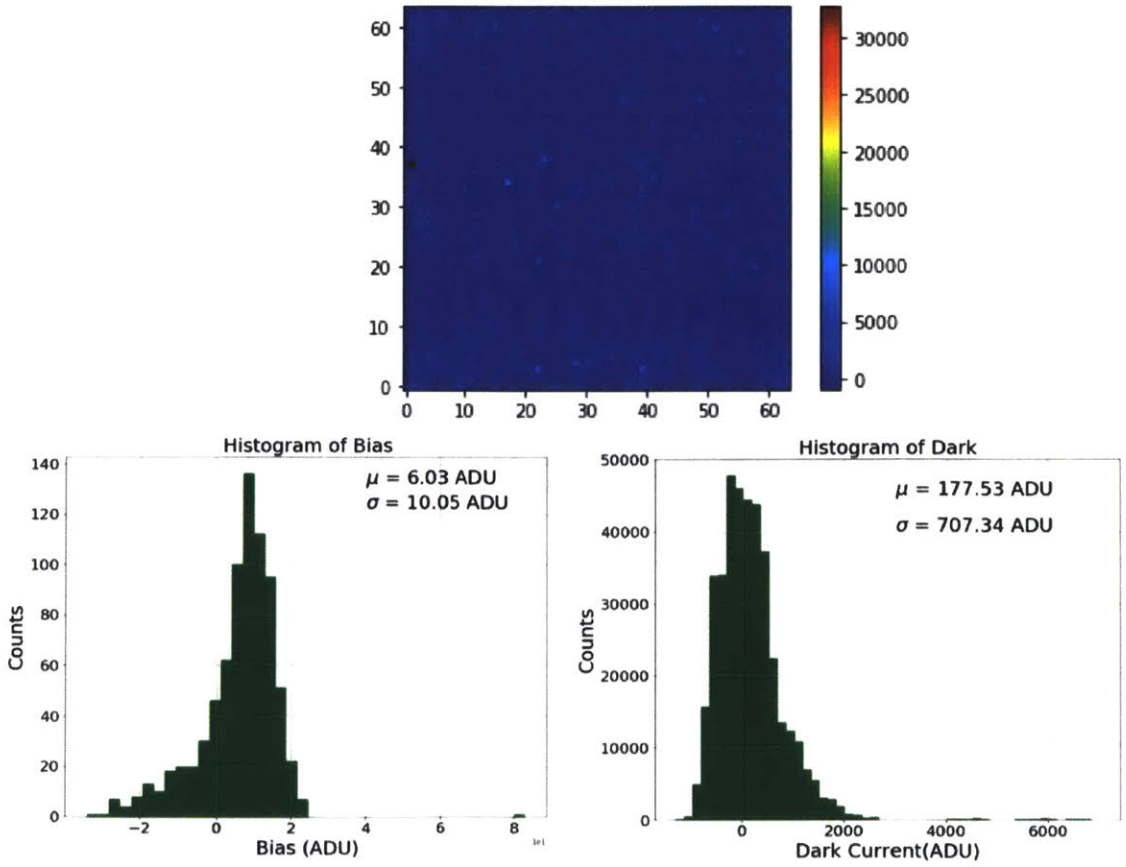

Figure 5-23: Example 64x64 pixel calibration frame after column-wise bias subtraction showing the dark rows (0:16) at the bottom edge of the window. 0:8 rows of pixels are optically dark and used to estimate dark current. 8:16 rows of pixels are electrically dark and used to estimate bias.

We take 760 calibration windows simultaneously with science frames, such that

they are directly below or above the simulated star and aligned with the electrically and optically dark rows specific to the simulated star. The windowed frame in Figure 5-23 shows the 64x64 pixel calibration frame after column-wise bias subtraction showing the dark rows (0:16) at the bottom edge of the window. 0:8 rows of pixels are optically dark and used to estimate dark current. 8:16 rows of pixels are electrically dark and used to estimate bias.

We then median-combine each column to produce a single bias value per column per frame. Then, we perform a frame-by-frame subtraction by taking the median bias for each column and removing that from every pixel in the corresponding column of the target star window. Next, we take the median of the corrected calibration frames, and produce the histogram in Figure 5-23 for the bias and dark rows separately. The mean charge in the bias histogram gives the bias noise count while the standard deviation that is the uncertainty in bias gives read noise count. Similarly, the mean charge in the dark histogram gives the mean dark current and the standard deviation gives dark current non-uniformity. We can calculate the noise contributions from these sources by taking the square root of the charge and normalizing with the median pixel charge over the entire frame.

Table 5.2 shows the calculated values for dark current, bias and read noise contributions. The numbers are in agreement with the data sheet, where dark current is listed as <35 e^-/pix/s and read noise is 2 e^-/pix/s. The two methods of measuring dark noise, one where we take dark frames by covering the detector with a shutter and the other, where we use calibration windows at the bottom or top of the detector both give comparable results. From this result, we conclude that we can use either method can be used in the flight data analysis pipeline. Given that we do not have dark frames

Flat Frames

We use an integrating sphere, illustrated in Figure 5-24, to produce uniform illumination of the detector. In order to do that, we remove the Carl Zeiss lens and replace it with an integrating sphere, by placing it as close to the detector as possible. A fiber

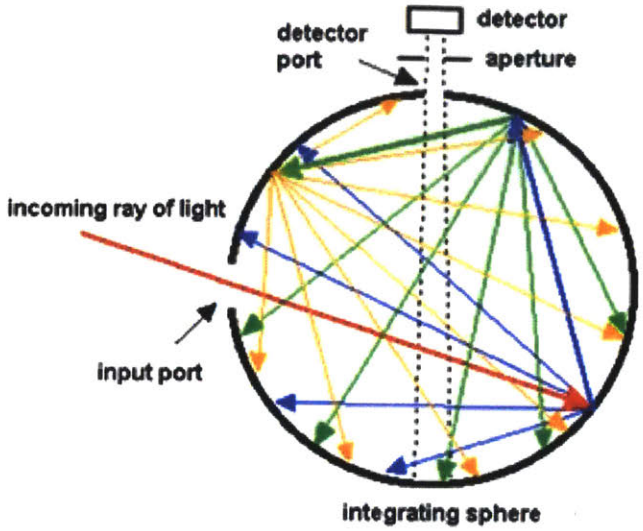

Figure 5-24: Illustration of an integrating sphere. The integrating sphere has a very reflective coating that reflects the incoming light rays in turn causes secondary and tertiary reflections. The light that exits the integrating sphere is uniform. [100]

optic cable connects the beam splitter to the integrating sphere. We take full frame images to adjust the light intensity to approximately 50% of the full well capacity which corresponds to 1000 ADU on the image. Then, we take 120 windowed images using a sequence at the two locations where the stellar images were also taken. Figure 5-40 shows a 1-minute co-added flat median frame after dark subtraction. The accompanying histogram shows a 1-sigma pixel response non-uniformity of 0.6%.

Photon Transfer Curve

The photo transfer curve shows detector response (i.e. signal) when exposed to uniform illumination of various levels of light intensity as a function of noise. A typical photon transfer curve is illustrated in Figure 5-26 [102] . The photon transfer curve has three regimes: read noise dominated, shot noise dominated and fixed pattern or pixel non-uniformity noise dominated.

Read noise is the random noise measured under dark conditions, and limited by on-chip amplifier noise. Whereas, shot noise is dependent on the signal level and associated with the random arrival of photons on the CMOS detector. The

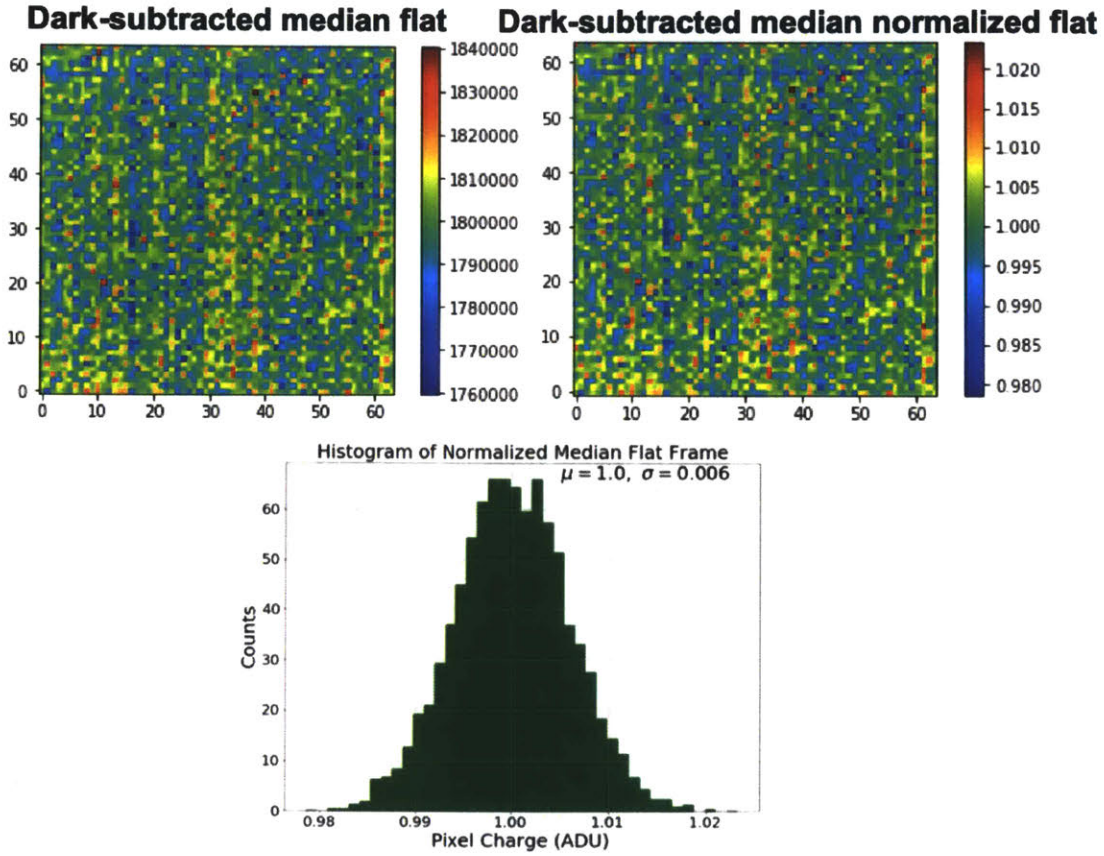

Figure 5-25: Histogram of the PRNU for a single output. The 1-sigma width of this distribution of 0.6%

uncertainty in the quantity of charge intercepted is characterized by a slope of 1/2 as shown in Figure 5-26, and is modeled using Poisson statistics where shot noise is proportional to the square root of the incoming signal. The fixed pattern noise is dependent on the inter-pixel response variations due to photomask misalignment and fabrication variations among pixels leading to varying response. The fixed pattern noise regime is characterized by a slope of 1.

In order to generate the photon transfer curve in the laboratory, we take flat frames at different illumination levels. We then calculate a median frame at each illumination level, and mean signal for each frame. We remove the dark current and bias by doing a dark subtraction prior to calculating the mean signal. We plot the mean signal minus offset as a function of noise or standard deviation of the median

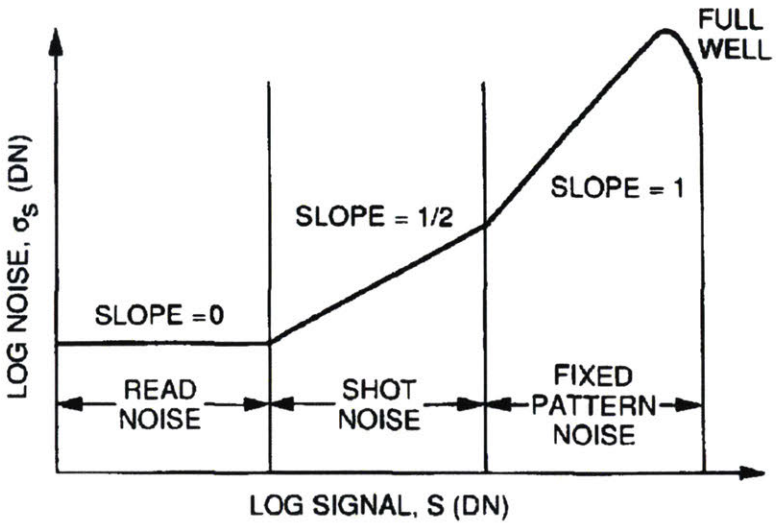

Figure 5-26: Example photon transfer for a CCD detector showing the three noise regimes: read noise, shot noise and fixed pattern noise. [101]

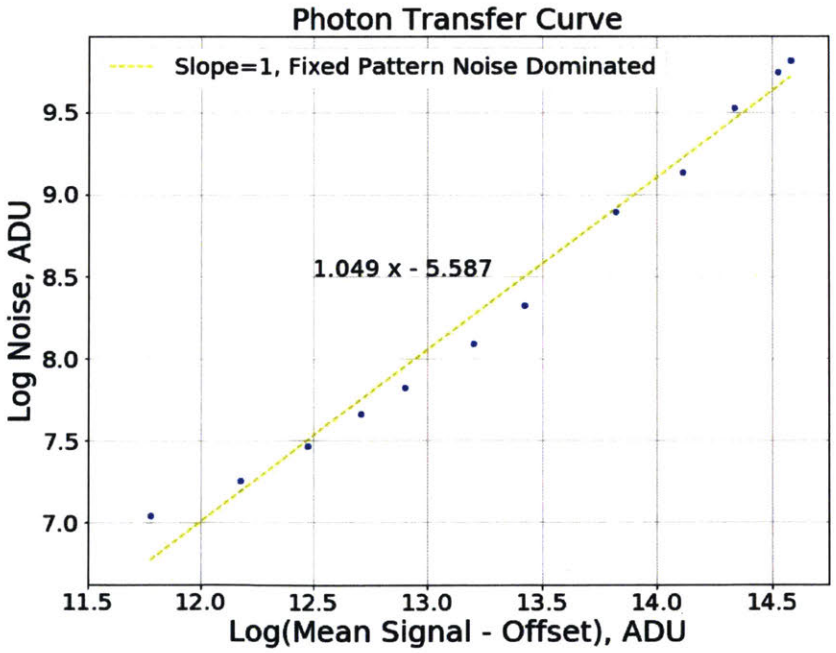

Figure 5-27: Photon transfer curve showing mean signal minus offset as a function of noise or standard deviation.

dark-subtracted flat frame as shown in Figure 5-27. The illumination levels that we expect for our science observations fall under the fixed-pattern-noise-dominated regime as shown by the slope of 1 in the figure. We discuss the characteristics of the fixed pattern noise and how to remove these effects from the data in Section 5.4.1.

Gain Measurement

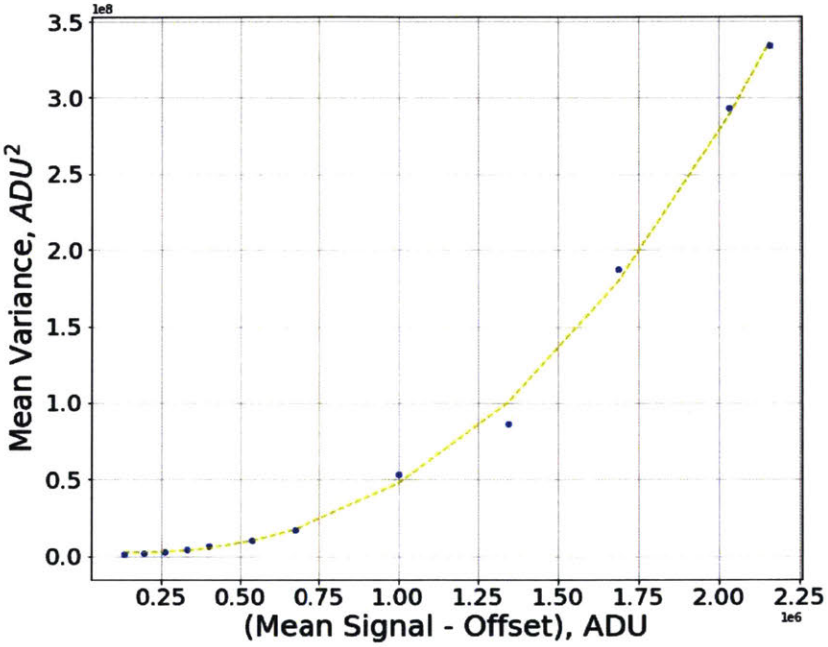

Figure 5-28: Mean signal minus offset as a function of squared mean variance.

We measure gain (analog-to-digital conversion factor) using the photon transfer curve. Gain is given by Equation 5.2 [101] where S is the mean signal in ADU and σ_S is the noise or standard deviation of the signal in ADU.

$$Gain = \frac{S}{\sigma^2} \tag{5.2}$$

We plot mean signal minus the offset as a function of mean variance of the signal as shown in Figure 5-28. We calculate gain for the shot noise dominated regime of the plot, which is given by the inverse slope of the curve. This process is not valid for higher illumination levels due to increased charge sharing between pixels leading

to artificial shifts in gain. By removing the read noise and fixed pattern noise from the data and taking the inverse of the slope, we obtain the gain. The average gain was $6.4 \pm 0.1\ e^-$/ADU.

Fixed Pattern Noise

We develop a model to calculate the gain variations (due to the pixel and column amplifiers) and offsets (due to the ADC converters at each column) at each pixel. We then produce two matrices; one for pixel-by-pixel gain correction and another for pixel-by-pixel offset correction [103]. We use the gain and offset correction matrices in Section 5.4.1 to illustrate the efficiency of the method in removing fixed pattern noise from the laboratory data.

We begin by taking flat frames at increasing levels of uniform illumination. We take two adjacent sets of data that have an illumination level closest to the target star. Each illumination level has a unique set of gain and offset matrices as fixed pattern noise varies with light intensity. Hence, it is important to use the right illumination level when correcting for fixed pattern noise. We take the median of each set of flat frames, $V_{avg}(\phi_1)$ and $V_{avg}(\phi_2)$. We take two flat frames each with $V_{ij}(\phi_1)$ and $V_{ij}(\phi_2)$ being pixel ADU values at pixel (i, j). Then, a_{ij} is the gain at pixel (i, j), and b_{ij} is the offset at pixel (i, j).

$$V_{avg}(\phi_1) = V_{ij}(\phi_1)a_{ij} + b_{ij} \tag{5.3}$$

$$V_{avg}(\phi_2) = V_{ij}(\phi_2)a_{ij} + b_{ij} \tag{5.4}$$

We obtain the gain, a_{ij} and offset, b_{ij} matrices by solving the simultaneous equations 5.3 and 5.4 [103], and are shown in Figures 5-29 and 5-30. We perform a pixel-by-pixel offset subtraction and gain division to correct for the fixed pattern noise.

$$a_{ij} = \frac{V_{avg}(\phi_1) - V_{avg}(\phi_2)}{V_{ij}(\phi_1) - V_{ij}(\phi_2)} \tag{5.5}$$

$$b_{ij} = \frac{V_{ij}(\phi_1)V_{avg}(\phi_2) - V_{ij}(\phi_2)V_{avg}(\phi_1)}{V_{ij}(\phi_1) - V_{ij}(\phi_2)} \tag{5.6}$$

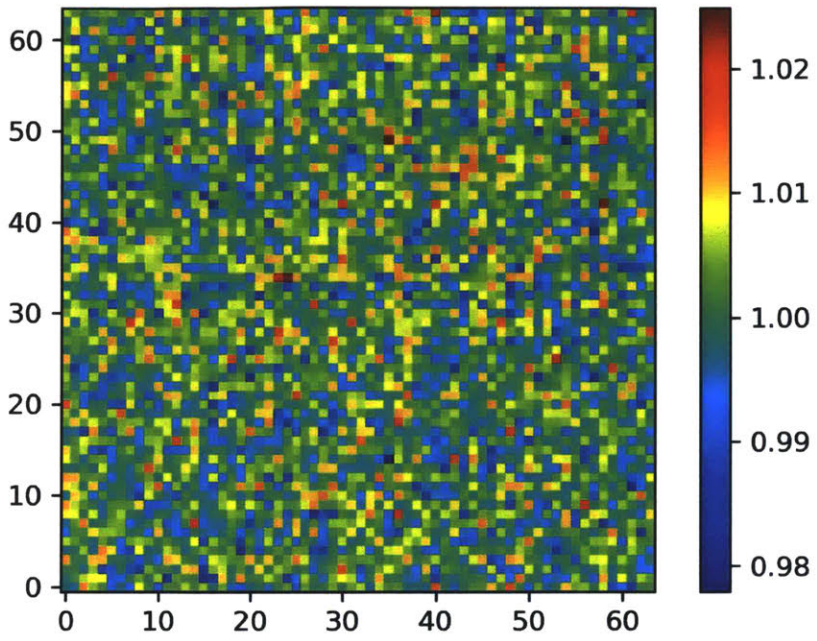

Figure 5-29: Illustration of the gain matrix obtained by solving the simultaneous equations for two sets of flat frames taken at very close illumination levels.

Laboratory Data Reduction

We develop a data reduction pipeline to process the laboratory data, calibrate and correct for systematics, and perform aperture photometry. The goal is to assess the photometric performance in the laboratory, in addition to developing a framework for systematics calibration which can then be adapted for flight data analysis. Given that CMOS detectors have not been used to perform sub-millimag high precision photometry in space, we rely on data analysis techniques for CCDs to begin with, and then develop methods to tackle systematic effects that are unique to CMOS detectors.

We study a wide variety of methods, in different orders and combinations to assess their impact on photometry. We illustrate four examples in Figure 5-31. We test

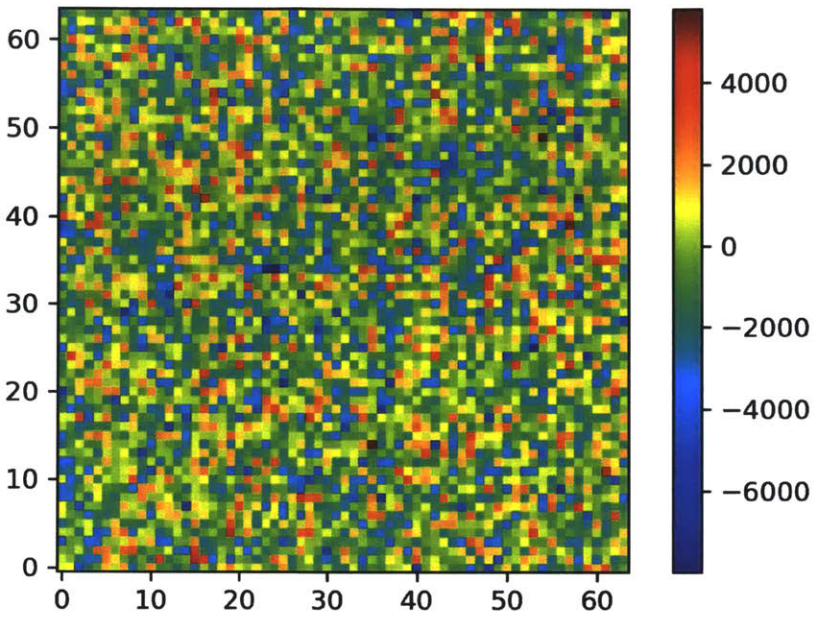

Figure 5-30: Illustration of the offset matrix obtained by solving the simultaneous equations for two sets of flat frames taken at very close illumination levels.

techniques typically used with CCD detectors such as bias and dark subtraction, flat fielding (division by a bias-subtracted median flat frame), local background subtraction, etc. The second and third options in the figure show techniques we developed for the CMOS detector to remove the column-dominated and row-dominated effects. These effects are due to gain variations at each pixel, and gain variations and offset at each column. We get considerable improvement when we switch from median bias and dark subtraction to column-averaged bias and dark subtraction, where we take the median charge in every column and subtract that from every pixel in that column.

We implement pixel-by-pixel pixel response non-uniformity (PRNU) correction to remove the effects of interpixel variations. For CCD detectors, we collect a series of flat frames at uniform illumination, and dark frames with no illumination. We subtract the median of all the dark frames from the median of all flat frames. Then, we divide the science frame by the dark-subtracted median flat frame. For CMOS detectors, this method does not remove the fixed pattern noise completely, leaving behind some residual column-dependent stripes. Instead, we calculate gain and offset

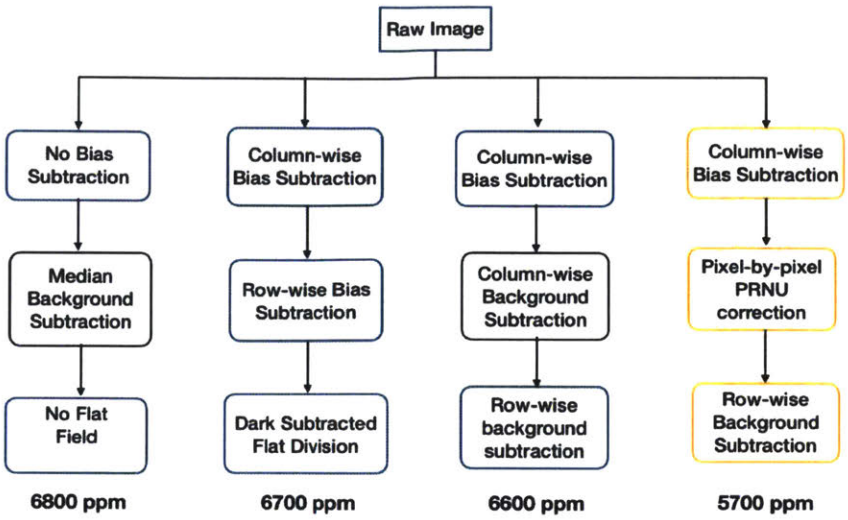

Figure 5-31: Four examples of different combinations of reduction techniques that were studied while developing an optimal data analysis framework for ASTERIA, along with 1-min photometric precision in ppm obtained using each method.

matrices as shown in the previous subsection, where each element of the gain and offset matrices corresponds to a pixel on the detector. Then, we divide each science frame pixel-by-pixel by the corresponding gain, and subtract the corresponding offset.

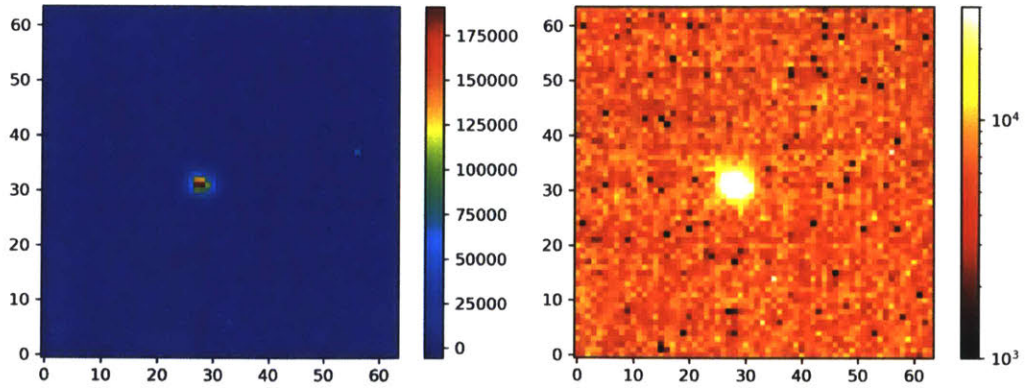

Figure 5-32: Example corrected science frame after performing column-dependent gain and offset corrections, row-dependent corrections and pixel-by-pixel response corrections. The image on the left is the final corrected frame and the picture to the right shows the same image on log scale to highlight the pixel-to-pixel variations. The pixel values, however, had to be offset in this frame in order to remove negative values.

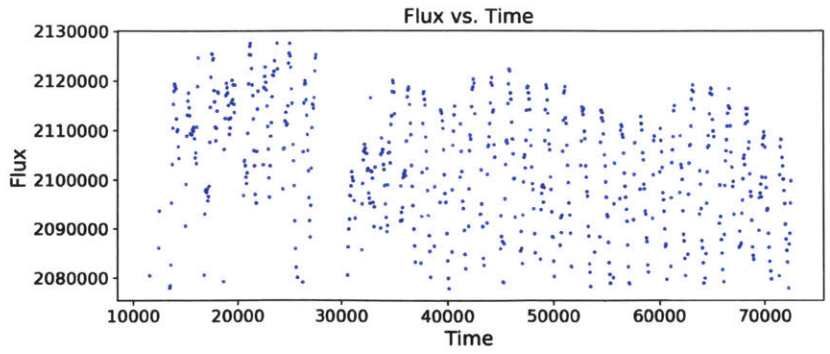

Figure 5-33: Corrected light curve obtained after column-dependent gain and offset variations, and inter-pixel variations were removed.

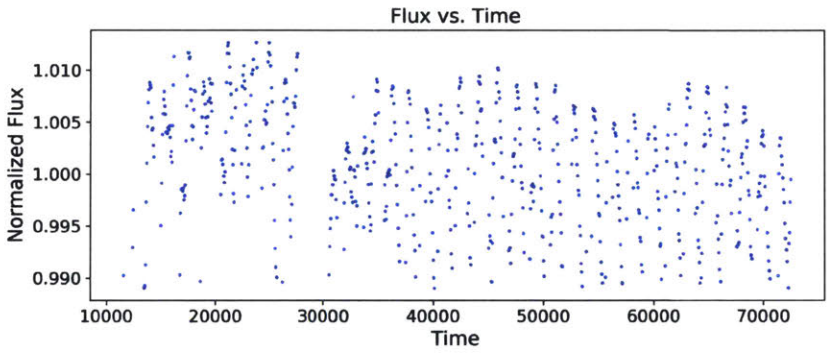

Figure 5-34: Normalized corrected light curve obtained after column-dependent gain and offset variations, and inter-pixel variations were removed.

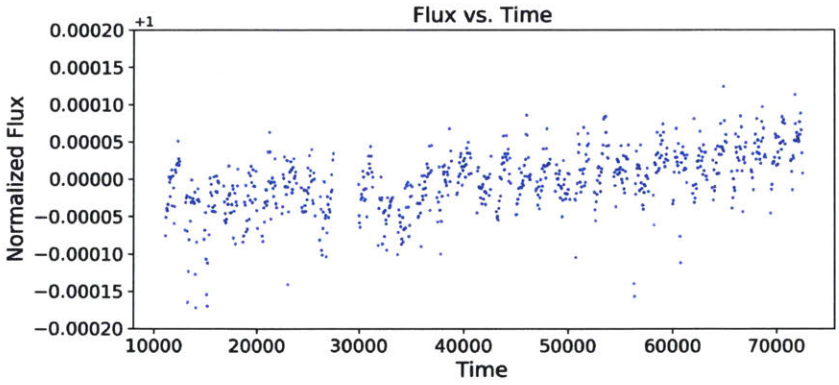

Figure 5-35: Background flux within an aperture in the neighborhood of the target star that is not illuminated, plotted against time.

My data analysis pipeline comprises of three steps: preparing the bias columns by performing a median background subtraction on the calibration frames. We take the median value of the electrically dark pixels for every column and subtract that value from each pixel in that column in the science frame. Here we use the simulated stellar frames shown in Figure 5-21. We then perform the pixel-by-pixel PRNU correction discussed in the previous subsection. Next, we perform yet another additional correction where we take a part of the science frame that is devoid of stars and calculate the median value for each row and subtract that value from every pixel in that row. This results in an efficiency mitigation of residual column and row dependent gain variations. We then perform aperture photometry on the corrected science frames (shown in Figure 5-32) by summing the charge within a circular aperture mask placed on the pixels containing the stellar image. We calculate the photometric precision of the light curve, and optimize the size of the aperture mask by repeating this procedure for different aperture sizes until the improvement in signal-to-noise ratio is overcome by the increase in background noise. Lastly, we calculate the residual background noise from the background flux shown in Figure 5-35.

Detrending

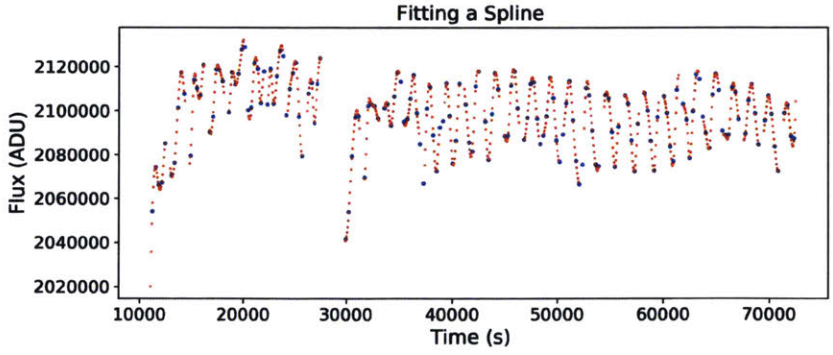

Figure 5-36: Illustration of spline fitting to the corrected light curve.

The main reason for higher noise in the laboratory compared to flight data, is the inherent flux variation in the laser light source as light source itself is not stabilized in

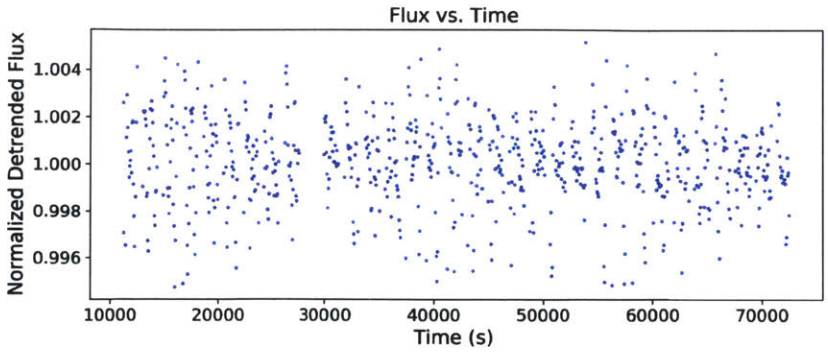

Figure 5-37: Detrended and normalized light curve.

Data Reduction Step	1-min Photometric Precision (ppm)
Background and bias subtraction	6768
Pixel-by-pixel flat correction	5720
Detrending	1874

Table 5.3: Photometric precision improvement after every step in the data reduction process.

the laboratory, as seen in the light curve. We remove these long-term trends by fitting a spline, as shown in Figure 5-36. The detrended light curve in Figure 5-37 shows vast improvement in photometric performance as shown in Table 5.5. We also tabulate the rest of the noise sources calculated in the previous subsections in Table5.6. The residual systematic noise is 1379 ppm.

Source	Mean Flux	1-min Error (ppm)
Photon Noise	33000 ADU/pixel	335
Background Noise	257.16 ADU/pix/min	7.8
Bias	6.03 ADU/pix/min	11
Dark Current	131.44 ADU/pix/min	45.5
Read Noise	10.05 ADU/pix/min	95.7
Residual Systematic Noise	-	1379

Table 5.4: Various noise sources and contributions to the systematic error. All values are normalized using the mean flux (2100880 ADU). The residual systematic noise for the laboratory experiments is 1379 ppm.

5.4.2 Optimal Calibration Framework for Flight Data

Due to the absence of ground calibration tests on the detector and flight camera assembly prior to launch, the ASTERIA operations team had to perform a series of in-flight calibration tests required for flight data reduction. The key observations required, in addition to the science frames, were the calibration windows with the electrically and optically dark rows for bias and dark subtraction, and flat frames to mitigate inter-pixel variations. The ASTERIA telescope did not have a shutter. Hence, it was challenging to take zero exposure frames in space. Attempts were made to turn to a part of the sky devoid of bright stars greater than magnitude V=8.0. However, there was still considerable contamination from stars in the vicinity. Hence, we rely on calibration windows to mitigate dark current and bias from the flight data. As we discussed in the previous section, calibration windows are a reasonable replacement for the dark and bias frames.

In the following subsections, we illustrate the flight data analysis process by presenting example in-flight calibration data acquired for one of the science targets, HD219134. HD219134 is known to have transiting super Earths HD219134 b and c, both of which were discovered first using radial velocity [104] ([105] and then using Spitzer [105] [106]. The radial velocity study also detected two longer period planets, d and f. ASTERIA observed HD219134 with the goal to confirm if the planets d and f transit. In addition to being a science target in the extended mission, HD219134 was also used to demonstrate fine pointing performance and thermal control during ASTERIA's prime mission [95].

The raw image of HD219134 is shown in Figure 5-38. The star is masked by dominant column-dependent fixed pattern noise that is a result of gain variations and offsets due to amplifiers and ADC converters respectively.

Calibration Windows

We take calibration frames simultaneously with the science frames by matching the target window coordinates and aligning with the calibration rows directly above or

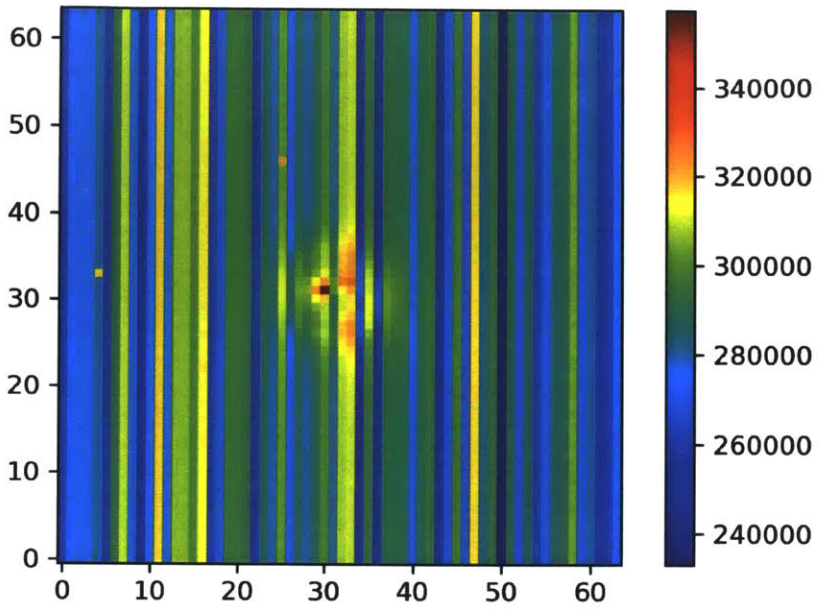

Figure 5-38: Raw science frame of target star HD219134 with V=5.57.

below the science frame, depending on which half of the detector the science target lies on. Each target star frame has a corresponding calibration window, which we use to calibrate that frame. First, we remove the the gain variations by taking the median charge value of every column and subtracting that value from every pixel in that column.

An example of this reduced calibration frame is shown in Figure 5-39. In this figure, rows 48:56 are bias rows and 56:64 are dark rows. We note that the electrically and optically dark rows look visibly different from the rest of the detector. The figure also shows a distribution of charge in a median calibration window by taking the median of the bias rows over the entire times series, and repeating the same for the dark rows. The dark current is given by the mean pixel charge from the dark histogram. The standard deviation gives the dark current non-uniformity. The calculation of dark current noise follows Poisson statistics, and goes as the square root of the dark current.

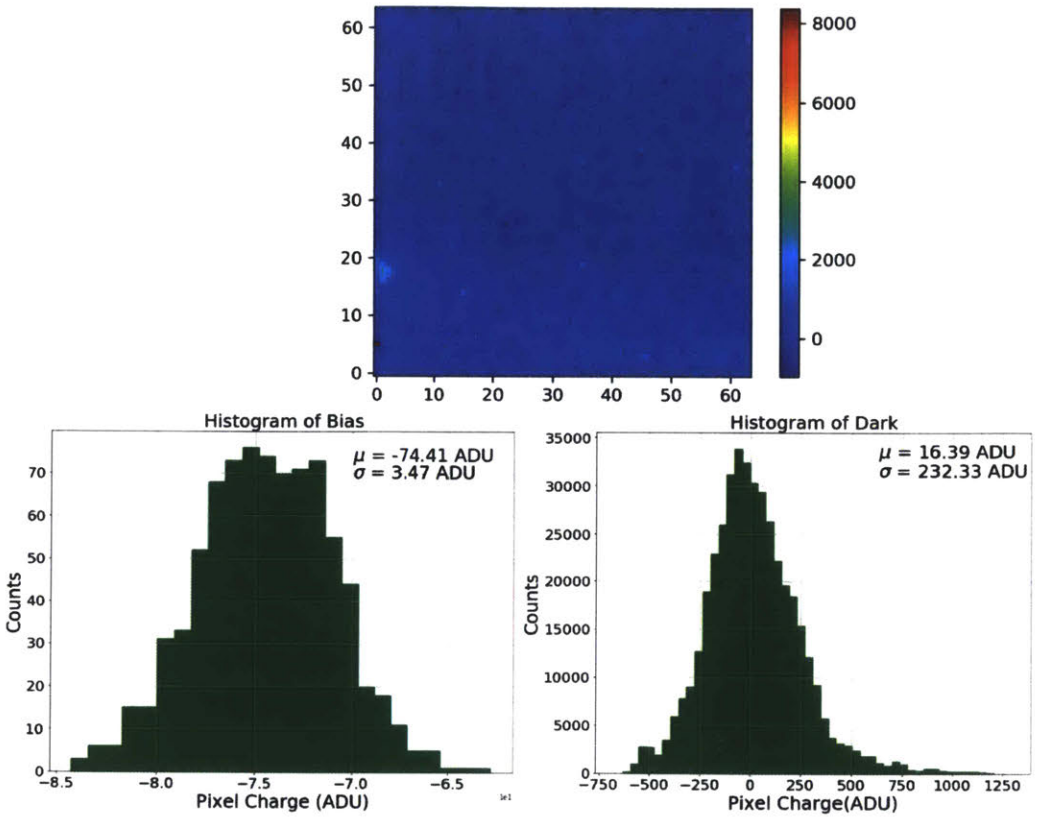

Figure 5-39: (Top) Example reduced calibration frame. (Bottom left) Histogram of the median calibration frame for rows 48:56. (Bottom right) Histogram of the median calibration frame for rows 56:64.

Read Noise

Read noise is the number of electrons per pixel introduced during the ADC conversion process because it is not perfectly repeatable. The standard deviation of the bias values from the calibration window obtained by plotting on a histogram gives read noise, as shown in Figure 5-39. The mean value is 29 ADU which is the read noise per 1-min image. Each 1-minute image has 1200 frames. The read noise per 50 ms frame per pixel is 0.84 ADU RMS. Using a gain conversion factor of 6.42 e-/ADU, the read noise is 5.39 e- RMS per 50 ms frame per pixel.

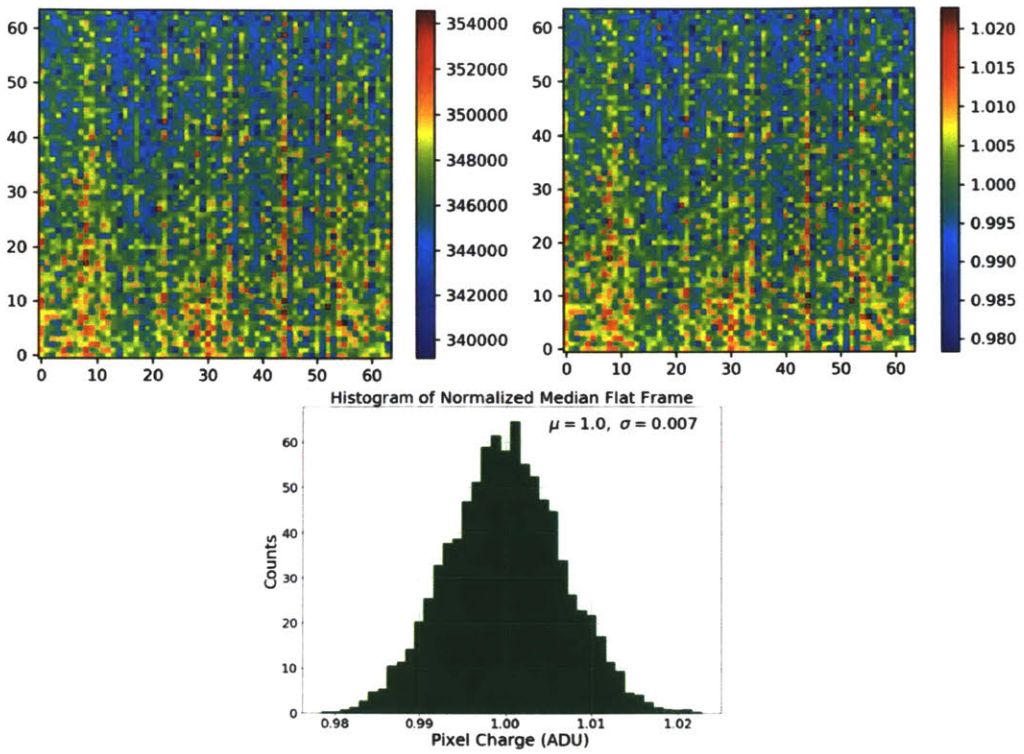

Figure 5-40: (Top left) Median flat frame. (Top Right) Normalized median flat frame. (Bottom) Histogram of the distribution of the median flat frame.

Flat Frames

We generate flat frames by uniformly illuminating the detector and taking images with the same integration time as the target star such that we fill 50% full well capacity. The challenge with taking flat frames in space is the absence of a uniform light source to simultaneously illuminate all the pixels in the detector at the same level. Using spacecraft rotation along the camera boresight vector, we attempt to uniformly illuminate the detector. The angle between the spacecraft and sun vector is maintained at 40 degrees and then the spacecraft is rotated about this angle to get a uniform illumination of the stray light on the detector.

We reduce the flat frames taken during the in-flight observation using the corresponding calibration windows. We perform column-subtraction of the median bias values. We then median-combined the flat frames and normalized them to arrive at the master flat shown in Figure 5-40. There appears to be a gradient going from top

half to bottom half with the top half receiving less illumination than the bottom half of the detector. The histogram shows a pixel response non-uniformity of about 0.7%. This is 14% higher than the laboratory result presented in the previous section. The additional variation is due to the non-uniform illumination of the detector and not attributed to the inter-pixel response variations. The pixel-by-pixel gain and offset correction did not yield the same improvement in photometric precision as the laboratory results. Hence, we use a bias-subtracted median flat frame to correct for gain variations pixel-by-pixel.

5.5 Photometric Performance Validation and Improvement

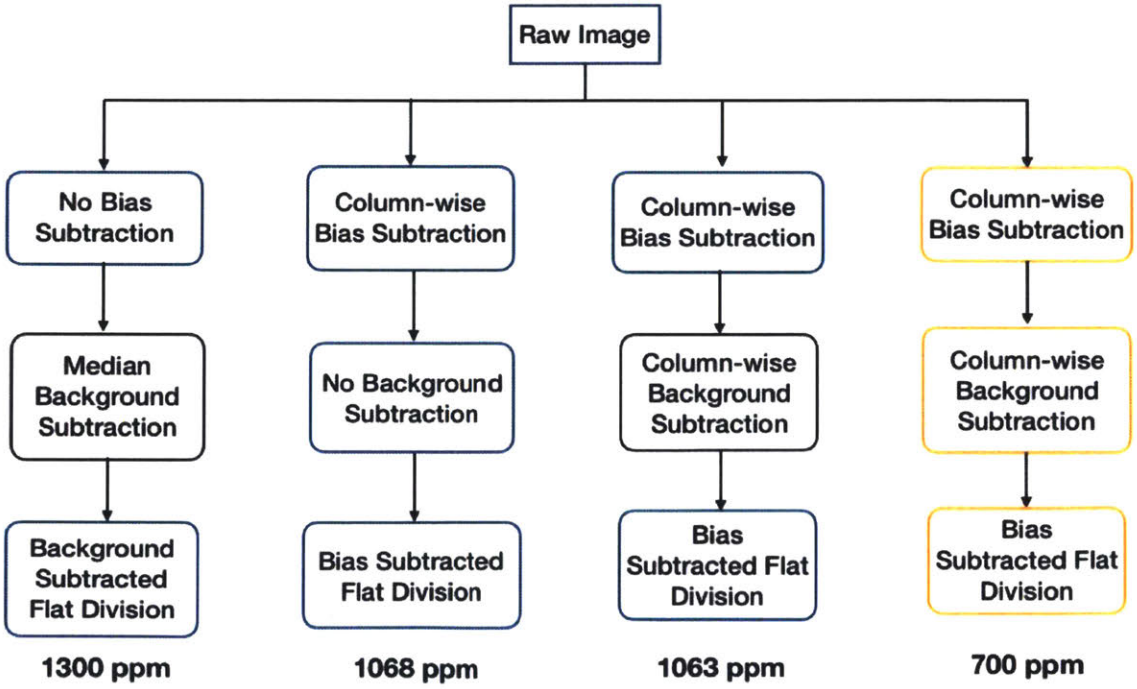

Figure 5-41: Four example data reduction methods that we use to correct for various systematic noise sources. The 1-min photometric precision for each method is shown for each method.

We now develop optimal systematics correction techniques to improve the photo-

metric performance of ASTERIA. We begin the data reduction process by reviewing every frame from the science observations. We discard frames that were obtained during the orbital "sunrise" or "sunset". These frame appear either in the beginning of an orbit or towards the end of the orbit, and display significant background contamination. Retaining these frames leads to a lower signal-to-noise ratio. A step-by-step study of different calibration frameworks was then performed. A few examples are listed in Figure 5-41. We explain results from the fourth method that yield the best results. After discarding frames with visible background contamination, we proceed to perform bias correction by subtracting the median of the bias column (from the calibration window) from all pixels in the respective column in the science frame. We then select a few pixels (rows 0-15) in the neighborhood of the target that are devoid of any stellar flux to remove background or sky noise. We take the median of the pixels for each column, and subtract the median value from every pixel in that column. Next, we subtract the median of the bias rows column by column from every flat frame, and take the median of the reduced flat frame. Lastly, we perform a pixel-by-pixel division of the target star pixels with the reduced flat frame pixels values. The output of this step is shown in Figure 5-42. The target star is visually cleaner than the raw image, although there is still some residual column-dependent noise as shown in Figure 5-42. The final photometric precision is given by the RMS scatter of the normalized light curve. For HD219134, the photometric precision after data reduction (before detrending) is 700.02 ppm.

We analyze a time series of the background flux and calculate the noise contribution of the background to the systematic noise as shown in Figure 5-43. The background noise accounts for 2474 ADU which translates to 21 ppm contribution to the residual systematic noise.

5.5.1 Temperature Variations

Temperature variations also affect the photometric precision of the science observations. Figure 5-45 shows the variation of lens temperature with time for an example HD219134 observation. By splitting the data by orbit and fitting a spline to detrend

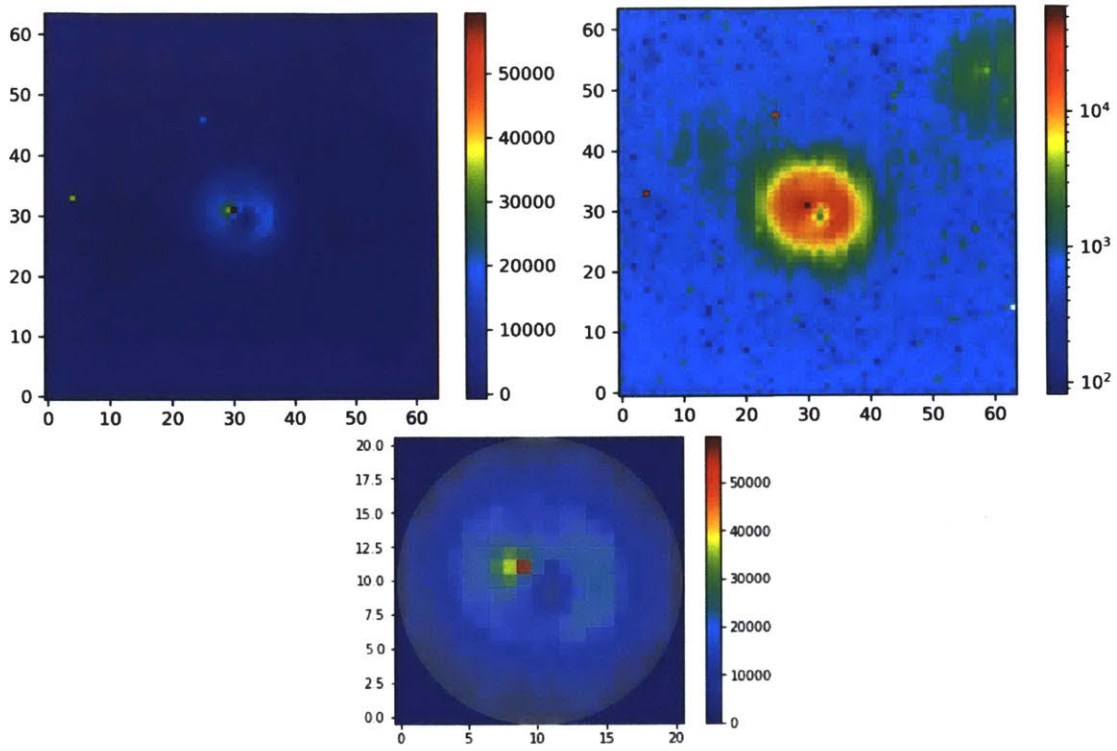

Figure 5-42: (Top left) Stellar image after performing removal of bias and background, and correction for flat field variations. (Top right) Reduced image in the log scale still showing column-dependent gain variations especially around the target. (Bottom) Illustration of the circular aperture mask placed over the target star to capture all of the stellar flux.

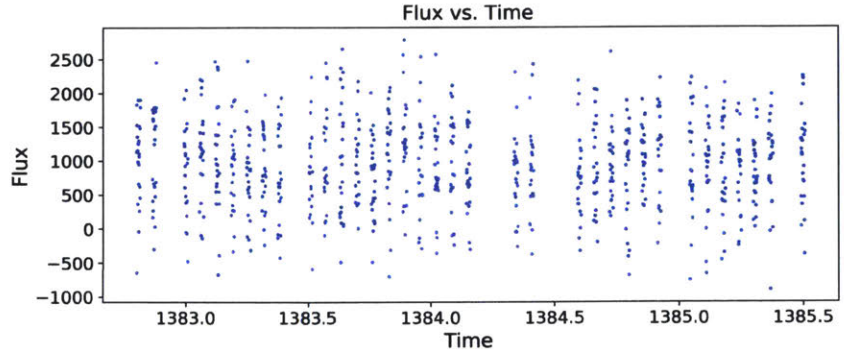

Figure 5-43: Background flux time series produced by taking a few pixels in the vicinity of the star that is devoid of the stellar flux, and summing the pixel charge for each frame in the time series.

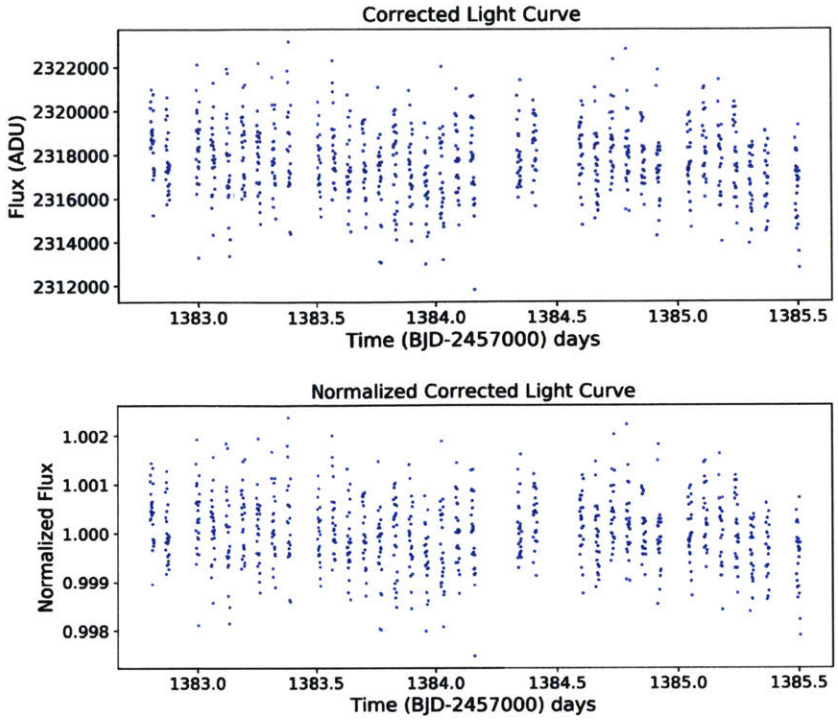

Figure 5-44: (Top) Corrected light curve obtained after data reduction. (Bottom) Normalized corrected light curve.

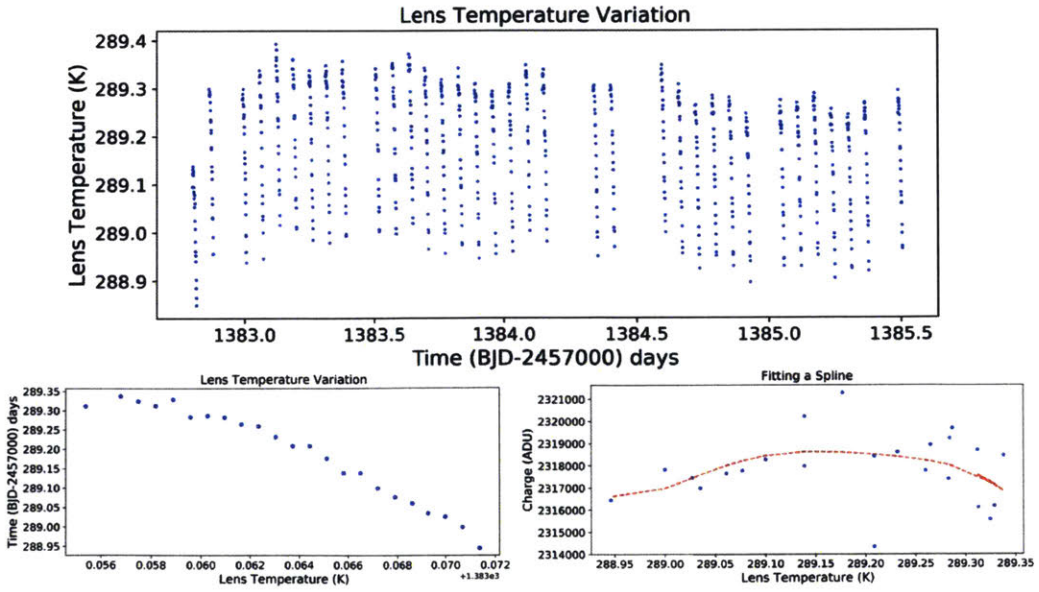

Figure 5-45: Lens temperature as a function of time.

Data Reduction Step	1-min Photometric Precision (ppm)
Background subtraction	1300.12
Column-wise bias correction	1068.78
Flat Correction	700.02
Detrending	574.9

Table 5.5: Improvement in photometric precision after every step in the data reduction and detrending process.

the temperature effects for each orbit, we can remove the systematic effect due to variation in lens temperature.

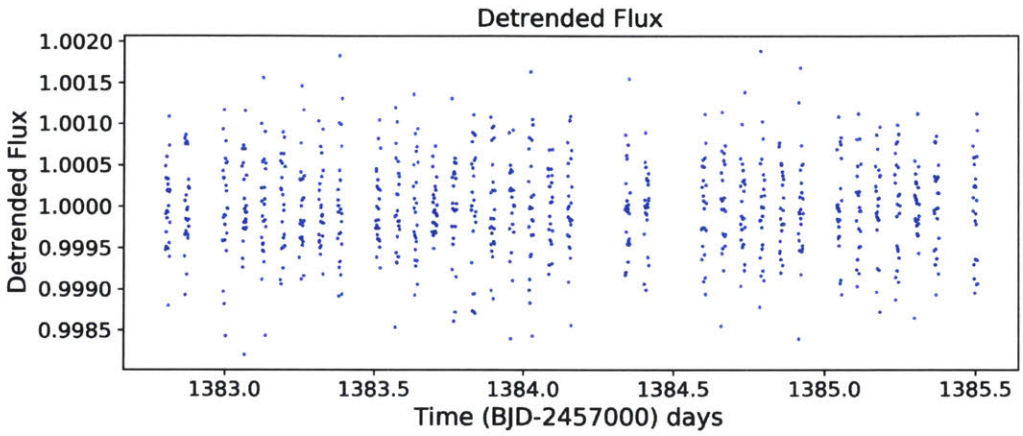

Figure 5-46: Detrended and normalized light curve.

Each orbit produces roughly 24 science frames. The camera is power-cycled and reinitiated at the beginning of each orbit, and at the end of the orbit, in to reduce the sync loss between the camera FPGA and flight computer. Hence, the lens temperature drops during each orbit and resets again in the beginning of every orbit. This causes the flux produced to also change depending on the QE at that temperature, in addition to potential focus changes due to changes in the lens temperature.

Figure 5-45 shows the lens temperature time series that clearly captures the change in lens temperature from the start of an orbit until the end of the orbit. Each dotted line refers to data taken during one orbit. The detrended flux with an improved precision of 574.9 ppm is shown in Figure 5-46, which is an 18% improvement in photometric precision after the data reduction step. The overall improvement in

Source	Mean Flux	1-min Error (ppm)
Photon Noise	3220 ADU	310
Background Noise	2474 ADU	21
Dark Current	16.39 ADU/pix	31
Read Noise	3.47 ADU/pix	26
Residual Systematic Noise	-	186.9 ppm

Table 5.6: Contribution of various sources of noise along with a calculation of residual systematic noise is shown. A mean flux of 2320000 ADU is used to normalize sll the numbers.

photometric precision from both the data reduction and detrending methods is shown in Table 5.5. The 1-hour residual systematic noise for HD219134 is 189 ppm.

5.5.2 Alpha Centauri

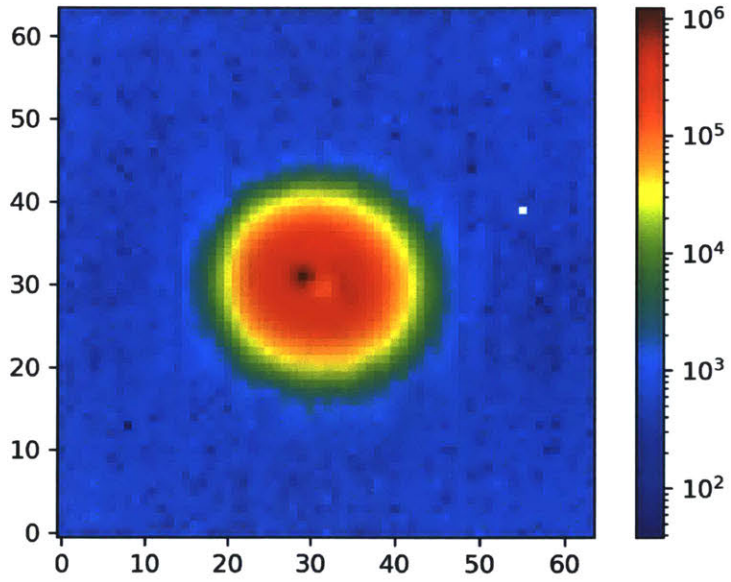

Figure 5-47: Reduced science frame for Alpha Centauri after applying optimal systematics correction and data reduction.

Alpha Centauri A and B (V = -0.27) are the closest star system to the Sun. Both are Sun-like stars and are of interest for exoplanet searches [107] [16]. However, most transit searches cannot observe Alpha Cen due to saturation of the detector as the star is too bright. In order to prevent the frames from saturating, we reduce the

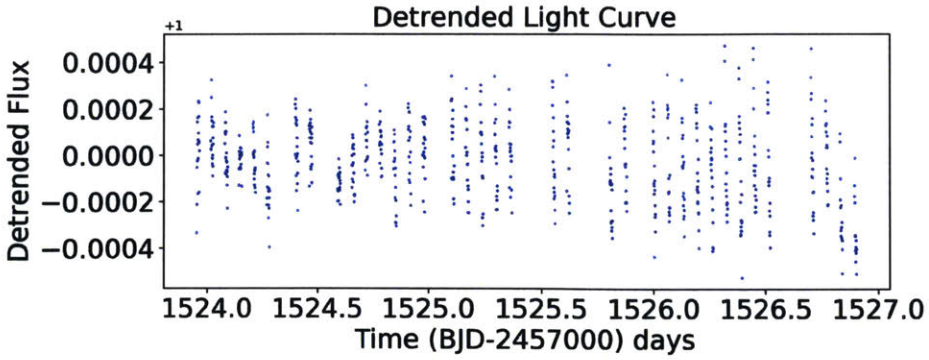

Figure 5-48: Detrended light curve for Alpha Centauri. The 1-min photometric precision was calculated as 172.66 ppm.

integration time for Alpha Cen from 50 ms to 7.5 ms per frame. A 1-min coadded image only has 9 seconds of data. Figure 5-47 shows an example science frame for Alpha Cen after data reduction with the corresponding light curve. The photometric precision for Alpha Cen at 1-min is 172.66 ppm.

5.5.3 Time Bin Size

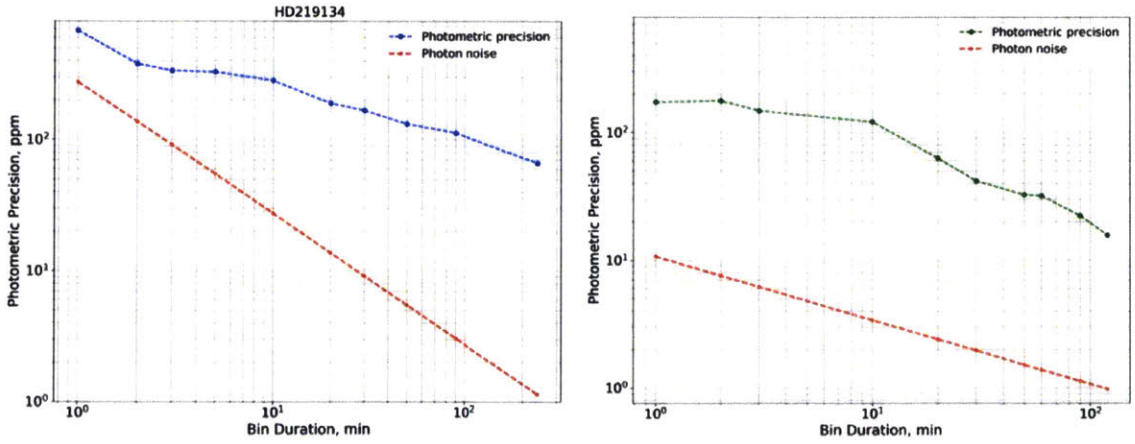

Figure 5-49: Photometric precision and shot noise for various time bin durations for (Left)HD218134 and (Right) Alpha Centauri.

We bin the data to various time bin durations to assess the photometric precision variation with time bin size. Figure 5-49 shows photometric precision and shot noise

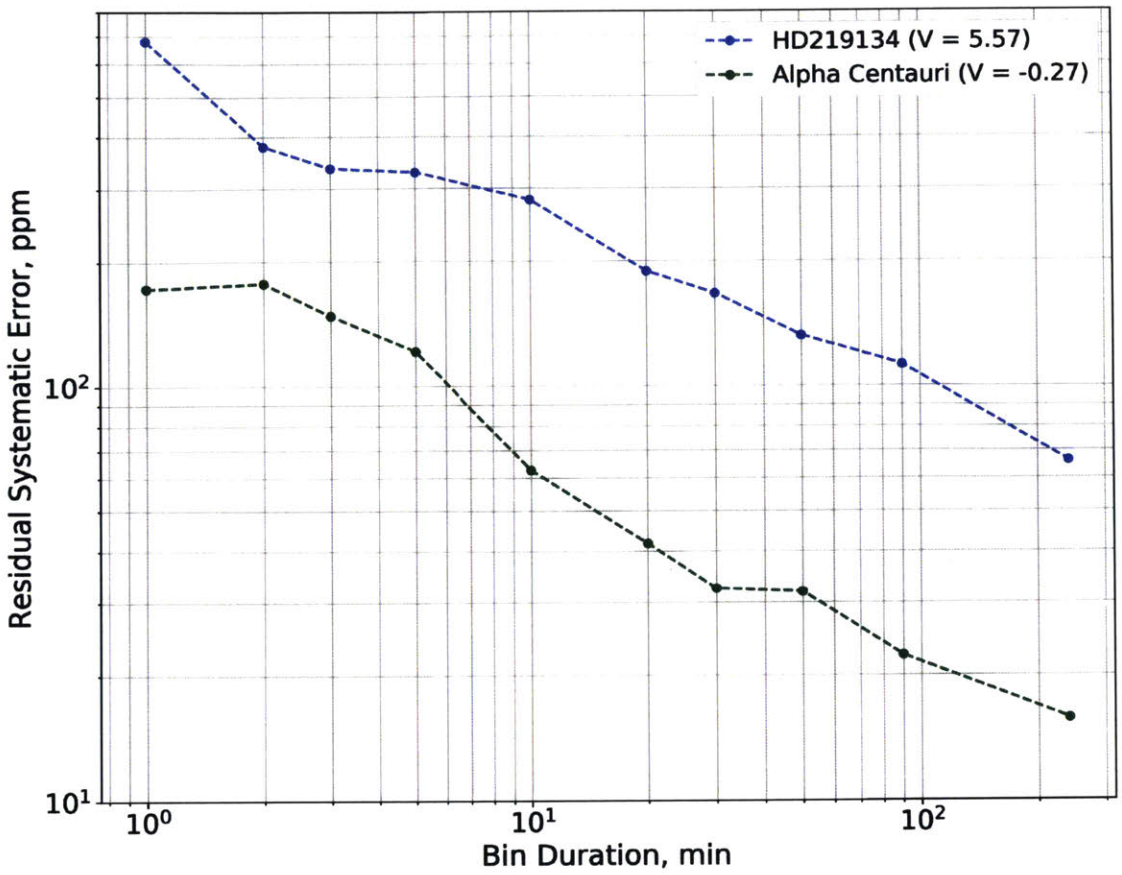

Figure 5-50: Residual systematic noise as a function of time bin duration for both HD219134 and Alpha Centauri.

for various time bin durations for HD219134 and Alpha Centauri, and their corresponding shot noise or photon noise variation when averaged to the same timsecales. Further, removing photon noise, read noise and background noise gives the residual systematic error shown in Figure 5-50. The residual systematic error for HD219134 at 2-hour is 65 ppm and for Alpha Centauri, the 2-hour residual systematic error is 15 ppm.

5.5.4 Jitter Analysis

In this subsection, we discuss results from on-orbit characterization of the three ACS operating modes: 'XACT only' where the ACS system is used to point the spacecraft,

'XACT with feedback' where centroiding of stars on the detector provides feedback to the ACS system, and 'fine pointing control' where a piezoelectric stage translates the camera assembly to stabilize the observed star field. For each of the three modes, we analyze the pointing performance over various observations of target stars of different stellar magnitudes. The observations were performed by the ASTERIA operations team, and raw images were produced.

We investigate the effect of spacecraft jitter at different timescales and estimate the contribution of jitter to the overall systematic error. We then perform photometric performance analysis for each mode, and analyze the effects of jitter and pointing uncertainties on photometric performance as a function of stellar magnitude.

The centroiding algorithm receives the eight windowed frames with 64x64 pixels each [95]. After calculating the centroid for each target, the algorithm performs bias and background subtraction to remove column-dependent artifacts. The pointing control algorithm centers the target star by computing the offset and commanding the location with the target star to have zero control error while the rest of the guide stars can have some residual error. The variance increases as stars get fainter. Hence, the algorithm assigns higher weight to brighter guide stars than fainter stars. Next, the piezo stage algorithm calculates the tilt and title offset and a roll command offset. For every command, an attitude quaternion command is constructed and sent to the XACT.

Figure 5-51 shows the pointing error with and without the piezo-stage active [95]. In one case, the piezo stage is actively moving the detector in one case, while in the other it only sending quaternion commands to the XACT which we called 'XACT + feedback' mode. The blue line traces the path of the star on the detector when there is only feedback to the XACT and piezo stage is not active, while the orange path that's contained within a much tighter spot is the path traced by the star when the piezo stage is active. The figure also show the power spectral density and the cumulative mean square value. The plot flattens out between 10 Hz and 4 HZ and below 2 Hz, the pointing control removes significant portion of the attitude error. In the XACT only case, as shown in Figure 5-52, the noise goes up at lower frequencies.

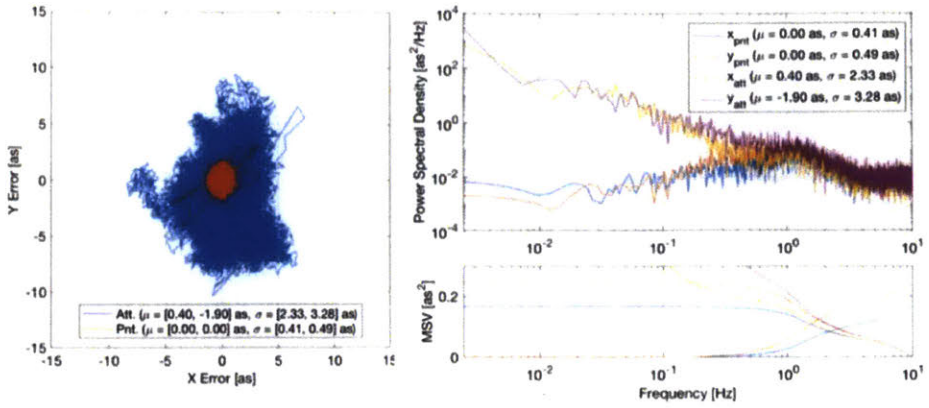

Figure 5-51: The pointing error with and without the piezo-stage active. The blue line traces the path of the star on the detector when there is only feedback to the XACT and piezo stage is not active, while the orange path that's contained within a much tighter spot is the path traced by the star when the piezo stage is active. [95]

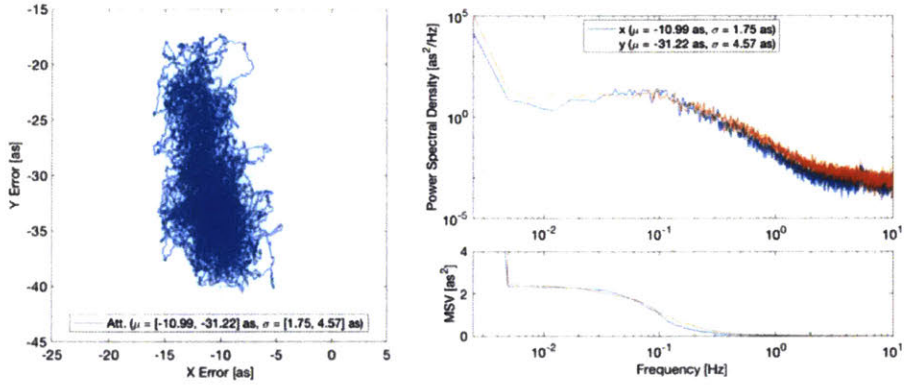

Figure 5-52: The pointing error with and without the piezo-stage active. The blue line traces the path of the star on the detector when there is only feedback to the XACT and piezo stage is not active, while the orange path that's contained within a much tighter spot is the path traced by the star when the piezo stage is active. [95]

With a low frequency feedback, from the payload to the XACT, this effect could be reduced.

We study the effect of the three modes on photometric performance, as shown in Figure 5-53. The data shown in the figure corresponds to five stars: Polaris, Tau Ceti, Tau Boo, HD219134, 14 Hercules of varying magnitudes. The photometric precision is significantly higher for the fine pointing control mode, compared to the other two

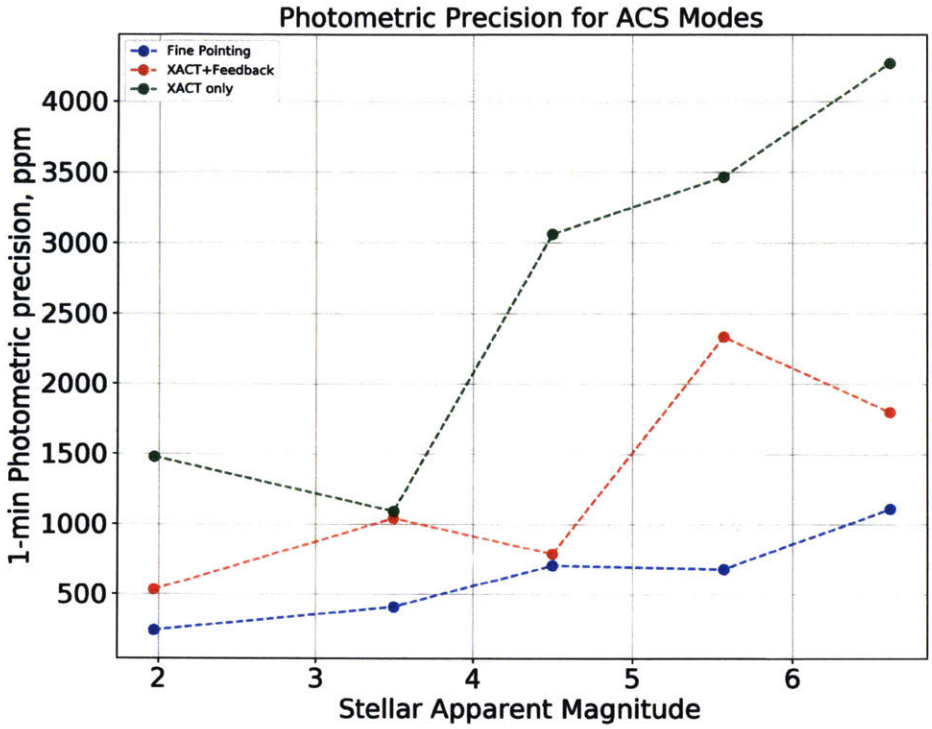

Figure 5-53: Photometric performance as a function of stellar magnitude for the three ACS modes.

modes. The fine pointing mode provides an improvement in photometric precision of 75%-85% compared to XACT only mode. There is also a slight dependence on stellar magnitude due to two reasons. First, the photometric precision has shot noise which is dependent on stellar brightness, and second, the accuracy of the centroiding algorithm is just slightly better for brighter stars.

5.6 Results Summary

In this chapter, we demonstrated the integrated systematics calibration framework as applicable to ASTERIA. We performed photometric precision assessment, along with jitter noise estimation using a photometry simulation and modeling of the CMOS detector. We developed laboratory techniques to characterize the noise sources in the laboratory and narrowed in on an optimal calibration framework. Further, we

performed flight data calibration to further develop an optimal flight data reduction framework as shown in Figure 5-54. Lastly, we established the noise floor for ASTERIA by using optimal systematics correction. We effectively used feedback mechanisms to utilize results from each step to inform various other steps in the process.

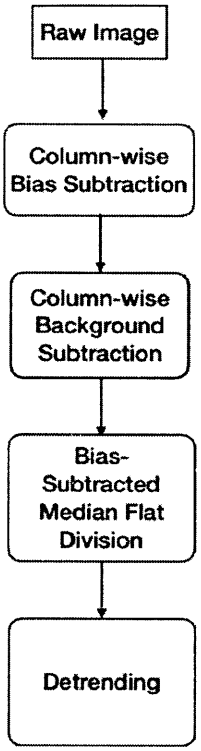

Figure 5-54: Optimal Flight Data Reduction Framework for ASTERIA.

The key results for this section are summarized below.

- We successfully demonstrated the use of CMOS detectors and CubeSats for high precision photometry applications. We accomplished this by developing an optimal data reduction and systematic correction framework for ASTERIA.
- Using a simulation of the detector and realistic jitter profiles, we first assessed the photometric performance of ASTERIA and the contributions of various noise sources including sub-pixel response variations to photometric precision.
- We then developed laboratory techniques to study the systematic effects in the

CMOS detector and telescope assembly due to the lack of calibration data from prior to launch. We demonstrated the efficacy of pixel-by-pixel corrections for the column-dependent gain and offset variations, and showed an improvement of 15% in photometric performance using this method.

- We developed in-flight tests to calibrate the science data, and analyzed the science frames for HD219134. We demonstrated an improvement in performance of over 55% using the optimal data reduction framework, shown in Figure 5-54. The photometric precision achieved for HD219134 using bias subtraction, background subtraction and flat correction techniques is about twice photon noise limit. The residual systematic noise for HD219134 at 2-hour was about 65 ppm.

- We established a residual systematic noise floor of about 15 ppm at 2-hour for Alpha Cen using the piezo-stage fine pointing control system.

Chapter 6

Application to Future Missions

In this chapter, we present the application of key takeaways from Chapter 4 and Chapter 5 to future missions. First, we present the noise budget for the ASTERIA constellation mission based on the noise floor obtained for TESS and ASTERIA. We also present a detector trade study to understand specifications of detectors currently available. The detector selection drives the noise budget due to their direct impact on the shot noise calculations.

Second, we present a novel pipeline-driven approach to noise budgeting and calibration test plan development for the SPARCS mission. We draw from the data reduction pipeline for ASTERIA to inform the SPARCS mission of key tests that ought to be performed on the ground prior to launch, and may not be performed in space. This approach is especially useful for CubeSat missions due to the schedule and cost constraints that often prevent extensive testing of the payload. Additionally, developing an apparoach that is traceable to the data analysis pipeline ensures that we perform tests that are not directly traceable to the requirements but are crucial for the flight data analysis.

6.1 ASTERIA Constellation

The search for an Earth analog is indeed the ultimate goal for many scientists and engineers of this generation. We propose a constellation of dozens of non-interacting

satellites in the Geostationary-Earth orbit (GEO) to study the brightest Sun-like stars, and search for Earth-size planets in Earth-like orbits around these stars [108]. The constellation is uniquely positioned to detect an Earth analog due to it's ability to observe stars in any part of the sky simultaneously, which a single platform is not capable of. The constellation will build on the technology demonstration of the prototype ASTERIA, and it's excellent line-of-sight pointing stability of 0.5 arcseconds RMS over 20-min observations and focal plane temperature stability of within 5 milliKelvin over a 20-minute period.

The main advantage of the transit method is that the planet radius can be determined from the magnitude of the drop in the star's brightness seen in the light curves. When combined with the radial velocity data, which provides the planet's mass, the planet's density can be estimated. In addition, by monitoring the depth of the transits at different wavelengths, the absorption spectrum, and hence the atmospheric composition can be deduced. By observing both the primary and secondary transits, the planet's actual spectrum and temperature can be inferred. As of November 2019, the transit method has discovered 3157 planets out of a total of 4099 confirmed planets. Despite very successful missions such as Kepler and TESS, we do not yet have a telescope that is capable of finding an Earth analog.

We propose a constellation of 30 12U satellites with a total budget of $300 M. Each satellite will continuously monitor a very bright Sun-like star ($V < 6.0$) for 2-8 weeks before switching targets to derive a stellar inclination by asteroseismology. The satellites will continue to observe the stars for a period of three years if the inclination is higher than 80 degrees.

6.1.1 Photometric precision

An Earth-size planet transiting a sun-like star has a transit depth of 84 ppm. The photometric precision requirement for a 5σ detection per transit is 16.8 ppm. Although the transit of an Earth-like planet across the center of the star lasts for 13 hours, the photometric precision requirement is typically adopted for 6.5 hours, half the transit duration. Hence, the photometric precision requirement is 16.8 ppm in

6.5 hours. This requirement along with the 12U form factor of 20 cm x 20 cm x 30 cm drives the requirement on the upper limit for aperture diameter.

6.1.2 Aperture Diameter

We estimate the incoming flux from the standard reference star Vega using Equation 6.1. In this equation, F_v is the flux for a target star of stellar magnitude V, F is the reference flux for Vega (9.6e+10 $photon/m^2/s/microns$), B is the band-pass of 0.4 micros, T is the throughput efficiency of 0.8 that includes lens transmission, detector efficiency and fill factor, f is the number of frames, and t is the integration time in s, and A is the aperture area in m^2.

$$F_v = F * 10^{(\frac{-V}{2.5})} * B * T * A * f * t \tag{6.1}$$

We calculate the incoming flux for the target star using Equation 6.2. In this equation P is the period of interest of 6.5 hours, C is the time per co-addition of images of 60 s, and n is the shot noise allocation for the period of interest.

$$F_v = \frac{1}{n^2(P/C)} \tag{6.2}$$

Given the noise floor of 16.8 ppm, we conservatively allocate a shot noise of half the photon noise limit at V=7.0. From the aperture area, we estimate the upper limit for the aperture diameter to be 17 cm.

6.1.3 Noise Budget and Science Capability

We study the effect of photometric precision on the science capability of ASTERIA constellation. Figure 6-1 shows photon noise as a function of stellar brightness. The photon noise calculation assumes a 17 cm aperture, 0.4 bandpass, 0.8 combined transmission and QE, and a 6.5 hour observation duration. We use Equations 6.1 and 6.2 to calculate photon noise for different stellar magnitudes. The gap between the blue line showing photometric precision requirement of 16.8 ppm at V = 6.0

and the photon noise line is allocated to instrument noise and stellar variability. A photometric precision below the blue line gives a 5-sigma detection of an Earth-size planet around a Sun-size star in an Earth-like orbit.

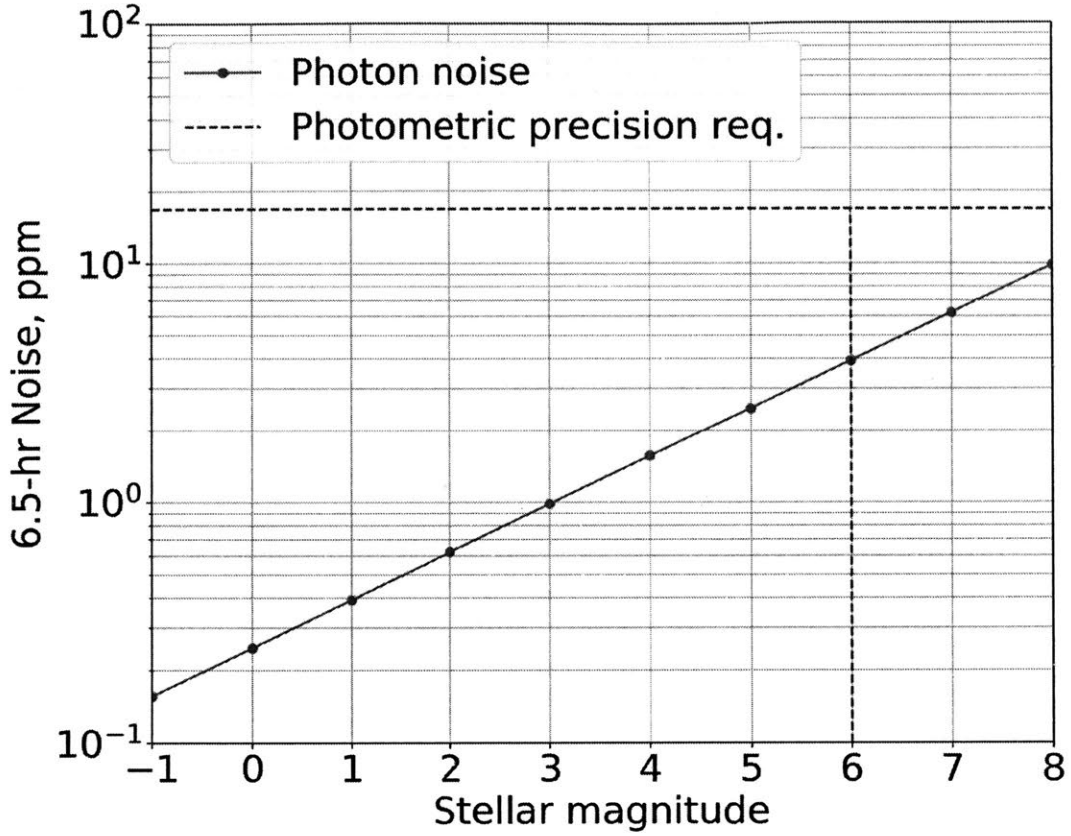

Figure 6-1: Photon noise as a function of stellar magnitude. The photon noise calculation assumes a 17 cm aperture, 0.4 bandpass, 0.8 combined transmission and QE, and a 6.5 hour observation duration. The photometric precision requirement of 16.8 ppm at V = 6.0 gives a 5-sigma detection of an Earth-size planet around a Sun-size star in an Earth-like orbit. The horizontal blue line minus the photon noise (red line) gives the margin available for noise due to instrument systematics and stellar variability.

Kepler's instrument noise floor was calculated as 14.1 ppm [66]. In this thesis, we also calculated TESS' instrument noise floor as 16 ppm at 4-hour timescales. Given that this noise floor is achievable, we assign a conservative noise budget of 2x photon noise and an additional 14 ppm instrument noise floor for the ASTERIA constellation. We calculate the smallest detectable planet radius as a function of stellar brightness. Any planet size above the solid blue line in Figure 6-2 can be detected assuming a 17

cm aperture in a 6.5 hour observation period. Thus, an Earth-size planet around a Sun-size star can be detected for target stars brighter than V=6.0 provided the total noise is below 16.8 ppm.

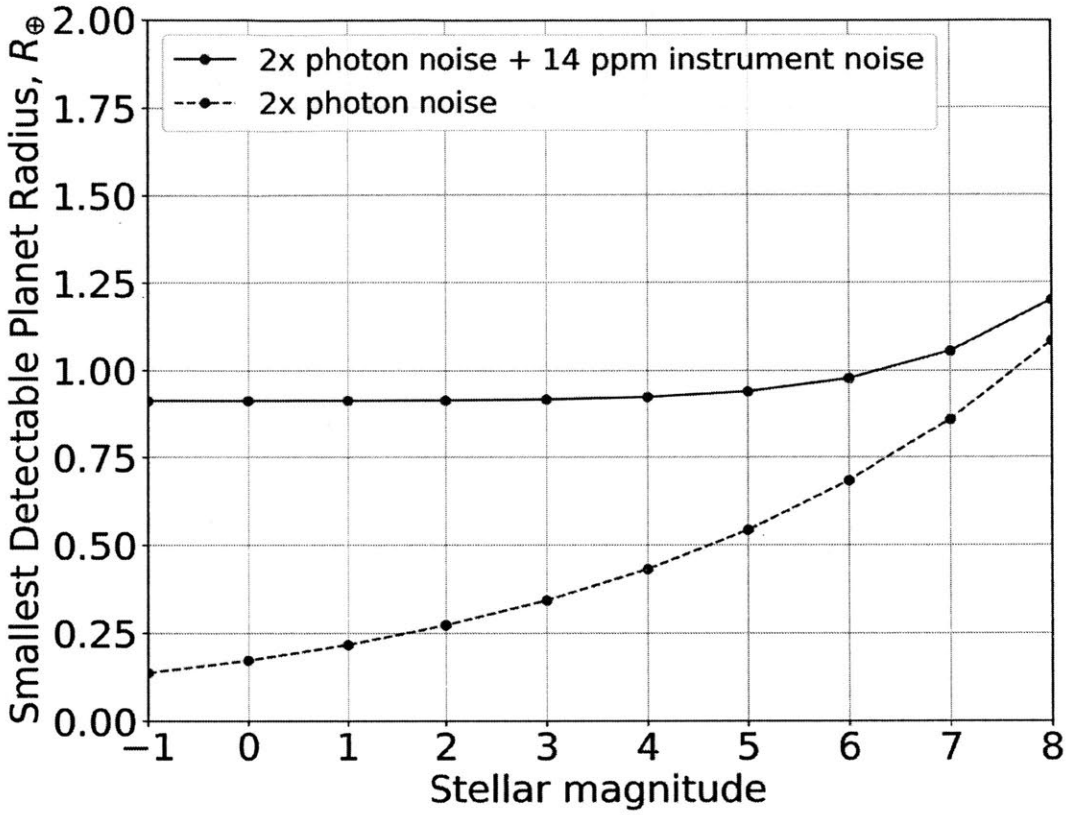

Figure 6-2: Smallest detectable planet radius as a function of stellar brightness. Any planet size above the solid blue line can be detected assuming a 17 cm aperture in a 6.5 hour observation period, and a noise allocation of 2 times the photon noise plus 14 ppm instrument noise (Kepler's instrument noise floor).

6.1.4 Tradespace Exploration for Detector Selection

For several decades, Charge Coupled Device (CCD) detectors have dominated space-based imaging and spectroscopy due to their single-photon sensitivity and moderate frame rates. More recently, scientific Complementary Metal Oxide Semiconductor (sCMOS) detectors that provide lower readout noise at higher frame rates have been developed, thus providing distinct advantages over CCD detectors for ultra-low-light applications. sCMOS detectors can be operated at room temperature as they generate

ultra-low-dark current (20 e-/pixel/s) compared to 250-500 e-/pixel/s generated by CCDs at the same temperature [109]. Hence, sCMOS detectors do not require passive cooling systems that would otherwise add significantly to the mass and size of the spacecraft.

sCMOS detectors with increased sensitivity (>95 at 560 nm at all incident angles) and dynamic range have now been created using back-illuminated sensor technology. In addition to CCD-like quantum efficiency (QE) in the visible wavelengths, a significant improvement in QE in the UV (>80 at 250 nm) and in the near Infrared (>25 at 950 nm) wavelengths has also been achieved providing a broader spectral range of 200-1100 nm.

The back-illiuminated sCMOS architecture provides a vast improvement over front-illuminated sCMOS detector technology previously used in the ASTERIA mission. Combined with optimized electronics, the back-illuminated sCMOS detectors have significantly better noise profile and reduced fixed pattern noise which is a dominant source of residual systematic noise in the previous ASTERIA detector. Detector specifications for back-illuminated CCD, and back-illuminated sCMOS detectors are listed in Table 6.1, specifically Teledyne e2v's back-illuminated frame transfer CCD [110], and Princeton Instruments' KURO back-illuminated sCMOS detector [111]. The back-illuminated sCMOS detector has lower read noise, higher dynamic range and ultra-low dark current at room temperature operation with a wide spectral range (200-1100 nm) and improved QE sensitivity (95% at 600 nm).

6.2 Systematics Calibration for CubeSat-based Science Missions

Almost all space telescopes have encountered cost overruns, schedule delays and utilized some portion of science operations time for in-flight systematics calibration. CubeSats, on the other hand, have a very compressed schedule to build and launch the spacecraft. In addition to lack of time, there is little budget allocated to per-

Specification	Teledyne CCD	Kuro CMOS R
Active array size	1024 x 1024	2048 x 2048
Peak QE	95 at 600 nm	95 at 600 nm
Read noise	2 e- rms at -40 C	1.3 e- rms at 20 C
Dark current	200-500 e-/pixel/s at 20 C	1.9 e-/pixel/s at -10 C
Full well capacity	100,000 e- at -40 C	80,000 e- at 20 C
Pixel size	13 μm x 13 μm	11 μm x 11 μm
Spectral sensitivity	200-1100 nm	200 nm âĂŞ 1100 nm
PRNU	<3 RMS	-
Dynamic range	50,000:1	61,500:1
Maximum frame rate	4 fps	47 fps (at 2048 x 64 res.)

Table 6.1: Comparison of characteristics and properties of different detectors currently available. The Teledyne detector refers to the e2v CCD47-20 Back Illuminated Frame Transfer CCD, and KURO refers to the 2048B Back-illuminated sCMOS detector.

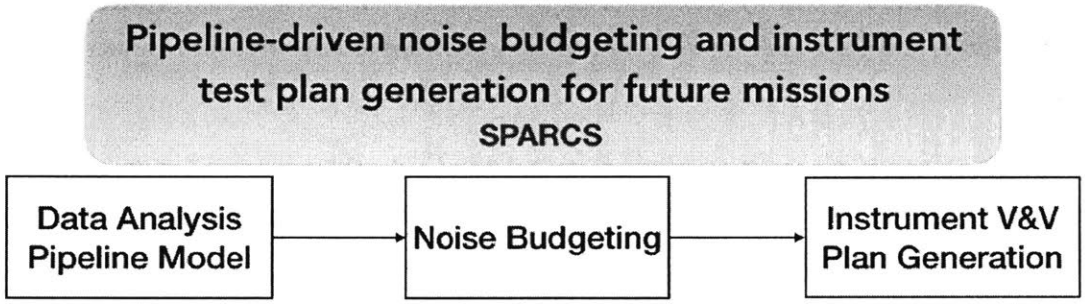

Figure 6-3: Pipeline-driven approach to generate instrument calibration test plan. The SPARCS mission will be presented as a case-study and an incompressible test list will be developed.

form ground testing and calibration, and for most missions, the payload is launched without thorough characterization of all systematic noise sources. This further bleeds into the operations cost, when more than the allocated time in space is spent doing in-flight calibration tests rather than taking science data. In many cases, these problems have been traced to deficiencies in the error budgeting and ground calibration test plan prioritization. The methodology shown in Figure 6-3 aims to improve early design phase error budgeting and calibration test plan generation through the use of pipeline-driven models in order to calibrate major noise sources on ground, and save valuable science operations time and cost. Adding systems engineering rigor to the calibration test plan generation process and using a pipeline-driven approach to gen-

erate an incompressible test list (ITL) will simplify operations during commissioning and in-flight calibration [98] [112].

We begin by developing a schematic of the science data analysis pipeline along with inputs and outputs required for each software operation. Based on the requirements, instrument design and detector datasheets, we develop a noise budget for each input in the pipeline. Typically, for larger missions, the calibration tests flow down from the requirements. For CubeSats, often times, the requirements definition is vague or does not cover calibration requirements in great detail. In the absence of clear requirements that define acceptable margin and uncertainty levels for each calibration test, we calculate an allocate these parameters based on current best estimate of the error sources.

We then develop an IT flow with traceability to requirements, if present, and specify the environment (optical testbench, TVAC, ground calibration, in-flight calibration) and the level of integration (chip level, camera level, telescope/payload level) for each test. We evaluate the statistical power by calculating the number of samples required to meet the assigned margins and uncertainty levels. This step is often a point of discussion and negotiation, as the constraint in terms of available time for testing is almost always lesser than the number of tests required. In order to prioritize the more important tests, we rank the test list based on engineering difficulty and science utility. The incompressible test list (ITL) lists and defines all tests that must be done prior to launch, and that cannot be performed in space.

6.2.1 SPARCS Mission Overview

SPARCS is a NASA-funded UV photometry mission scheduled for launch in 2021 into a sun synchronous terminator orbit to facilitate long observation duration for all target stars [114]. SPARCS is a collaboration between Arizona State University (ASU) and JPL, with a payload developed to study the UV time-domain behavior of low mass stars, and is integrated with a 6U CubeSat [17]. The payload consists of a 9-cm reflector telescope paired with two high sensitivity 2D-doped CCDs and associated electronics. The detectors are UV-optimized, Teledyne e2V CCD47-20, 1k

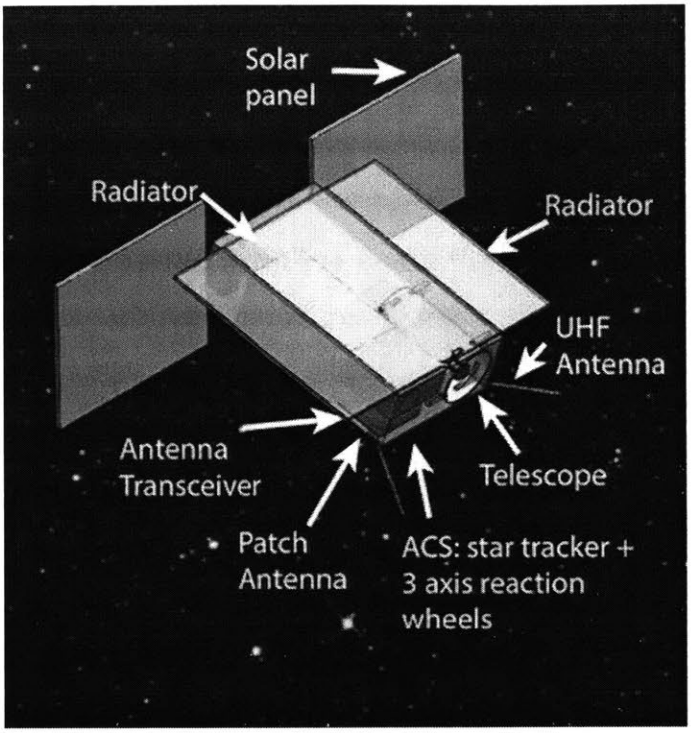

Figure 6-4: Schematic of the SPARCS CubeSat. [113]

x 1k back-illuminated, AR-coated CCDs [113].

SPARCS will perform absolute calibration and measure brightness changes in M-dwarfs in two UV bands. Short and long term variability is measured in the near-UV at 280 nm while flare frequency and energy are measured at far-UV at 160 nm. The two bands enable sampling of different emission regions within the stellar atmosphere. A schematic of the SPARCS CubeSat is shown in Figure 6-4.

6.2.2 Relevant Requirements

The relevant requirements from the SPARCS requirements documents pertaining to calibration testing of the camera and telescope are shown below. As with most CubeSat missions, the requirements on margin of error and uncertainty level on each calibration measurement are not well-defined. Hence, we define a margin of error for every measurement before calculating the sample size required to achieve the desirable standard deviation and standard error on the measurements.

- PL3.12 NUV SENSITIVITY: In 10 minutes the payload NUV imager system shall be capable to measure with S/N = 21 a flux of 0.7mJy.

- PL3.13 FUV SENSITIVITY: In 10 minutes the payload FUV imager system shall be capable to measure with S/N = 19 a flux of 0.8mJy.

- PL3.19 TOTAL THROUGHPUT MEASUREMENTS: The payload total system throughput shall be known to 1.4% within the ±2FWHM of the bandpass average wavelength and 30% otherwise.

- PL3.40 EXPOSURE TIMES:The payload camera exposure times shall be selectable between 1s and 30 min.

- PLP4.11 FLAT FIELD AND DARK CURRENT: The payload processor shall perform bias subtraction, flat fielding, and dark current correction of all newly acquired science target frames.

- PLP4.13 IMAGE AVERAGING: The payload processor shall be able to perform image averaging.

- CAM4.12 TOTAL THROUGHPUT MEASUREMENT PRECISION SPARCam: Throughput for each channel shall be known to 1% precision (TBR) within 2xFWHM of the filter peak, and 20% otherwise for all wavelengths spanning 115 to 1000 nm.

- CAM4.13 TOTAL THROUGHPUT MEASUREMENT RESOLUTION: SPARCam throughput for each channel shall be known to 2 nm resolution (TBR) within 2xFWHM of the filter peak, and 20 nm otherwise for all wavelengths spanning 115 to 1000 nm.

- CAM4.20 GAIN: SPARCam shall have selectable gain (range TBR).

- CAM4.21 INTEGRATION TIMES: SPARCam shall be capable of integration times between 1 second and 30 minutes.

- TC4.9 DETECTOR OPERATIONAL TEMPERATURE RANGE: The thermal control system shall limit the operational temperature of the detectors to a minimum of -40°C (233 K) and a maximum of 20°C (293 K).

6.2.3 Photometric Model

The signal-to-noise ratio is calculated using Equation 6.3. Photon noise, read noise, dark current noise, zodiacal noise and jitter noise have been described and characterized in Chapter 4. Air glow refers to line emission and red leak noise refers to emission during non-flare periods as target stars emit most of their light in the visible and IR spectral ranges. Hence, suppression of long-wavelength contributions is important. In this equation, the Cts_{InBand} or signal is calculated using Equation 6.4, where $\text{Cts}_{OnDetector}$ refers to the total signal from the star after performing aperture photometry. We remove the dark current (DC), bias (O) and pixel response non-uniformity (FF) contributions. We also remove in-band background and out-of-band contributions. In order to calculate the flare frequency f_λ, we use Equation 6.5 which requires the aperture area (A), detector QE, filter transmission (F) and total throughput (T). In this equation, η is the in-band dichroic throughput and ϵ is the fraction of out of band to total counts.

$$\frac{S}{N} = \frac{Cts_{InBand}}{\sqrt{\sigma^2_{Poisson} + \sigma^2_{read\ noise} + \sigma^2_{dark\ current} + \sigma^2_{sky} + \sigma^2_{jitter} + \sigma^2_{air\ glow} + +\sigma^2_{red\ leak}}} \tag{6.3}$$

$$Signal = FF[Cts_{OnDetector} - DC - O] - Cts_{BackgroundInBand} - Cts_{OutofBand} \tag{6.4}$$

$$Signal = \eta * (1 - \epsilon) * \int \frac{f_\lambda}{h\nu} * A * QE * F * T \, d\lambda \tag{6.5}$$

6.2.4 Pipeline-Driven Approach

We propose a systematic approach to instrument calibration test plan generation, which is driven by the data analysis pipeline. This bottom-up approach is aimed at compelling the science team to put together a data analysis pipeline model in before the I&T phase to aid in better scheduling and planning of calibration testing.

The data analysis pipeline model has inputs that are data products produced by the instrument. The output is the science result that the scientists and data analysts are interested in. For SPARCS, the inputs include science target star images, and calibration data such as dark, bias, flat frames, detector QE, throughput, and other noise sources as shown in Figure 6-5. The output will be calibrated time-series of the absolute flux measurements, which is further used to calculate the flare frequency. This pipeline model provides a framework for the development of the data processing pipeline. Based on the inputs into the data processing pipeline and the expected outputs, we develop an error budget and an incompressible test list.

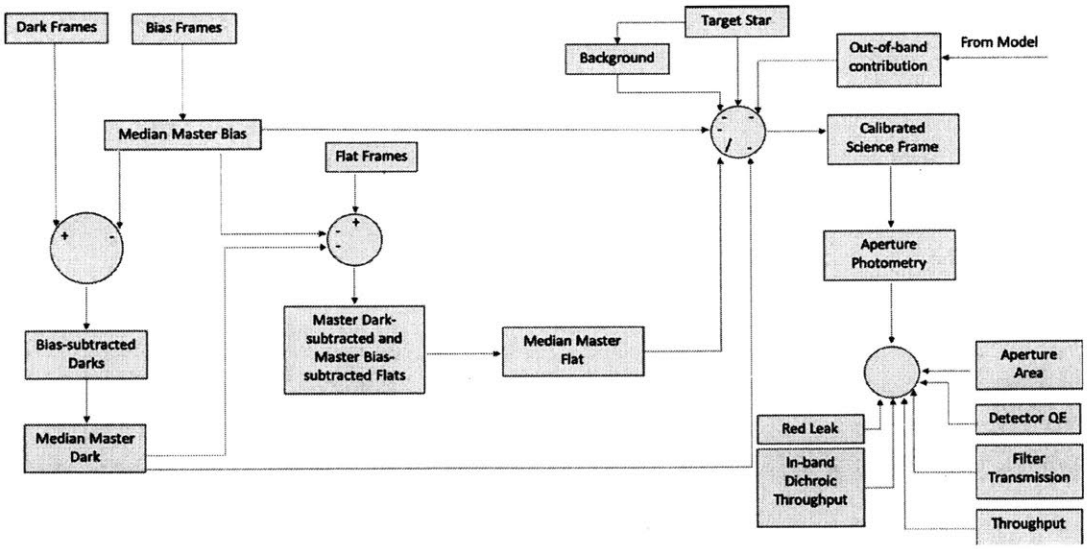

Figure 6-5: Data analysis model for SPARCS.

6.2.5 Error Budgeting

We develop an error budget based on the data analysis pipeline model as shown in Figure 6-6. The figure shows a noise budget with key contributions from read noise, zodiacal noise, red leak, dark noise, bias, jitter noise and photon or shot noise. In addition, we assign acceptable margin of error for calibration measurements for each noise source and the confidence interval. Using these numbers, we estimate the sample size of measurements required.

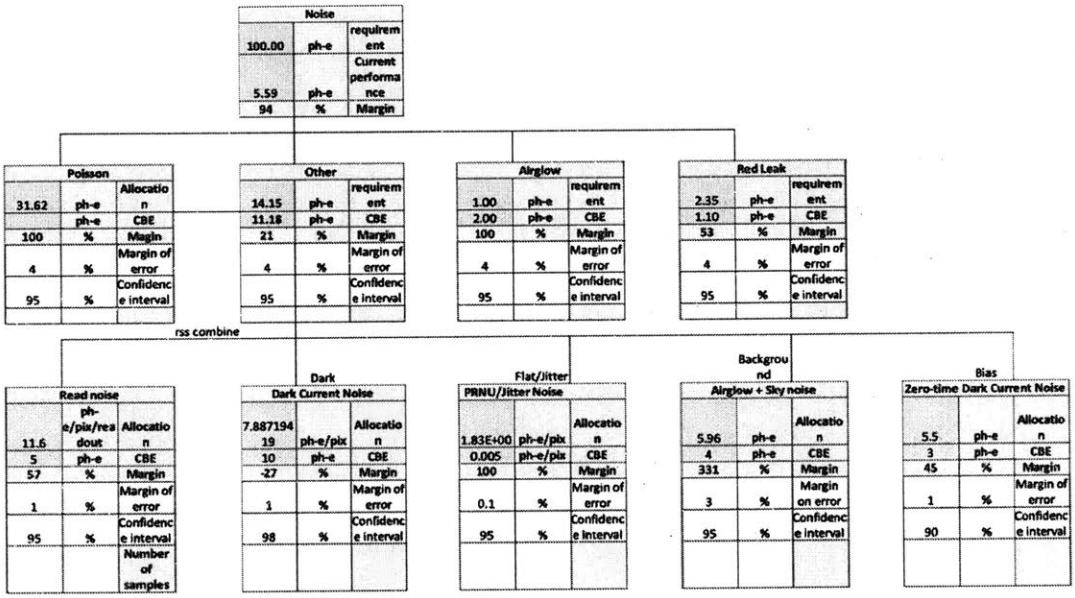

Figure 6-6: Error budget for SPARCS.

6.2.6 Incompressible Test Plan (ITL)

An incompressible test list (ITL) is a list of tests that are required to be completed prior to launch, and cannot be performed in space. These tests are crucial in data processing and arriving at the final science result, and in turn achieving the primary mission objectives. The list provided in Figure 6-7 identifies calibration tests for SPARCS with a description of integration level at which the test should be performed, whether the test can be performed in-flight, the environment for ground

testing, variable parameters, integration time for the images, sample size and estimated duration for each test. Note that the estimated duration only accounts for the time duration for collecting the number of frames at the integration time specified, and does not account for time to cool down or performance tests that are mandatory and performed each time before performing calibration tests. It is critical to understand the duration required for each test to help with scheduling the tests, given that SPARCS has only 10 days (8 hours per day) allocated for calibration testing.

Test	Integration Level	Ground/ In-Flight	Environment	Variable Parameters	Integration Time	Sample Size	Duration (hrs)	Ranking: Science Value / Utility	Ranking: Engineering Difficulty / Cost
Dark	Camera	Ground	TVac	Temperature -50 C -40 C -30 C -20 C	1s 10s 60s 2 min 3 min 5 min 10 min 15 min 30 min	1000 100 15 8 6 5 5 4 2	18.488889	5	1
Bias	Camera	Ground In-Flight	TVac		0 s 0 s	200 200	0.05	5	1
Flat Field / PRNU	Camera Payload	Ground Gound	TVac TVac	Illumination level 25% FW 50% FW 75% FW 100% FW	10 s 10 s	1000 1000	11.11	5	3
Detector QE Throughput	Camera	Ground	TVac	Wavelengths from 120 nm to 1000 nm Temperature -50 C -40 C -30 C -20 C	1 s	400 per wavelength 100 per temp.	18.88	5	5
PTC for Gain and Read Noise	Telescope	Ground	TVac	Different illumination levels 30 points	1 s	200 per point 6000	1.66	5	3
Point Source	Telescope	Ground	Tvac	9 Positions Illumination level 25% FW 50% FW 75% FW	1 s	200 per point 5400	1.5	5	4

Figure 6-7: Incompressible test list for SPARCS.

The tests listed are absolutely necessary for flight data analysis, and cannot be obtained via in-space tests (except for bias measurements). We rank each test by

scientific value and utility based on how crucial the test is in arriving at the science result. Additionally, we also assign a ranking for engineering difficulty and cost of test equipment based on ease of execution and requirement for specialized test equipment to perform these tests.

6.3 Chapter Summary

In this chapter, we demonstrated the contribution of results and takeaways from Chapters 4 and 5 by developing noise budget for the ASTERIA constellation concept and analyzing the feasibility of detecting an Earth analog based on current capabilities. We also provided an overview of SPARCS, an upcoming UV photometry mission, and developed a novel pipeline-driven approach to identify the incompressible test list ITL that presents crucial calibration tests that are absolutely necessary for flight data analysis, and cannot be performed in space. Further, we allocated margin of error and confidence intervals required for these measurements, and estimated testing time that helps with better planning and scheduling ahead of the I&T phase of the mission.

Chapter 7

Summary and Future Work

In this section, we summarize the results from TESS and ASTERIA, and discuss opportunities for improvement and future work. The objective of this thesis was to develop a integrated framework using results from high-fidelity simulations, high-precision laboratory characterization, in-flight calibration testing, and flight data analysis to assess, validate and improve the photometric precision for two missions, TESS and ASTERIA, and present application of results to future missions, ASTERIA constellation and SPARCS.

7.1 Thesis Summary

Chapter 1 presented an introduction to high precision photometry and metrics used to evaluate the performance of these missions. We also presented the motivation for the thesis, specifically, the need for an integrated approach to systematics calibration and noise floor estimation. We discussed the need for performance improvement for large space telescopes, and CubeSat-based transit photometry missions. We also discussed the need for advancing detector technology for CubeSats, in addition to developing a pipeline-driven approach to calibration testing for CubeSat-based science missions.

Chapter 2 focused on providing a background to various methods used for exo-planet discovery and a literature review of the state-of-the art laboratory and flight data analysis techniques developed for high precision transit photometry. We also

Characteristics	Simulation	Laboratory Characterization	Flight Data Calibration
Dark current noise	Yes	Yes	No
Background noise	Yes	Yes	Yes
Read noise	Yes	No	No
Absolute QE	No	Yes	No
QE variation with temperature	No	Yes	Yes
Charge saturation and blooming	No	Yes	Yes
Undershoot	No	Yes	No
Straps	No	Yes	No
Pixel response non-uniformity	Yes	No	No
Inter-pixel variations	Yes	No	No
Intra-pixel variations	Yes	No	No
Jitter effects	Yes	No	Yes
Temperature effects	No	No	Yes
Aperture size	Yes	No	Yes

Table 7.1: TESS systematic noise characteristics and detector properties characterized and calibrated using the integrated framework.

discussed the traditional approach to instrument systematics calibration and the research gap namely, the lack of an integrated framework that draws from results from various areas such as simulations, laboratory characterization, and flight data analysis.

In Chapter 3, we introduced the fully-integrated systematics calibration framework with inherent feedback mechanisms for results from various steps in the process. We used these feedback mechanisms to maximize the utility of results from three key functional areas. We used the results from photometric precision assessment in developing models for systematics characterization and calibration, and assessing the noise floor. We used the results from both systematics calibration to inform flight data analysis steps, and the results from flight data analysis to assess the noise floor. We demonstrated an improvement in bright star photometry using the framework.

In Chapter 4, we applied the integrated framework to TESS. Table 7.1 summarizes all the systematic noise sources and detector properties that we investigated using the integrated framework. We developed a high fidelity simulation of the TESS detector along with all the relevant noise sources. We incorporated flight jitter profiles to esti-

mate jitter error as a function of stellar magnitude. Additionally, we also established that jitter error is linearly proportional to jitter amplitude. Next, we developed precision laboratory techniques to study detector properties such as absolute quantum efficiency, charge saturation and blooming that directly affect photometric precision. We characterized absolute quantum efficiency with an accuracy of less than 2% in the laboratory. Further, we concluded that changes in temperature of the order of 20-25 deg C, that we see in Sector 4, can affect the detector response by over 5% at 1000 nm, which can significantly impact photometric precision. The results from the laboratory experiments directly contributed to the operating temperature selection of the detectors.

We developed a flight data analysis pipeline and performed an ensemble study to understand and characterize the systematics in TESS flight data. We developed a model for jitter noise as a function of jitter amplitude based on the simulation results. Then, we selected the quietest bright stars in sector 6, and estimated the contribution of jitter error. We discovered that there is a source of error in addition to jitter that we term "other error" that contributes significantly to the noise floor. Plausible sources for "other error" could be subpixel sensitivity variations, heater noise and electronics.

Next, we established the noise floor for TESS to be 30 ppm at 1-hour and 16 ppm at 4-hour. The analysis can be repeated on fainter stars to establish a noise floor for specific stellar magnitudes. At 1-hour, most of the jitter noise is removed, and the residual jitter error is about 5 ppm. The remaining error referred to in the thesis as other error is caused due to unknown noise sources. Further investigation into subpixel response variations, heater temperature variations, and noise from electronics will provide an insight into plausible causes for the other error.

We assessed the effect of huge temperature variations on photometric precision. We determined that a temperature change of 20 deg C would decrease the 1-hour photometric precision by 33 ppm. We can remove the temperature effects by detrending with temperature measurements rather than detrending with spline-fitting that does not effectively remove the temperature error.

Lastly, we assessed the outliers with RMS values over 200 ppm. We found two

main causes for the increased noise in these targets. First cause is stellar variability that can be removed using whitening techniques, demonstrated by SPOC [[92]]. The second cause was insufficient pixels in the aperture. We demonstrated an improvement in precision of over 80% by using an aperture of optimal size.

In Chapter 5, we successfully demonstrated the use of CMOS detectors and CubeSats for high precision photometry applications. We accomplished this by developing one of the first data analysis pipelines for CMOS science. In addition, we developed an optimal data reduction and systematic correction framework for ASTERIA. Tabel 7.2 summarizes the systematic noise characteristics and detector properties that we characterized and calibrated using the integrated framework.

Using a simulation of the CMOS detector and realistic jitter profiles, we first assessed the photometric performance of ASTERIA and the contributions of various noise sources including sub-pixel response variations to photometric precision. We then developed laboratory techniques to study the systematic effects in the CMOS detector and telescope assembly due to the lack of calibration data from prior to launch. We demonstrated the efficacy of pixel-by-pixel corrections for the column-dependent gain and offset variations, and showed an improvement of 15% in photometric performance using this method.

We developed in-flight tests to calibrate the science data, and analyzed the science frames for HD219134. We demonstrated an improvement in performance of over 55% using the optimal data reduction framework. The photometric precision achieved for HD219134 using bias subtraction, background subtraction and flat correction techniques is about twice photon noise limit. The residual systematic noise for HD219134 at 2-hour was about 65 ppm. We established a residual systematic noise floor of about 15 ppm at 2-hour timescales for very bright stars like Alpha Cen using the piezo-stage fine pointing control system.

In Chapters 4 and 5, we effectively demonstrated the integration of results from each step and utility of the integrated framework in improving our understanding of instrument systematics and developing techniques to characterize and correct for these effects. We developed an optimal systematics correction pipeline and established

Characteristics	Simulation	Laboratory Characterization	Flight Data Calibration
Dark current noise	No	Yes	Yes
Bias	No	Yes	Yes
Background noise	Yes	Yes	Yes
Read noise	No	Yes	Yes
Pixel response non-uniformity	Yes	Yes	No
Inter-pixel variations	Yes	No	No
Intra-pixel variations	Yes	No	No
Column-dependent gain and offset variations	Yes	Yes	No
Jitter effects	Yes	No	Yes
Temperature effects	No	No	Yes

Table 7.2: ASTERIA systematic noise characteristics and detector properties characterized and calibrated using the integrated framework.

the noise floor, in addition to applying the results to future missions.

In Chapter 6, we demonstrated how the TESS and ASTERIA noise floor serves as a metric for designing upcoming missions such as the ASTERIA constellation. We developed the noise budget and feasibility study for the constellation concept, in addition to presenting the tradespace for detector technology currently available.

We also developed and presented a pipeline driven approach to calibration test plan generation for SPARCS, a UV photometry mission due for launch in 2021. We developed a noise budget and an incompressible test list that consists of a list of all tests that are crucial for flight data analysis and ought to be performed prior to launch.

7.2 Thesis Contributions

We discuss the contributions of this thesis to future missions and the scientific community below:

1. Drove TESS throughput and photon noise limit calculations, and setting of operating temperature of the TESS detectors

- By characterizing the absolute QE with an accuracy of 2% by integrating a very

precise light source stabilization and minimizing noise in every measurement.

- Found that response of the detector varies by 5% at 1000 nm for a 20 deg C change that drove temperature stability criteria on detectors.

2. Established the noise floor for TESS: it is 16 ppm at 4-hours

- Also quantified the effect of temperature variation on photometric precision: 30 ppm at 1-hour.

- Based on ensemble study of non-variable bright stars during a quiet period of the orbit.

3. Established one of the first data analysis pipelines for CMOS science

- Demonstrated photometric precision for HD219134 to within 2 times photon noise (65 ppm at 2-hour).

- Established a residual systematic noise floor of 15 ppm at 2-hours for the brightest of stars like Alpha Cen.

4. Demonstrated improvement of 15% in photometric precision for ASTERIA flight-like detectors

- Using a laboratory characterization framework for pixel-by-pixel correction and removal of column dependent gain and offset variations.

- Can be applied to flight calibration for future missions.

5. Developed noise budget and detector trade study for ASTERIA constellation concept

- Based on TESS noise floor and prototype ASTERIA performance metrics.

6. Developed an incompressible test list for systematics calibration for SPARCS

- Based on a novel pipeline-driven approach to calibration test plan generation.

- This will serve as a valuable tool for future science CubeSat missions.

7.3 Future Work

In this section, we discuss future work as applicable to TESS, ASTERIA and SPARCS missions.

TESS

1. The next step would be to study the contribution of subpixel variations to instrument systematic noise. To do this, we run a series of laboratory experiments on the precision testbed with very high photometric stability. We simulate stellar images and translate the images using various intrapixel positions and phases. By doing this, we can calculate the variation in response that is directly correlated with the phase and position of the target star on the detector.

2. Extend the TESS noise floor study to all the sectors, and perform the analysis on a wider sample of stars adapting and optimizing the spline detrending to each individual star. This would give a more comprehensive understanding of TESS instrument behavior over various sectors of operation.

3. Assess the behavior of the heaters and their potential influence on photometric precision. As we noted in Chapter 4, one of the reasons for the "other error" could be heater noise. We have seen that the heater response has noise levels at various timescales but we have not yet performed a detailed analysis on its effect on precision.

ASTERIA

1. The present work utilizes data sets for HD219134 and Alpha Centauri from observations with the best signal-to-noise ratio, and analyzes systematics contribution from jitter, and background contamination. The next step would be to extend the analysis to the entire available dataset to get a better understanding of instrument behavior over the last two years of operation.

2. As we refine the ASTERIA constellation concept further, one of the key tasks will be to assess the feasibility of achieving the 14 ppm instrument noise floor. Based on the data that we have from ASTERIA and TESS, a comprehensive study of the instrument noise floor at the ASTERIA constellation timescale of 6.5-hour can be performed.

SPARCS

1. Future work includes detailed calibration test plan development based on the pipeline-driven incompressible test list. As the mission progresses into integration and testing in the next few months, one of the key tasks will be scheduling and writing detailed test plans. With the ITL, we can better estimate the time required for each test and schedule tests accordingly.

Appendix A

List of Acronyms

FFI Full Frame Images

CCD Charge Coupled Devices

CMOS Complementary Metal Oxide Semiconductor

TESS Transiting Exoplanet Survey Satellite

ASTERIA Arcsecond Space Telescope Enabling Research In Astrophysics

PRNU Pixel Response Non-Uniformity

PSF Point Spread Function

QE Quantum Efficiency

PDC Pre-search Data Conditioning

SAP Simple Aperture Photometry

PDCSAP Pre-search Data Conditioned Simple Aperture Photometry

TPF Target Pixel File

FITS Flexible Image Transport System

HDU Header Data Unit

TIC TESS Input Catalog

DVA Differential Velocity Aberration

CDPP Cumulative Differential Photometric Precision

TCEs Threshold Crossing Events

DV Data Validation

DHU Data Handling Unit

SPOC Science Processing Operations Center

LDLS Laser-Driven Light Source

FOV Field-of-View

SSS Super Stable Source

RMS Root Mean Square

MAST Mikulski Archive for Space Telescopes

FWHM Full Width Half Maximum

ACS Attitude Control System

ADU Analog-to-Digital Unit

Tvac Thermal Vacuum

Appendix B

Quiet Star Selection for Jitter Analysis

In this Appendix, we show the TICIDs, TESS magnitudes, 1-hr photometric precision, detrended light curves of the 17 quiet stars from sector 6 that were selected for the jitter analysis.

TICID	TESS Magnitude	1-hr Photometric Precision ppm
30960202.0	5.99	38.85
52687259.0	5.34	34.56
93281916.0	5.69	38.10
124854318.0	5.86	36.62
140690428.0	5.82	40.30
156712422.0	5.77	30.73
170225363.0	4.69	36.39
172734582.0	5.89	40.94
176521059.0	5.26	44.05
177075997.0	5.51	44.44
192789761.0	5.56	35.28
255686390.0	4.38	24.20
260416268.0	5.46	35.17
300865934.0	5.82	42.83
333042609.0	5.97	43.99
355275755.0	4.98	42.03
442956224.0	5.67	43.15

Table B.1: 1-hr photometric precision and timescale.

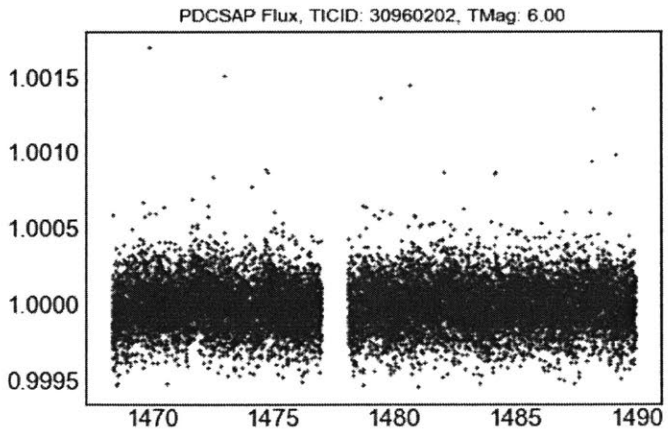

Figure B-1: Detrended 2-min PDCSAP light curve

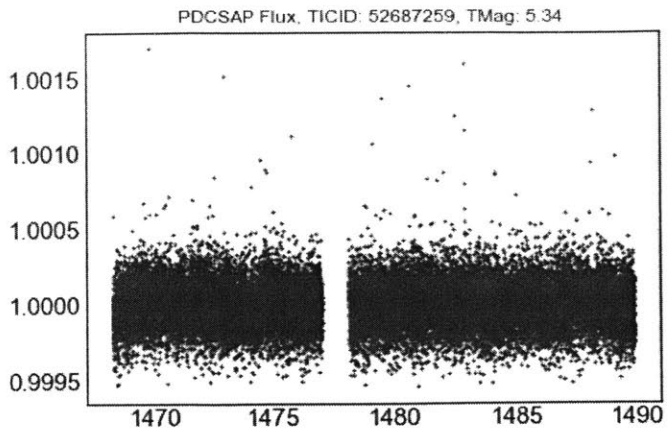

Figure B-2: Detrended 2-min PDCSAP light curve

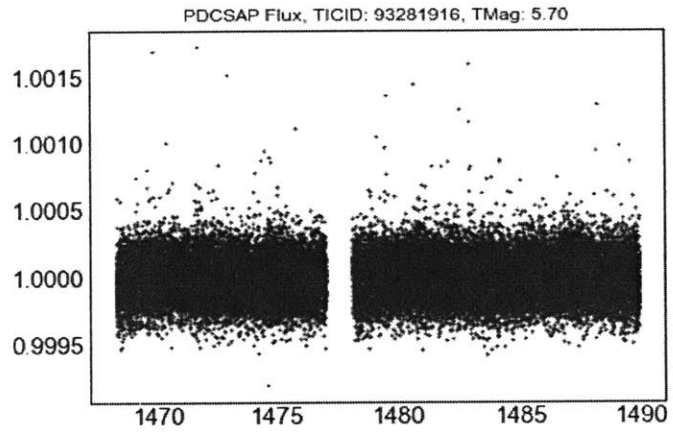

Figure B-3: Detrended 2-min PDCSAP light curve

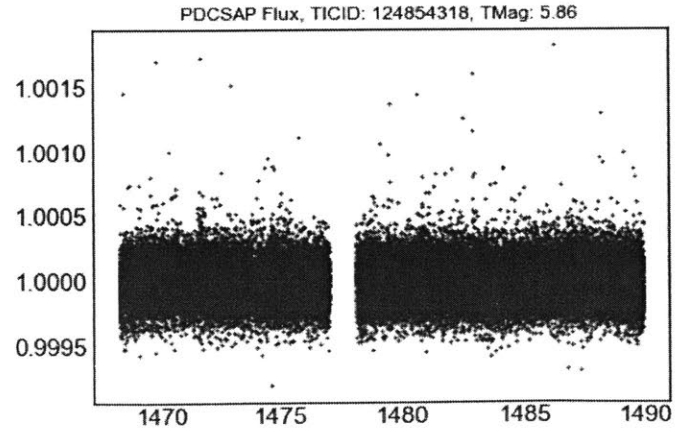

Figure B-4: Detrended 2-min PDCSAP light curve

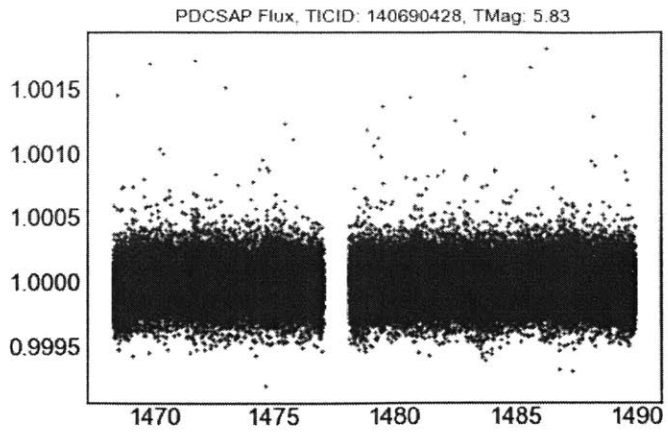

Figure B-5: Detrended 2-min PDCSAP light curve

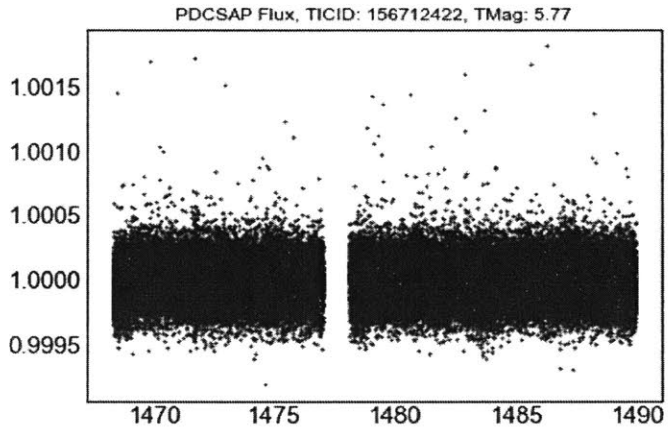

Figure B-6: Detrended 2-min PDCSAP light curve

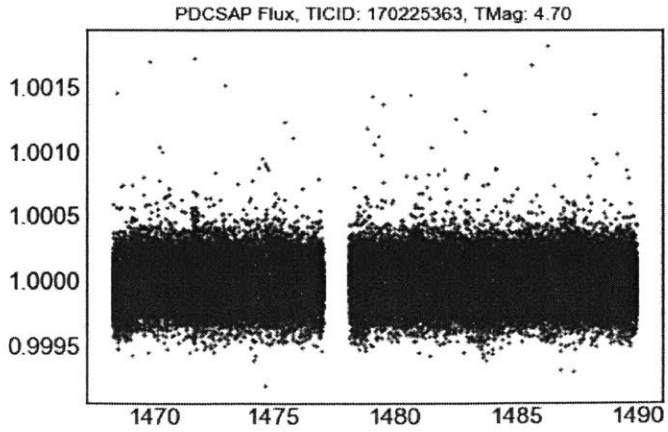

Figure B-7: Detrended 2-min PDCSAP light curve

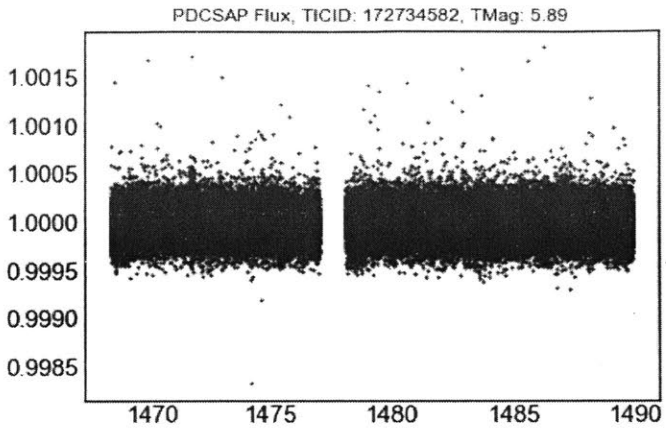

Figure B-8: Detrended 2-min PDCSAP light curve

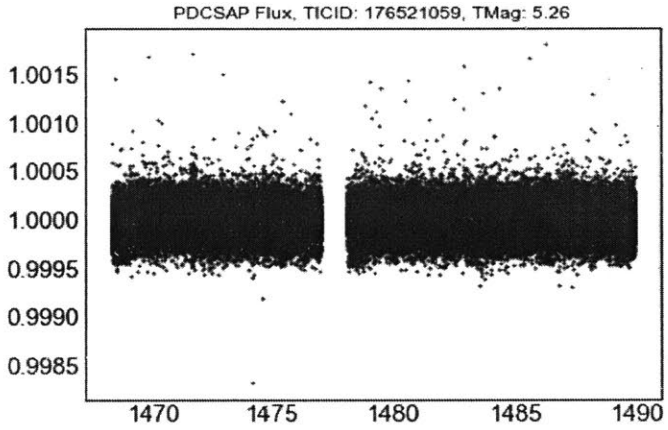

Figure B-9: Detrended 2-min PDCSAP light curve

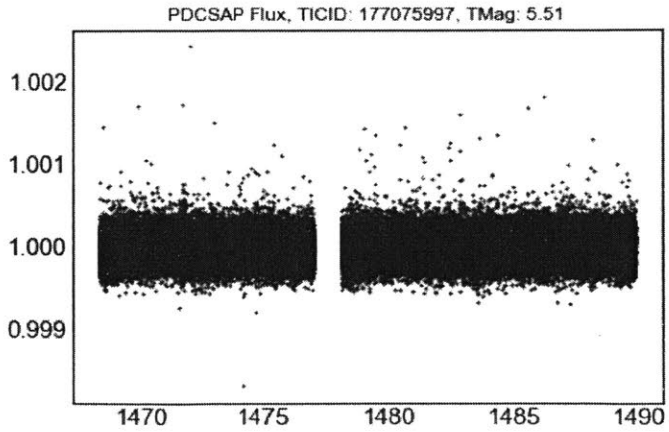

Figure B-10: Detrended 2-min PDCSAP light curve

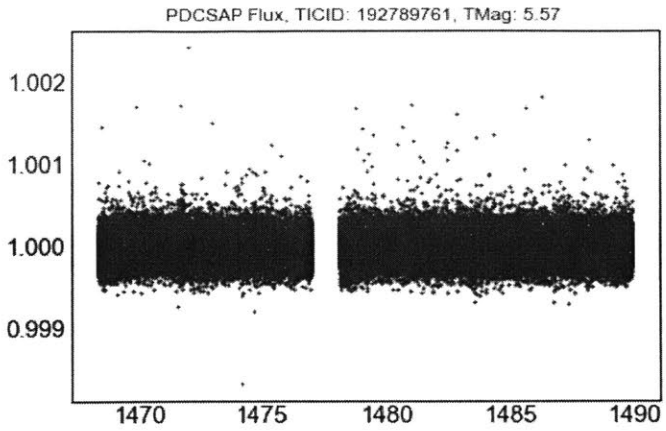

Figure B-11: Detrended 2-min PDCSAP light curve

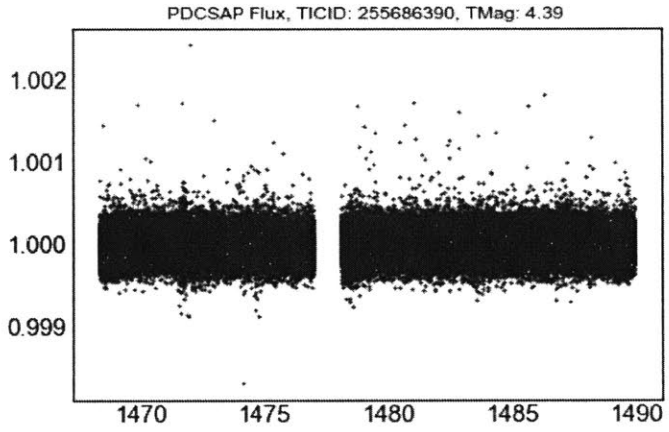

Figure B-12: Detrended 2-min PDCSAP light curve

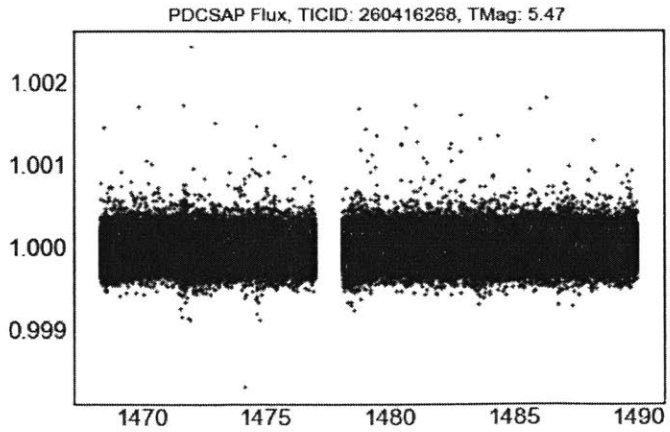

Figure B-13: Detrended 2-min PDCSAP light curve

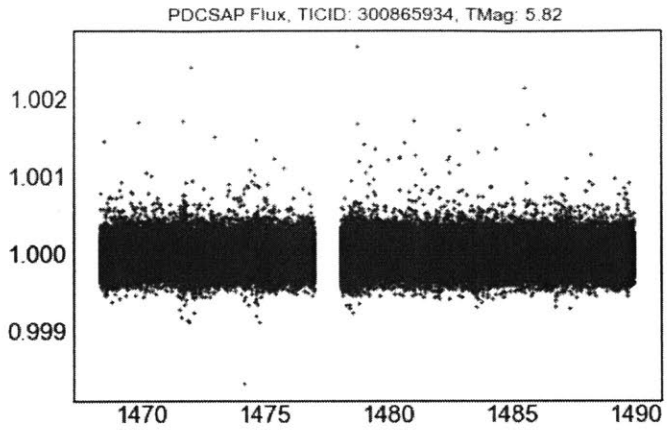

Figure B-14: Detrended 2-min PDCSAP light curve

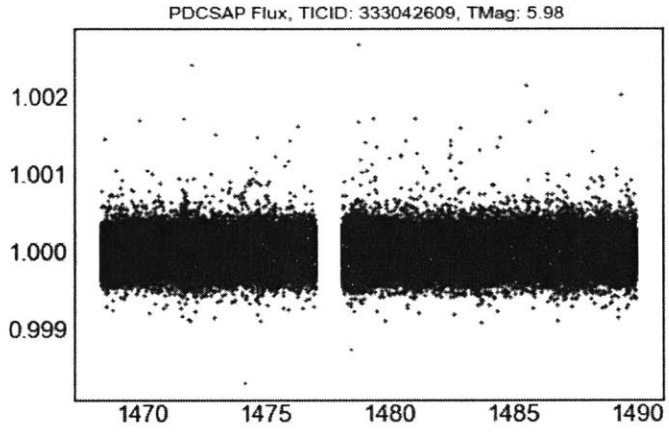

Figure B-15: Detrended 2-min PDCSAP light curve

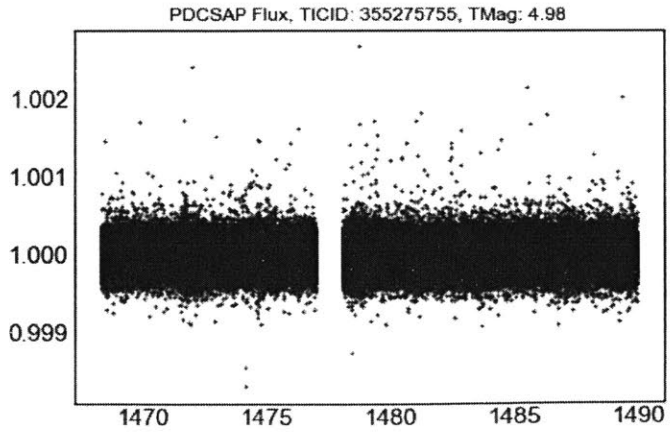

Figure B-16: Detrended 2-min PDCSAP light curve

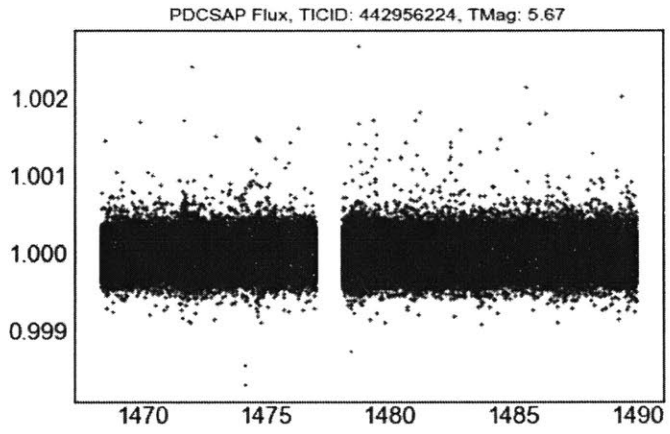

Figure B-17: Detrended 2-min PDCSAP light curve

Appendix C

Quiet Star Selection for Temperature Analysis

In this Appendix, we show the TICIDs, TESS magnitudes, and 2-min detrended PDCSAP light curves of the 16 quiet stars from sector 4 that were selected for the temperature analysis.

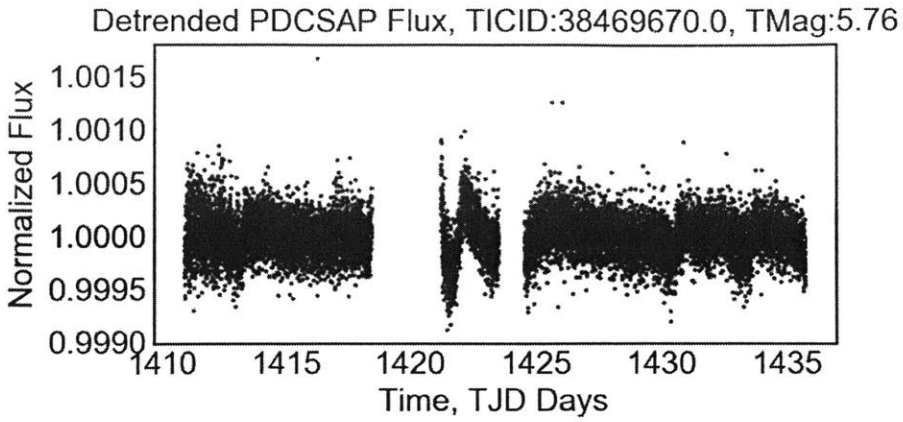

Figure C-1: Detrended 2-min PDCSAP light curve

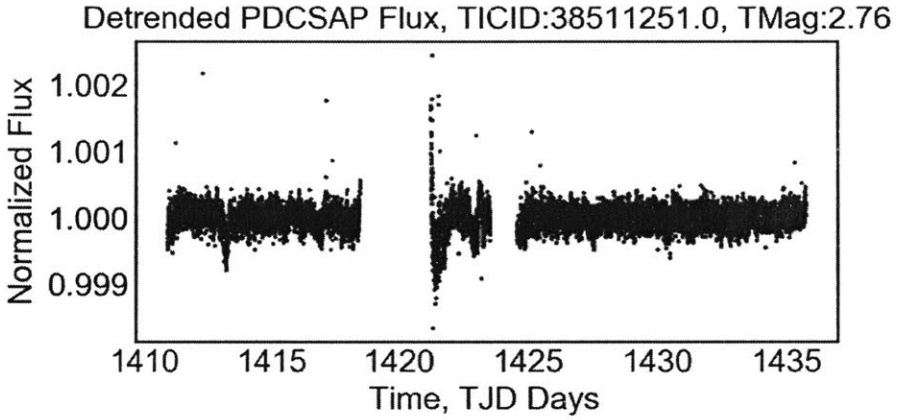

Figure C-2: Detrended 2-min PDCSAP light curve

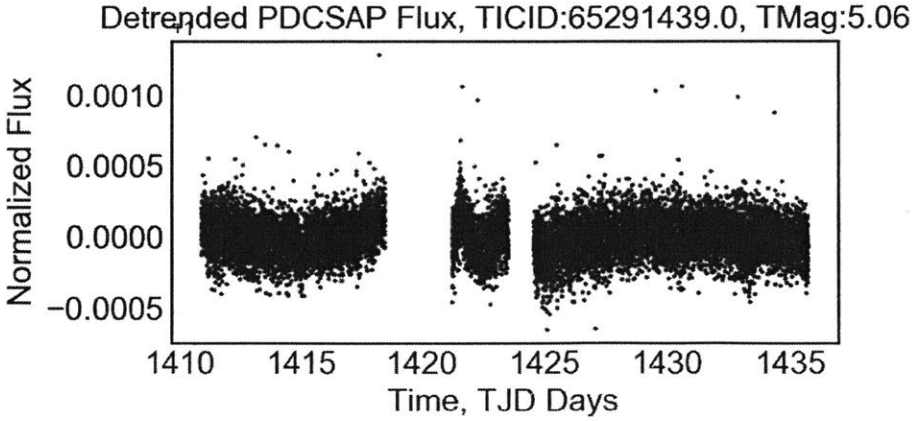

Figure C-3: Detrended 2-min PDCSAP light curve

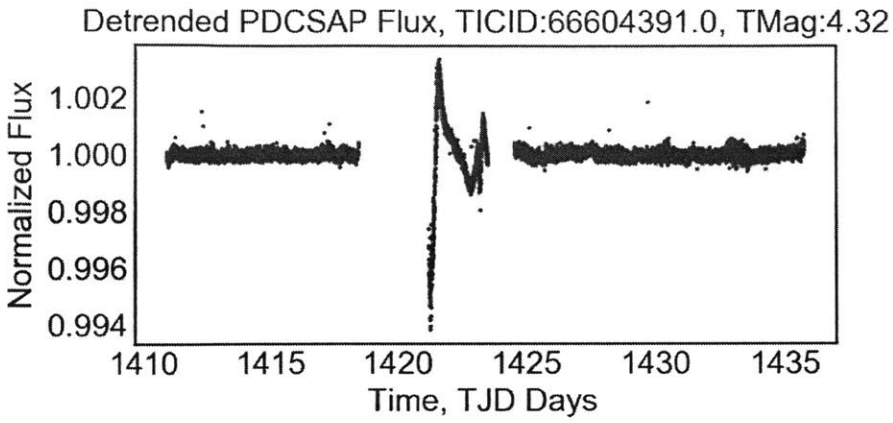

Figure C-4: Detrended 2-min PDCSAP light curve

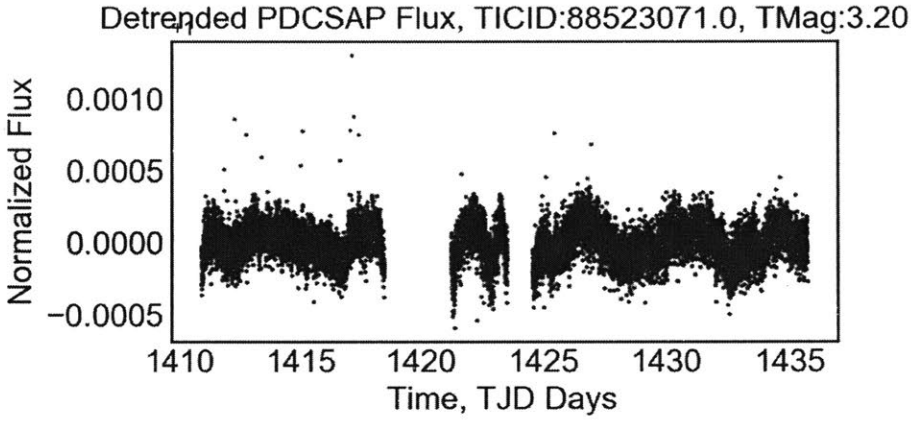

Figure C-5: Detrended 2-min PDCSAP light curve

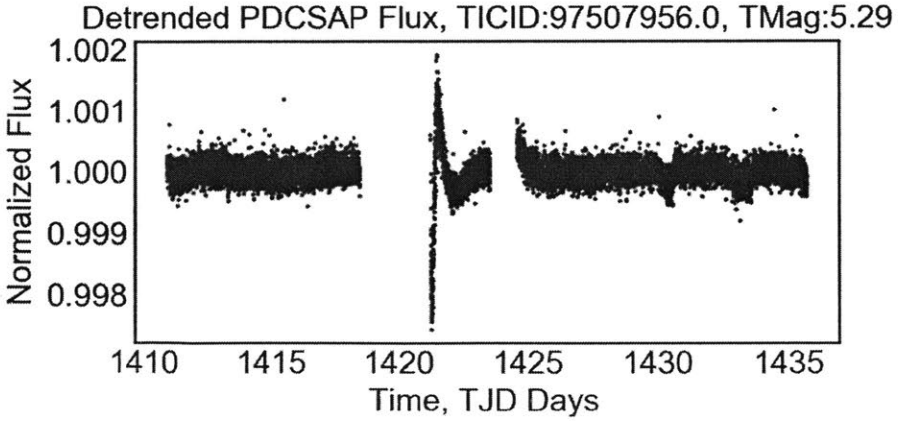

Figure C-6: Detrended 2-min PDCSAP light curve

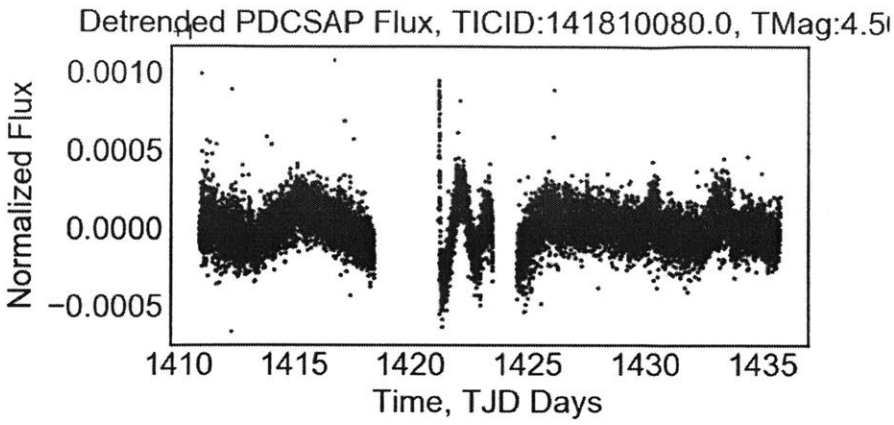

Figure C-7: Detrended 2-min PDCSAP light curve

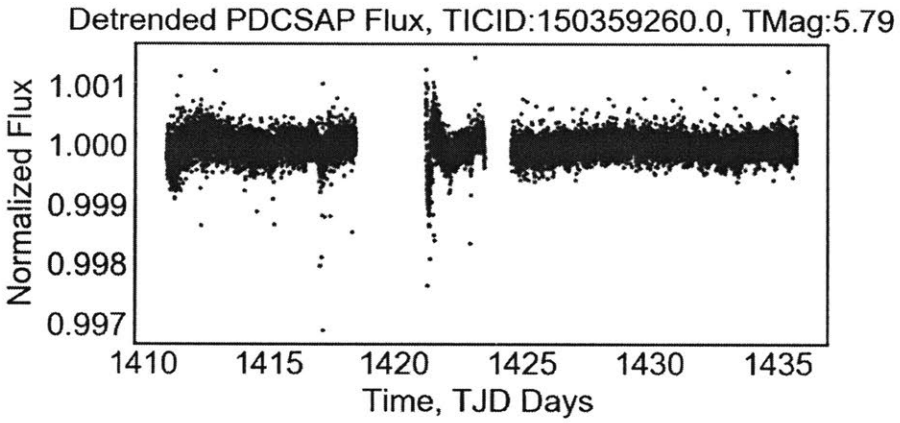

Figure C-8: Detrended 2-min PDCSAP light curve

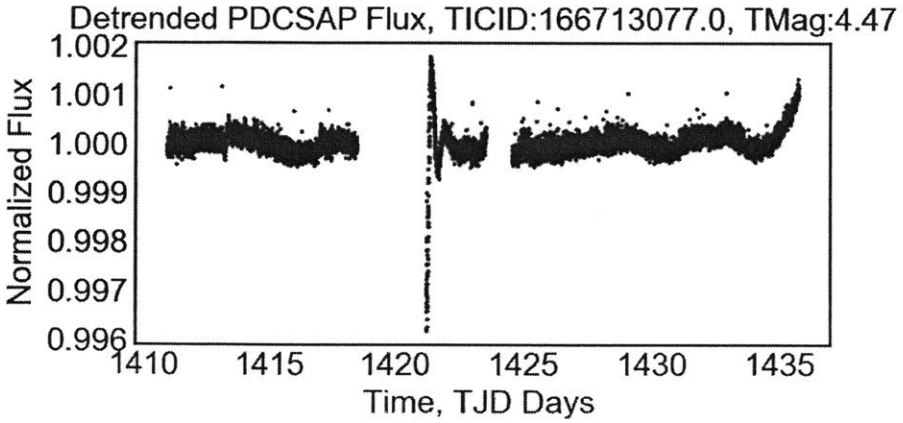

Figure C-9: Detrended 2-min PDCSAP light curve

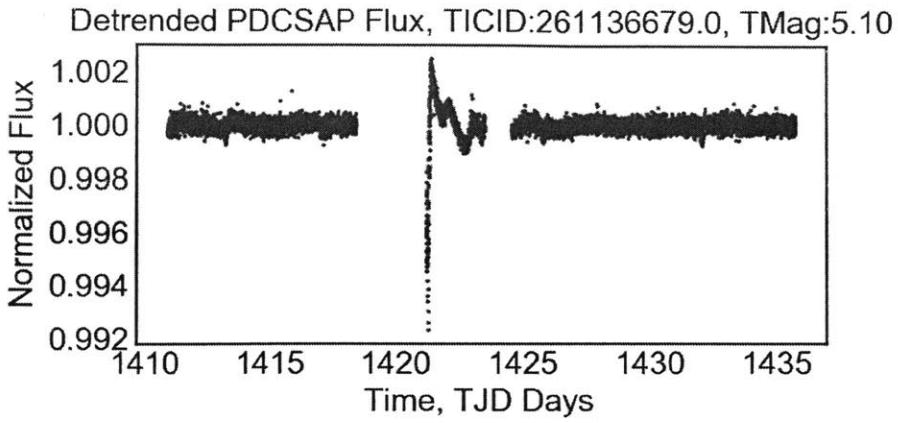

Figure C-10: Detrended 2-min PDCSAP light curve

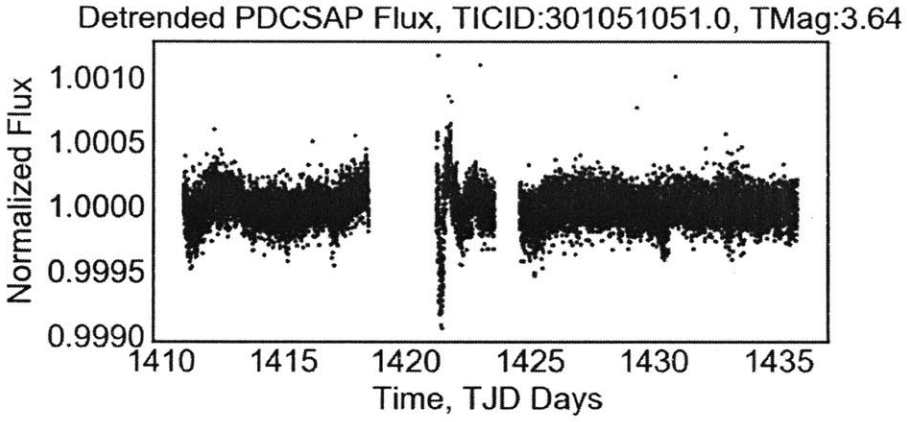

Figure C-11: Detrended 2-min PDCSAP light curve

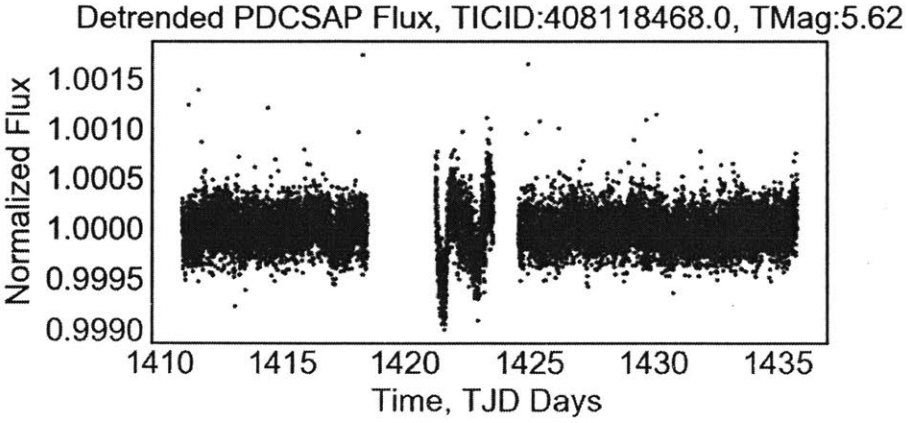

Figure C-12: Detrended 2-min PDCSAP light curve

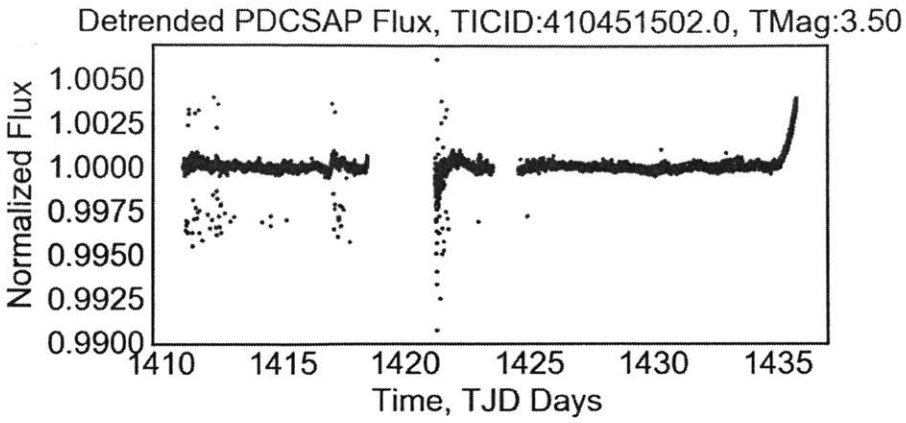

Figure C-13: Detrended 2-min PDCSAP light curve

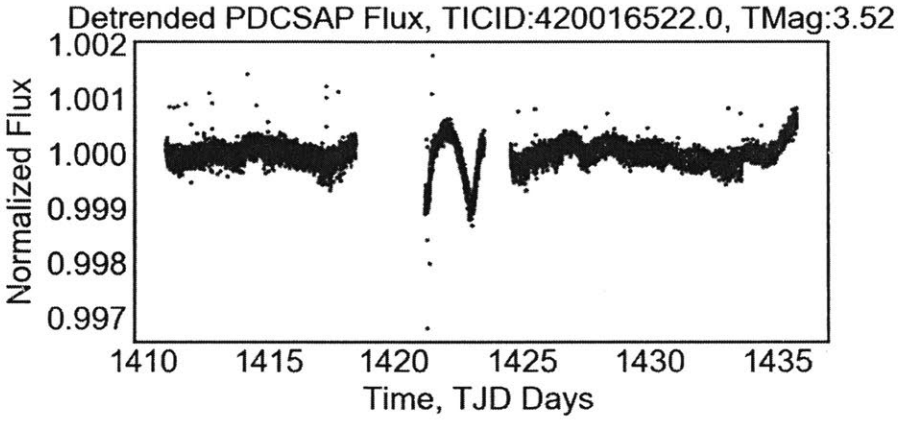

Figure C-14: Detrended 2-min PDCSAP light curve

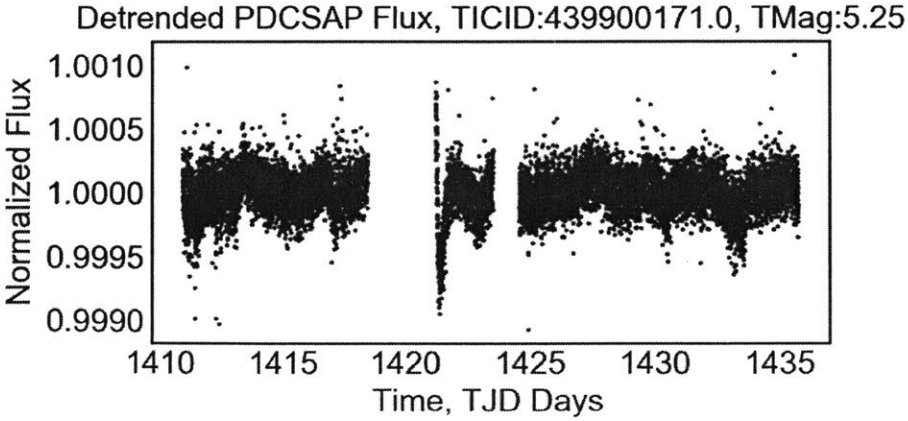

Figure C-15: Detrended 2-min PDCSAP light curve

Bibliography

[1] Michel Mayor and Didier Queloz. A jupiter-mass companion to a solar-type star. *Nature*, 378(6555):355, 1995.

[2] Sara Seager. Exoplanets. *Exoplanets*, 2010.

[3] Heike Rauer, Conny Aerts, J Cabrera, PLATO Team, et al. The plato mission. *Astronomische Nachrichten*, 337(8-9):961–963, 2016.

[4] Charles Beichman, Bjoern Benneke, Heather Knutson, Roger Smith, Pierre-Olivier Lagage, Courtney Dressing, David Latham, Jonathan Lunine, Stephan Birkmann, Pierre Ferruit, et al. Observations of transiting exoplanets with the james webb space telescope (jwst). *Publications of the Astronomical Society of the Pacific*, 126(946):1134, 2014.

[5] Karl R Stapelfeldt, Frank G Dekens, Michael P Brenner, Keith R Warfield, Ruslan Belikov, Paul B Brugarolas, Geoffrey Bryden, Kerri L Cahoy, Supriya Chakrabarti, Serge Dubovitsky, et al. Exo-c: a probe-scale space observatory for direct imaging and spectroscopy of extrasolar planetary systems. In *Techniques and Instrumentation for Detection of Exoplanets VII*, volume 9605, page 96050T. International Society for Optics and Photonics, 2015.

[6] Sara Seager, Margaret Turnbull, William Sparks, Mark Thomson, Stuart B Shaklan, Aki Roberge, Marc Kuchner, N Jeremy Kasdin, Shawn Domagal-Goldman, Webster Cash, et al. The exo-s probe class starshade mission. In *Techniques and Instrumentation for Detection of Exoplanets VII*, volume 9605, page 96050W. International Society for Optics and Photonics, 2015.

[7] Debra A Fischer, Andrew W Howard, Greg P Laughlin, Bruce Macintosh, Suvrath Mahadevan, Johannes Sahlmann, and Jennifer C Yee. Exoplanet detection techniques. *arXiv preprint arXiv:1505.06869*, 2015.

[8] R Vanderspek, J Doty, M Fausnaugh, and J Villasenor. Tess instrument handbook. Technical report, Tech. rep., Kavli Institute for Astrophysics and Space Science, 2018.

[9] Philip Nutzman, D Charbonneau, J Irwin, C Burke, Z Berta, and EE Falco. The mearth observatory and the search for transiting habitable superearths. In *AAS/Division for Planetary Sciences Meeting Abstracts# 41*, volume 41, 2009.

[10] D Pollacco, I Skillen, A Cameron, D Christian, J Irwin, T Lister, R Street, R West, W Clarkson, N Evans, et al. The wasp project and superwasp camera. In *Close Binaries in the 21st Century: New Opportunities and Challenges*, pages 251–253. Springer, 2006.

[11] Joshua Pepper, Richard W Pogge, DL DePoy, JL Marshall, KZ Stanek, Amelia M Stutz, Shawn Poindexter, Robert Siverd, Thomas P OâĂŹBrien, Mark Trueblood, et al. The kilodegree extremely little telescope (kelt): A small robotic telescope for large-area synoptic surveys. *Publications of the Astronomical Society of the Pacific*, 119(858):923, 2007.

[12] Emmanuël Jehin, Michaël Gillon, Didier Queloz, Pierre Magain, Jean Manfroid, Virginie Chantry, Monica Lendl, Damien Hutsemékers, and Stephane Udry. Trappist: Transiting planets and planetesimals small telescope. *The Messenger*, 145(2), 2011.

[13] RL Akeson, X Chen, D Ciardi, M Crane, J Good, M Harbut, E Jackson, SR Kane, AC Laity, S Leifer, et al. The nasa exoplanet archive: data and tools for exoplanet research. *Publications of the Astronomical Society of the Pacific*, 125(930):989, 2013.

[14] George R Ricker, Joshua N Winn, Roland Vanderspek, David W Latham, Gáspár Á Bakos, Jacob L Bean, Zachory K Berta-Thompson, Timothy M Brown, Lars Buchhave, Nathaniel R Butler, et al. Transiting exoplanet survey satellite. *Journal of Astronomical Telescopes, Instruments, and Systems*, 1(1):014003, 2014.

[15] Matthew W Smith, Sara Seager, Christopher M Pong, Jesus S Villaseñor, George R Ricker, David W Miller, Mary E Knapp, Grant T Farmer, and Rebecca Jensen-Clem. Exoplanetsat: detecting transiting exoplanets using a low-cost cubesat platform. In *Space Telescopes and Instrumentation 2010: Optical, Infrared, and Millimeter Wave*, volume 7731, page 773127. International Society for Optics and Photonics, 2010.

[16] Brice-Olivier Demory, David Ehrenreich, Didier Queloz, Sara Seager, Ronald Gilliland, William J Chaplin, Charles Proffitt, Michael Gillon, Maximilian N Günther, Björn Benneke, et al. Hubble space telescope search for the transit of the earth-mass exoplanet α centauri b b. *Monthly Notices of the Royal Astronomical Society*, 450(2):2043–2051, 2015.

[17] Evgenya Shkolnik. Monitoring the high-energy radiation environment of exoplanets around lowmass stars with sparcs (star-planet activity research cubesat). *NASA APRA Proposal*, 2016.

[18] David G Koch, William J Borucki, Gibor Basri, Natalie M Batalha, Timothy M Brown, Douglas Caldwell, Jørgen Christensen-Dalsgaard, William D Cochran,

Edna DeVore, Edward W Dunham, et al. Kepler mission design, realized photometric performance, and early science. *The Astrophysical Journal Letters*, 713(2):L79, 2010.

[19] FP Wildi, A Deline, and B Chazelas. A white super-stable source for the metrology of astronomical photometers. In *Techniques and Instrumentation for Detection of Exoplanets VII*, volume 9605, page 96051T. International Society for Optics and Photonics, 2015.

[20] Mark A Martella, Don A Byrd, Stew Willis, Peter Spuhler, Noah Siegel, and Chris Stewart. Optical testing of the kepler photometer in a thermal vacuum environment at ball aerospace. In *UV/Optical/IR Space Telescopes: Innovative Technologies and Concepts IV*, volume 7436, page 74360S. International Society for Optics and Photonics, 2009.

[21] Drake Deming, Heather Knutson, Joshua Kammer, Benjamin J Fulton, James Ingalls, Sean Carey, Adam Burrows, Jonathan J Fortney, Kamen Todorov, Eric Agol, et al. Spitzer secondary eclipses of the dense, modestly-irradiated, giant exoplanet hat-p-using pixel-level decorrelation. *The Astrophysical Journal*, 805(2):132, 2015.

[22] Rodrigo Luger, Eric Agol, Ethan Kruse, Rory Barnes, Andrew Becker, Daniel Foreman-Mackey, and Drake Deming. Everest: pixel level decorrelation of k2 light curves. *The Astronomical Journal*, 152(4):100, 2016.

[23] Liang Yu, Andrew Vanderburg, Chelsea Huang, Christopher J Shallue, Ian JM Crossfield, B Scott Gaudi, Tansu Daylan, Anne Dattilo, David J Armstrong, George R Ricker, et al. Identifying exoplanets with deep learning. iii. automated triage and vetting of tess candidates. *The Astronomical Journal*, 158(1):25, 2019.

[24] Christopher J Shallue and Andrew Vanderburg. Identifying exoplanets with deep learning: A five-planet resonant chain around kepler-80 and an eighth planet around kepler-90. *The Astronomical Journal*, 155(2):94, 2018.

[25] Jason A Dittmann, Jonathan M Irwin, David Charbonneau, Xavier Bonfils, Nicola Astudillo-Defru, Raphaëlle D Haywood, Zachory K Berta-Thompson, Elisabeth R Newton, Joseph E Rodriguez, Jennifer G Winters, et al. A temperate rocky super-earth transiting a nearby cool star. *Nature*, 544(7650):333, 2017.

[26] C Broeg, A Fortier, D Ehrenreich, Yann Alibert, W Baumjohann, Willy Benz, Magali Deleuil, Michaël Gillon, A Ivanov, René Liseau, et al. Cheops: A transit photometry mission for esa's small mission programme. In *EPJ Web of Conferences*, volume 47, page 03005. EDP Sciences, 2013.

[27] Andrea Fortier, Thomas Beck, Willy Benz, Christopher Broeg, Virginie Cessa, David Ehrenreich, and Nicolas Thomas. Cheops: a space telescope for ultra-high

precision photometry of exoplanet transits. In *Space Telescopes and Instrumentation 2014: Optical, Infrared, and Millimeter Wave*, volume 9143, page 91432J. International Society for Optics and Photonics, 2014.

[28] Space Studies Board, Engineering National Academies of Sciences, Medicine, et al. *Achieving Science with CubeSats: Thinking Inside the Box.* National Academies Press, 2016.

[29] Armen Poghosyan and Alessandro Golkar. Cubesat evolution: Analyzing cubesat capabilities for conducting science missions. *Progress in Aerospace Sciences*, 88:59–83, 2017.

[30] Gregory W Henry, Geoffrey W Marcy, R Paul Butler, and Steven S Vogt. A transiting âĂIJ51 peg-likeâĂİ planet. *The Astrophysical Journal Letters*, 529(1):L41, 1999.

[31] David Charbonneau, Timothy M Brown, David W Latham, and Michel Mayor. Detection of planetary transits across a sun-like star. *The Astrophysical Journal Letters*, 529(1):L45, 1999.

[32] A Collier Cameron, DM Wilson, RG West, L Hebb, X-B Wang, S Aigrain, F Bouchy, DJ Christian, WI Clarkson, B Enoch, et al. Efficient identification of exoplanetary transit candidates from superwasp light curves. *Monthly Notices of the Royal Astronomical Society*, 380(3):1230–1244, 2007.

[33] GÁ Bakos, G Kovács, G Torres, DA Fischer, DW Latham, RW Noyes, DD Sasselov, T Mazeh, A Shporer, RP Butler, et al. Hd 147506b: a supermassive planet in an eccentric orbit transiting a bright star. *The Astrophysical Journal*, 670(1):826, 2007.

[34] A Léger, D Rouan, Jodi Schneider, P Barge, M Fridlund, B Samuel, M Ollivier, E Guenther, M Deleuil, HJ Deeg, et al. Transiting exoplanets from the corot space mission-viii. corot-7b: the first super-earth with measured radius. *Astronomy & Astrophysics*, 506(1):287–302, 2009.

[35] Michael W Werner, TL Roellig, FJ Low, George H Rieke, M Rieke, WF Hoffmann, E Young, JR Houck, B Brandl, GG Fazio, et al. The spitzer space telescope mission. *The Astrophysical Journal Supplement Series*, 154(1):1, 2004.

[36] David K Sing, F Pont, Suzanne Aigrain, D Charbonneau, J-M Désert, N Gibson, R Gilliland, W Hayek, G Henry, H Knutson, et al. Hubble space telescope transmission spectroscopy of the exoplanet hd 189733b: high-altitude atmospheric haze in the optical and near-ultraviolet with stis. *Monthly Notices of the Royal Astronomical Society*, 416(2):1443–1455, 2011.

[37] David Charbonneau, Timothy M Brown, Robert W Noyes, and Ronald L Gilliland. Detection of an extrasolar planet atmosphere. *The Astrophysical Journal*, 568(1):377, 2002.

[38] David Charbonneau, Lori E Allen, S Thomas Megeath, Guillermo Torres, Roi Alonso, Timothy M Brown, Ronald L Gilliland, David W Latham, Georgi Mandushev, Francis T OâĂŹDonovan, et al. Detection of thermal emission from an extrasolar planet. *The Astrophysical Journal*, 626(1):523, 2005.

[39] D Charbonneau, TM Brown, A Burrows, and G Laughlin. Protostars and planets v, ed. *Reipurth, D. Jewitt and K. Keil*, 701, 2007.

[40] David Charbonneau, Heather A Knutson, Travis Barman, Lori E Allen, Michel Mayor, S Thomas Megeath, Didier Queloz, and Stéphane Udry. The broadband infrared emission spectrum of the exoplanet hd 189733b. *The Astrophysical Journal*, 686(2):1341, 2008.

[41] Drake Deming, Sara Seager, L Jeremy Richardson, and Joseph Harrington. Infrared radiation from an extrasolar planet. *Nature*, 434(7034):740, 2005.

[42] Drake Deming, Joseph Harrington, Sara Seager, and L Jeremy Richardson. Strong infrared emission from the extrasolar planet hd 189733b. *The Astrophysical Journal*, 644(1):560, 2006.

[43] Drake Deming, Joseph Harrington, Gregory Laughlin, Sara Seager, Sarah B Navarro, William C Bowman, and Karen Horning. Spitzer transit and secondary eclipse photometry of gj 436b. *The Astrophysical Journal Letters*, 667(2):L199, 2007.

[44] Carl J Grillmair, D Charbonneau, A Burrows, L Armus, J Stauffer, V Meadows, J Van Cleve, and D Levine. A spitzer spectrum of the exoplanet hd 189733b. *The Astrophysical Journal Letters*, 658(2):L115, 2007.

[45] Carl J Grillmair, Adam Burrows, David Charbonneau, Lee Armus, John Stauffer, Victoria Meadows, Jeffrey Van Cleve, Kaspar Von Braun, and Deborah Levine. Strong water absorption in the dayside emission spectrum of the planet hd 189733b. *Nature*, 456(7223):767, 2008.

[46] Joseph Harrington, Brad M Hansen, Statia H Luszcz, Sara Seager, Drake Deming, Kristen Menou, James Y-K Cho, and L Jeremy Richardson. The phase-dependent infrared brightness of the extrasolar planet ÊŁ andromedae b. *Science*, 314(5799):623–626, 2006.

[47] Joseph Harrington, Statia Luszcz, Sara Seager, Drake Deming, and L Jeremy Richardson. The hottest planet. *Nature*, 447(7145):691, 2007.

[48] Heather A Knutson, David Charbonneau, Lori E Allen, Jonathan J Fortney, Eric Agol, Nicolas B Cowan, Adam P Showman, Curtis S Cooper, and S Thomas Megeath. A map of the day–night contrast of the extrasolar planet hd 189733b. *Nature*, 447(7141):183, 2007.

[49] Heather A Knutson, David Charbonneau, Lori E Allen, Adam Burrows, and S Thomas Megeath. The 3.6-8.0 μm broadband emission spectrum of hd 209458b: Evidence for an atmospheric temperature inversion. *The Astrophysical Journal*, 673(1):526, 2008.

[50] Heather A Knutson, David Charbonneau, Nicolas B Cowan, Jonathan J Fortney, Adam P Showman, Eric Agol, Gregory W Henry, Mark E Everett, and Lori E Allen. Multiwavelength constraints on the day-night circulation patterns of hd 189733b. *The Astrophysical Journal*, 690(1):822, 2008.

[51] Mark R Swain, Gautam Vasisht, and Giovanna Tinetti. The presence of methane in the atmosphere of an extrasolar planet. *Nature*, 452(7185):329, 2008.

[52] MR Swain, G Vasisht, G Tinetti, J Bouwman, Pin Chen, Y Yung, D Deming, and P Deroo. Molecular signatures in the near-infrared dayside spectrum of hd 189733b. *The Astrophysical Journal Letters*, 690(2):L114, 2008.

[53] B Scott Gaudi. Microlensing surveys for exoplanets. *Annual Review of Astronomy and Astrophysics*, 50:411–453, 2012.

[54] Ian A Bond, A Udalski, M Jaroszyński, NJ Rattenbury, B Paczyński, I Soszyński, L Wyrzykowski, MK Szymański, M Kubiak, O Szewczyk, et al. Ogle 2003-blg-235/moa 2003-blg-53: a planetary microlensing event. *The Astrophysical Journal Letters*, 606(2):L155, 2004.

[55] Christian Marois, Bruce Macintosh, Travis Barman, B Zuckerman, Inseok Song, Jennifer Patience, David Lafrenière, and René Doyon. Direct imaging of multiple planets orbiting the star hr 8799. *Science*, 322(5906):1348–1352, 2008.

[56] PF Lazorenko, M Mayor, M Dominik, F Pepe, D Segransan, and S Udry. Precision multi-epoch astrometry with vlt cameras fors1/2. *Astronomy & Astrophysics*, 505(2):903–918, 2009.

[57] MAC Perryman and T Schulze-Hartung. A&a 525. *A65*, 2011.

[58] Michael Perryman, Joel Hartman, Gáspár Á Bakos, and Lennart Lindegren. Astrometric exoplanet detection with gaia. *The Astrophysical Journal*, 797(1):14, 2014.

[59] Carl J Grillmair, Sean J Carey, John R Stauffer, Mark E Fisher, Ryan Olds, James G Ingalls, Jessica E Krick, William J Glaccum, Seppo Laine, Patrick J Lowrance, et al. Pointing effects and their consequences for spitzer irac exoplanet observations. In *Observatory Operations: Strategies, Processes, and Systems IV*, volume 8448, page 84481I. International Society for Optics and Photonics, 2012.

[60] Stephen R Kane. Detecting the signatures of uranus and neptune. *Icarus*, 214(1):327–333, 2011.

[61] M Auvergne, P Bodin, L Boisnard, J-T Buey, S Chaintreuil, G Epstein, M Jouret, T Lam-Trong, P Levacher, A Magnan, et al. The corot satellite in flight: description and performance. *Astronomy & Astrophysics*, 506(1):411–424, 2009.

[62] Douglas A Caldwell, Jeffery J Kolodziejczak, Jeffrey E Van Cleve, Jon M Jenkins, Paul R Gazis, Vic S Argabright, Eric E Bachtell, Edward W Dunham, John C Geary, Ronald L Gilliland, et al. Instrument performance in kepler's first months. *The Astrophysical Journal Letters*, 713(2):L92, 2010.

[63] Stephen T Bryson, Peter Tenenbaum, Jon M Jenkins, Hema Chandrasekaran, Todd Klaus, Douglas A Caldwell, Ronald L Gilliland, Michael R Haas, Jessie L Dotson, David G Koch, et al. The kepler pixel response function. *The Astrophysical Journal Letters*, 713(2):L97, 2010.

[64] Michael R Haas, Natalie M Batalha, Steve T Bryson, Douglas A Caldwell, Jessie L Dotson, Jennifer Hall, Jon M Jenkins, Todd C Klaus, David G Koch, Jeffrey Kolodziejczak, et al. Kepler science operations. *The Astrophysical Journal Letters*, 713(2):L115, 2010.

[65] Jessie L Christiansen, Jon M Jenkins, Douglas A Caldwell, Christopher J Burke, Peter Tenenbaum, Shawn Seader, Susan E Thompson, Thomas S Barclay, Bruce D Clarke, Jie Li, et al. The derivation, properties, and value of keplerâĂŹs combined differential photometric precision. *Publications of the Astronomical Society of the Pacific*, 124(922):1279, 2012.

[66] Ronald L Gilliland, William J Chaplin, Edward W Dunham, Vic S Argabright, William J Borucki, Gibor Basri, Stephen T Bryson, Derek L Buzasi, Douglas A Caldwell, Yvonne P Elsworth, et al. Kepler mission stellar and instrument noise properties. *The Astrophysical Journal Supplement Series*, 197(1):6, 2011.

[67] Ronald L Gilliland, William J Chaplin, Jon M Jenkins, Lawrence W Ramsey, and Jeffrey C Smith. Kepler mission stellar and instrument noise properties revisited. *The Astronomical Journal*, 150(4):133, 2015.

[68] NASA Astrophysics Division Senior Review. The nasa kepler mission: Exoplanet discovery, exoplanetary system architecture, stellar astrophysics, and the search for eta earth., 2012.

[69] Jon M Jenkins, Douglas A Caldwell, Hema Chandrasekaran, Joseph D Twicken, Stephen T Bryson, Elisa V Quintana, Bruce D Clarke, Jie Li, Christopher Allen, Peter Tenenbaum, et al. Overview of the kepler science processing pipeline. *The Astrophysical Journal Letters*, 713(2):L87, 2010.

[70] Jeffrey E Van Cleve and Douglas A Caldwell. Kepler instrument handbook. *Kepler Science Document, KSCI-19033-002, Edited by Michael R. Haas and Steve B. Howell*, 2016.

[71] Andrew Vanderburg and John Asher Johnson. A technique for extracting highly precise photometry for the two-wheeled kepler mission. *Publications of the Astronomical Society of the Pacific*, 126(944):948, 2014.

[72] Steve B Howell, Charlie Sobeck, Michael Haas, Martin Still, Thomas Barclay, Fergal Mullally, John Troeltzsch, Suzanne Aigrain, Stephen T Bryson, Doug Caldwell, et al. The k2 mission: characterization and early results. *Publications of the Astronomical Society of the Pacific*, 126(938):398, 2014.

[73] Erik A Petigura and Geoffrey W Marcy. Identification and removal of noise modes in kepler photometry. *Publications of the Astronomical Society of the Pacific*, 124(920):1073, 2012.

[74] Albert Piterman and Zoran Ninkov. Sub-pixel sensitivity maps for a back-illuminated ccd and the effects of non-uniform response on measurement accuracy. *Opt. Eng.*, 41:1192–1202, 2002.

[75] Daniel Kavaldjiev and Zoran Ninkov. Influence of non-uniform ccd pixel response on aperture photometry. *Opt. Eng*, 40(2):162–169, 2001.

[76] Tim Hardy, MR Baril, J Pazder, and JS Stilburn. Intra-pixel response of infrared detector arrays for jwst. In *High Energy, Optical, and Infrared Detectors for Astronomy III*, volume 7021, page 70212B. International Society for Optics and Photonics, 2008.

[77] Swaraj Bandhu Mahato, Joris De Ridder, Guy Meynants, Gert Raskin, and Hans Van Winckel. Measuring intra-pixel sensitivity variations of a cmos image sensor. *IEEE Sensors Journal*, 18(7):2722–2728, 2018.

[78] G Bruce Berriman. The nasa/ipac infrared science archive (irsa) as a resource in supporting observatory operations. In *Observatory Operations: Strategies, Processes, and Systems II*, volume 7016, page 701618. International Society for Optics and Photonics, 2008.

[79] James G Ingalls, Jessica E Krick, Sean J Carey, Seppo Laine, Jason A Surace, William J Glaccum, Carl C Grillmair, and Patrick J Lowrance. Intra-pixel gain variations and high-precision photometry with the infrared array camera (irac). In *Space Telescopes and Instrumentation 2012: Optical, Infrared, and Millimeter Wave*, volume 8442, page 84421Y. International Society for Optics and Photonics, 2012.

[80] Sarah Ballard, David Charbonneau, Drake Deming, Heather A Knutson, Jessie L Christiansen, Matthew J Holman, Daniel Fabrycky, Sara Seager, and Michael F A'Hearn. A search for a sub-earth-sized companion to gj 436 and a novel method to calibrate warm spitzer irac observations. *Publications of the Astronomical Society of the Pacific*, 122(897):1341, 2010.

[81] eoPortal Directory. Institute, space telescope science. hubble space telescope. http://www.stsci.edu/hst/wfpc2/analysis/wfpc2_dither_all.html.

[82] Peter W Sullivan, Joshua N Winn, Zachory K Berta-Thompson, David Charbonneau, Drake Deming, Courtney D Dressing, David W Latham, Alan M Levine, Peter R McCullough, Timothy Morton, et al. The transiting exoplanet survey satellite: simulations of planet detections and astrophysical false positives. *The Astrophysical Journal*, 809(1):77, 2015.

[83] V Suntharalingam, I Prigozhin, DJ Young, et al. Deep depletion ccd detectors for the transiting exoplanet survey satellite. In *Proc SPIE*, volume 9915, 2016.

[84] C Thayer, J Villasenor, S Kissel, B LaMarr, E Morgan, G Prigozhin, I Prigozhin, G Ricker, T Sauerwein, V Suntharalingam, et al. Testing and characterization of the tess ccds. In *Space Telescopes and Instrumentation 2016: Optical, Infrared, and Millimeter Wave*, volume 9904, page 99042X. International Society for Optics and Photonics, 2016.

[85] Akshata Krishnamurthy, Joel Villasenor, Sara Seager, George Ricker, and Roland Vanderspek. Precision characterization of the tess ccd detectors: Quantum efficiency, charge blooming and undershoot effects. *Acta Astronautica*, 160:46–55, 2019.

[86] A Krishnamurthy, J Villasenor, S Kissel, G Ricker, and R Vanderspek. An optical test bench for the precision characterization of absolute quantum efficiency for the tess ccd detectors. *Journal of Instrumentation*, 12(05):C05013, 2017.

[87] Luca Poletto, Alessio Boscolo, Maria-Guglielmina Pelizzo, Leonardo Placentino, and Giuseppe Tondello. Quantum efficiency measurement on a ccd detector in the 0.3-to 1100-nm spectral region. In *EUV, X-Ray, and Gamma-Ray Instrumentation for Astronomy VIII*, volume 3114, pages 617–624. International Society for Optics and Photonics, 1997.

[88] Donald E Groom, Christopher J Bebek, Maximilian Fabricius, Armin Karcher, William F Kolbe, Natalie A Roe, and Jens Steckert. Quantum efficiency characterization of lbnl ccd's: Part i. the quantum efficiency machine. In *Sensors, Cameras, and Systems for Scientific/Industrial Applications VII*, volume 6068, page 60680F. International Society for Optics and Photonics, 2006.

[89] Maximilian H Fabricius, Chris J Bebek, Donald E Groom, Armin Karcher, and Natalie A Roe. Quantum efficiency characterization of back-illuminated ccds: Part ii. reflectivity measurements. In *Sensors, Cameras, and Systems for Scientific/Industrial Applications VII*, volume 6068, page 60680G. International Society for Optics and Photonics, 2006.

[90] A Krishnamurthy, J Villasenor, C Thayer, S Kissel, G Ricker, S Seager, R Lyle, A Deline, E Morgan, T Sauerwein, et al. Quantum efficiency measurement of the transiting exoplanet survey satellite (tess) ccd detectors. In *Space Telescopes*

and Instrumentation 2016: Optical, Infrared, and Millimeter Wave, volume 9904, page 99042W. International Society for Optics and Photonics, 2016.

[91] Frank Scholze, Hans Rabus, and Gerhard Ulm. Spectral responsivity of silicon photodiodes: high-accuracy measurement and improved self-calibration in the soft x-ray spectral range. In *EUV, X-Ray, and Gamma-Ray Instrumentation for Astronomy VII*, volume 2808, pages 534–543. International Society for Optics and Photonics, 1996.

[92] Jon M Jenkins, Joseph D Twicken, Sean McCauliff, Jennifer Campbell, Dwight Sanderfer, David Lung, Masoud Mansouri-Samani, Forrest Girouard, Peter Tenenbaum, Todd Klaus, et al. The tess science processing operations center. In *Software and Cyberinfrastructure for Astronomy IV*, volume 9913, page 99133E. International Society for Optics and Photonics, 2016.

[93] Michael Fausnaugh. Tess psd plots for pointing error for sector 6 data, 2019.

[94] Christopher Masaru Pong, Matthew William Smith, Matthew W Knutson, Sungyung Lim, David W Miller, Sara Seager, Jesus Noel Samonte Villasenor, and Shawn D Murphy. One-arcsecond line-of-sight pointing control on exoplanetsat, a three-unit cubesat. 2011.

[95] Christopher M Pong. On-orbit performance and operation of the attitude and pointing control subsystems on asteria. In *Proc. of the 32nd Annual AIAA/USU Conf. on Small Satellites*, 2018.

[96] Matthew W Smith, Amanda Donner, Mary Knapp, Christopher M Pong, Colin Smith, Jason Luu, P Pasquale, and Brian Campuzano. On-orbit results and lessons learned from the asteria space telescope mission. In *Proceedings of the AIAA/USU Conference on Small Satellites, The Year in Review, SSC18-I-08. http://digitalcommons. usu. edu/smallsat/2018/all2018/08*, 2018.

[97] Mary Knapp, Sara Seager, Brice-Olivier Demory, Matthew Smith, Akshata Krishnamurthy, Christropher Pong, Amanda Donner, et al. Demonstrating high precision photometry with a cubesat: Asteria observations of 55 cancri e. *in-prep*, 2019.

[98] Matthew William Smith et al. *Model-based requirement definition for instrument systems.* PhD thesis, Massachusetts Institute of Technology, 2014.

[99] BAE systems. Fairchild imaging cis2521f cmos imager datasheet, man 0101rev h, 2014.

[100] Ophir. Mks instruments integrating spheres. `https://www.ophiropt.com/laser--measurement/knowledge-center/article/10145`.

[101] James R Janesick. Photon transfer. *Bellingham: SPIE*, 2007.

[102] James R Janesick et al. *Scientific charge-coupled devices*, volume 117. SPIE press Bellingham, 2001.

[103] Changmiao Hu, Yang Bai, and Ping Tang. Denoising algorithm for the pixel-response non-uniformity correction of a scientific cmos under low light conditions. *The International Archives of Photogrammetry, Remote Sensing and Spatial Information Sciences*, 41:749, 2016.

[104] Steven S Vogt, Jennifer Burt, Stefano Meschiari, R Paul Butler, Gregory W Henry, Songhu Wang, Brad Holden, Cyril Gapp, Russell Hanson, Pamela Arriagada, et al. Six planets orbiting hd 219134. *The Astrophysical Journal*, 814(1):12, 2015.

[105] F Motalebi, S Udry, Michaël Gillon, C Lovis, D Ségransan, Lars A Buchhave, BO Demory, L Malavolta, Courtney Danielle Dressing, D Sasselov, et al. The harps-n rocky planet search-i. hd 219134 b: A transiting rocky planet in a multi-planet system at 6.5 pc from the sun. *Astronomy & Astrophysics*, 584:A72, 2015.

[106] Michaël Gillon, Brice-Olivier Demory, Valérie Van Grootel, Fatemeh Motalebi, Christophe Lovis, Andrew Collier Cameron, David Charbonneau, David Latham, Emilio Molinari, Francesco A Pepe, et al. Two massive rocky planets transiting a k-dwarf 6.5 parsecs away. *Nature Astronomy*, 1(3):0056, 2017.

[107] Xavier Dumusque, Francesco Pepe, Christophe Lovis, Damien Ségransan, Johannes Sahlmann, Willy Benz, François Bouchy, Michel Mayor, Didier Queloz, Nuno Santos, et al. An earth-mass planet orbiting α centauri b. *Nature*, 491(7423):207, 2012.

[108] Sara Seager and et al. A constellation of small satellites to search for a transiting earth-size planet in an earth-like orbit about a bright sun-like star). *in prep*, 2020.

[109] eoPortal Directory. Teledyne e2v datasheet for ccd47-20 back illuminated aimo frame transfer high performance ccd sensor. `https://www.teledyne-e2v.com/shared/content/resources/File/documents/Imaging\%202017/CCDs\%20-\%20Frame\%20Transfer\%20Scientifc/CCD47-20/3.\%20BI,\%20AIMO/A1A-100041_9_v1.pdf`.

[110] eoPortal Directory. Teledyne e2v back-illuminated scmos detector datasheet. `https://www.e2v.com/resources/account/download-datasheet/3664`.

[111] eoPortal Directory. Kuro 2048b back-illuminated scmos detector datasheet. `https://www.princetoninstruments.com/userfiles/files/assetLibrary/Datasheets/KURO-datasheet-ver-A2_3-10-19-17.pdf`.

[112] Mark A Chodas. *Addressing deep uncertainty in space system development through model-based adaptive design.* PhD thesis, Massachusetts Institute of Technology, 2019.

[113] Evgenya L Shkolnik, David R Ardila, Travis Barman, Matthew Beasley, Bowman Judd, Varoujan Gorjianb, Daniel Jacobs, April Jewell, Joe Llama, Mary Knapp, et al. A dedicated ultraviolet cubesat for astrophysics, sparcs (star planet activity research cubesat). In *AGU Fall Meeting Abstracts*, 2018.

[114] David R Ardila, Evgenya Shkolnik, Paul Scowen, April Jewell, Shouleh Nikzad, Judd Bowman, Michael Fitzgerald, Daniel Jacobs, Constance Spittler, Travis Barman, et al. The star-planet activity research cubesat (sparcs): A mission to understand the impact of stars in exoplanets. *arXiv preprint arXiv:1808.09954*, 2018.